

Development, Modeling and Design Optimization of a Variable Stiffness and Damping Bypass MR Fluid Damper with Annular-Radial Gap

Moustafa Abdalaziz

A Thesis
in the Department of
Mechanical, Industrial, and Aerospace Engineering

Presented in Partial Fulfilment of the Requirements
for the Degree of

Doctor of Philosophy (Mechanical Engineering) at

Concordia University
Montreal, Quebec, Canada

December 2022

© Moustafa Abdalaziz, 2022

CONCORDIA UNIVERSITY
SCHOOL OF GRADUATE STUDIES

This is to certify that the thesis prepared

By: Moustafa Abdalaziz

Entitled: Development, Modeling and Design Optimization of a Variable Stiffness and Damping Bypass MR Fluid Damper with Annular-Radial Gap

and submitted in partial fulfillment of the requirements for the degree of

Doctor of Philosophy (Mechanical, Industrial, and Aerospace Engineering)

complies with the regulations of the University and meets the accepted standards with respect to originality and quality.

Signed by the final examining committee:

_____ Chair
Dr. Aiman Hanna

_____ External Examiner
Dr. Norman Wereley

_____ External to Program
Dr. Emre Erkmen

_____ Examiner
Dr. Subhash Rakheja

_____ Examiner
Dr. Ayhan Ince

_____ Thesis Supervisor
Dr. Ramin Sedaghati

Approved by

_____ Dr. Muthukumaran Packirisamy, Graduate Program Director

December 13, 2022

_____ Dr. Mourad Debbabi, Dean
Gina Cody School of Engineering and Computer Science

ABSTRACT

Development, Modeling and Design Optimization of a Variable Stiffness and Damping Bypass MR Fluid Damper with Annular-Radial Gap

Moustafa Abdalaziz, Ph.D.
Concordia University, 2022.

Magneto-rheological (MR) fluid dampers (MRFDs) are adaptive semi-active devices that hold great promise for real-time vibration control applications due to their field-dependent damping properties, fail-safe feature, fast response (in milliseconds), and low power requirement. While MRFDs have been successfully developed for on-road vehicles and civil engineering applications, very limited studies have been conducted on the development of MRFDs for off-road and particularly tracked vehicles. Furthermore, MRFDs with combined annular and radial bypass fluid channels have recently shown superior performance compared with those conventional MRFDs with single annular/radial fluid gaps. However, limited studies have been dedicated toward developing such MRFDs with the combined fluid flow path. There are also limited research studies on MRFDs with variable damping and variable stiffness (VSVD), which can significantly enhance the vibration isolation performance as compared with traditional variable damping MRFDs. Many key aspects of VSVD-MRFDs, such as design, physic-based modelling, and experimental characterization, have yet to be addressed. The existing VSVD devices are complicated in design and have a limited capacity to be implemented in practical applications.

To address the above-mentioned knowledge gaps, in this research dissertation, a large-scale bypass MRFD with an annular-radial valve was designed and developed. The developed MRFD possesses VSVD properties and can be implemented in off-road tracked vehicles. For this purpose, first, a quasi-static physic-based model of the proposed MRFD was formulated using the Bingham plastic characteristics of the MR fluids. The magnetic circuit of the MR valve (MRV) was analytically formulated to evaluate the magnetic flux densities in MR fluid gap regions. Magneto-static finite element model of the MR valve has also been conducted to verify the analytical results. A design optimization problem was subsequently formulated to identify the optimal geometrical parameters of the MRV to maximize the damper dynamic range under specific volume, geometrical and magnetic field constraints. The optimized MRV can theoretically generate an on-state damping force and high dynamic range of 7.4 kN and 6.7 under a piston velocity of 12.5 mm/s. The damper also has a large piston stroke of 180 mm that makes it suitable for off-road vehicle applications.

In the next step, a physic-based model was developed to theoretically investigate the non-linear dynamic behaviour of the proposed MRFD. The developed physic-based model, which is also based on MR fluid Bingham behaviour, can consider the unsteady behaviour of the MR fluid. In contrast to widely use phenomenological models, which are experiment based in which their characteristic parameters must be identified from experimental data, the proposed dynamic model depends only on the physics of the problem with no parameters to be identified experimentally. This is of paramount importance for the analysis and design of MRFDs at early design stages. Results from the model suggest that the MRFD experiences non-linear hysteresis behaviour due to the unsteady MR fluid behaviour at high loading conditions (e.g., large deformation and high frequency). The dynamic model was further modified to consider the fluid compressibility effect,

which has been mostly neglected in previous studies, despite its significant contribution to the hysteretic response of MRFDs at low-velocity regions.

The proposed MRFD was fabricated and experimentally characterized to validate the design optimization strategy and examine the developed quasi-static, dynamic, and modified dynamic models. Extensive experimental tests were conducted to investigate the dynamic characteristics of the proposed MRFD considering wide ranges of excitation frequency, loading amplitude, and electrical currents. Figure of merits, including equivalent viscous damping and dynamic range obtained from experimental data under varied loading conditions were in good agreement with those obtained theoretically. Results also suggest the proposed modified physic-based dynamic model could provide an accurate description of the non-linear hysteresis behaviour of the MRFDs observed experimentally.

Finally, the developed bypass MRFD has been designed and integrated with a mechanical spring to realize VSVD capability for the MRFD. The proposed bypass VSVD-MRFD with an annular-radial gap was also experimentally characterized. The dynamic characteristics of the VSVD-MRFD were conducted under a wide range of excitation frequency, loading amplitude, and electrical current. The force-displacement, and the force-velocity hysteresis curves were obtained. Both the equivalent stiffness and damping, dynamic range, and their dependency on the loading conditions were investigated. The results revealed that the VSVD-MRFD is capable of adjusting its stiffness and damping properties to a large extent, thereby providing a high damping force and dynamic range.

The developed dynamic physic-based model can provide an essential guidance on development of bypass MRFD with annular-radial gap at early design stages. The proposed novel VSVD-MRFD can also be potentially employed in off-road suspension systems for suppressing the vibration amplitude under unexpected loading conditions.

Dedication

This Ph.D. dissertation is dedicated to my beloved family

To my father's soul

To my mother and my brothers

To my wife and my kids

for their endless love, support, and encouragement.

Acknowledgment

First and foremost, I would like to thank “ALLAH”. You have given me the power to believe in myself and pursue my dreams. I could never have done this without the faith I have in you, the Almighty.

I would also like to express my deepest sense of gratitude to my thesis supervisor, Prof. Ramin Sedaghati for providing such an unparalleled opportunity for me to be a part of his research group, and for his patience, motivation, crucial guidance, support, and immense knowledge. This thesis would not have been possible without his continuous support and encouragement. His guidance and critiques have helped me to do more in-depth research, write a better research article, and showed me how I could improve my work. I am really admiring him so much. I have been very lucky to have a supervisor like him.

Special thanks to the Egyptian government that financially supported my program, giving me this golden opportunity to complete my graduate studies at Concordia University, one of the best universities here in Canada.

I sincerely acknowledge the truthful advice and enriching discussions from my examination committee members, Dr. Norman Wereley, Dr. Subhash Rakheja, Dr. Ayhan Ince and Dr. Emre Erkmen.

I would like to thank Prof. Subhash Rakheja for his support, valuable comments and for providing all facilities during the experimental stages.

I gratefully acknowledge Dr. Hossein Vatandoost for his valuable comments, participation, and assistance in conducting experimental tests. I would also like to thank Dr. Wael Elsaady for his appreciated advice since 2011.

Likewise, I would like to thank all my professors in Military Technical College, Cairo, Egypt. Their great help and support during my undergraduate and graduate studies really helped me to have a strong academic background and to continue my thesis program to achieve what I aimed for.

Most importantly, none of this would have been possible without the love and patience of my family. I would like to express my love and gratitude to my father. He is still alive inside me. I would like to extend my thanks and appreciation to my mother and brothers: Ahmed and Islam. Although you are thousands of miles away, you were always there whenever I needed you. I am thankful to you for your inspiration and encouragement. I would like to thank my wife’s family for their support, kindness and encouragement.

Lastly, most of all for my loving, supportive, encouraging, and patient wife Shereen and my kids Eyad, Talia and Saif. Thanks for your faithful support during all the stages of this research is so appreciated. Thank you so much.

Table of Contents

List of Figures.....	x
List of Tables.....	xv
Nomenclature.....	xvi
1. INTRODUCTION AND SCOPE OF THE THESIS	1
1.1 Literature review.....	4
1.1.1 MR fluid.....	4
1.1.2 MR fluid dampers (MRFDs) Technology	8
1.1.3 Variable stiffness and damping MRFDs.....	14
1.2 Motivations and objectives	17
1.3 Organization of the Dissertation	19
2. QUASI-STATIC MODELING AND DESIGN OPTIMIZATUON OF A LARGE- CAPACITY ANNULAR-RADIAL BYPASS MAGNETORHEOLOGICAL DAMPER21	
2.1 Introduction.....	21
2.2 Principal and configuration of the proposed MRFD	23
2.2.1 Principal of the design.	23
2.2.2 Configuration of the MRFD	24
2.3 Quasi-static Formulation for the MR fluid damper	26
2.3.1 Analytical analysis of MR valve magnetic circuit.....	31
2.3.2 Magneto-static finite element analysis	34
2.4 Design optimization formulation of the of the MRFD	35
2.5 Results of Simulations	38
2.5.1 Optimization results.....	38
2.5.2 Magnetic circuit results.....	40
2.6 Experimental Method	43
2.6.1 Experimental validation of the magnetic circuit model.....	45
2.6.2 Experimental validation of the otimization strategy of the fabricated MRFD	47
2.7 Summary.....	51
3. DYNAMIC PHYSIC MODELING OF ANNULAR-RADIAL MAGNEORHEOLOGICAL DAMPER.....	53
3.1 Introduction.....	53

3.2 Configuration of the annular-radial MRFD	56
3.3 Quasi-static model of MRFD with bypass annular-radial gaps considering friction effect	58
3.4 Dynamic Modelling of bypass MRFD	60
3.4.1 Mathematical modeling of unsteady fluid behaviour	60
3.4.2 Modified dynamic model: considering the fluid compressibility effect.....	66
3.5 Validation of the Dynamic modeling	69
3.6 Summary.....	75
4. COMPREHENSIVE DYNAMIC CHARACTERIZATION OF A LARGE-CAPACITY ANNULAR-RADIAL MAGNETORHEOLOGICAL DAMPER	77
4.1 Introduction.....	77
4.2 Development of the MRFD prototype.....	80
4.3 Experimental characterization	81
4.3.1 Test setup	81
4.3.2 Experimental measurements	82
4.3.3 Friction test	83
4.4 Experimental analysis.....	84
4.4.1 Friction analysis.....	84
4.4.2 Nonlinear hysteresis dynamic analysis of the MRFD	87
4.4.3 Dynamic range and equivalent viscous damping	93
4.5 Modification in the MR bypass valve design	98
4.6 Summary.....	102
5. DYNAMIC CHARACTERIZATION OF VARIABLE STIFFNESS- VARIABLE DAMPING MAGNETORHEOLOGICAL DAMPER.....	103
5.1 Introduction.....	103
5.2 Design and analysis of the VSVD-MRFD.....	105
5.2.1 Structure configuration of the proposed VSVD-MRFD.....	105
5.2.2 Working principle.....	107
5.2.3 Fabrication of the proposed VSVD-MRFD.....	108
5.3 Experimental characterization of the VSVD-MRFD	110
5.3.1 Test setup	110
5.3.2 Experimental measurements	111
5.4 Results and discussion	111
5.4.1 Nonlinear hysteresis dynamic analysis of the VSVD-MRFD	111

5.4.2 Dynamic range analysis	117
5.4.3 Damping variability	118
5.4.4 Stiffness variability	120
5.5 Summary	123
6. CONTRIBUTIONS, CONCLUSIONS AND RECOMMENDATIONS.....	124
6.1 Major contributions	124
6.2 Major Conclusions.....	125
6.3 Publications.....	128
6.4 Recommendations for future works.....	129
7. REFERENCES.....	130
8. Appendix A	163
9. Appendix B	165
10. Appendix C	170
11. Appendix D	173
12. Appendix E	184

LIST OF FIGURES

Figure 1-1	Effect of magnetic Field on MR fluid (a) magnetic field off and (b) magnetic field on.	5
Figure 1-2	MR fluid operation modes [38].	6
Figure 1-3	General behaviour of MR fluids in post-yield region.	8
Figure 1-4	Construction of MRFD (a) internal valve [37] (b) bypass valve [69].	8
Figure 1-5	VSVD working principles (a) connection in Series (b) connection in Parallel.	15
Figure 2-1	M113 off-road vehicle suspension system (a) M113 tracked vehicle undercarriage components [174] and (b) shock absorber's dimensions.	24
Figure 2-2	Cross-sectional view of the proposed outer bypass MRFD (a) its related MR valve consists of both annular and radial fluid flow channels and (b). annular-radial MR fluid bypass valve gaps.	25
Figure 2-3	Shear yield strength of MRF-132DG.	29
Figure 2-4	MR fluid bypass valve main dimensions.	30
Figure 2-5	MR valve Magnetic Circuit (a) annular gap circuit and (b) radial gap circuit.	32
Figure 2-6	The B-H curve of MR fluid and bypass valve material (a) B-H curve MRF-132 DG [175] and b) B-H curve steel 1006 [179].	34
Figure 2-7	By-pass MRFD with main identified design parameters.	36
Figure 2-8	Iteration history of the optimized parameters.	39
Figure 2-9	Magnetic flux distribution at excitation current 1.5 A.	41
Figure 2-10	Magnetic flux density along the annular-radial path length under different applied current.	41
Figure 2-11	Magnetic flux intensity along the annular-radial path length under different applied current.	42
Figure 2-12	Magnetic flux density at different coil currents (a) annular gap and (b) radial gap.	43
Figure 2-13	Fabricated MRFD (a) MRFD components and (b) the prototype MRFD.	44
Figure 2-14	Measurement of the magnetic flux density along the MRFD's annular gap.	46
Figure 2-15	Magnetic flux distribution at excitation current 2 A.	46
Figure 2-16	Comparison of the measured and FE estimation of the average magnetic flux density along the annular gap of the MR valve.	47
Figure 2-17	Test setup of the fabricated bypass MRFD.	48
Figure 2-18	The measured data at excitation frequency of 1 Hz and displacement of 1 mm (a) force-displacement and (b) force-velocity.	49
Figure 2-19	The measured data at excitation frequency of 2 Hz and displacement of 1 mm(a) force-displacement and (b) force-velocity.	49
Figure 2-20	Variation of the controllable damping force with applied currents(a) excitation frequency of 1 Hz and amplitude of 1 mm and (b) excitation frequency of 2 Hz and amplitude of 1 mm.	50
Figure 2-21	Variation of the damping coefficient with applied currents (a) excitation frequency of 1 Hz and amplitude of 1 mm and (b) excitation frequency of 2 Hz and amplitude of 1 mm.	51
Figure 2-22	Variation of the dynamic range of the novel MRFD with respect to the applied current (a) excitation frequency of 1 Hz and amplitude of 1 mm and (b) excitation frequency of 2 Hz and amplitude of 1 mm.	51

Figure 3-1	(a) Annular-radial MRFD, (b) MR bypass valve geometrical parameters.	57
Figure 3-2	Variation of the magnetic flux density with respect to current in (a) annular gap and (b) radial gap.	60
Figure 3-3	(a) MR fluid in rectangular flow duct schematic and (b) differential fluid element.	61
Figure 3-4	MRFD characteristics under sinusoidal excitation of frequency 2 Hz and displacement of 1 mm at applied current of 0.5 A(a) force-displacement, (b) force-velocity.	70
Figure 3-5	MRFD characteristics under sinusoidal excitation of frequency 2 Hz and displacement of 1 mm at applied current of 1 A (a) force-displacement, (b) force-velocity.	70
Figure 3-6	MRFD characteristics under sinusoidal excitation of frequency 2 Hz and displacement of 1 mm at applied current of 2 A (a) force-displacement, (b) force -velocity.	71
Figure 3-7	MRFD characteristics under sinusoidal excitation of frequency 20 Hz and displacement of 10 mm at applied current of 1 A (a) force-displacement, (b) force-velocity.	72
Figure 3-8	MRFD characteristics under sinusoidal excitation of frequency 20 Hz and displacement of 30 mm at applied current of 1 A (a) force-displacement, (b) force -velocity.	72
Figure 3-9	MRFD characteristics under sinusoidal excitation of frequency 40 Hz and displacement of 30 mm at applied current of 1 A (a) force-displacement, (b) force -velocity.	73
Figure 3-10	MRFD characteristics under sinusoidal excitation of frequency 2 Hz and displacement of 1mm at applied current of 0.5 A(a) force-displacement, (b) force-velocity.	74
Figure 3-11	MRFD characteristics under sinusoidal excitation of frequency 2 Hz and displacement of 1 mm at applied current of 1 A(a) force-displacement, (b) force-velocity.	74
Figure 3-12	MRFD characteristics under sinusoidal excitation of frequency 2 Hz and displacement of 1 mm at applied current of 2 A (a) force-displacement, (b) force-velocity.	75
Figure 4-1	MRFD prototyped	81
Figure 4-2	Experimental characterization test setup: (a) the prototyped MRFD filled with MR fluid, and (b) the full test rig for implementing the dynamic analysis of the MRFD.	82
Figure 4-3	Friction surfaces in the proposed MRFD.	84
Figure 4-4	The measured friction force of the MRFD under loading frequency of 1 Hz in the absence of the MR fluid: (a) force-time, (b) force-displacement and (c) force-velocity.	85
Figure 4-5	The measured friction force of the MRFD under displacement amplitude of 3 mm in the absence of the MR fluid: (a) force-displacement and (b) force-velocity.	86
Figure 4-6	The measured friction force of the MRFD under displacement amplitude of 5 mm in the absence of the MR fluid: (a) force-displacement and (b) force-velocity.	86

Figure 4-7	The measured friction force of the MRFD under excitation frequency of 0.09 Hz and displacement of 3, 5 and 10 mm in the presence of the MR fluid: (a) force-displacement and (b) force-velocity.	87
Figure 4-8	The measured time-response (a), force-displacement (b) and force-velocity (c) characteristics of the MRFD under loading frequency of 0.5 Hz at the displacement amplitude of 5 mm.	88
Figure 4-9	The measured time-response (a), force-displacement (b) and force-velocity (c) characteristics of the MRFD under loading frequency of 1 Hz at the displacement amplitude of 2.5 mm.	89
Figure 4-10	The frequency dependent characteristics of the MRFD under zero electrical current and constant displacement amplitude of 2.5 mm: (a) force-displacement and (b) force-velocity.	90
Figure 4-11	The frequency dependent characteristics of the MRFD under 0.5 A electrical current and constant displacement amplitude of 2.5 mm: (a) force-displacement and (b) force-velocity.	91
Figure 4-12	The amplitude dependent characteristics of the MRFD under zero electrical current and constant loading frequency of 1 Hz: (a) force-displacement and (b) force-velocity.	92
Figure 4-13	The amplitude dependent characteristics of the MRFD under 1.5 A electrical current and constant loading frequency of 1 Hz: (a) force-displacement and (b) force-velocity.	93
Figure 4-14	The measured data (a) force-displacement and (b) force-velocity characteristics of the MRFD under loading frequency of 4 Hz at the displacement amplitude of 7 mm.	93
Figure 4-15	The effect of displacement amplitude and loading frequency on the dynamic range of the fabricated MRFD under: (a) loading frequency of 2 Hz and (b) displacement amplitude of 2.5 mm.	95
Figure 4-16	The schematical representation of the equivalent viscous damping coefficient (C_{eq}) as the slope of major axis of the measured force-velocity curves under loading frequency of 2 Hz and displacement amplitude of the 1mm.	96
Figure 4-17	The variations of the calculated the equivalent viscous damping coefficient (C_{eq}) with respect to applied current considering different displacement amplitudes. C_{eq} calculated by the energy method (a) and the slope of major axis of the measured force-velocity curves (b) under loading frequency of 1 Hz.	97
Figure 4-18	The variations of the calculated the equivalent viscous damping coefficient (C_{eq}) with respect to applied current considering varied loading frequencies. C_{eq} calculated by the energy method (a) and the slope of major axis of the measured force-velocity curves (b) under displacement amplitude of 2.5 mm.	98
Figure 4-19	The comparison of force–displacement and force-velocity characteristics of the MR damper with modified MR valve (a), (b) with the initial design of MR valve (c), (d) under at excitation frequency of 2 Hz and displacement of 1 mm.	100
Figure 4-20	The comparison of the dynamic indices (dynamic range (a) and equivalent damping (b)) characteristics of the modified MR valve with the initial design	101

	of MR valve under at excitation frequency of 2 Hz and displacement of 1 mm.	
Figure 5-1	Cross-sectional view of the proposed VSVD-MRFD with annular-radial bypass valve.	106
Figure 5-2	Scheme of the working principle of the VSVD-MRFD.	107
Figure 5-3	Basic dimensions of the proposed VSVD-MRFD.	108
Figure 5-4	(a). The main components of the proposed VSVD-MRFD and (b) the prototyped VSVD-MRFD.	109
Figure 5-5	Photograph of the full test setup implemented with the fabricated VSVD-MRFD.	111
Figure 5-6	The measured dynamic characteristics of VSVD-MRFD under loading frequency of 0.5 Hz at the displacement amplitude of 1 mm (a) force-displacement and (b) force-velocity.	112
Figure 5-7	The measured dynamic characteristics of VSVD-MRFD under loading frequency of 1 Hz at the displacement amplitude of 2.5 mm (a) force-displacement and (b) force-velocity.	113
Figure 5-8	The measured dynamic characteristics of VSVD-MRFD under loading frequency of 2 Hz at the displacement amplitude of 1 mm (a) force-displacement and (b) force-velocity.	113
Figure 5-9	The frequency dependent characteristics of the VSVD-MRFD under 1 A electrical current and constant displacement amplitude of 1 mm: (a) force-displacement, (b) force-velocity.	114
Figure 5-10	The frequency dependent characteristics of the VSVD-MRFD under 2 A electrical current and constant displacement amplitude of 1 mm: (a) force-displacement, (b) force-velocity.	115
Figure 5-11	The amplitude dependent characteristics of the VSVD-MRFD under 0.5 A electrical current and constant loading frequency of 1 Hz: (a) force-displacement, (b) force-velocity.	116
Figure 5-12	The amplitude dependent characteristics of the VSVD-MRFD under 1.5 A electrical current and constant loading frequency of 1 Hz: (a) force-displacement, (b) force-velocity.	116
Figure 5-13	The measured data (a) force-displacement and (b) force-velocity characteristics of the VSVD-MRFD under loading frequency of 4 Hz at the displacement amplitude of 2.5 mm.	117
Figure 5-14	The effect of displacement amplitude and loading frequency on the dynamic range of the VSVD-MRFD under: (a) loading frequency of 1 Hz, (b) displacement amplitude of 2.5 mm.	118
Figure 5-15	The variations of the calculated the equivalent viscous damping coefficient (C_{eq}) with respect to applied current considering different displacement amplitudes. C_{eq} calculated by the energy method (a) and the slope of major axis of the measured force-velocity curves (b) under loading frequency of 2 Hz.	119
Figure 5-16	The variations of the calculated the equivalent viscous damping coefficient (C_{eq}) with respect to applied current considering varied loading frequencies. C_{eq} calculated by the energy method (a) and the slope of major axis of the measured force-velocity curves (b) under displacement amplitude of 2.5 mm.	120

Figure 5-17	The variations of the calculated equivalent stiffness coefficient (Keq) with respect to applied current considering different displacement amplitudes (a) under loading frequency of 1 Hz and (b) under loading frequency of 2 Hz.	121
Figure 5-18	The variations of the calculated equivalent stiffness coefficient (Keq) with respect to applied current considering varied loading frequencies. (a) under displacement amplitude of 1 mm and (b) under displacement amplitude of 2.5 mm.	122
Figure C-1	APC M113 undercarriage b- M113 half mathematical model [276].	171
Figure D-1	MRFD cylinder.	173
Figure D-2	MRFD piston rod.	174
Figure D-3	MRFD main piston.	175
Figure D-4	Floating piston.	176
Figure D-5	Upper cylinder cover.	177
Figure D-6	Piston rod guider.	178
Figure D-7	Piston rod end cap.	179
Figure D-8	Cylinder end cap.	180

LIST OF TABLES

Table 2-1	The proposed MRFD initial parameters.	30
Table 2-2	Magnetic circuit parameters of the MR fluid bypass valve (Annular gap).	33
Table 2-3	Magnetic circuit parameters of the MR fluid bypass valve (Radial gap).	34
Table 2-4	Main design parameters and their assigned lower and bounds.	36
Table 2-5	MR fluid and valve material properties.	36
Table 2-6	Genetic Algorithm optimum points in (mm).	39
Table 2-7	SQP global optimum solution (mm).	40
Table 2-8	Initial base design and Optimized geometrical dimensions and performance indices	40
Table 2-9	Analytical results for annular and radial ducts magnetic circuit.	40
Table 2-10	Average numerical results for annular and radial gaps magnetic circuit using FEMM.	42
Table 2-11	Comparison between the parameters and performance of the optimized and fabricated MR bypass valve.	45
Table 3-1	Annular-radial MRFD parameters and MR fluid properties.	58
Table 3-2	Main parameters of the model.	69
Table 4-1	The test matrix of the friction experiments.	83
Table 4-2	The calculated equivalent viscous damping coefficient (C_{eq}) of the MRFD using two methods.	97
Table 4-3	Comparison of physical parameter and dynamic index of the initial MR valve with the modified design.	99
Table 4-4	Comparison of research MRFD to reported studies for off-road vehicles.	102
Table 5-1	Main parameters of the proposed VSVD-MRFD.	110
Table 5-2	Specification of the Springs.	110
Table 5-3	The calculated equivalent viscous damping coefficient (C_{eq}) of the MR damper using two approaches.	119
Table 5-4	The calculated equivalent stiffness coefficient (K_{eq}) of the VSVD-MRFD under different applied currents.	122
Table C-1	Summarized studies for improving M113 suspension dynamics	171

NOMENCLATURE

F_d	Static damper force	B	Magnetic flux density
F_{sg}	Spring force	A_f	Floating piston cross-sectional area
F_η	Viscous force	D_f	Floating piston diameter
F_τ	Controllable yield force	C_{vis}	Passive viscous coefficient
ΔP_η	Pressure drop due to viscous	R_d	Annular channel radius
ΔP_τ	Pressure drop due to shear stress	R_o	Radial gap outer radius
ΔP_a	Pressure drop in the annular gap	R_i	Radial gap inner radius
$\Delta P_{\eta a}$	Pressure drop due to viscous in the annular gap	λ_d	Dynamic range
$\Delta P_{\tau a}$	Pressure drop due to shear stress in the annular gap	F_{on}	On-state damping force
ΔP_r	Pressure drop in the radial gap	F_{off}	Off-state damping force
$\Delta P_{\eta r}$	Pressure drop due to viscous in the radial gap	L	MR valve height
$\Delta P_{\tau r}$	Pressure drop due to shear stress in the radial gap	w_c	Coil width
ΔP_o	Pressure drop in the orifice duct	μ_f	MR fluid relative permeability
A_p	Cross-sectional area of the piston	μ_j	Steel relative permeability
A_r	Cross-sectional area of the piston rod	μ_o	Permeability of free space
Q	Volume flow rate	d_w	Copper wire (gage AWG22) diameter
d	Flow channel annular or radial gap size	N_c	Number of coils (turns)
D_m	Annular channel diameter	c	Flow velocity profile function coefficient
D_o	Radial gap outer diameter	P	MR Fluid pressure
D_i	Radial gap inner diameter	τ_{xy}	Fluid shear stress at the coordinate y
c_a	Flow velocity profile coefficient in annular gap	m	Mass of the a given fluid element
c_r	Flow velocity profile coefficient in radial gap	u	Fluid velocity
η	MR fluid base viscosity	ρ	Fluid density
L_o	Orifice duct length	h_o	Distance from the centerline to the point that the fluid begins to deform.
L_a	Length of the annular flow duct	u_p	Inlet velocity
L_c	MR valve coil length	$Q(t)$	Inlet volume flow rate
\dot{x}_p	Piston velocity	U_{max}	Maximum flow velocity
$\tau(B)$	Field dependent yield stress of the MR fluid	B_a	Magnetic flux density in annular gap

B_r	Magnetic flux density in radial gap	U	Energy dissipated over one cycle
ν	Kinematic viscosity	f	Frequency
ψ_p	Particular solution	C_{eq}	Equivalent damping
z_j	Poles	X_0	Amplitude of the input excitation
n	Order of poles z_j	$[F_d]_{v_{max}}$	Maximum damping force corresponding to the maximum piston velocity
A_0	Excitation Amplitude	$[F_d]_{v_{min}}$	Minimum damping force corresponding to the minimum piston velocity
ω	Excitation frequency	K_{eq}	Equivalent Stiffness
A, B	Constant parameters	$[F_d]_{D_{max}}$	Maximum damping force corresponding to the maximum piston stroke
β	Dynamic friction coefficient	$[F_d]_{D_{min}}$	Minimum damping force corresponding to the minimum piston stroke
V_{ui}	Initial volume of upper chamber	v_{max}	Maximum piston velocity
V_{li}	Initial volume of lower chamber	v_{min}	Minimum piston velocity
V_{fi}	Initial volume of air chamber	D_{max}	Maximum piston stroke
P_u	Pressure in upper chamber	D_{min}	Minimum piston stroke
P_l	Pressure in lower chamber	I	Applied current
β	Dynamic friction coefficient	B_u	Bulk modulus of MR fluid in upper chamber
V_{ui}	Initial volume of upper chamber	B_l	Bulk modulus of MR fluid in lower chamber
L_u	Length of the upper chamber	B_{air}	Reference bulk modulus of MR fluid
L_l	Length of the lower chamber	B_f	Reference bulk modulus of air
L_f	Length of the air chamber	MRFD	Magnetorheological fluid damper
φ_u	Air volume fractions in the rebound	MRV	Magnetorheological valve
φ_l	Air volume fractions in the compression	VSVD	Variable stiffness and variable damping
V_{li}	Initial volume of lower chamber	BP	Bingham Plastic
V_{fi}	Initial volume of air chamber		
P_u	Pressure in upper chamber		
P_l	Pressure in lower chamber		

CHAPTER 1

INTRODUCTION AND SCOPE OF THE THESIS

Vibration has a significant adverse effect on human operating ground vehicles which may range from chronic neck and back pain and reduced functionality to spinal injury under prolonged exposure to whole-body vibration (WBV) [1–4]. Moreover, excessive vibration can cause the premature failure of elements in vehicles[5,6]. The vehicle’s primary suspension system plays a major role in the mitigation of WBV [7,8]. Suspension systems can be categorized as passive, active, and semi-active systems. The passive suspension systems typically consist of spring and damping elements in which their constant parameters are designed for specific operating condition (e.g., around a fixed frequency). Although passive systems have been widely used in vehicle suspension systems due to their reliability and cost-effective features, they have shown performance limitations under varied operating conditions [9]. The active suspension systems can perfectly neutralize vibration in a broad range of excitation frequencies by providing variable external actuation forces. However, the practical implementation of such active systems has been generally limited mainly partly due to the complex control hardware and large power requirements to generate the required control forces, apart from reliability issues [9]. Semi-active suspension systems, alternatively, are able to provide a unique compromise between the passive and active suspension systems. Since they have a fail-safe system, thereby providing the reliability of passive systems while maintaining the fast response and adaptability of active systems without requiring complex control systems and large power [10–12]. Semi-active systems are being designed based on smart materials, in which their properties can be reversibly controlled via external stimuli. Among many smart stimuli-responsive materials for developing semi-active systems, magneto-rheological (MR) materials (MR fluids and elastomers) have shown great promise for such applications as they possess fast and adjustable properties in response to an external magnetic field. Compared with MR elastomer devices, MR fluid-based devices, such as MR fluid dampers (MRFDs), have received growing interest in developing semi-active seat suspensions. This is due to the unique capability of MR fluid devices that can provide variable large damping force by changing their rheological properties (yield strength and apparent viscosity) through the application of an external magnetic field while, more importantly, allowing larger stroke/deformation as compared with MR elastomer based devices [13].

MRFDs consist of typical cylinder-piston units integrated with an MR valve. MRFDs can also be classified into internal and external (or bypass) configurations depending on the location of their MR valves [14–17]. The internal MRFDs typically offer a more compact design as compared to bypass MRFDs. Internal MRFDs, however, can generate quite lower damping force, and they also offer lower stroke limits in comparison with bypass MRFDs. Moreover, the assembly, fabrication and maintenance of the internal MRFDs are associated with many complexities and limitations. In contrast, bypass MRFDs can provide larger damping force and permit larger strokes with easy maintenance and design modifications compared to internal MRFDs. Bypass MRFDs unavoidably require more space to be integrated within mechanical systems as compared with internal MRFDs.

MRFDs, typically possess annular or radial fluid paths, can offer mainly variable damping characteristics without offering any significant stiffness modulation [18]. MRFDs with combined annular and radial fluid channels have recently shown superior performance as compared with those conventional MRFDs with single annular/radial fluid gap [19–21]. Nonetheless, limited studies have focused on developing MRFDs with a combined annular-radial gap. Besides, the current state-of-the-art MRFDs have been designed and commercialized in small-scale sizes for applications in on-road vehicles [22,23]. However, the development of large-scale MRFDs has been mainly limited to civil infrastructures [24,25]. Limited works have considered designing MRFDs for off-road vehicles especially tracked vehicles, which generally operate in extreme road excitation conditions that affect the vehicle's dynamic performance.

Vehicle suspension systems consist mainly of two major components, the elastic element and the damping element. Apart from damping elements, as the controllability of the elastic elements increases, they can provide better vibration isolation performance under a wider range of frequencies [26]. Recently, MRFDs with variable stiffness and variable damping (VSVD) capabilities have become increasingly desirable as they can provide vibration control over a wider range of frequencies compared with traditional MRFDs with just damping variability. The damping adjustability can only reduce the vibration amplitude, particularly at the resonance frequency, whereas stiffness tuneability can vary the natural frequency, thereby mitigating vibration significantly. Using VSVD devices, the transmission of vibrations across a wide range of frequencies can be efficiently reduced [27,28]. Furthermore, being able to vary the stiffness

allows for good ride comfort without sacrificing good handling. This is because good ride comfort requires a soft suspension, whereas good handling demands a stiffer suspension. VSVD-MRFDs are currently in their infancy stage. The design, and developments of VSVD-MRFDs, have yet to be addressed. It is also worth noting that most of the developed models that permit designing MRFDs in their early stage of design, are based on quasi-static models. While these models can effectively use to predict the damping force as well as the equivalent viscous and MR effect, they are not able to capture the dynamic hysteresis behaviour of MRFDs due to ignoring the unsteady behaviour of MR fluids. Moreover, despite the important effect of fluid compressibility, it has been mostly neglected in the literature [29,30]. Hence, the development of physic-based dynamic models for MRFDs has also yet to be addressed.

This dissertation research, thus, presents the development, modelling, optimal design, and dynamic characterization of large-capacity bypass VSVD-MRFDs with annular-radial MR valve (MRV) for applications in off-road vehicles. A theoretical quasi-static model was firstly formulated using the Bingham plastic behaviour of MR fluids. In parallel, analytical and numerical evaluations have been implemented to analyze magnetic flux density within the magnetic circuit of the designed MR valve. In order to achieve a high dynamic range, the magnetic circuit parameters and geometrical dimensions of the MR bypass valve were optimized. The dynamic range is defined as the ratio of the maximum damping force occurring at the maximum applied current to the corresponding damping force at the off-state condition. In the early stages of the design process, without experimental identification of the damper's parameters, a physics-based dynamic model based on the Bingham-plastic model was also developed to predict the proposed MRFD behaviour considering unsteady fluid behaviour. The proposed model was further modified to consider the fluid compressibility effect on the hysteretic responses of MRFDs. For validation of the design optimization strategy, the developed quasi-static, dynamic, and modified dynamic models, a comprehensive experimental dynamic characterization of the fabricated MRFDs has been conducted under various magneto-mechanical loading conditions (displacement, rate, and current). The dynamic properties of the proposed VSVD-MRFD in terms of dynamic range, equivalent viscous damping, and equivalent stiffness were also investigated.

2.1 Literature review

In this section, the pertinent reported studies related to the development of MRFDs and VSVD-MRFDs are briefly discussed to illustrate the critical knowledge gaps and formulate the dissertation's scope. The subsequent chapters summarize the reported studies relevant to the specific topics.

2.1.1 MR fluid

Magnetorheological (MR) fluids are smart materials that their behaviour can be varied under the application of a magnetic field. MR fluid (first discovered by Jacob Rabinow in the late 1940s) was employed in the development of adaptive variable damping devices that were realized in the early 1990s [31,32]. The rheological properties (e.g., apparent viscosity) of MR fluids can be rapidly, reversibly, and dramatically changed by applying an external magnetic field. Significant research was conducted by Lord Corporation [33] to design and fabricate different types of stable MR fluids that could be practically utilized under different environmental conditions. The MR fluid is basically composed of micron-sized ferromagnetic particles such as carbonyl iron particles dispersed in a carrier liquid such as silicon oil, surfactants and other additives for improving oxidation stability. Typically, ferromagnets that cause changes in fluid properties are preferred to have high saturation magnetization amplitudes, low coercivity and are coated with anticoagulant materials of low density [13]. Optimizing the volume fraction of the particles is essential since a lower volume fraction makes sedimentation easier to control, but also results in lower yield stress. These particles within a specific diameter size distribution (approximately in the range of 0.1 to 10 μm) can have a maximum volume fraction without causing an unacceptable increase in zero field-viscosity. Ideally, carrier fluids should have low viscosity, high lubricity, low-temperature viscosity dependent properties, and low cost. They also should be compatible with ferromagnetic particles and be environmentally friendly [34]. Surfactants such as ferrous naphthenate, stearic and oleic acids are generally added to reduce the sedimentation of the heavy magnetic particles in the liquid medium and also to enhance the distribution of the particles in the carrier [35,36].

In the absence of the applied magnetic field, the MR fluid particles are randomly dispersed inside the fluidic medium, as shown in Figure 2-1(a). Once the magnetic field is applied, the magnetic particles form chain-like structures along the direction of the applied magnetic field, as shown in Figure 2-1(b), thus varying the rheological properties (yield strength and apparent

viscosity) of the MR fluid. Therefore, MR fluids can vary from free-flowing fluid condition to a semi-solid state through variation in the applied magnetic field. Like other non-Newtonian fluids, the MR fluid does not flow (pre-yield) until the induced shear stress reaches and exceeds the yield strength of the material (post-yield). The yield strength and apparent viscosity of MR fluids directly depend on the applied magnetic field and increase by increasing the applied magnetic field intensity. It is preferred that MR fluids have low zero-field viscosity and coercivity of particles and can achieve maximum yield stress in the presence of the magnetic field. The MR fluid yield stress can be increased by increasing the volume fraction of MR particles or increasing the strength of the applied magnetic field. However, increasing the volume fraction of MR particles results in increasing the material's overall off-state viscosity besides increasing the weight of the MR-based devices. On the other side, increasing the magnetic field demands a higher power requirement.

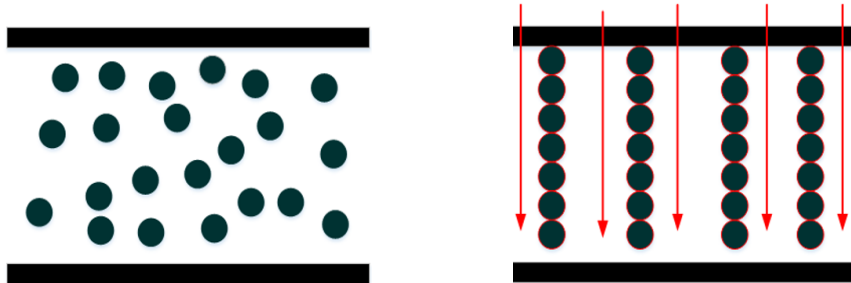


Figure 2-1. Effect of magnetic Field on MR fluid (a) magnetic field off and (b) magnetic field on.

It has been shown that the developed shear yield stress in MR fluids can be approximated as either the exponential function or the polynomial function of order two or three with respect to the applied magnetic field density as [37]:

$$\text{Exponential function: } \tau_y(H) = \tau_0 + \alpha H^\beta \quad (2-1)$$

$$\text{Polynomial function: } \tau_y(H) = \tau_0 + C_1 H + C_2 H^2 + C_3 H^3 \quad (2-2)$$

The exponential function can accurately predict the magnetic saturation of MRF yield stress; however, at low magnetic fields, it exhibits large errors. When the intensity of the applied magnetic field is low, the polynomial function is effective at predicting MRF yield stress. Furthermore, the higher order polynomials can predict the yield stress more accurately. Practically, third order polynomials are appropriate. Polynomial functions, however, cannot accurately describe the saturation of yield stresses. Consequently, a saturation constraint needs to be included in the function.

It is noted that MR fluids in MR fluid-based devices may operate under the valve (flow), shear, squeeze, combined valve and shear, and pinch modes, as shown in Figure 2-2 [38].

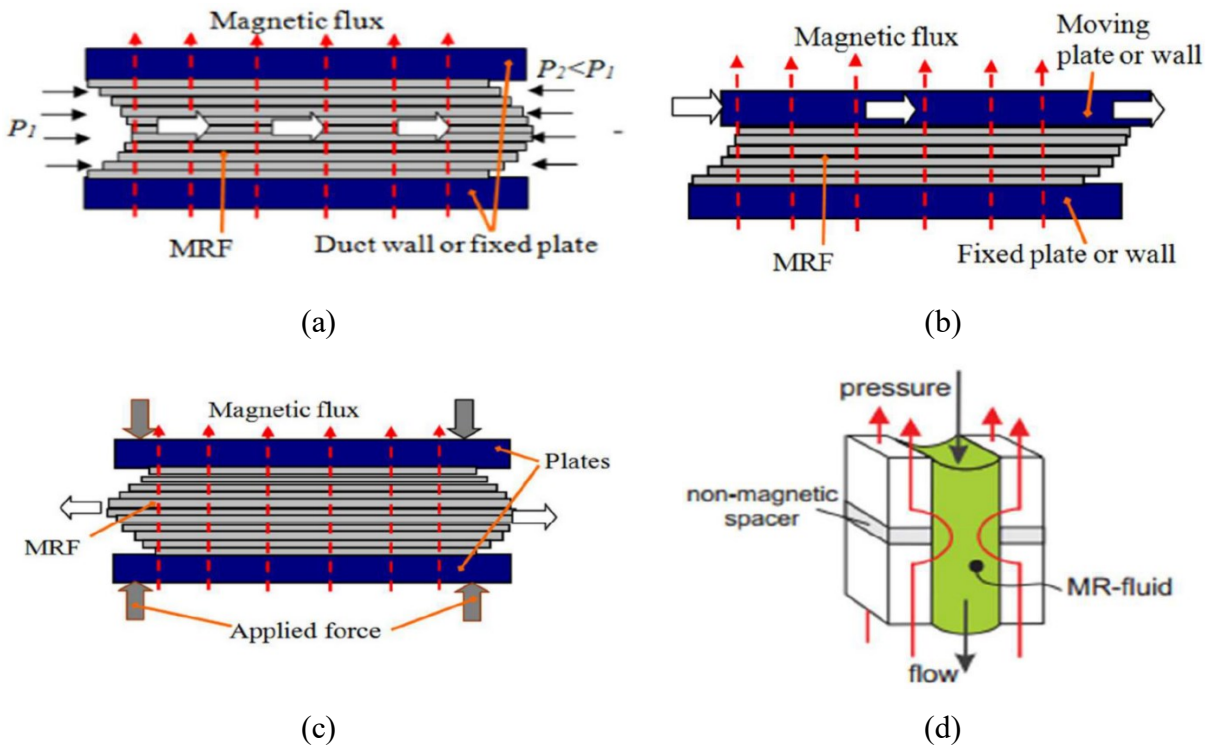


Figure 2-2. MR fluid operation modes [38]
 (a) valve mode, (b) shear mode, (c) squeeze mode, (d) pinch mode.

In the flow mode, shown in Figure 2-2(a), the pressure difference between two points on the fluid path causes an MR fluid to move between two parallel surfaces (plates). The valve or flow mode is typically used in MRFDs for primary vehicle suspension systems and seat suspension [39–41], bridges and buildings stable cables [42–44] and recoil systems [45]. Also, the flow mode can be used in landing gear [46] and vibration isolation mounts for large magnitude excitation [47]. The shear mode is illustrated in Figure 2-2(b), in which fluid flows between two parallel plates due to the relative motion of one plate with respect to the other plate. Since it requires a large area to generate enough force, the shear mode is generally less efficient than the valve mode [48]. Vibration isolation mounts for small magnitude excitation [49,50], MR fluid brakes [51–53] and MR fluid clutches [54] typically operated in the shear mode. A squeeze mode, exhibited in Figure 2-2(c), involves the fluid being squashed between two parallel plates moving perpendicular to the fluid flow direction. In order to squeeze the MR fluid, a considerable amount of force is required, thus the squeeze mode is used in locking devices and vibration isolation systems for small

magnitude excitations, such as the engine mount [55], journal bearing [38] and MR fluid dampers [56]. In the pinch mode, depicted in Figure 2-2(d), the magnetic poles are arranged axially with the MR fluid flow and separated by a non-magnetic material. Consequently, the magnetic flux passes in a parallel direction to the fluid flow and generates a non-uniform concentrated magnetic field in the vicinity of the non-magnetic spacer. This mode is utilized in controllable orifice valves [57,58] and medical applications [59].

Modelling of MR fluids is a fundamental necessity for the development of physic-based modeling and optimal design of MR fluid based-devices. Different models have been formulated to describe the linear visco-elasticity (pre-yield region) and visco-plasticity (post-yield region) behaviour of MR fluids. Maxwell and Kelvin–Voigt models [60] have been widely employed to describe the linear viscoelastic behaviour of MR fluids in pre-yield region. In MRFDs, MR fluids are mainly operating in post-yield region and thus the effect of pre-yield region is generally neglected [61–63]. The Bingham plastic and the Herschel-Bulkley models [64,65] are the most popular visco-plastic models to describe the post-yield behaviour of MR fluids. Bingham plastic model has been widely used to model the MR fluids shear stress-shear strain-rate behaviour in the post-yield region [66,67]. At a very high shear rate, MR fluids may experience shear thinning or shear thickening behaviour. Hershel-Bulkley's model has been effectively utilized to capture these phenomena [68]. The Bingham and Hershel-Bulkley models can be described by the following equation in which $n=1$ represents the Bingham model while ($n<1$) and ($n>1$) represent the Hershel-Bulkley model addressing the shear thinning and shear thickening behaviour, respectively.

$$\tau = \tau_y + \eta \left(\frac{du}{dy} \right)^n \quad (2-3)$$

Figure 2-3 shows the behaviour of MR fluids based on these models in the post-yield region. It should be noted that in the pre-yield region, MR fluids typically behave like linear viscoelastic materials with field-dependent complex shear modulus.

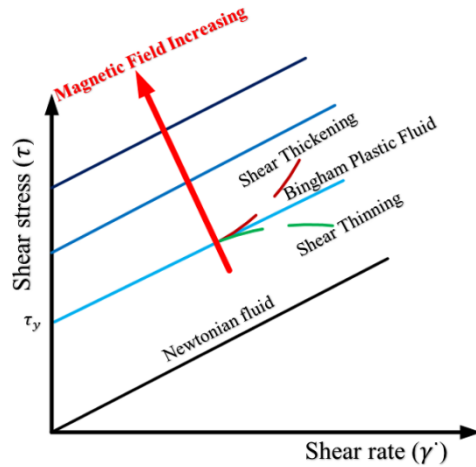


Figure 2-3. General behaviour of MR fluids in post-yield region.

2.1.2 MR fluid dampers (MRFDs) Technology

MRFDs are semi-active adaptive devices that utilize the field-dependent properties of MR fluids to generate controllable damping forces for many vibration control applications. A typical internal MRFDs mainly consists of a piston with an orifice and embedded magnetic coil travelling inside a cylindrical housing filled with the MR fluid, an accumulator with a diaphragm, and sealing, as shown in Figure 2-4(a). In bypass MRFDs, the MR valve is placed outside of cylindrical housing, as shown in the double-ended bypass MR damper shown in Figure 2-4(b).

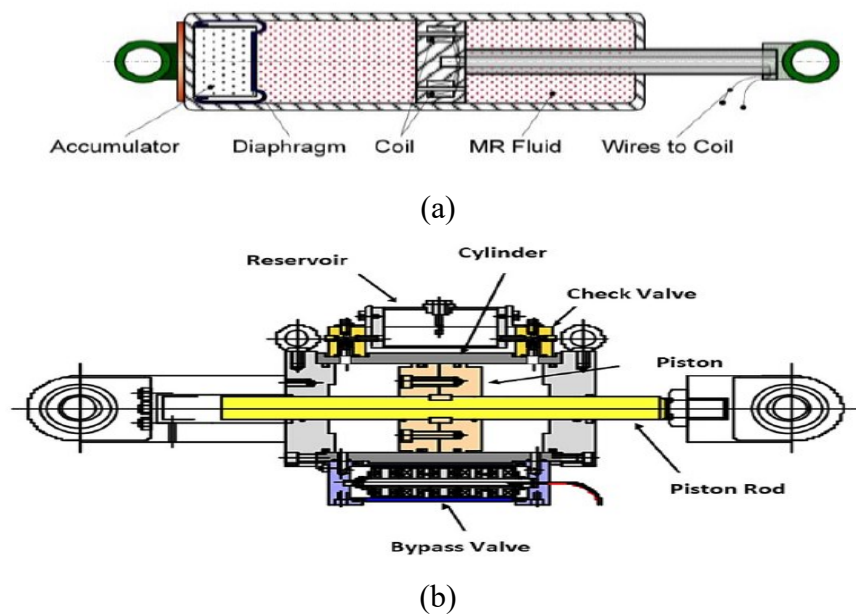


Figure 2-4. Construction of MRFD (a) internal valve [37] (b) bypass valve [69].

MRFDs are mainly operating in valve mode. The MR fluid passes through the small orifice in the piston (also MR valve) due to the pressure drop across the orifice caused by the movement of the piston inside the cylinder. The MR fluid is then magnetically activated through the orifice passage using an embedded electromagnet. Through the application of the magnetic field, the apparent viscosity and yield strength of the MR fluid vary and subsequently, change the equivalent viscous damping of the device. Thus, by applying current to the electro-magnetic coil, the damping force can be continuously controlled. The amount of damping force is proportional to the applied current and excitation velocity but only can be controlled via the applied current.

MRFDs have been implemented in various applications including suspension systems of many luxury cars [70,71], motorcycles [72], military vehicles [73–75], helicopters [76], ambulances [77] and railway [78], vehicles seat suspension [79,80], civil buildings and bridges cushions [24,81], medical applications such as prosthetic leg, dental implant surgery and robotic surgery [82,83], washing machines [84], aircraft landing gears [85,86], and gun recoil systems [87,88]. The performance of different MRFDs used in various applications is represented in Appendix A. The data manifest that MRFDs can offer a wide range of force, velocity and displacement for integrating with real-world applications. The force scales of MRFDs in automotive applications are relatively lower than those being used for railway and civil applications. In the households and prosthetics applications, the scale of damping forces is significantly smaller than in the other applications mentioned. Also, commercial MRFDs for automotive applications operate at low values of motion frequency and amplitude. However, military tracked vehicles operate at a wider range of frequencies and large-scale amplitudes. In addition, these types of vehicles require high damping forces and dynamic ranges [89]. Nonetheless, designing large-scale MRFDs are associated with many challenges as compared with small-scale MRFDs, largely due to the effects of inertia (which can cause unsteady behaviour of MR fluid), turbulence, viscoelasticity and fluid compressibility [87,90]. MRFDs can be classified according to the design and application requirements into three types: the mono-tube [91], the twin-tube [92], and the double-ended [93]. Among them, the mono-tube MRFDs are the most common and widely used MRFDs due to their simple design and compactness. Another classification of MRFD is based on the number of coils known as single coil and multiple coils MRFDs [94,95]. Single-coil MRFDs are compact and have less design complexity, but they have lower dynamic range, efficiency and responsiveness [96]. According to geometrical arrangements

of the fluid gaps, MRFDs may also be categorized into annular gaps, radial gaps and multiple annular and radial gaps [94,97]. Advantages of the annular gap in MRVs include but not limited to compact design, faster response time and high efficiency in on/off state [98]. However, it leads to elongation of the MRV, especially when high damping force is required. On the other hand, the radial gap MRVs have the flexibility to generate high damping force with the shorter longitudinal flow channel length. Besides, they are easier to be fabricated. However, the radial gap MRVs are hard to be designed in a compact size [99]. Multiple annular-radial MRVs can attain greater performance by producing higher yield stress, but they have a complex design and are difficult to be manufactured [19,100,101]. An annular-radial gaps MRV was investigated by Wang et al.[102]. In contrast to other types of MRVs, this arrangement offered a high-pressure drop.

MRVs are the main unit of the MRFDs, which are responsible for controlling the damping force and magnetic actuation [103]. According to the placement of the MR valve with respect to the MRFDs cylinder, these valves can be categorized as internal (bypass) valves [104–107] and external (bypass) valves [108–111], as shown in Figure 2-4. Internal valves are typically fitted within damper main pistons, with their magnetic circuits supplied by current flowing through the piston rod [106]. The viscous damping force is controlled by changing the ratio of the MR fluid gap cross-sectional area to the piston cross-sectional area [75]. Due to their high performance, compactness, sedimentation controllability, and ease of design, internal valve MRFDs have been implemented in a variety of applications [15,93,112,113]. The internal valve MRFDs, however, have many drawbacks, such as limited damping force and stroke in a specific volume, and restricted valve installation space. In addition to wiring complexity, difficulty in fabrication, assembly, maintenance and modifications, excessive thermal heat affects the operation of the magnetic circuit [114]. External coil or bypass MRFDs are simpler in design, have more heat transfer capability, and more importantly, offer higher damping force as compared with internal MRFDs [94].

The bypass valve is not integrated into the damper main piston, thus there is no need for the magnetic wire to pass through the piston rod [109,111]. The performance of the bypass MRFDs is largely dependent on the MRV materials properties, piston area, cylinder length, thickness and arrangement of bypass fluid flow gaps. As mentioned above, the MRFDs with bypass MRV can provide large damping force as well as a dynamic range while also providing larger stroke

[105,115]. Idris et al. [105], for instance, developed an external bypass MRFD that outperformed 1.5 times the conventional MRFDs. Placing the bypass valve outside the damper cylinder has many benefits such as easy installation, maintenance, design modification and easy accessibility to all the valve components. Moreover, there are no constraints on the MR valve dimensions due to the size of the damper piston and cylinder. However, the current state-of-the-art bypass MRFDs possess either an annular gap or radial gap, thereby relatively having a bulky configuration, as shown in Figure 2-4(b) when a large damping force is required. As a result, the development of a compact bypass MRFD to be installed in a specific space is of paramount importance.

The magnetic circuits in MRVs are being designed in such a way that the apparent viscosity and yield strength of the MR fluid are maximum in the presence of the magnetic field. In some MRFDs, a permanent magnet is combined with an electromagnet to shift the off-state viscosity of the MR fluid to a specific value, while the electromagnet is used to control the variations around this value [37]. In order to calculate the controlled damping force, the magnetic circuit should be fully analyzed. Solving the magnetic circuit can be accomplished using two approaches: analytical analysis and numerical analysis using the finite element method (FEM). By applying Ampere's circuital law to a magnetic circuit with constant flux and assuming uniform flux density and linear relation between magnetic flux density (B) and magnetic field intensity (H), an analytical procedure can be formulated for MRVs to evaluate the magnetic flux density in the fluid gap regions. Magnetostatic finite element models can provide a more accurate estimation of the generated non-uniform magnetic flux density in MR fluid gaps by relaxing the above assumptions.

The generated damping force in an MRFD depends on the analysis of both electromagnetic and fluid systems. Therefore, improving MRFDs performance depends on the multidisciplinary design optimization MRVs considering geometrical dimensions and magnetic circuit parameters. The objective function may include the damping force, dynamic force range [116], inductive time constant of the damper [117], valve ratio [97,118], control energy, time response or power consumption [119]. Rosenfield and Wereley [120] presented an analytical design optimization for their proposed MRV magnetic circuit to prevent the magnetic circuit from premature saturation. Gavin et al.[121] optimized an MRFD by considering force capacity, electrical characteristics, and the size of the damper to minimize the power consumption and induction time constant. The optimized damper generated a 4 kN force at 10 A current, but for a very short period of time of a

few milliseconds. Nguyen et al. [118] established an analytical design optimization methodology for maximizing the damping force of an MRFD in a constrained specific volume. Nguyen and Choi [122] also optimized MRV dimensions for vehicle suspension systems by finite element analysis to maximize the damping force and dynamic range.

Despite the fact that MRFDs can exhibit exceptional characteristics, their inherent non-linear dynamic hysteresis behaviour is a major drawback for practical implementation. Therefore, the development of dynamic models that can accurately predict the hysteresis behaviour and generated MR damping force at any time instant is of paramount importance for the design, control synthesis and practical implementation of real-time vibration control applications. Different models have been developed to predict the generated damping force and hysteresis behaviour in MRFDs. These models may be classified into quasi-static and dynamic models.

Quasi-static models have been investigated in many studies and they are generally based on Bingham and Herschel-Buckley fluid behaviour [123–125]. Philips [67] used the Bingham model to determine the gradient of pressure in a parallel duct using a set of nondimensional variables. Using the same approach, Gavin et al. [126] developed an axisymmetric model to describe the MRFD's quasi-static behaviour. Kamath and Wereley [127] developed an axisymmetric quasi-static model for an MRFD with annular gaps and assumed constant yield stress. Wang and Gordaninejad [125] and Lee and Wereley [128], described the MR fluid shear thickening/thinning characteristics using the Hershel-Bulkley model. However, the above-mentioned quasi-static models contain many assumptions such as incompressible steady-state fluid, laminar flow, axisymmetric flow, unidirectional flow and pressure variation and generally the gravity and inertial effects are being neglected. More importantly, while the significant effect of MR fluid compressibility on MRFDs hysteretic response have been confirmed in several proof-of-concept investigations, they have not been considered in most of the developed models. Despite the limitation of quasi-static models, these models can provide a relatively good estimation of damping force and MR effect. Moreover, they can reasonably predict the force-displacement and force-velocity behaviour of MRFDs operating under very low frequencies and small amplitude excitations.

Various dynamic models have alternatively, been developed to alleviate the above-mentioned shortcomings of quasi-static models in describing MRFD nonlinear behaviour [123]. For instance,

fluid compressibility, inertia, viscoelasticity and potential turbulence are the main factors that contribute to hysteretic behaviour, which is a nonlinear phenomenon [85,129,130]. Dynamic models can be classified into parametric and non-parametric models [130]. Parametric models such as the Bingham, Bouc-Wen, and modified Bouc-Wen models [42,90,131] are based on mechanical idealization involving different arrangements of springs and viscous dashpots. According to Stanway et al. [132], a dashpot is placed in parallel to a Coulomb friction element in the simple Bingham model. Gamota and Fillsko [133] proposed a viscoelastic-plastic model based on the Bingham model. A smooth hysteretic model has been formulated and generalized as the Bouc-wen model [134,135] which is capable of capturing the force roll-off in the low-velocity region that is observed in the experimental testing. Based on the Bouc-Wen hysteresis model, phenomenological models for MRFDs have been proposed to describe a wide range of hysteretic behaviour [42]. Several nonlinear hysteresis systems have been modelled using the Bouc-Wen model, which can capture a wide range of hysteresis loop shapes in a continuous manner. Nevertheless, determining the Bouc-Wen model parameters is a complex and time-consuming process and also require extensive experimental data. This model is also not suitable for varying loading conditions since these parameters are only valid under specific excitation condition. Therefore, the estimated parameters must be re-evaluated if a different combination of excitation parameters is desired. This can be extremely cumbersome and computationally expensive [136].

Non-parametric models are, also, being developed using regression models, whose parameters are identified through curve-fitting procedure using available experimental data. These curve fitting methods are included but not limited to Chebyshev polynomials [137], the black-box model [138], the multifunction model [139], the query-based model [140], the neural network model [141], Ridgenet model [142] and self-tuning Lyapunov-based fuzzy model [143]. While these models do not possess the physical elements representing the mechanics of the MRFDs like those in parametric models, they have been shown to be robust and applicable to linear, non-linear and hysteretic systems [42] These models can also be effectively utilized for the development of inverse models, which greatly facilitate the control synthesis of MRFDs [129,130].

The current state-of-the-art developed dynamic models are generally empirical as their characteristic's parameters must be identified through experimental study. While, these models may be efficiently used for the development of control strategies, they are mainly applicable to

excitation conditions considered during experimental tests. Moreover, they do not provide any physical insight on the behaviour of the MRFD and thus cannot be used to evaluate the dynamic performance of MRFDs at early stages of design. For instance, Nguyen and Choi [29] developed a physic-based dynamic model based on unsteady MR fluid behaviour through an annular duct to describe the hysteresis behaviour of an electrorheological (ER) damper. Simulation results were validated with experimental data. The parameters identification of the model did not require any experimental measurement. However, the fluid compressibility was neglected in their analysis. Nguyen and Choi [122] also proposed another dynamic model using the lumped parameters method for the same ER damper. Unsteady fluid behaviour and fluid compressibility were considered in this model. The simulation results were compared with experimental results under various piston rod excitation. Du et al.[144] recently developed a dynamic model for predicting the unsteady behaviour of MR fluid in an MRFD. But the fluid compressibility has been neglected in their analysis. However, the literature lacks a physic-based dynamic model for the MRFDs considering both the compressibility and unsteady behaviour.

2.1.3 Variable stiffness and damping MRFDs.

MRFDs with variable stiffness and variable damping (VSVD) capability have recently received growing interest as they have shown better performance to control vibration in a broad range of frequencies compared with conventional MRFDs with only damping variability. Damping is mainly effective to reduce vibration amplitude, particularly at the resonance frequency. In contrast, variation in the stiffness allows to adaptively vary the natural frequency of the system. This is extremely important as the transmitted vibration can be efficiently attenuated over a broad range of frequencies [27,145]. Moreover, the stiffness variability permits overcoming the conflict between ride comfort and good handling of suspension stiffness design as good ride comfort requires a soft stiffness while good handling and vehicle stability requires the suspension system to be stiff. Liu et al. [146] proposed a VSVD structure and the experimental results manifested that the system equipped with an MRFD exhibited perfect vibration isolation performance [147,148]. Sun et al. [149] experimentally proved that the sprung mass acceleration of quarter car system with the VSVD suspension can be reduced significantly. Besides, it can improve the ride comfort when comparing with other types of the suspension system. Deng et al. [150] integrated a VSVD device in an off-road military vehicle seat suspension subjected to harsh operation excitations with low frequencies and large amplitudes. The results revealed the importance of the VSVD characteristics

in reducing the vibration amplitude at resonance and changing the natural frequency of the system, respectively.

MRFD can control the system stiffness through two working principles. The first one is a series connection between the MRFD and stiffness element, as shown in Figure 2-5(a). This type is easier to be applied in the suspension vibration control. The second type is a parallel connection, and it is also called Voigt element as shown in Figure 2-5(b). This kind of variable stiffness is suitable for large stiffness variation range applications [151]. The configuration, however, will be bulky and costly. The equivalent stiffness and damping relationships for each type can be derived as:

Connection in Series

$$K_{eq} = k_2 + \frac{ck_1\omega^2}{c^2\omega^2 + k_1^2} \quad (2-4)$$

$$C_{eq} = \frac{ck_1^2}{c^2\omega^2 + k_1^2} \quad (2-5)$$

Connection in Parallel

$$K_{eq} = \frac{k_1k_2(k_1 + k_2) + k_2c^2\omega^2}{c^2\omega^2 + (k_1 + k_2)^2} \quad (2-6)$$

$$C_{eq} = \frac{c\omega k_2^2}{c^2\omega^4 + (k_1 + k_2)^2} \quad (2-7)$$

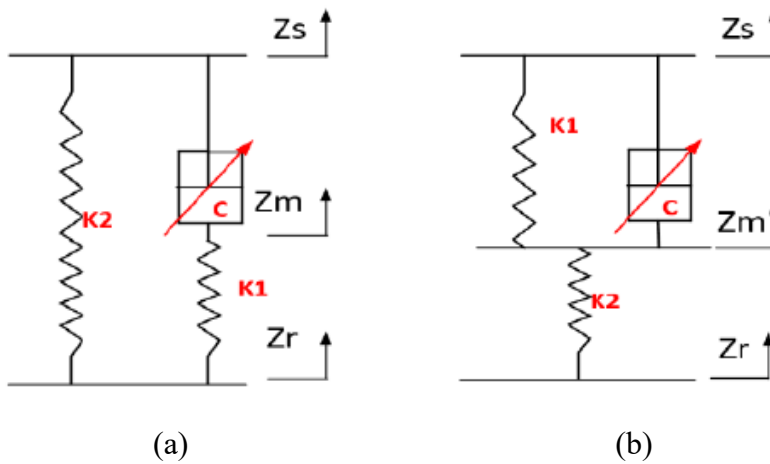


Figure 2-5. VSVD working principles (a) connection in Series (b) connection in Parallel.

Based on these two working principles, there are three methods to accomplish stiffness variability by using MR elastomer [152–154], air spring based on MRV (damper) or a mechanical system [148,155]. Analysis of Table B-1 in Appendix B shows that the development of VSVD systems using MR fluid dampers in connection with spring elements manifests the importance of

such systems in vibration isolation. While there are a number of studies to realize the stiffness and damping variability devices and several conceptual designs have been provided, the research in this area is still at the early stages.

Pneumatic springs generally offer high payload, good reliability, low maintenance cost, and low natural frequency that can meet wide applications [156]. However, VSVD systems featuring MR air spring have also many drawbacks associated with the high cost and non-compactness as well as the complex control design due to the coupling between the dynamics of the fluid and pneumatic dynamics to obtain the required damping force. Youn and Hac' [155] proposed a VSVD suspension system based on using air spring. The system stiffness varied between three definite values. This system was tested experimentally to demonstrate the effectiveness of stiffness variability on vibration control. Li et al. [157] developed a system based on the variation of the air spring stiffness and damping by controlling the applied current passing through the MRV coil. Zhang et al. [158] presented an MR fluid with VSVD isolator. Stiffness variability was attained using MRV to control the MR fluid flow between two connectors. MRV can control the fluid flow by applied external current, and consequently the stiffness and damping characteristics can be controlled. However, the developed VSVD isolator was very bulky, thus limiting its practical application. Moreover, an air pump or accumulator was required to control the air spring that's lead to the high cost and complex design and control. Zhu et al. [156] proposed an MRFD with an embedded pneumatic vibration isolator in a compact structure. The stiffness was adjusted through changing the average pressures of the working gas chambers using four pneumatic high speed on-off valves.

Generally, the developed VSVD mechanical systems have a bulky design as they require two spring elements and two controllable dampers to achieve variable stiffness and damping independently. Liu et al. [148] proposed a compact VSVD system by using two Voigt elements in series and they subsequently utilized two independent MR controllable dampers to mitigate the lateral vibration for a single DOF system. They also explored different control strategies to demonstrate the effectiveness of the system in vibration isolation. It is noted that although the stiffness of the spring elements is constant, the equivalent stiffness of the system varies by varying the damping coefficient in the Voigt element. They showed that the equivalent stiffness and damping coefficient of the single DOF system can be varied by 2.8 and 3.6 times, respectively. It

was also found that the stiffness variation significantly depends on the ratio between the two springs. The smaller the stiffness ratio, the larger the stiffness variation.

Sun et al. [145] proposed a mechanical system based on a series connection. The system consists of two damping cylinders (upper and lower) that are connected in series using a spring element. The stiffness and damping can be varied through the application of the current to the upper and lower cylinders respectively. Sun et al. [159] later enhanced their design by presenting another mechanical device based on the parallel connection assembly of two coaxial damping cylinders, two springs, and two connectors. The results stated that the loading frequency has a negligible effect on the equivalent stiffness and damping. However, the two designs proposed by Sun [145,159] have a short stroke that limits their applications, in addition to design complexity, unreliability, stiffness control difficulty, and high cost associated with two dampers and other components. While the design proposed by Zhu et al. [27] seems to be compact with a large stroke of 105 mm, their cost is high due to requiring another adjustable damper for achieving both damping and stiffness variability. Although the proposed system of Petter et al. [160] is a simple design with no moving parts, it is not suitable for application due to complex control between stiffness and damping, and discrete stiffness variation. The maximum achievable stroke by previous designs is not suitable for off-road vehicles that require a large stroke.

In summary, the compact design, low cost, limited stiffness variation, small strokes and independent stiffness and damping control are the major challenges that are facing the design of VSVD devices. The current VSVD MR based adaptive systems have many issues concerning practical implementation and compactness. Moreover, the current designs have a limited variability of stiffness and damping besides restricted stroke for adaption in real applications. The detailed modelling and characterization of the VSVD MR based devices suitable for off-road vehicles have not yet been addressed. adapted VSVD suspension system.

2.2 Motivations and objectives

Although considerable research has been conducted on the development of small-scale MRFDs for cars and seat suspension, as presented in previous sections, these dampers are only able to control the energy dissipation properties (damping). Many applications require large-scale controllable MRFDs for vibration suppression. Limited studies have been conducted on the development of large-scale MRFDs suitable for automotive applications, especially for off-road

and tracked vehicles suspension system. Also, developing a high dynamic force range with a large damping force MRFD required developing a long annular gap MR valve which necessitates complicated design and manufacturing of MR valve. To develop an MRFD with a high dynamic range that can be fitted in a specific space in the vehicle, it is essential to develop a practical design optimization strategy for the MR valve geometrical parameters. There are no studies on the design optimization of annular-radial MRFDs that can generate high damping force suitable for tracked vehicle suspension systems. Development of physic-based models that can accurately predict dynamic hysteresis behaviour of MRFDs are of paramount importance at early design stages. The reported quasi-static and dynamic models are not able to fully predict the hysteresis behaviour of MRFDs. The development of large-scale MRFDs featuring variability in damping and stiffness suitable for off-road vehicles have not been yet addressed.

The overall goal of this dissertation research is thus the development of a large-scale VSVD MRFD with a bypass MR valve with an annular-radial gap capable of generating high damping force and dynamic range for applications in off-road tracked vehicles. The specific objectives of this research dissertation are summarized as:

- I. Development of a quasi-static model to predict the generated damping force and force-displacement behaviour of the proposed MRFD with an annular-radial bypass fluid valve.
- II. Development of a multidisciplinary design optimization strategy for the proposed MRFD considering both the geometric and magnet circuit parameters as design variables to maximize the dynamic force range of the MRFD.
- III. Development of a physic-based dynamic model considering both fluid inertia and compressibility to accurately capture the nonlinear hysteresis behaviour of the proposed MRFD.
- IV. Fabrication and experimental characterization of the proposed optimally designed MRFD under different excitation conditions to validate the design optimization strategy and the developed physic-based models.
- V. Characterization of the proposed VSVD-MRFD under different loading conditions and magnetic field excitation to investigate its dynamic properties and stiffness and damping variability.

2.3 Organization of the Dissertation

This dissertation has been compiled according to the requirements described in “Thesis Preparation and Thesis Examination Regulation” booklet of the School of Graduate Studies at Concordia University. This dissertation research is organized into six chapters which address the research goals mentioned above. Introduction and critical literature review are included in Chapter 1, while Chapter 6 concludes the dissertation with some recommendations for future work. It is noted that the research has resulted in 4 journal articles representing Chapters 2-5. These articles are published/summitted in premium journals in the area including the journal of smart materials and structures (SMS, published), Journal of Intelligent Material Systems and Structures (JIMSS, under review), Journal of Sound and Vibration (JSV, under review) and journal of smart materials and structures (SMS, under review).

In Chapter 2 firstly a quasi-static model was formulated based on the quasi-static Bingham plastic characteristic of MR fluids. The magnetic flux density in the MR valves’ gaps was solved analytically and the solution was compared numerically using the developed magnetostatic finite element model. Next, a multidisciplinary design optimization problem has been formulated to identify the MR valve geometrical and magnetic parameters to maximize the damper dynamic range under specific volume and magnetic field constraints. The proposed design optimization formulation allowed to realize a miniaturized MR fluid bypass valve with both annular and radial gaps to generate a relatively large damping force and dynamic range for the MRFD.

The optimized MRFD can theoretically generate 1.1 kN of the off-state damping force and 7.4 kN of controllable damping force at 12.5 mm/s damper piston velocity. The proposed damper was also designed in such a way that permits the realization of a large piston stroke of 180 mm. The optimally designed MRFD was subsequently fabricated and experimentally characterized to investigate its performance in view of peak damping force, equivalent viscous damping coefficient and dynamic range to validate the developed model. The results show that the proposed MRFD damper is able to provide large damping forces with a high dynamic range under different excitation conditions.

In Chapter 3 a non-linear dynamic model was formulated to predict the unsteady behaviour of the designed MRFD with an annular-radial bypass valve under sinusoidal excitation on the basis of MR fluid Bingham plastic behaviour. Using the Laplace transform technique and Cauchy

residue theory, the velocity profile and the pressure drop have been derived by solving the fluid momentum equation. The dynamic model was further modified to consider the fluid compressibility effect on the hysteretic response of the designed MRFD. The force-displacement and force-velocity results based on the formulated dynamic and modified dynamic models were then compared with those obtained based on the quasi-static model as well as experimental results under varied mechanical and magnetic loading conditions. Results showed that the MRFD experience non-linear hysteresis due to unsteady behaviour at high loading conditions. Also, fluid compressibility is the main source of the non-linear hysteresis behaviour, especially at low velocity regions.

Chapter 4 presents a comprehensive experimental characterization of the designed large-capacity MRFD equipped with a compact annular-radial MRV. Extensive experimental tests were conducted to investigate the dynamic characteristics of the proposed MRFD considering wide ranges of excitation frequency, loading amplitude, and electrical current. The equivalent viscous damping together with the dynamic range were calculated as functions of loading conditions considered. A maximum damping force and dynamic range of 5.54 kN and 2.3, were, obtained, respectively under a maximum current of only 1.5 A using the initial MRV design. The effectiveness of the proposed MR damper was subsequently identified by comparing its dynamic range with other conventional MR dampers in previous studies. The results confirmed the potential of the proposed MR damper for the development of highly adaptive ground vehicle suspensions for off-road wheeled and tracked vehicles. The MRV was further modified to expand the damping force and dynamic range of the MRFD. The modification yielded dramatically higher dynamic indices, including a maximum dynamic range of 5.06 and a maximum damping force of 6.61 kN.

Chapter 5 presents the development and experimental characterization of a novel compact large-scale VSVD-MRFD with an annular-radial bypass valve. A wide range of excitation frequencies, loading amplitudes, and electrical currents was used to determine the dynamic characteristics of the proposed MR damper. Responses including force displacement, and hysteresis force-velocity curves were obtained. Further investigation of damper dynamic properties was conducted in terms of equivalent damping, equivalent stiffness dynamic range, and their dependence on loading conditions. Results show a good damping force, a high dynamic range, and a good stiffness variability for the proposed novel VSVD MR damper.

CHAPTER 2

QUASI-STATIC MODELING AND DESIGN OPTIMIZATION OF A LARGE-CAPACITY ANNULAR-RADIAL BYPASS MAGNETORHEOLOGICAL DAMPER

3.1 Introduction

The MR fluid valves typically consist of a magneto-conductive body with an embedded electromagnet which can magnetically activate the MR fluid during passage through a valve orifice. This will yield variation in the fluid apparent viscosity and yield strength that results in resistance to the fluid flow [161]. The MR fluid valve is typically fitted internally in the MRFD or externally, so-called as a MR fluid bypass valve. The configuration of valve gaps can be annular, radial or a combination of both. The geometrical structure of MR valves can significantly impact its dynamic performance, thus optimizing the valve's geometrical structure is a crucial part of designing MR valves, irrespective of their application. For instance, the gap size has been identified as an important parameter to be optimized as it significantly affects the dynamic performance of the MR valves [162,163]. Wider gaps generally reduce viscous and controllable yield damping forces, while a smaller gap increases the pressure drop but it may also cause valve blockage. Practically, the gap size ranges between 0.5 mm and 2 mm [94,163,164], depending on the design requirements.

At the early design stages of MRFDs, the Bingham plastic model based on quasi-static fluid behaviour has been extensively used to predict the damping force as a function of applied currents [165]. Later in the design process, phenomenological or parametric dynamic models can be applied to predict the damping forces based on the magnetic field, excitation frequency, and displacement amplitude. Significant research studies have been conducted on the design and optimization of MR valves to maximize dynamic range (high on-state and low off-state damping forces) while minimizing the time response [116,166,167]. Rosenfeld et al. [120], for instance, presented a design strategy guideline for analytical optimization under constrained volumes based on assuming a constant magnetic flux through the magnetic circuit. This assumption may result in suboptimal results since the MR valve performance depends on the magnetic circuit as well as the geometrical dimension of the valve. Nguyen et al. [166] introduced an optimal design for the determination of geometrical dimensions of MR valves featuring annular configurations to minimize the

electromagnetic coil energy consumption and time response. The golden-section algorithm and local quadratic fitting technique were used as optimization methods to find the optimum solution. The results asserted the importance of the optimal design of the MR valve structural parameters. It was also reported that the wire diameter has less importance and thus can be neglected in minimizing power consumption. Nguyen et al. [118] later presented analytical design optimization for the identification of geometrical parameters of single and double coil annular MR valves that are constrained in a specific volume to maximize the controllable pressure drop. The optimum analytical solution was verified with a finite element optimal solution. The error between the two methods was reported to be less than 7 % . Hadadian et al. [168] proposed an optimum design strategy for an annular MR valve with a single-coil constrained in a specific volume. They developed smooth response surface functions for magnetic field intensity in active MR fluid region using the response surface method and design of experiments. The genetic algorithm (GA) and the sequential quadratic programming (SQP) methodology were used to capture the global optimum solution.

Most of the above-mentioned studies have conducted design optimization of MR valves based on annular gap configuration. However, enhancing the valve dynamic performance generally requires increasing the annular gap length or increasing the number of coils which both substantially increase the MR valve size, complicity and cost. The annular-radial integration design may overcome the limitations associated with the annular-gap design. In a few studies, the integrated annular-radial gap design has been successfully applied to the development of high-performance MR valves [169,170]. Hu et al. [171], for instance, developed an MR fluid valve with a tunable conical annular gap between 1 mm to 2 mm by rotating the valve spool to increase the pressure drop without enlarging the valve size or consuming more power. The experimental results showed that the pressure drop could fluctuate between 130 kpa to 1150 kpa. They later proposed an annular-radial MR valve with variable radial gaps to meet different working conditions [162]. The gap variability has been achieved by replacing washers with different thicknesses. A maximum damping force of 4.72 kN at applied current 2 A and a dynamic range of nearly 7 were achieved. Imaduddin et al. [172] proposed an MR valve with multiple annular and radial gaps in order to extend the MR fluid path. Also, the effect of the gap size on the pressure drop was discussed. The experimental results reported that the valve could cause a pressure drop of more than 2.5 Mpa.

Although the reported studies focusing on designing MR valves with annular-radial gap confirmed that the dual gap configurations can offer high damping force and dynamic range, the current designs may not be suitable for off-road vehicles as they don't permit large stroke, apart from large dynamic force and dynamic range. It should be noted that off-road vehicles are normally subjected to harsh loading conditions (e.g., high frequencies and amplitudes) that require high damping force, and dynamic range, together with large piston stroke. Furthermore, the current designs do not meet the reasonably well compact design requirement to be easily integrated into such applications.

In this chapter, a compact bypass annular- radial MRFD adapted for off-road tracked vehicles has been developed, modeled and optimally designed. The mathematical formulation was established based on the MR fluid Bingham plastic model. The performance of the valve's magnetic circuit has been first evaluated analytically by calculating the magnetic flux density in the MR fluid active region. The analytical results were then verified using a magnetic finite element method. The valve's geometrical dimensions have been subsequently optimized to achieve a high dynamic range. The GA and SQP algorithms in a successive manner were utilized to obtain the global optimum solution. The developed optimally designed MRFD has been finally fabricated, assembled and experimentally tested. The validation of the analytical model and high dynamic range of the proposed MRFD were further provided.

3.2 Principal and configuration of the proposed MRFD

3.2.1 Principal of the design.

The proposed MRFD was designed to be adapted for off-road tracked vehicles operating in harsh conditions for defense applications (a review of tracked vehicles suspension system is presented in Appendix C). Even at low excitation frequencies and modest displacement amplitudes, these vehicles require substantial damping force, high dynamic range, and a large stroke shock absorber. The focus in this research is on M113 tracked vehicles (Appendix C). The existing hydraulic shock absorber of M113 tracked vehicles, shown in Figure 3-1, limit the vehicle mobility, speed, maneuverability and adaptability for various operating conditions and excitations [120]. Thus, it is important to develop a compact VSVD-MRFD with a large stroke while providing large dynamic range in view of both the stiffness and damping variability. The conventional damper used in M113 has a stroke of 180 mm and it can generate a constant damping

force equal to 467 N at low piston rod speed of 12.5 mm/s [173]. As a result, the proposed MRFD in this study was developed in order to match the size and capacity of the M113 tracked vehicle's shock absorber that has the dimension show in Figure 3-1(b). The aim is to replace the passive shock absorber with an MRFD having large dynamic range and stroke to reduce the vehicle vibration under a wide range of loading circumstances. It is noted that while the focus in this research is on the development and design of MRFDs for this type of tracked vehicles, the developed modelling and design optimization strategies can be generally applied to MRFDs designed for other types of vehicles.

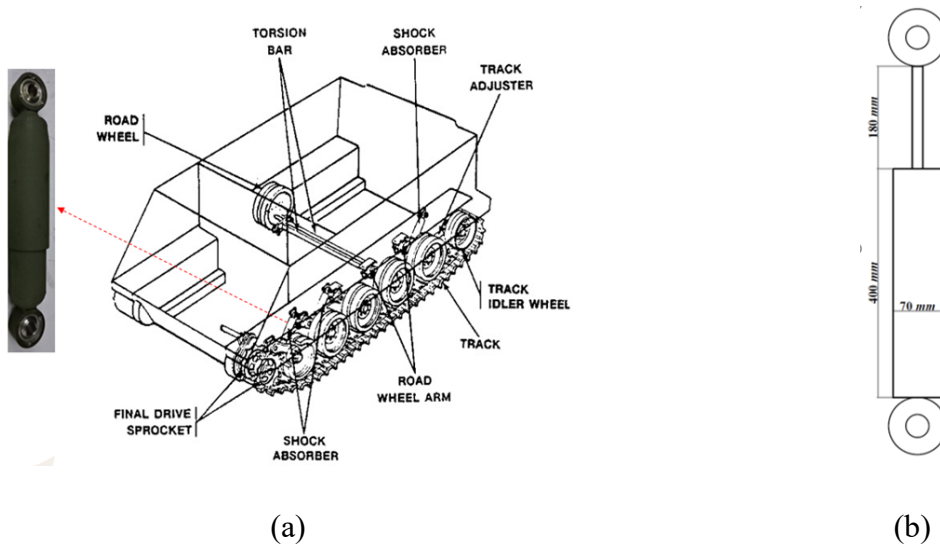


Figure 3-1. M113 off-road vehicle suspension system (a) M113 tracked vehicle undercarriage components [174] and (b) shock absorber's dimensions.

3.2.2 Configuration of the MRFD

The proposed MRFD, shown in Figure 3-2, consists of a single rod cylinder-piston and integrates an external MR bypass valve. The cylindrical housing is composed of two chambers, upper and lower chambers which are filled with MR fluid. As shown in Figure 3-2, the piston rod has an internal hole from one side, while from the other side is connected to the end connectors. Conventionally, gas chambers have been employed to compensate the added volume of the rod entered into the cylinder. To compensate for volume change and also prevent the cavitation phenomenon, occurred on the lower pressure side of dampers, an internal spring has been placed inside the internal hole of the piston rod and pre-loaded with a floating piston, as shown in Figure 3-2. The proposed internal spring provides a more compact design and allows increasing the damper stroke even for large-scale applications-based MRFDs compared with conventional gas

accumulator. The piston rod is attached to the housing by a sealed sliding guider. The MR valve, shown in Figures 2-2(a) and (b) consists of an outer shell, a bobbin with an embedded coil and a spacer. The designed MR valve has both the annular and radial fluid flow channels, thereby dramatically increasing the resistance to the fluid passing through the MR valve, as shown in Figure 3-2(b). The MR fluid moves from the lower chamber (compression) to the upper chamber (rebound) during downward movement of piston, thus creating damping force.

It is worth noting that the designed MRFD with a MR valve having both the annular and radial fluid flow has a large stroke of 180 mm. Also, the assembly and maintenance of the proposed damper as well as MR valve are quite simple due to the absence of the gas chamber and internal MR valve.

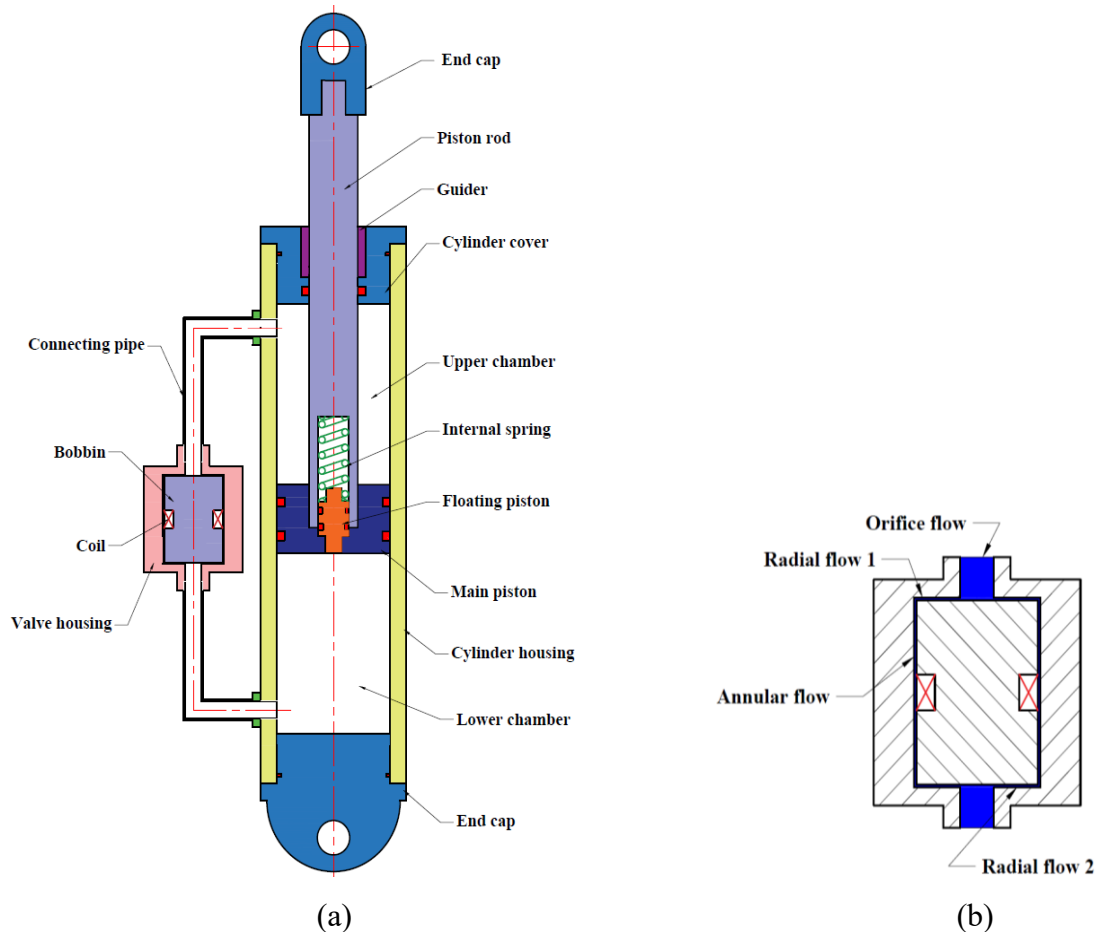


Figure 3-2. Cross-sectional view of the proposed outer bypass MRFD (a) its related MR valve consists of both annular and radial fluid flow channels and (b). annular-radial MR fluid bypass valve gaps.

3.3 Quasi-static Formulation for the MR fluid damper

The proposed MR bypass valve is used to regulate the damping force via activation of MR fluids passing through both annular and radial gaps as shown in Figure 3-2(b). By assuming Bingham plastic characteristics for MR fluid and neglecting the unsteady MR fluid effect, friction force, inertia effect and compressibility of the MR fluid, the generated total damper force can be written as:

$$F_d = P_l A_p - P_u (A_p - A_r) \quad (3-1)$$

where P_l and P_u respectively are the pressure in the lower and upper chamber. A_p and A_r respectively, are the cross-sectional area of the piston and piston rod. At equilibrium position, the pressure inside the lower and upper chambers of MR Fluid dampers with an accumulator chamber can be expressed as follows:

$$P_l \cong P_a; \quad P_u = P_a - \Delta P \quad (3-2)$$

where P_a is the pressure inside the accumulator chamber. The total damping force can be calculated as:

$$F_d = P_a A_r + \Delta P (A_p - A_r) \quad (3-3)$$

In the proposed MRFD, a floating piston connected to a mechanical spring is used to serve as an accumulator. The accumulator force can be approximated as a spring force, thus:

$$P_a A_r = F_{sg} \quad (3-4)$$

Now, the total damping force can be represented as:

$$F_d = F_{sg} + \Delta P (A_p - A_r) \quad (3-5)$$

The generated total damper force can also be written as:

$$F_d = F_{sg} + F_\eta + F_\tau \quad (3-6)$$

The total damper force is a combination of the spring force (F_{sg}), viscous force (F_η), and controllable yield force (F_τ). F_η and F_τ are, respectively, related to the pressure drop due to viscous resistance (ΔP_η) and yield shear stress (ΔP_τ) generated due to the application of the magnetic field to MR fluid through gaps. Hence Eq. (3-6) may be written as:

$$F_d = F_{sg} + (\Delta P_\eta + \Delta P_\tau)(A_p - A_r) \quad (3-7)$$

where A_p and A_r respectively, are the cross-sectional area of the piston and piston rod.

Based on the Bingham-plastic model, the mathematical expression describing the pressure drop in the annular gap (ΔP_a) and the pressure drop in the radial gap, (ΔP_r) due to viscous and fluid shear stress and the pressure drop in the orifice duct (ΔP_o), due to viscous damping can be formulated as:

$$\Delta P_a = \Delta P_{\eta a} + \Delta P_{\tau a} = \frac{12\eta L_a Q}{\pi D_m d^3} + \frac{c_a(L_a - L_c)}{d} \tau_{ya}(B) \quad (3-8)$$

$$\Delta P_r = \Delta P_{\eta r} + \Delta P_{\tau r} = \frac{6\eta Q}{\pi d^3} \ln\left(\frac{D_o}{D_i}\right) + \frac{c_r \tau_{yr}(B)}{2d} (D_o - D_i) \quad (3-9)$$

$$\Delta P_o = \frac{128 \eta L_o Q}{\pi D_i^4} \quad (3-10)$$

where

$$D_m = (D_o + d) \quad (3-11)$$

where in the above equations, $\Delta P_{\eta a}$, $\Delta P_{\tau a}$, $\Delta P_{\eta r}$, and $\Delta P_{\tau r}$ are the pressure drop due to viscous and shear stress in the annular and radial gaps respectively. d is the flow channel annular or radial gap size, η is the fluid base viscosity (the field-independent plastic viscosity), Q is the volume flow rate, L_o is the orifice duct length, L_a is the length of the annular flow duct, L_c is the MR valve coil length, D_m is the annular channel diameter, D_i and D_o represent the radial duct length from input to the output of the flow channel, $\tau(B)$ is the field-dependent yield stress of the MR fluid, B is the magnetic flux density. c_a , and c_r are the flow velocity profile function coefficient of the annular (radial) gap.

Since the MR fluid bypass valve consists of two orifices, two radial gaps and one annular gap, then the total pressure drop within the MR valve (ΔP_v) can be calculated as:

$$\Delta P_v = (\Delta P_{\eta a} + 2\Delta P_{\eta r} + 2\Delta P_o) + (\Delta P_{\tau a} + 2\Delta P_{\tau r}) \quad (3-12)$$

Thus, by substituting Eqs. (3-8) to (3-10) into Eq. (3-12), the total pressure drop can be expressed as:

$$\Delta P_v = \left[\frac{12\eta L_a Q}{\pi D_m d^3} + \frac{12\eta Q}{\pi d^3} \ln \left(\frac{D_o}{D_i} \right) + \frac{256 \eta L_o Q}{\pi D_i^4} \right] + \left[\frac{c_a(L_a - L_c)\tau_{ya}}{d} + \frac{c_r(D_o - D_i)\tau_{yr}}{d} \right] \quad (3-13)$$

It is noted that the Q in Eq. (3-8) can be obtained as:

$$Q = (A_p - A_r)\dot{x}_p \quad (3-14)$$

where \dot{x}_p is the piston velocity, $c_{a(r)}$, the flow velocity profile function coefficient of the annular (radial) gap which can be evaluated with respect to the ratio between pressure drop due to field-dependent shear stress to the viscous pressure drop. $c_{a(r)}$ ranges from a minimum value of 2.07 to a maximum value of 3.07 based on Eq. (3-15) or it can be calculated approximately using Eq. (3-16), which is described in [166] as:

$$c_{a(r)} = \begin{cases} 2.07, & \frac{\Delta P_{\tau a(r)}}{\Delta P_{\eta a(r)}} < 1 \\ 3.07, & \frac{\Delta P_{\tau a(r)}}{\Delta P_{\eta a(r)}} > 1 \end{cases} \quad (3-15)$$

$$c_{a(r)} = 2.07 + \frac{12Q\eta}{12Q\eta + 1.6\pi D_m d^2 \tau_{ya(r)}} \quad (3-16)$$

Hence, the total damping force presented in Eq. (3-6) can also be described in the following form:

$$F_d = F_{sg} + c_{vis}\dot{x}_p + F_{\tau}sgn(\dot{x}_p) \quad (3-17)$$

where c_{vis} is the passive viscous coefficient. The spring force can be calculated as:

$$F_{sg} = k \left(\frac{A_r - A_f}{A_f} \right) x_p \quad (3-18)$$

where k is the stiffness coefficient of the inner spring that is set at 120 kN/m, and A_f is the floating piston area (floating piston diameter, D_f , is equal to 19.05 mm). Using Eqs. (3-7) and (3-12) to (3-14), the c_{vis} and F_{τ} , can be obtained as:

$$c_{vis} = \left[\frac{12\eta L_a}{\pi D_m d^3} + \frac{12\eta}{\pi d^3} \ln \left(\frac{D_o}{D_i} \right) + \frac{256\eta L_o}{\pi D_i^4} \right] (A_p - A_r)^2 \quad (3-19)$$

and

$$F_{\tau} = \left[\frac{c_a(L_a - L_c)\tau_{ya}}{d} + \frac{c_r(D_o - D_i)\tau_{yr}}{d} \right] (A_p - A_r) \quad (3-20)$$

The equivalent field-dependent viscous damping coefficient may also be formulated as:

$$C_{eq} = \frac{F_{sg} + C_{vis}\dot{x}_p + F_{\tau}sgn(\dot{x}_p)}{\dot{x}_p} \quad (3-21)$$

It should be noted that providing a wide control range of the MRFD force depends on the dynamic range of the damper. It is defined as the ratio of the peak damping force under a maximum current input to the damping force generated under zero current input. Alternatively, it is the ratio of the total force to the viscous force and can be mathematically described as:

$$\lambda_d = \frac{F_{on}}{F_{off}} = \frac{F_{sg} + F_{\eta} + F_{\tau}}{F_{sg} + F_{\eta}} = \frac{F_{sg} + C_{vis}\dot{x}_p + F_{\tau}sgn(\dot{x}_p)}{F_{sg} + C_{vis}\dot{x}_p} \quad (3-22)$$

The employed MR fluid (MRF-132DG) for the proposed MRFD is purchased from the Lord corporation [175]. This MR fluids has a dark gray appearance with viscosity of 0.112 Pa.s and average density of 3.05 g/cm³. Using available experimental testing of the MRF-132DG [176], Figure 3-3 shows the variation between shear yield strength of MRF-132DG and applied magnetic flux density.

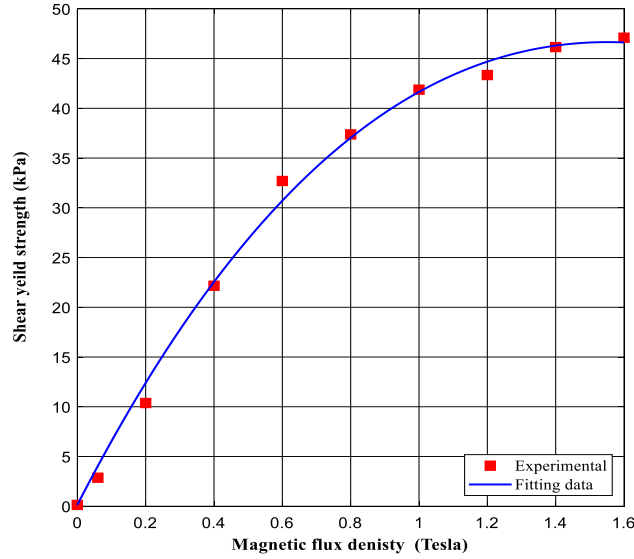


Figure 3-3. Shear yield strength of MRF-132DG.

Using Figure 3-3, field-dependent shear yield stress ($\tau_{ya(r)}(B)$) in the annular and radial gaps $\tau_{ya(r)}$ can be estimated using following polynomial equation of order 3:

$$\tau_{ya(r)}(B) = 2.866B_{a(r)}^3 - 28.22B_{a(r)}^2 + 66.87B_{a(r)} + 0.132 \quad (3-23)$$

By evaluating the magnetic flux density in the annual and radial gaps at different applied currents, the $\tau_{ya(r)}(B)$ can be calculated using Eq. (3-23). Subsequently by having the geometrical parameters of the MR valve, damper and piston velocity, the generated damping force can be subsequently determined using Eqs. (3-17) to (3-20). In this study, the initial geometrical parameters of the MRFD valve geometrical parameters (shown in Figure 3-4) are chosen based on the capacity, size and damping force of the conventional shock absorber of M113 tracked vehicle, mentioned in section 3.2. These geometrical parameters are summarized in Table 3-1.

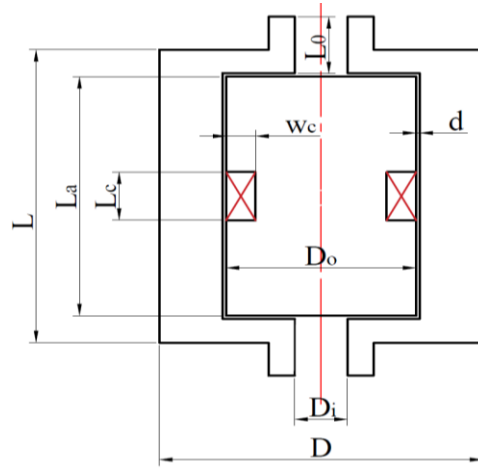


Figure 3-4. MR fluid bypass valve main dimensions.

Table 3-1. The proposed MRFD initial parameters.

Parameter	Symbol	Value (mm)
Duct gap	d	0.9
Coil width	w_c	7
Piston diameter	D_p	55
Piston rod diameter	D_r	30
Radial duct outer diameter	D_o	32.1
Radial duct inner diameter	D_i	10
MR valve whole diameter	D	90
Annular duct length	L_a	50

Coil length	L_c	10
MR valve height	L	67.8

3.3.1 Analytical analysis of MR valve magnetic circuit

In this study, the magnetic circuit analysis has been conducted to evaluate the magnetic flux density in the MR fluid within active regions of the MR valve for different coil currents. First an approximate analytical approach based on the Ampere's law has been formulated and the results have then been compared with those found using numerical approach based on the open-source magneto-static finite element method magnetic (FEMM) software. The equivalent magnetic circuit path for the proposed MR fluid bypass valve with annular and radial gaps is shown in Figure 3-5. Using the Ampere's law, the relation between the magnetic field intensity and the applied current through the MR valve coil can be described as:

$$N_c I = \sum H_j L_j \quad (3-24)$$

where N_c is the number coil turns in the electromagnet, I is the applied current, H_j is the magnetic field intensity for j th circuit links (or elements) and L_j is the effective length of this link. The mathematical expression for the magnetic flux conservation through the circuit as well as the relation between the magnetic flux density and the magnetic flux intensity can be written as:

$$\Phi = B_j A_j \quad (3-25)$$

$$B_j = \mu_o \mu_{rj} H_j = \mu_j H_j \quad (3-26)$$

where Φ is the magnetic flux passing within the circuit and A_j is the effective cross-sectional area at the midpoint of j th link, B_j is the magnetic flux density of the j th link. μ_o is the magnetic permeability of free space ($\mu_o = 4\pi \times 10^{-7}$ H/m) and μ_{rj} is the relative magnetic permeability of the material, which has a considerable effect in the evaluation of the magnetic flux density. It is noted that at low applied magnetic field the relationship between B and H is linear, however as the applied magnetic field intensity increases, the relationship becomes nonlinear due to the saturation of the magnetic induction at high magnetic fields. This is mainly due to the dependency of μ_j to the applied magnetic field, as the magnetic field intensity increases. In analytical magnetic circuit analysis, it is assumed that the applied magnetic field intensity is well below the saturation so that the linear assumption is valid.



Figure 3-5. MR valve Magnetic Circuit (a) annular gap circuit and (b) radial gap circuit.

The magnetic flux within the designed MR valve perpendicularly crosses both the annular and radial gaps as shown, respectively, in Figures 2-5(a) and (b). The magnetic circuit of the single-coil MR bypass valve configuration for both gaps is divided into total eight links. Six of these links represent the metallic core links for bobbin and the remaining two links represent the MR fluid within two gaps. Hence, Eqs. (3-24) and (3-25) can be formulated for the annular and radial gaps as:

$$N_c I = \sum_{j=1}^6 L_j H_j + 2dH_f \quad (3-27)$$

$$\Phi = B_f A_f = B_j A_j \quad (3-28)$$

where H_f and B_f are magnetic flux intensity and density through the MR fluid gap respectively. By substituting Eq. (3-26) into Eq. (3-27), the Eq. (3-27) can be further simplified as:

$$N_c I = \sum_{j=1}^6 \frac{B_j L_j}{\mu_j} + 2d \frac{B_f}{\mu_f} \quad (3-29)$$

It is noted that μ_j is the permeability of the valve core and housing material and μ_f is the permeability of the MR fluid. Substituting the Eq. (3-33) into Eq. (3-29) yields:

$$N_c I = \sum_{j=1}^6 \frac{B_f A_f L_j}{\mu_j A_j} + 2d \frac{B_f}{\mu_f} \quad (3-30)$$

or

$$N_c I = B_f \left[A_f \sum_{j=1}^6 \left(\frac{L_j}{\mu_j A_j} \right) + 2 \frac{d}{\mu_f} \right] \quad (3-31)$$

where

$$A_f = \begin{cases} \pi D_m d & , \text{ for annular duct} \\ \frac{\pi}{4} (D_o^2 - D_i^2) & , \text{ for radial gap} \end{cases} \quad (3-32)$$

Now using Eq. (3-31), the induced magnetic flux density in the MR fluid within active regions can be estimated as:

$$B_f = \frac{N_c I}{\frac{2d}{\mu_f} + A_f S_j} \quad (3-33)$$

where S_j is the total reluctance of the bobbin's links, which can be described as:

$$S_j = \sum_1^6 \frac{L_j}{\mu_j A_j} \quad (3-34)$$

The magnetic circuit parameters for both annular and radial gaps of the MR valve have been formulated and are summarized in Tables 3-2 and 3-3 respectively. The number of coil turns in electromagnet can also be estimated using relation reported in [177] as:

$$N_c = \frac{2w_c L_c}{1.68d_w^2} \quad (3-35)$$

Table 3-2. Magnetic circuit parameters of the MR fluid bypass valve (Annular gap).

Link No	Length L_j	Area A_j	Reluctance S_j
1	$L_1 = \frac{(D_o + 2w_c)}{4}$	$A_1 = 2\pi \left(\frac{L_a - L_c}{2} \right) \left(\frac{3D_o + 2w_c}{8} \right)$	$S_1 = \frac{L_1}{\mu_s A_1}$
2	$L_2 = \frac{(D - D_o - 2d)}{4}$	$A_2 = 2\pi \left(\frac{D - D_o - 2d}{2} \right) \left(\frac{D + 3D_o + 6d}{8} \right)$	$S_2 = \frac{L_2}{\mu_s A_2}$
3	$L_3 = \frac{L_a + L_c}{2}$	$A_3 = \pi \left[\frac{D^2}{4} - \left(\frac{D + D_o + 2d}{4} \right)^2 \right]$	$S_3 = \frac{L_3}{\mu_s A_3}$
4	$L_4 = \frac{(D - D_o - 2d)}{4}$	$A_4 = 2\pi \left(\frac{D - D_o - 2d}{2} \right) \left(\frac{D + 3D_o + 6d}{8} \right)$	$S_4 = \frac{L_4}{\mu_s A_4}$
5	$L_5 = \frac{(D_o + 2w_c)}{4}$	$A_5 = 2\pi \left(\frac{L_a - L_c}{2} \right) \left(\frac{3D_o + 2w_c}{8} \right)$	$S_5 = \frac{L_5}{\mu_s A_5}$
6	$L_6 = \frac{L_a + L_c}{2}$	$A_6 = \pi \left(\frac{D_o - 2w_c}{2} \right)^2$	$S_6 = \frac{L_6}{\mu_s A_6}$

Table 3-3. Magnetic circuit parameters of the MR fluid bypass valve (Radial gap).

Link No	Length L_j	Area A_j	Reluctance S_j
1	$L_1 = \left(\frac{D + 2d + 2w_c}{4}\right)$	$A_1 = 2\pi \left(\frac{L - L_c}{2}\right) \left(\frac{2D + D_o + 2w_c}{8}\right)$	$S_1 = \frac{L_1}{\mu_s A_1}$
2	$L_2 = \frac{L + L_a + 2d}{2}$	$A_2 = \pi \left[\frac{D^2}{4} - \left(\frac{D + D_o + 2d}{4}\right)^2 \right]$	$S_2 = \frac{L_2}{\mu_s A_2}$
3	$L_3 = \left(\frac{D + 2d + 2w_c}{4}\right)$	$A_3 = 2\pi \left(\frac{L - L_c}{2}\right) \left(\frac{2D + D_o + 2w_c}{8}\right)$	$S_3 = \frac{L_3}{\mu_s A_3}$
4	$L_4 = \frac{L - L_a - 2d}{4}$	$A_4 = \frac{\pi}{4} [D^2 - D_i^2]$	$S_4 = \frac{L_4}{\mu_s A_4}$
5	$L_5 = L_a$	$A_5 = \pi \left(\frac{D_o - 2w_c}{2}\right)^2$	$S_5 = \frac{L_5}{\mu_s A_5}$
6	$L_6 = \frac{L - L_a - 2d}{4}$	$A_6 = \frac{\pi}{4} [D^2 - D_i^2]$	$S_6 = \frac{L_6}{\mu_s A_6}$

3.3.2 Magneto-static finite element analysis

Finite element analysis of the MR fluid bypass valve has also been conducted using an open source Finite Element Method Magnetics (FEMM) software [178]. FEMM can be effectively used to accurately predict the intensity and distribution of magnetic flux in the magnetic circuits (DC or low frequency applied currents) on two-dimensional axisymmetric domain. The FE model was then developed using FEMM corresponding to the designed MR fluid bypass valve. The B-H curves of the employed MR fluid (MRF-132DG) and the magnetic material of the valve core and housing (AISI 1006) are shown in Figures 2-6(a) and (b), respectively.

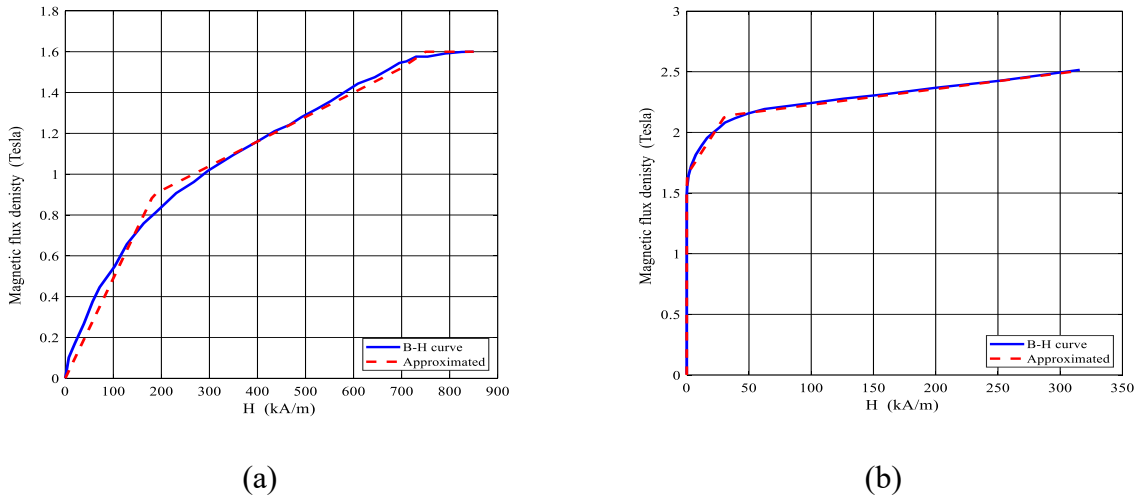


Figure 3-6. The B-H curve of MR fluid and bypass valve material (a) B-H curve MRF-132 DG [175] and b) B-H curve steel 1006 [179].

Using the curve-fitting, the following piecewise linear relations can be used in FEMM to describe the B-H behaviour of MR fluid as well as magnetic core material and housing as:

$$B_f = \begin{cases} 0.00049 H & , 0 \leq H \leq 200 \\ 0.6814 + 0.00012H & , 200 \leq H \leq 700 \\ 1.6, & H > 700 \end{cases} \quad (3-36)$$

$$B_s = \begin{cases} 1.5 & , H \leq 1 \\ 1.6467 + 0.0159H & , 1 \leq H \leq 30 \\ 2.0969 + 0.0013H & , 30 \leq H \leq 300 \\ 2.5, & H > 300 \end{cases} \quad (3-37)$$

where B_f is the MR fluid magnetic flux density and B_s is the magnetic flux density of the valve's material (AISI 1006).

The MR valve coil wire is chosen to be Gauge 22 AWG copper wire with a resistance per unit length of 52.96 mΩ/m and maximum applied current of 7 A. As mentioned before the field-dependent yield strength of the employed MR fluid, MRF-132DG, under varied applied magnetic flux density can be obtained using Eq. (3-23). The average magnetic flux density in the MR fluid active regions for annular and radial gaps has been evaluated by averaging the induced magnetic flux density along the length of the annular and radial gaps using the following relation:

$$B_{av} = \frac{1}{l} \int_0^l B(s) ds \quad (3-38)$$

3.4 Design optimization formulation of the of the MRFD

The dynamic range of the MR fluid bypass valve is an important performance index to be considered in design optimization of MRFDs. Increasing the dynamic range of the MRFD will greatly enhance its capability to attenuate vibration under wide range of frequencies. The objective of the proposed design optimization is to formulate a multidisciplinary problem in order to identify the geometrical and magnetic circuits parameters, which maximize the dynamic range of the proposed MRFD under given volume, magnetic and damping force constraints.

The main design variables that represent the geometrical parameters of the MRFD and MR fluid bypass valve and its magnetic circuit are $d, w_c, D_p, D_r, D_o, D_i, D, L_a, L_c$ and L , as shown in Figure 3-7. For the sake of clarity, the description of the design variables together with their lower

and upper bounds are summarized in Table 3-4. The MR fluid and the magnetic circuit properties are also provided in Table 3-5. The piston velocity is considered to be 12.5 mm/s.

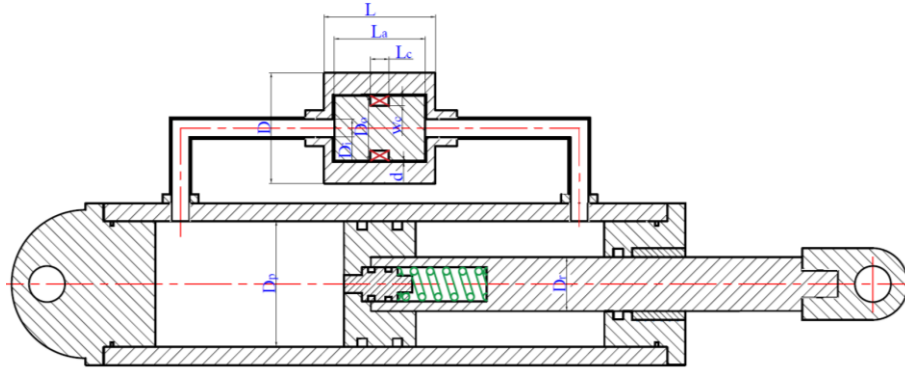


Figure 3-7. By-pass MRFD with main identified design parameters.

Table 3-4. Main design parameters and their assigned lower and bounds.

No	Description	Variables	Bound (mm)
1	Duct gap	$x_1 = d$	0.5-2
2	Coil width	$x_2 = w_c$	5-20
3	Piston diameter	$x_3 = D_p$	40-70
4	Piston rod diameter	$x_4 = D_r$	20-50
5	Radial gap outer diameter	$x_5 = D_o$	10-80
6	Radial duct inner diameter	$x_6 = D_i$	5-30
7	MR valve whole diameter	$x_7 = D$	50-90
8	Annular gap length	$x_8 = L_a$	20-70
9	Coil length	$x_9 = L_c$	5-25
10	MR valve height	$x_{10} = L$	50-80

Table 3-5. MR fluid and valve material properties.

Parameter	Symbol	Value	Unit
MR fluid density	ρ	3050	kg/m ³
MR fluid viscosity	η	0.112	pa.s
MR fluid relative permeability	μ_{rf}	5	
Steel (1006) relative permeability	μ_{rj}	1404	
Permeability of free space	μ_o	$4\pi \times 10^{-7}$	TmA ⁻¹
Copper wire (gage AWG22) diameter	d_w	0.7131	mm

Constraints imposed on the MR fluid bypass valve have been categorized into geometrical, and physical (e.g., magnetic circuit) constraints. Side constraints are considered for all design parameters (see Table 3-4), so that design optimization can be conducted within a given design space and volume (V_{mr}), thus allowing a compact design of the MR fluid bypass valve. Moreover, the induced magnetic flux density in the MR fluid's active regions should be lower than the saturation limit of the MR fluid. This avoid temprature rise in the coil, thereby allowing valve to operate continuously over a longer period of time. Also, the magnetic flux saturation of the MR valve's core material should not occur before that of MR fluid. Here a factor (γ) is defined as the ratio of the magnetic flux in the MR valve bobbin to that in the MR fluid. To guard against saturation limits and also provide compact design the factor γ has been limited to be between the range of 1.02 to 1.07 [180]. It is noted that the saturation limit of the MR fluid is approximately 1.6 Tesla, as shown in Figure 3-6(a) and the core (steel AISI 1006) is saturated approximately at 2.5 Tesla.

The off-state damping force should not be less than 467 N based on the specification of the vehicle conventional shock absorber in Figure 3-1. The minimum yield damping force of the MRFD is also considered to be at least 950 N to assure dynamic range of greater than 2. Considering the above-mentioned design requirements, the design optimization problem can be formally formulated as:

Find $X = [d, w_c, D_p, D_r, D_o, D_i, D, L_a, L_c, L]$, a design variable vector of dimension ten, to minimize

$$f(X) = \frac{F_s + C_{vis}\dot{x}_p}{F_s + C_{vis}\dot{x}_p + F_\tau \text{sgn}(\dot{x}_p)} = \frac{F_{off}}{F_{on}} = \frac{1}{\lambda_d} \quad (3-39)$$

Subject to

$$\left\{ \begin{array}{l} -\frac{F_{off}}{467} + 1 \leq 0 \text{ } N \\ -\frac{F_{\tau}}{950} + 1 \leq 0 \text{ } N \\ \frac{V_{mr}}{4.31 \times 10^5} - 1 \leq 0 \text{ } mm^3 \\ -\gamma + 1.02 \leq 0 \\ \gamma - 1.07 \leq 0 \\ 0.5 \leq x_1 \leq 2 \text{ } mm \\ 5 \leq x_2 \leq 20 \text{ } mm \\ 40 \leq x_3 \leq 70 \text{ } mm \\ 20 \leq x_4 \leq 50 \text{ } mm \\ 10 \leq x_5 \leq 80 \text{ } mm \\ 5 \leq x_6 \leq 30 \text{ } mm \\ 50 \leq x_7 \leq 90 \text{ } mm \\ 20 \leq x_8 \leq 70 \text{ } mm \\ 5 \leq x_9 \leq 25 \text{ } mm \\ 50 \leq x_{10} \leq 80 \text{ } mm \end{array} \right. \quad (3-40)$$

The formulated design optimization problem was successfully solved using the successive implementation of GA, which is a stochastic-based optimization technique, and the SQP algorithm, which is a powerful nonlinear gradient-based optimization technique, to accurately capture the global optimum solution. Due to its stochastic nature, the GA can provide near global optimum solution. The optimum solution from GA is then used as the initial point for the SQP algorithm to accurately catch the global optimum solution. Using this hybrid approach, same optimal solutions were obtained using different randomly generated initial population for the GA.

3.5 Results of Simulations

The performance (e.g., damping force and dynamic range) of the initial design of the MR bypass valve (Table 3-1) are firstly evaluated and compared with those of optimally designed MRFD. The results of the magnetic circuit analyses including analytical and numerical approaches, have also been presented in this section.

3.5.1 Optimization results

As mentioned in section 3.4, the optimization problem was solved using a hybrid approach by combining GA and SQP algorithms to capture the true global optimum solution. Starting using different initial populations for GA resulted in different optimum solutions near the global

optimum. Table 3-6 provides the sample of optimum points obtained using GA. Using optimum GA values in Table 3-6 as initial points for the SQP algorithm has rendered a unique global optimum solution provided in Table 3-7. The iteration history of the SQP using different initial points (Table 3-6) is shown in Figure 3-8.

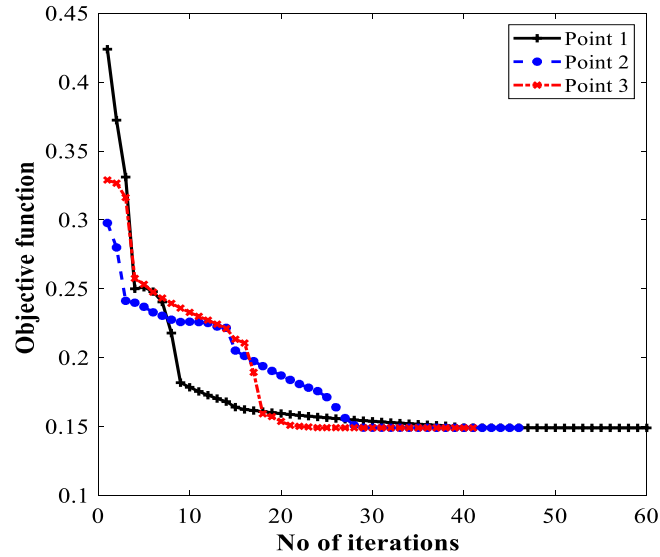


Figure 3-8. Iteration history of the optimized parameters.

The optimized damper can generate on-state damping force of 7.41 kN and dynamic range of 6.7 under applied current of 1.5 A. However, the initially designed damper (Table 3-1) revealed on-state damping force of 3.63 kN and and dynamic range of 4. The optimized and initially designed geometrical parameters are compared and summarized in Table 3-8. As it can be realized the dynamic range of the optimized damper has been improved by 67.5% as compared with initially designed damper. Using Eq. (3-35), the number of coil turns in optimal configuration is 175.

Table 3-6. Genetic Algorithm optimum points in (mm).

Iteration No	Design variables									
	x_1	x_2	x_3	x_4	x_5	x_6	x_7	x_8	x_9	x_{10}
1	2	6	50	40	50	10	50	60	24.6	80
2	0.9	12.3	70	21.2	25.6	5.1	51.3	35.5	13	50.5
3	0.5	4.4	47.2	34.9	26.8	5.3	80	30	10.3	80
4	0.6	15	65	30	49	6.5	90	26	13	60.3
5	0.7	7	69.9	30.6	45	10	70	30	11	61.6

Table 3-7. SQP global optimum solution (mm).

x_1	x_2	x_3	x_4	x_5	x_6	x_7	x_8	x_9	x_{10}
0.788	7	50	30	38.1	10	64.5	43.9	10.7	55.5

Table 3-8. Initial base design and Optimized geometrical dimensions and performance indices.

Parameter	Symbol	Initial Design (mm)	Optimized Design (mm)
Duct gap	d	0.9	0.788
Coil width	w_c	7	7
Piston diameter	D_p	55	50
Piston rod diameter	D_r	30	30
Radial duct outer diameter	D_o	32.1	38.1
Radial duct inner diameter	D_i	15	10
MR valve whole diameter	D	90	64.5
Annular duct length	L_a	50	43.9
Coil length	L_c	10	10.7
MR valve height	L	67.8	55.5
Performance Indices:			
Damping force (field-off), kN	F_{off}	0.91	1.1
Max damping force (field-on), kN	F_{on}	3.63	7.41
Dynamic range	λ_d	4	6.7

3.5.2 Magnetic circuit results

The solution of the magnetic circuit for the optimized MR valve was estimated analytically. The density (B) and intensity (H) of magnetic flux were approximately evaluated for both the annular and radial ducts under different excitation currents, as given in Table 3-9.

Table 3-9. Analytical results for annular and radial ducts magnetic circuit.

Current (A)	Annular duct		Radial duct	
	Magnetic flux density (Tesla)	Magnetic field intensity (A/m)	Magnetic flux density (Tesla)	Magnetic field intensity (A/m)
0.10	0.054	7.16×10^3	0.0455	6.03×10^3
0.25	0.135	1.79×10^4	0.1138	1.51×10^4
0.50	0.270	3.58×10^4	0.2277	3.02×10^4
0.75	0.405	5.37×10^4	0.3420	4.53×10^4
1.00	0.540	7.16×10^4	0.4553	6.04×10^4
1.50	0.621	8.24×10^4	0.5236	6.94×10^4

The magnetic circuit analytical results were then compared with simulation results based on the magnetic circuit finite element model developed in FEMM. A triangular mesh of 9327

elements and 4822 nodes were created with a precision of $1e-08$. The meshing and the magnetic flux density distribution in the MR valve gaps and the MR valve linkages under excitation current 1.5 A are shown in Figure 3-9. The results for magnetic flux density and the distribution of the magnetic field intensity along the annular-radial path length (from A to F shown in Figure 3-9) are shown in Figures 2-10 and 2-11, respectively. The average results of the numerical solution for the magnetic circuit for different applied currents are summarized in Table 3-10.

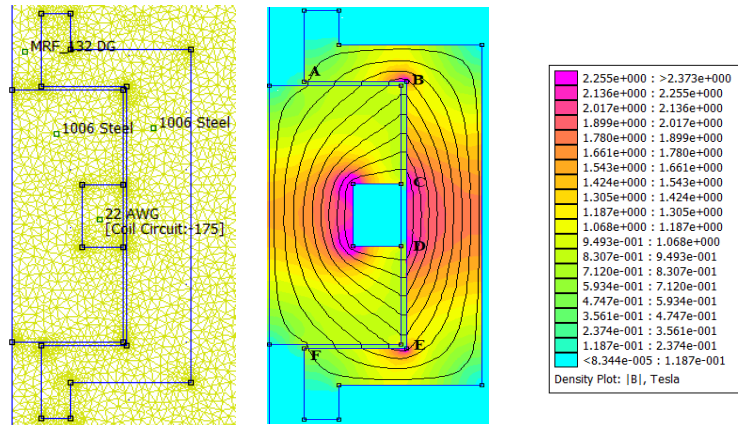


Figure 3-9. Magnetic flux distribution at excitation current 1.5 A.

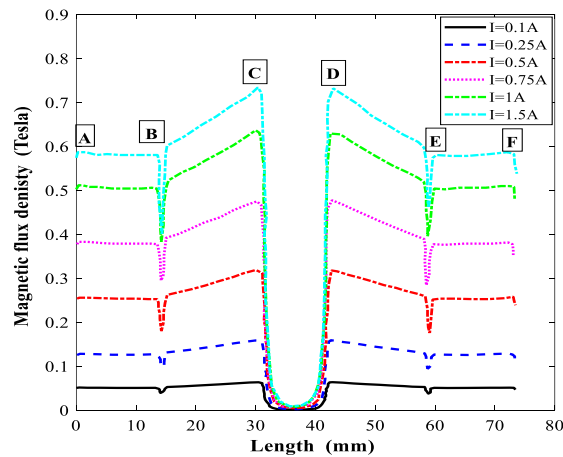


Figure 3-10. Magnetic flux density along the annular-radial path length under different applied current.

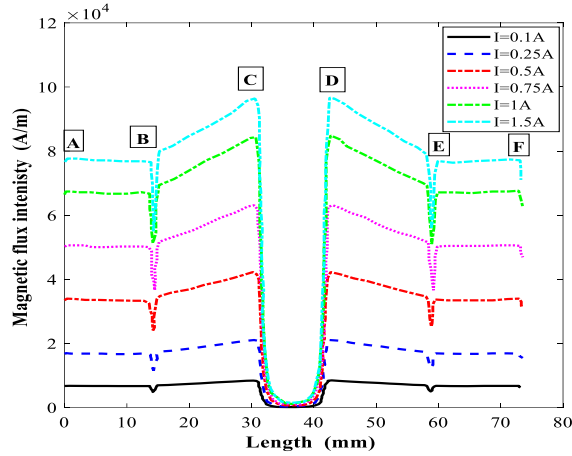


Figure 3-11. Magnetic flux intensity along the annular-radial path length under different applied current.

Table 3-10. Average numerical results for annular and radial gaps magnetic circuit using FEMM.

Current (A)	Annular duct		Radial duct	
	Magnetic flux density (Tesla)	Magnetic field intensity (A/m)	Magnetic flux density (Tesla)	Magnetic field intensity (A/m)
0.1	0.058	7.5×10^3	0.0504	6.6×10^3
0.25	0.146	1.85×10^4	0.125	1.68×10^4
0.5	0.293	3.82×10^4	0.253	3.34×10^4
0.75	0.426	5.73×10^4	0.378	5×10^4
1	0.584	7.71×10^4	0.504	6.6×10^4
1.5	0.667	8.79×10^4	0.58	7.7×10^4

The comparison of the numerical and analytical results for the average magnetic flux density in the annular and radial gaps are shown in Figures 2-12(a) and (b), respectively. Results show a reasonably good agreement between the analytical and numerical results. Besides, results show that the relation between magnetic flux density and applied coil current is linear when coil current is below 1 A, irrespective of the gap type. Furthermore, the induced magnetic flux density is relatively higher within annular gap than that of radial gap, irrespective of coil current.

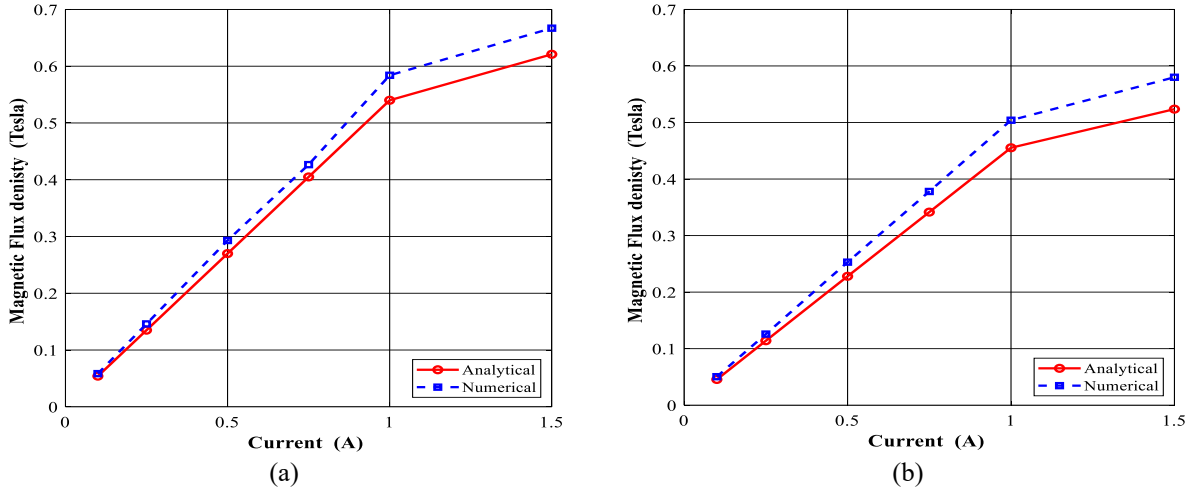


Figure 3-12. Magnetic flux density at different coil currents (a) annular gap and (b) radial gap.

3.6 Experimental Method

A prototype of the proposed MRFD is fabricated based on the optimal geometric and magnetic circuit parameters with some modifications. Figure 3-13 shows the components and assembled configuration of the fabricated MRFD. These components have been fabricated with the proper tolerances and surface roughness. Alloy steel 4140 is selected as the material for cylinder housing and piston rod, while low carbon steel 1117 is selected for the main and floating pistons. The damper is filled with the commercial MR fluid 132-DG from Lord corporation. A three-dimensional model and the detailed drawing of the proposed MRFD can be seen in Appendix D.

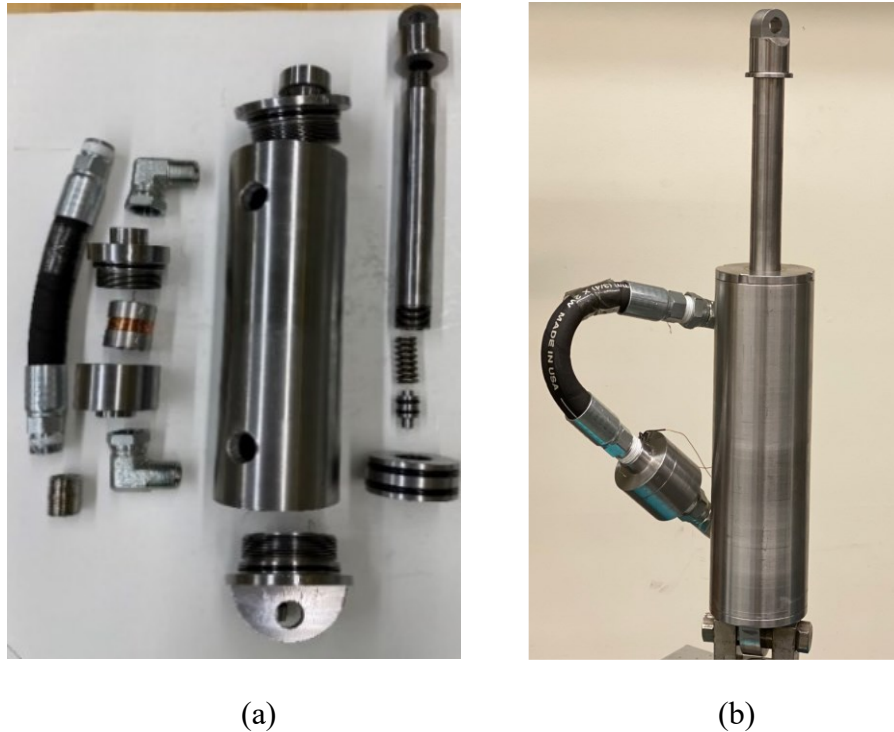


Figure 3-13. Fabricated MRFD (a) MRFD components and (b) the prototype MRFD.

Due to the limitation of the manufacturing tools and processing as well as cost-effectiveness, the manufactured MRFD slightly differs from the optimized MRFD. MR valve has a fluid gap of 1.2 mm instead of the optimal value of 0.778 mm while maintaining the dynamic range of at least 2 by enlarging the damper main piston diameter to 70 mm. The MR coil wire is chosen to be Gauge 24 AWG copper wire, thus the number of coil turns was increased to 215 turns to enhance the time response and overcome the short-circuit problem that occurred. The core material is chosen to be steel AISI 1117 that has a relative permeability of 1777 for overcoming the magnetic saturation due to increasing the number of turns. All the amendments are summarized in Table 3-11. The performance of the MR valve in terms of off-stat damping force, maximum damping force, and dynamic range has been subsequently re-evaluated based on the fabricated MRFD, via the mathematical formulations presented in Section 3.3. Table 3-11 also compares the performance indices of the fabricated MR valve with the firstly optimized MR valve under a peak piston velocity of 12.5 mm/s. As it can be realized the fabricated MRFD has nearly the same performance indices as the optimized configuration.

An experimental test has been designed to validate the simulation results for magnetic circuit of bypass MR valve and also to validate the predicted damping forces and dynamic range. Also,

the fabricated MRFD has been experimentally characterized for evaluating its dynamic performance.

Table 3-11. Comparison between the parameters and performance of the optimized and fabricated MR bypass valve.

Parameter	Symbol	Optimized MRFD (mm)	Modified MRFD (mm)
Duct gap	d	0.788	1.2
Coil width	w_c	7	7
Piston diameter	D_p	50	70
Piston rod diameter	D_r	30	30
Radial gap outer diameter	D_o	38.1	38.1
Radial gap inner diameter	D_i	10	10
MR valve whole diameter	D	64.5	64.5
Annular gap length	L_a	43.9	43.9
Coil length	L_c	10.7	10.7
MR valve height	L	55.5	60
Copper wire gauge	d_w	AWG22	AWG24
Number of coils (turns)	N_c	175	215
Bobbin core material		AISI 1006	AISI 1117
Performance Indices:			
Damping force,(field-off), kN	F_{off}	1.1	1.16
Max damping force (field-on), kN	F_{on}	7.41	5.78
Dynamic range	λ_d	6.7	4.98

3.6.1 Experimental validation of the magnetic circuit model

The FE model developed for solving the magnetic circuit of the MR valve (along the annular MR fluid gap) was validated by measuring the steady-state magnetic flux density in the MR fluid gap. As it was not possible to directly measure the magnetic flux density in the MR fluid gaps regions in-situ, the measurement has been conducted in the absence of MR fluid (in the air gap) by removing the valve from its enclosure. Then, the magnetic flux density was measured along the annular MR fluid gap. The magnetic flux density distribution using FEMM at the excitation current of 2 A is shown in Figure 3-15. The results were compared to those obtained experimentally by locating Gaussmeter at different locations along the annular gap. The setup of the experiment is shown in Figure 3-14. The MR valve coil was energized with different applied currents using a DC power supply (10 A, 100 V).

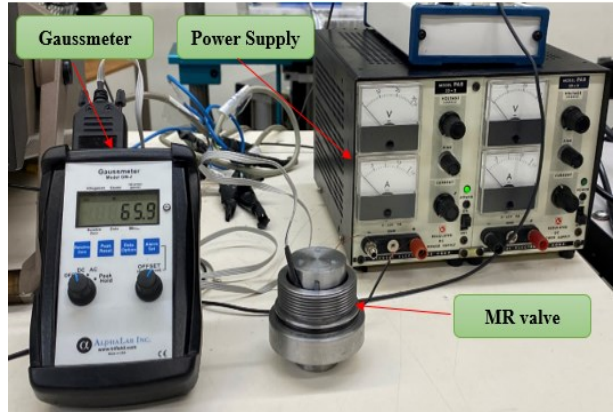


Figure 3-14. Measurement of the magnetic flux density along the MRFD's annular gap.

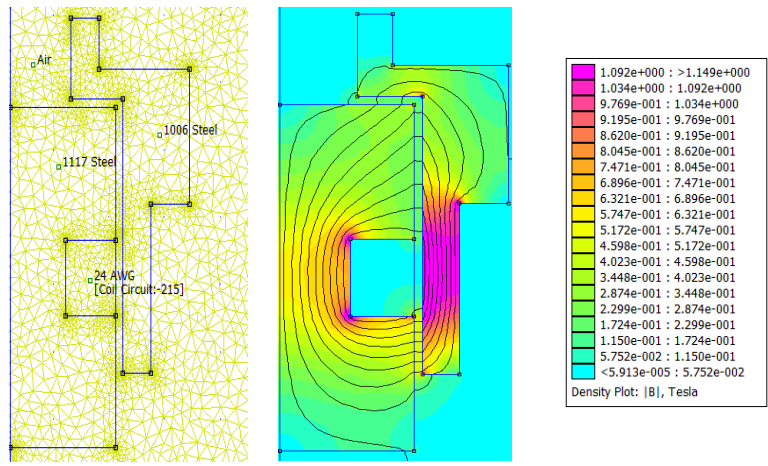


Figure 3-15. Magnetic flux distribution at excitation current 2 A.

The experimental results for the average magnetic flux density along the annular gap and their comparison with FE results as in sub-section 3.3.2 under different applied currents are shown in Figure 3-16. Results are suggestive of a relatively well agreement between the experimentally and numerically obtained magnetic flux density.

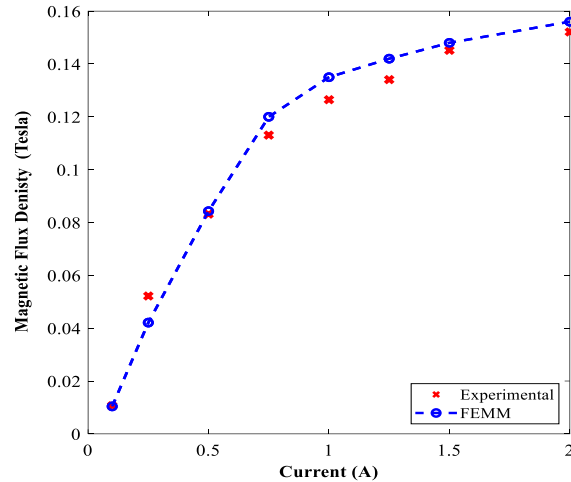


Figure 3-16. Comparison of the measured and FE estimation of the average magnetic flux density along the annular gap of the MR valve.

3.6.2 Experimental validation of the optimization strategy of the fabricated MRFD

Experimental characterization of the fabricated MRFD was performed to verify the modelling and design optimization formulation of the proposed bypass MRFD. The measurements were performed on a Material Testing System (MTS) machine, as shown in Figure 3-17. The MRFD was fixed between the upper and lower horizontal crossbeams of the loading frame of the MTS machine. The lower crossbeam contains a servo actuator that can apply sinusoidal excitations to the damper's cylinder. A built-in Linear Voltage Displacement Transducer (LVDT) measures the displacement of the damper cylinder. The upper crossbeam contains a load cell to measure the damping force. The measurements are transmitted to a National Instruments Data Acquisition board (DAQ) and then digitized and monitored on a PC using LabView software. The experimental measurements were performed for measuring force-displacement and force-velocity of the MRFD at low frequencies (1 and 2 Hz) and amplitudes of 1 mm respectively and under different excitation currents (0-2A).

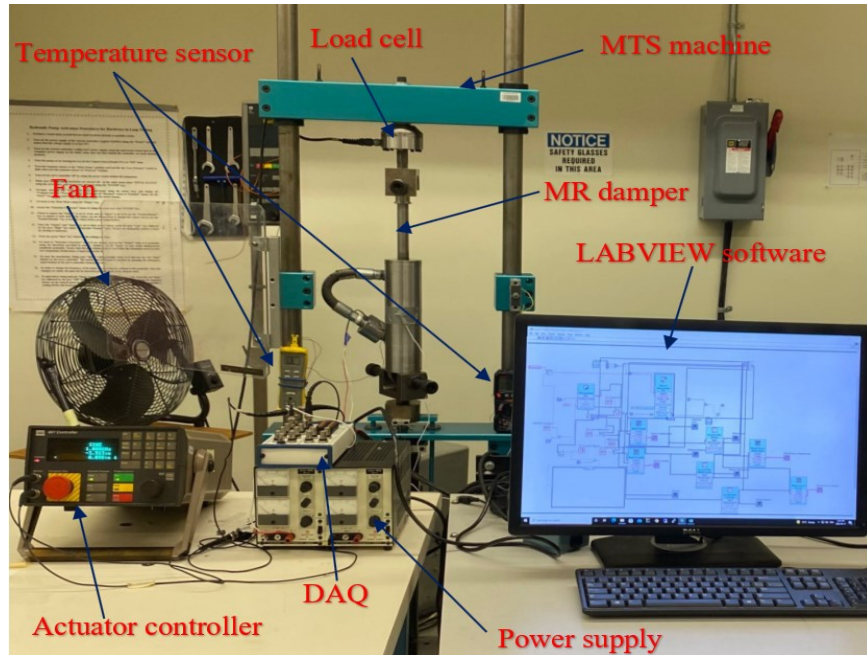
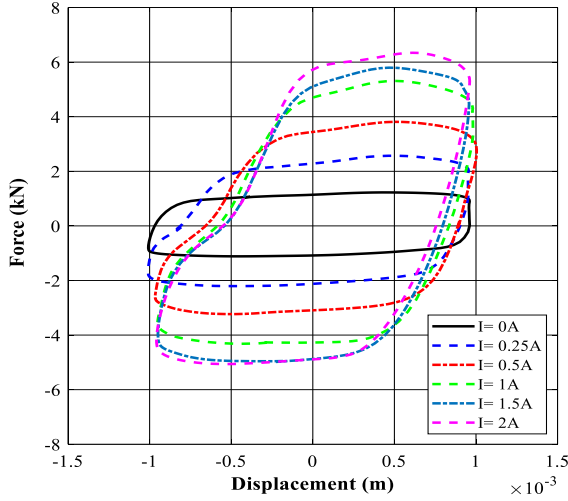
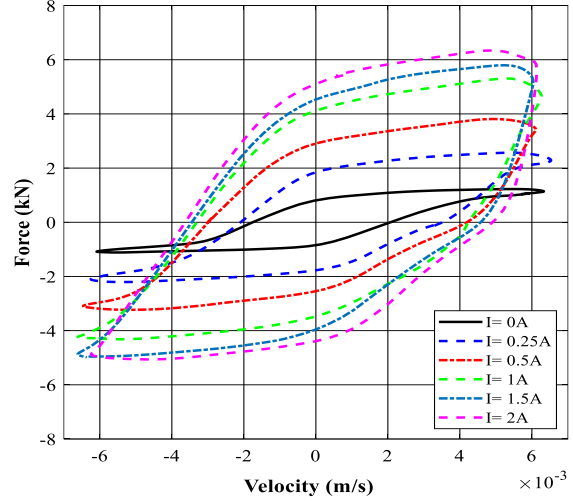


Figure 3-17. Test setup of the fabricated bypass MRFD.

Experimental characterization of the MRFD is conducted by measuring the force-displacement and force velocity at each loading condition. Figure 3-18 shows force-displacement and force-velocity hysteresis behaviour of MRFD under harmonic excitation with frequency of 1 Hz and loading amplitude of 1 mm, respectively. The presented results in Figure 3-18 were obtained at applied input current of (0-2 A). Figure 3-19 shows similar results for the excitation frequency of 2 Hz and loading amplitude of 1 mm. The results show that the area encircled by the force-displacement curve (representing the energy dissipation) substantially increases with increasing the applied current. The force-velocity curves also show that the damping force increases with increasing current as well as velocity. For instance, the damping force at a frequency of 2 Hz and displacement of 1 mm (peak velocity of 12.5 mm/s) ranges between 1.31 kN to 6.61 kN from off-state to on state (current 2 A), yielding a large dynamic range of nearly 5.06. These experimentally obtained indices are in good agreement with those indices presented in Table 3-11, which were obtained using analytical relation in Section 3.3.

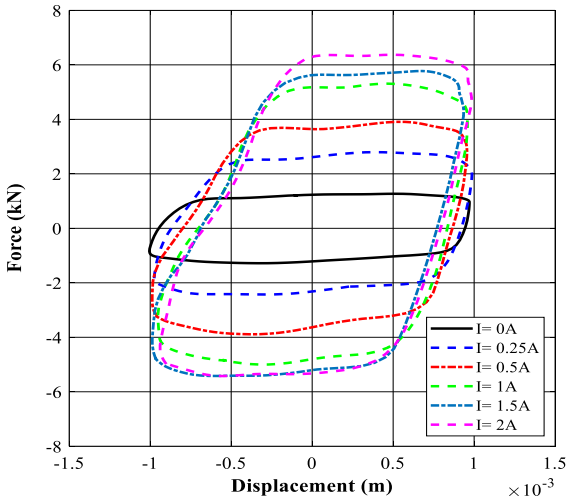


(a)

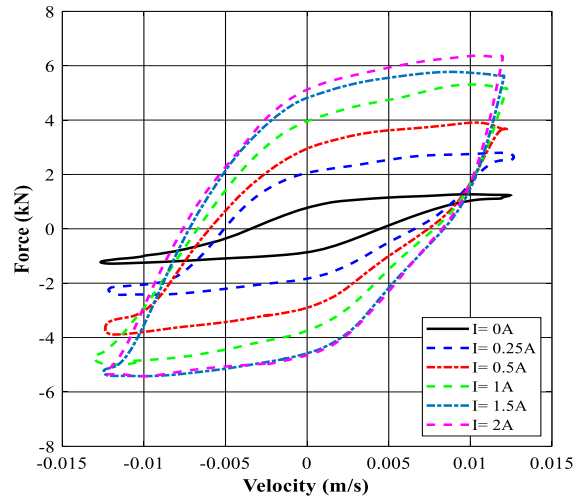


(b)

Figure 3-18. The measured data at excitation frequency of 1 Hz and displacement of 1 mm (a) force-displacement and (b) force-velocity.



(a)



(b)

Figure 3-19. The measured data at excitation frequency of 2 Hz and displacement of 1 mm (a) force-displacement and (b) force-velocity.

In order to validate the developed mathematical model of the proposed MRFD, the measured data has been compared with the design optimization results. Figure 3-20 shows the comparison of the controllable damping force obtained experimentally and using an analytical approach, Eq. (3-20), under varied applied currents and different excitation conditions. It is noted that the yield stress in the active region of annular and radial MR fluid gaps ($\tau_{ya(r)}(B)$) was obtained using Eq. (3-23). The yield stress depends on the magnetic flux density, as obtained using magnetic circuit

analysis in Eq. (3-33). Figure 3-21 also illustrates the equivalent damping coefficient C_{eq} evaluated experimentally using the energy dissipation obtained from the enclosed area in force-displacement hysteresis loops (Figures 2-18 and 2-19) and also analytically using Eq. (3-21). The variation of the MRFD dynamic range evaluated experimentally and analytically (using Eq. (3-22) with respect to applied current under different excitation conditions are also shown in Figure 3-22. Results show a reasonably good agreement between the simulation and experimental results and confirm the significant field-dependent controllability of the damper at different operation conditions. The slight deviation between the experimental and simulation modeling was observed. This may be partly attributed to the quasi-static modeling based on the Bingham plastic fluid behaviour in which other factors such as the inertia effect, fluid compressibility, non-uniform distribution of the magnetic flux and temperature effects, have been ignored.

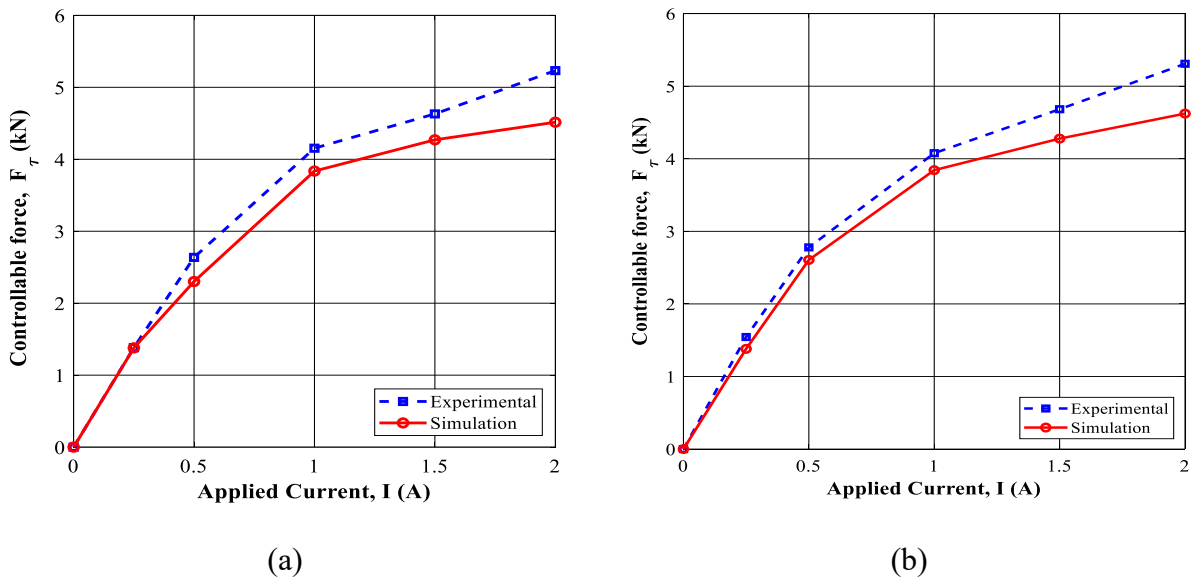
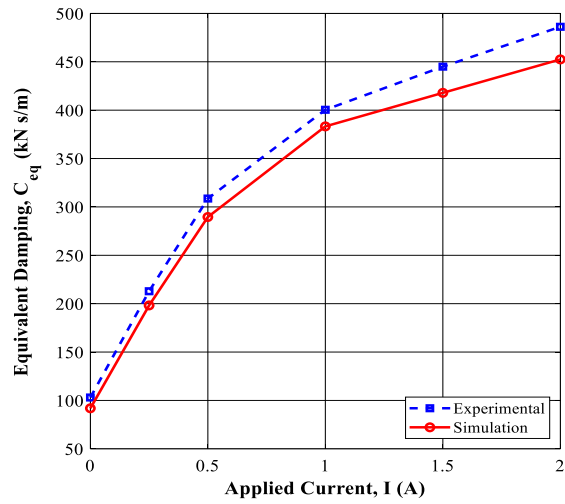
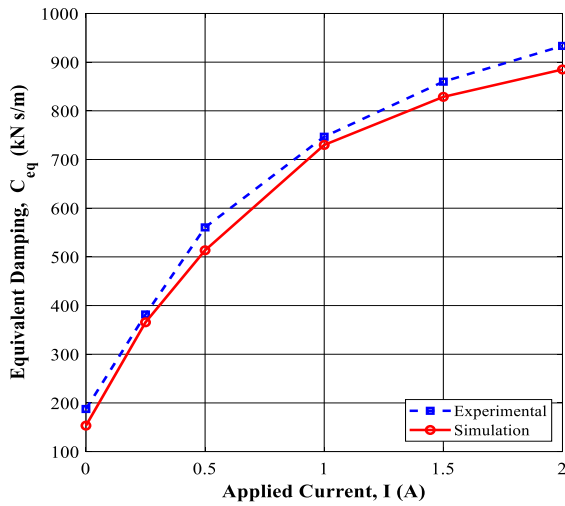


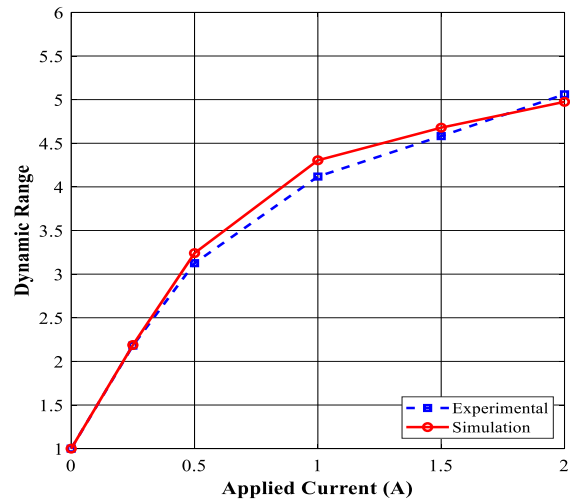
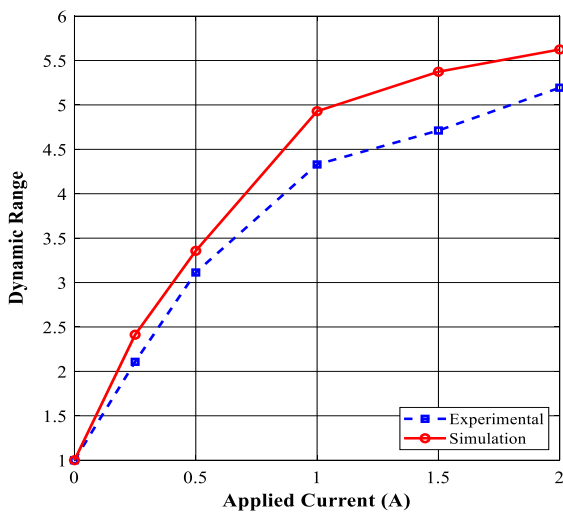
Figure 3-20. Variation of the controllable damping force with applied currents (a) excitation frequency of 1 Hz and amplitude of 1 mm and (b) excitation frequency of 2 Hz and amplitude of 1 mm.



(a)

(b)

Figure 3-21. Variation of the damping coefficient with applied currents (a) excitation frequency of 1 Hz and amplitude of 1 mm and (b) excitation frequency of 2 Hz and amplitude of 1 mm.



(a)

(b)

Figure 3-22. Variation of the dynamic range of the novel MRFD with respect to the applied current (a) excitation frequency of 1 Hz and amplitude of 1 mm and (b) excitation frequency of 2 Hz and amplitude of 1 mm.

3.7 Summary

In this chapter, a compact annular-radial magnetorheological damper has been modelled and optimally designed for the replacement of conventional shock absorbers in off-road applications.

Using the Bingham plastic model, a quasi-static model for determining the total damping force as a function of the MR bypass valve geometrical parameters, piston velocity and MR fluid yield shear stress has been developed. The magnetic circuit of the MR fluid bypass valve has been solved analytically to obtain the magnetic flux density through the MR fluid annular and radial gaps under different applied currents. The magnetic finite element analysis has also been conducted to validate the analytical magnetic circuit model and also better realize the distribution of the magnetic field in the MR fluid active regions. A formal multidisciplinary optimization problem based on both geometrical and magnetic circuit parameters was subsequently formulated to maximize the MRFD's dynamic range in a constrained specific volume to meet off-road vehicles requirement. Using a combination of GA and SQP algorithms, the global optimum solution was accurately evaluated. The optimally designed MRFD with some slight modifications has been fabricated and experimentally tested to evaluate the damper performance under different applied currents and excitation conditions. A steady-state magnetic flux density in the annular MR fluid gap was experimentally measured to validate the FE model developed for solving the magnetic circuit of the MR valve. Results showed very good agreement between simulation and experimental results for both magnetic circuit and damper performance (dynamic range and damping force). Under applied current of 2 A, the simulation and experimental results revealed a large damping force of 6.61 kN and 7.41 kN, respectively, as well as a high dynamic range of 5.06, and 6.7, correspondingly, under piston velocity of 12.5 mm/s. The prototyped MRFD can be effectively employed for vibration control applications, particularly, in off-road tracked vehicles.

CHAPTER 3

DYNAMIC PHYSIC MODELING OF ANNULAR-RADIAL MAGNEORHEOLOGICAL DAMPER

4.1 Introduction

Utilizing semi-active adaptive devices such as magnetorheological (MR) dampers can attenuate undesirable vibration in many application systems. For this, many models have been developed to predict damping force behaviour of MRFDs under varied excitations and applied magnetic fields. Such models can cost-effectively facilitate the early-stage design process and help design optimization, control and prototype developments. These models may be classified into quasi-static and dynamic models. Most of the studies have focused on developing the quasi-static models, which generally have considered Bingham plastic (BP) and Herschel-Buckley (HB) behaviour for MR fluids as [123–125,181–183]. These models are useful in early design, understanding the working principles along with optimization of MRFDs and have the ability to describe their dynamic behaviour. However, the quasi-static models mainly assume the MR flow behaviour in steady-state conditions and mostly neglect the gravity and inertial effects as well as fluid compressibility. These can lead to a considerable error when one would predict the unsteady, particularly rapid transient response of MR fluids/dampers as well as the dynamic hysteresis response of MRFDs [43]. MRFDs typically demonstrate hysteresis behaviour at low velocity region and have non-zero damping forces at instantaneous locations of zero velocity.

Alternatively, to alleviate the shortcomings associated with quasi-static models, several dynamic models have been proposed. These models can be classified into physic-based and phenomenological models. Phenomenological models can also be classified into parametric and non-parametric models. Parametric models include the Bingham model, and mathematical-based models, such as Chebyshev polynomials [137], the Bouc-Wen model and the modified Bouc-Wen model [42,90,131,184,185], which the latter group usually consists of several springs and viscous dashpots, apart from a hysteresis operator. The non-parametric models are included but not limited to the black-box model [139], the query-based model [140], the neural network model [141], the Ridgenet model [142] and self-tuning Lyapunov-based fuzzy [143]. Except for physic-based models, the rest of the models' characteristic parameters are required to be identified via costly experimental data. These experimentally derived dynamic models have been successfully

developed and improved for capturing the MRFD hysteresis phenomena accurately at the cost of expensive experimental characterization. Yang [43], for instance, proposed a dynamic model based on the Bouc-Wen hysteresis model incorporating the excitation current to describe the field-dependent hysteresis phenomenon in a full-scale MRFD. They demonstrated a good agreement between the model-predicted behaviour and the experimental results. Dominguez et al. [186] developed a model based on the modified Bouc–Wen model considering frequency, amplitude and current excitation as input variables to efficiently predict the hysteresis phenomenon of MRFD under varying mechanical and magnetic field excitations. The developed model was able to accurately capture the hysteresis behaviour of the MRFD under varying mechanical and magnetic field excitations. While the dynamic models are able to capture the non-linear hysteresis behaviour of MRFDs, they are experiment-based, thereby lacking physical insight and thus not suitable for analysis and design of MRFDs at the early stage of design. Typically, the dynamic models with experimentally derived parameters are being developed to characterize the behaviour of the tested MRFDs under specific excitation conditions and must be re-evaluated if a different combination of excitation parameters is desired. Therefore, these data-derived models may not be efficient in predicting the MRFDs' nonlinear behaviour due to the considerable influence of the rheological properties of MR fluids, particularly under higher loading rates [85,187–189]. It is noted that the non-linear behaviour of MRFDs can be in part attributed to the mechanical properties of the MR fluid, such as fluid compressibility [189–191], magnetic saturation [192], viscoelastic effect [191], unsteady fluid behaviour (fluid inertia effect, slow and rapid transient flow)), [193], heat generation, dry friction between damper components and wet friction between MR fluid and damper components [63,189,191,194]. Among the above-mentioned factors, the unsteady flow of MR fluids, which is due to the unsteady laminar boundary layer flow in a narrow-long gap of MRFDs [195], has been investigated to a far lesser extent. Thus, it is essential to develop models (particularly physic-based) to predict such nonlinear behaviour of MR fluids, especially in large-scale MRFDs under a wide range of loading conditions.

There are, albeit, a few studies that have developed a physic-based dynamic model to predict the unsteady behaviour of electrorheological (ER) fluids and MR fluids, especially within the gap channels of ER/MRFDs. For instance, Chen et al.[196] took advantage of Laplace transform to derive the velocity profile and subsequently model the pressure gradient of unsteady ER fluid passing unidirectionally between parallel plates. This method was further expanded in another

study by Yu et al. [29] for the ER dampers. They developed a dynamic model considering the unsteady behaviour of the ER fluids with experimental identification of the parameters. Using the variable separation method and considering the Bingham Plastic (BP) behaviour for the ER fluids, they analyzed the unsteady ER fluid flow on the ER damper's hysteresis behaviour, especially at high excitation frequencies. A small-scale MRFD was modeled to predict the unsteady fluid behaviour under sinusoidal excitation using Navier–Stokes equation [30]. Employing the average inertia method, Mao et al. [197] presented an unsteady flow model, based on the Bingham plastic behaviour of MR fluids. Despite the fact that the above-mentioned studies were able to consider the unsteady behaviour of MR fluids but they could not capture the hysteresis behaviour of MRFDs at low velocity regions. Du et al. [144] recently developed a dynamic model based on the BP behaviour of MR fluids for estimating the unsteady and hysteretic behaviour of an MRFD. However, in their analysis, the effect of loading displacement, and compressibility were not considered. More importantly, the parameters of the developed model for predicting the hysteresis phenomenon require experimental data.

It is worth mentioning that the MR fluid compressibility can considerably contribute to the hysteresis behaviour in MRFDs, apart from the friction force of the damper [144,189,190,198]. The compressibility effect can be attributed to the existence of air/gas volumes in MRFDs that result in reducing the bulk modulus of the fluid. The lower value of the fluid bulk modulus results in a wider hysteretic area. Çeşmeci and Engin [198] predicted the performance of an MRFD under low displacement-rate conditions using a quasi-static BP model. In their model development for predicting the hysteresis behaviour of the MRFD, an algebraic modification was applied to the model using several experimentally-derived parameters. Apart from BP fluid behaviour, other quasi-static models such as Herschel-Bulkley fluids model have also been developed to represent the hysteresis behaviour of MRFDs [124,190,199]. These model developments mostly represent the compressibility effect as a function of the fluid's compressibility index rather than the fluid bulk modulus. However, the utilization of the fluid bulk modulus in representing the compressibility effect permits the employment of different bulk moduli in compression and rebound chambers. Having considered varied bulk moduli in compression and rebound cycles has yielded a more accurate estimation of MR fluid compressibility effect on MRFD behaviour. However, the contribution of the MR fluid compressibility on the hysteresis behaviour of MRFDs has been mostly neglected [63,189].

All in all, despite the recent advancements in modeling the unsteady and hysteretic characteristics of MRFDs under quasi-static conditions, much work is needed to look at the role of such nonlinear behaviour of MRFDs under dynamic loading conditions. When it comes to bypass MRFDs, however, modeling these nonlinear features can be nontrivial in many cases, especially when the geometry valves become complicated such as that for bypass MRFDs with annular-radial MR valves. These MRFDs have shown superior performances (high damping force and dynamic force range) compared with annular or radial MRFDs only [200–203]. Thus, developing dynamic models for predicting these types of dampers' behaviour including unsteady and hysteretic characteristics, is required for the accurate analysis and design of advanced MRFDs.

In this chapter, a physic-based dynamic model was developed to predict the non-linear dynamic response of a large capacity bypass MRFD with an annular-radial MR valve. The proposed model considers the unsteady fluid behaviour as well as the fluid compressibility effect on the hysteresis response with no experimentally-driven parameters. For this, the dynamic pressure drop was firstly derived from the fluid momentum equation based on BP fluid behaviour in a rectangular channel. The Laplace transform technique combined with the Cauchy residue theorem was effectively used to analytically solve the governing equation of motion for the velocity profile and pressure drop of the unsteady MR fluid. Utilizing the derived dynamic pressure drop, the non-linear hysteresis behaviour of the annular-radial bypass valve due to unsteady fluid behaviour was captured. The dynamic model was subsequently modified by considering the MR fluid compressibility effect on the hysteretic response due to the variation of the fluid's bulk moduli. The continuity equation was utilized to evaluate the actual volume flow rate through the determination of the pressure inside the chambers of the MRFD. The results based on the developed theoretical dynamic model were afterward compared with those obtained from the quasi-static formulation and experimental results to reveal the important effect of the unsteady fluid flow and the compressibility on the MRFD dynamic behaviour.

4.2 Configuration of the annular-radial MRFD

A bypass MR damper with an annular-radial MR valve is designed and prototyped. Figure 4-1(a) shows its schematic. As shown in Figure 4-1, an internal spring was employed instead of an accumulator gas chamber, typically used in conventional MR dampers. This spring-based volume compensator has been integrated inside the damper in such a way that its upper side is

attached to the piston rod and from the lower side is connected to a floating piston, thereby providing a compact design. The spring's role is basically to compensate for the change of volume due to the movement of the piston rod within the cylinder. The external bypass MR valve comprises an outer shell and a bobbin integrated with an electromagnet coil. The valve is designed with both the annular and radial fluid gaps for generating high damping force in a given specific volume. The main geometrical parameters of the designed MR valve are shown in Figure 4-1(b). The commercial MRF-132 DG from Lord Corporation is used to fill the MRFD. The damper geometrical and material parameters together with the MR fluid 132 DG properties (identified in Chapter 2) are repeated in Table 4-1 for sake of clarity.

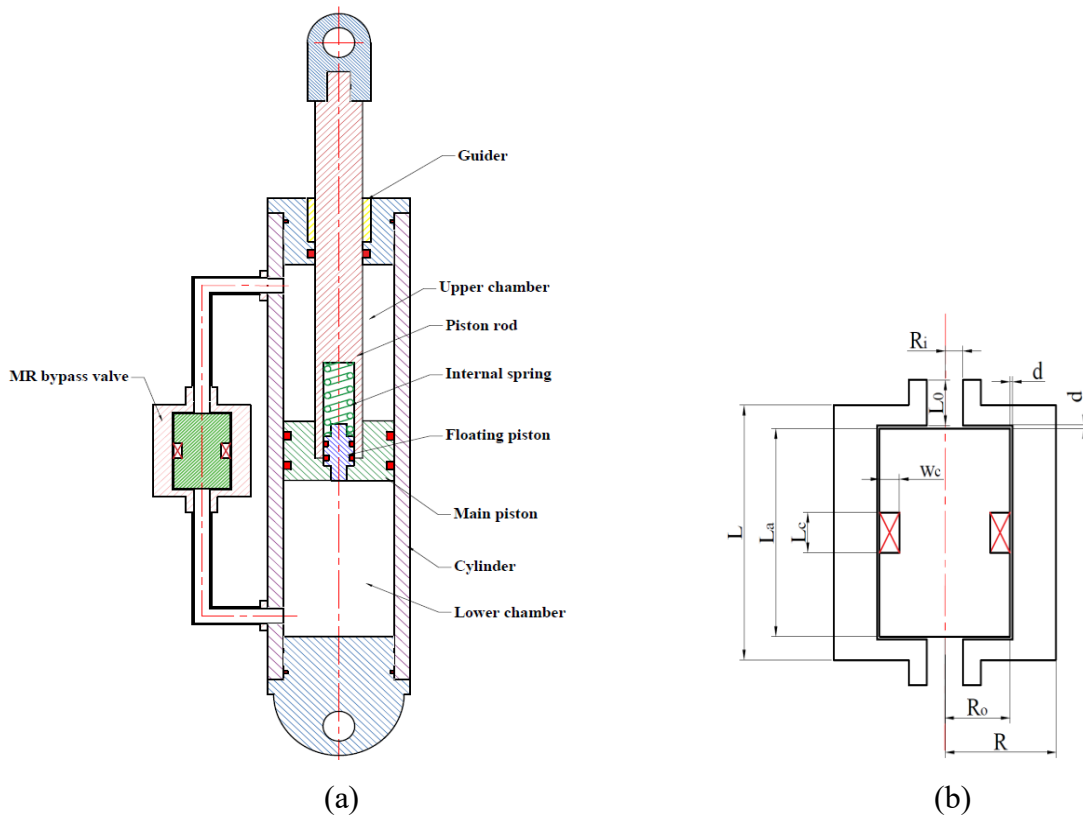


Figure 4-1. (a) Annular-radial MRFD, (b) MR bypass valve geometrical parameters.

Table 4-1. Annular-radial MRFD parameters and MR fluid properties.

Parameter	Symbol	Value	Unit
Duct gap	d	1.2	mm
Coil width	w_c	7	mm
Piston radius	R_p	35	mm
Piston rod radius	R_r	15	mm
Floating Piston radius	R_f	9.525	mm
Radial duct outer radius	R_o	19.05	mm
Radial duct inner radius	R_i	5	mm
MR valve whole radius	R	32.25	mm
Annular duct length	L_a	48.5	mm
Coil length	L_c	10.7	mm
MR valve height	L	60	mm
MR fluid density	ρ	3050	kg/m ³
MR fluid viscosity	η	0.112	pa.s
Copper wire (AWG24) diameter	d_w	0.511	Mm

4.3 Quasi-static model of MRFD with bypass annular-radial gaps considering friction effect

Prior to formulating the proposed dynamic model, this section presents the derivation of a quasi-static model for predicting the force response of the designed bypass MRFD. As shown in Figures 3-1(a) and (b), the clearances between the outer shell and bobbin create an annular and two radial gaps. In the absence of an external magnetic field, the damping force is only generated by the viscous fluid resistance in the annular-radial MRV. However, in the presence of the applied magnetic field, additional damping force will be generated due to the MR fluid yield stress. This generated damping force can be continuously varied by controlling the applied current to the electromagnet coil. The direction of the magnetic flux in the active radial and annular regions is perpendicular to the MR fluid flow motion. As discussed in Chapter 2, by assuming quasi-static BP rheological fluid behaviour and neglecting the unsteady fluid behaviour and compressibility of the MR fluid, the generated force by the MRFD consists of the contribution of the viscous force and yield stress. These forces can be related to the pressure drop within the valve as well as the spring force due to the internal spring embedded with the piston rod according to the configuration of the designed MR valve. The detailed derivation of generated static damping force (F_d) is described in section 3.3 in Chapter 2. It is noted in section 3.3, the effect of friction forces was neglected. Considering the effect of static and dynamic friction, the quasi-static damping force can be modified as:

$$\begin{aligned}
F_d &= F_{sg} + \Delta P(A_p - A_r) + F_f \text{sgn}(\dot{x}_p) \\
&= F_{sg} + (\Delta P_\eta + \Delta P_\tau)(A_p - A_r) + F_f \text{sgn}(\dot{x}_p)
\end{aligned} \tag{4-1}$$

in which F_f is the friction force due to the sealing O-rings embedded between the piston and cylinder as well as friction between MR fluids and cylinder internal surfaces.

In a similar approach described in section 2.3, the quasi-static damping force considering friction effect can be written as:

$$F_d = F_{sg} + C_{vis}\dot{x}_p + F_\tau \text{sgn}(\dot{x}_p) + F_f \text{sgn}(\dot{x}_p) \tag{4-2}$$

It is noted that total friction force friction force, F_f , can be represented as the summation of static and dynamic components as:

$$F_f = F_s + F_\beta \tag{4-3}$$

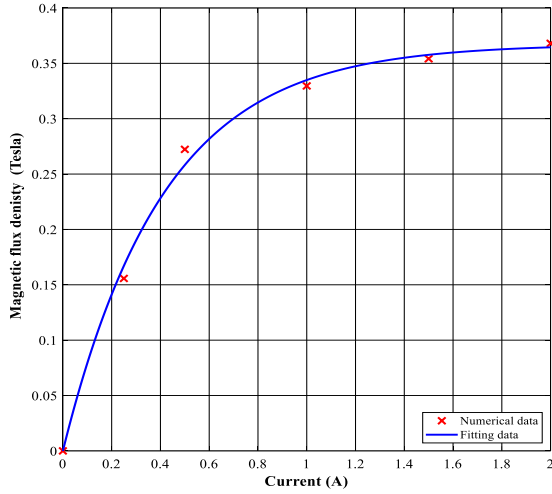
where, F_s and F_β are the static friction of the MRFD and the dynamic friction due to the friction between the MR fluid and MRV surfaces, respectively. The static friction can be estimated by the following relation as reported in [204]:

$$F_s = 32 \left(\frac{\omega}{2\pi} \right)^{-0.17} \tag{4-4}$$

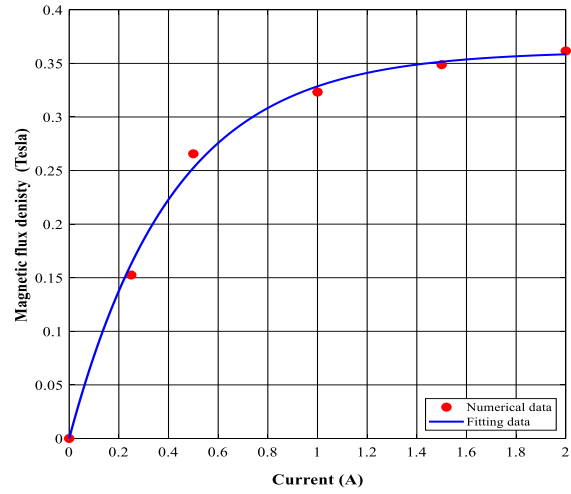
while the dynamic friction can be determined as [205].

$$F_\beta = \pi\beta R_d \left[L_a \frac{B_a^2}{\mu_f} + (R_o - R_i) \frac{B_r^2}{\mu_f} \right] \tag{4-5}$$

where β is the dynamic friction coefficient which is assumed to be 0.075, as reported in [205] and μ_f is the magnetic permeability of MR fluid. In above equation, B_a and B_r are estimated using magnetostatic finite element model (section 3.3.2) and using Eq. (3-38) under varied currents for the modified optimally designed MRFD. Results for variation of B_a and B_r with respect to current, I , are shown in Figures 3-2(a) and (b), respectively.



(a)



(b)

Figure 4-2. Variation of the magnetic flux density with respect to current in (a) annular gap and (b) radial gap.

Considering Figure 4-2, the following equations represent the relation between the magnetic flux density and applied current for the annular and radial gaps as:

$$B_a = 0.367(1 - e^{-2.427I}) \quad (4-6)$$

$$B_r = 0.361(1 - e^{-2.402I}) \quad (4-7)$$

It is worth mentioning that the above exponential functions can accurately described the magnetic saturation phenomenon observed at high magnetic field.

4.4 Dynamic Modelling of bypass MRFD

In the following sections, first mathematical model considering unsteady fluid behaviour due to MR fluid inertia is developed. The model is subsequently refined by considering the MR fluid compressibility.

4.4.1 Mathematical modeling of unsteady fluid behaviour

The quasi-static model of the MRFD assumes steady behaviour of the MR fluid flow annular and radial gaps. This assumption is valid only for small stroke dampers that operate at low frequencies and no longer suitable for large stroke dampers under high frequency excitations. Quasi-static models may represent the force-displacement behaviour of MRFDs with reasonable accuracy however they can't describe the force-velocity hysteresis behaviours of MRFDs. In this section the dynamic modelling of the proposed MR fluid bypass valve with annular-radial fluid

gaps is carried out by considering the unsteady unidirectional fluid flow through parallel rectangular plate. Parallel rectangular passage is a resorbable as the mean diameter of annular duct is much large than the gap (more than an order of magnitude). For revealing the influence of the unsteady fluid behaviour on the MRFD behaviour, the fluid is assumed to be incompressible and operating to in the laminar regime. Gravity and the pressure drop into damper's upper and lower chambers are also neglected. The MR fluid is restricted between two parallel plates of length L and width w , as shown in Figure 4-3. Considering differential fluid element shown in Figure 4-3(b), the governing dynamic momentum equation of flow motion can be written as:

$$-m\ddot{x} + Pw dy + \left(\tau_{yx} + \frac{\partial \tau_{yx}}{\partial y} dy \right) w dx - \left(P + \frac{\partial P}{\partial x} dx \right) w dy - \tau_{yx} w dx = 0 \quad (4-8)$$

where the element mass can be expressed as

$$m = \rho w dx dy \quad (4-9)$$

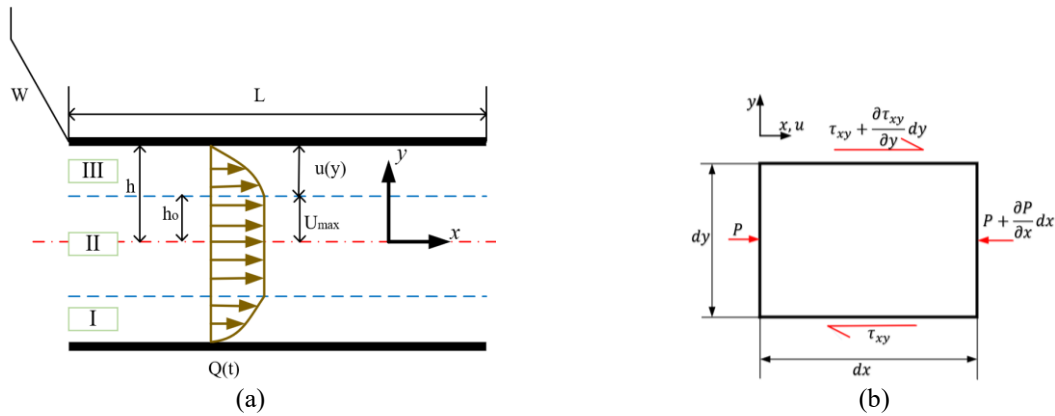


Figure 4-3. (a) MR fluid in rectangular flow duct schematic and (b) differential fluid element.

By substituting Eq. (4-9) into Eq. (4-8), the momentum equation of the flow can be represented as:

$$-\rho \frac{\partial u}{\partial t} + \frac{\partial \tau_{yx}}{\partial y} = \frac{\partial P}{\partial x} \quad (4-10)$$

where u is the flow velocity and τ_{yx} is the shear stress in $x - y$ plane. Assuming the BP behaviour for the MR fluid, the fluid shear stress can be described as:

$$\tau_{yx} = \tau_o + \eta \frac{\partial u}{\partial y} \quad (4-11)$$

where τ_o is the yield shear stress. Substituting Eq. (4-11) into Eq. (4-10) yields:

$$\rho \frac{\partial u}{\partial t} = -\frac{\partial P}{\partial x} + \eta \frac{\partial^2 u}{\partial y^2} \quad (4-12)$$

As it can be observed from Figure 4-3(a), the fluid velocity profile, between two parallel plates, can be separated into three regions: the viscous regions (Post-yield) (I, III), as well as the plug region (Pre-yield, II). The shear stress is higher in the viscous zones than yield shear stress, consequently, the fluid flows with a velocity varying from non-slip zero velocity to the plug region velocity U_{max} . The plug region has lower shear stress than the yield region, so there is no shear flow and the fluid moves as a rigid body. As a result, the following boundary conditions are held as:

$$u(h, t) = 0 \quad (4-13)$$

$$\frac{\partial u(h_o, t)}{\partial y} = 0 \quad (4-14)$$

Having known the fluid flow rate, $Q(t)$ and formulating the mass conservation law, yields:

$$\int_0^{h_o} U_{max}(h_o, t) dy + \int_{h_o}^h u(y, t) dy = u_p(t)h = \frac{Q(t)}{2} \quad (4-15)$$

where u_p is the inlet fluid velocity and h_o is the maximum height of the plug region, which can be determined from the plug flow equilibrium equation as [183]:

$$h_o = \frac{\tau_y L}{\Delta P} \quad (4-16)$$

Using Laplace transform, the Eqs. (4-12)- (4-15) can be transferred to Laplace domain as:

$$\frac{\partial^2 u(y, s)}{\partial y^2} - \frac{s}{v} u(y, s) = \frac{1}{\eta} \frac{dP(x, s)}{dx} \quad (4-17)$$

$$u(h, s) = 0 \quad (4-18)$$

$$\frac{du(h_o, s)}{dy} = 0 \quad (4-19)$$

$$\int_0^{h_o} U_{max}(h_o, s) dy + \int_{h_o}^h u(y, s) dy = u_p(s)h = \frac{Q(s)}{2} \quad (4-20)$$

where

$$v = \frac{\eta}{\rho} \quad (4-21)$$

and η and v are the dynamic and kinematic viscosities. The general solution of Eq. (4-17) can be written as:

$$u(y, s) = C_1 e^{\sqrt{\frac{s}{v}}y} + C_2 e^{-\sqrt{\frac{s}{v}}y} + \psi_p \quad (4-22)$$

where C_1 , C_2 , and are integration constants and, ψ_p is the particular solution. Under harmonic excitation, we can write:

$$u_p(t) = A_0 \sin(\omega t) \quad (4-23)$$

where A_0 and ω are amplitude and excitation frequency, respectively. Laplace transform of Eq. (4-23) yields:

$$u_p(s) = \frac{A_0 \omega}{s^2 + \omega^2} \quad (4-24)$$

Applying, the boundary conditions presented in Eqs. (4-18) and (4-19) and the mass conservation law in Eq. (4-20), the general solution for the flow velocity in the gaps can be written using the method of separation of variables as:

$$u(y, s) = \psi_p \left[1 - \frac{\cosh m(h_o - y)}{\cosh m(h - h_o)} \right] \quad (4-25)$$

in which $m = \sqrt{\frac{s}{v}}$. The detailed derivation of Eq. (4-25) is provided in Appendix E. The particular solution can also be represented as:

$$\psi_p = \frac{u_p(s)mh\Delta}{mh\Delta + mh_o + \epsilon} \quad (4-26)$$

where Δ and ϵ can be determined as:

$$\Delta = -\cosh m(h - h_o) \quad (4-27)$$

$$\epsilon = -\sinh m(h_o - h) \quad (4-28)$$

Finally, the flow velocity can be described by substituting Eq. (4-26) into Eq. (4-25) as:

$$u(y, s) = \frac{u_p(s)mh[\cosh m(h_o - y) - \cosh m(h - h_o)]}{mh\Delta + mh_o + \epsilon} \quad (4-29)$$

The pressure gradient due to damper piston excitation can also be calculated by substituting velocity in Eq. (4-25) into momentum equation, Eq. (4-17), as:

$$-\psi_p m^2 s = \frac{1}{\eta} \frac{dP(x, s)}{dx} \quad (4-30)$$

$$\frac{dP(x, s)}{dx} = -\rho s \psi_p \quad (4-31)$$

$$\frac{dP(x, s)}{dx} = -\rho s \frac{u_p(s)mh\Delta}{mh\Delta + mh_o + \epsilon} \quad (4-32)$$

By taking the Laplace inverse for the flow velocity profile in Eq. (4-29) using complex variable theory [206] and applying residue theorem (Appendix E), the flow velocity profile in the time domain can be expressed as:

$$u(y, t) = \frac{A_0 i}{2} [\Omega(y, -i\omega)e^{-i\omega t} - \Omega(y, i\omega)e^{i\omega t}] + \sum_{n=1}^{\infty} \frac{2A_0 \omega \alpha_n^2 v h [\cos \alpha_n(h - h_o) - \cos \alpha_n(y - h_o)]}{(\alpha_n^4 v^2 + \omega^2) \xi} e^{-\alpha_n^2 v t} \quad (4-33)$$

It is noted that the volume flow rate through the annular-radial MR valve can be obtained as:

$$Q(t) = (A_p - A_r)u(y, t) \quad (4-34)$$

Also, in a similar manner, the pressure gradient in Eq.(4-32) for duct with length L can be obtained as:

$$\Delta P(t) = -\frac{\rho L \omega A_0}{2} [\Gamma(-i\omega)e^{-i\omega t} + \Gamma(i\omega)e^{i\omega t}] + 2\rho L A_0 \omega v^2 h \sum_{n=1}^{\infty} \frac{\alpha_n^4}{(\alpha_n^4 v^2 + \omega^2)} \frac{[\cos \alpha_n (h - h_o)]}{\xi} e^{-\alpha_n^2 v t} \quad (4-35)$$

where

$$\xi = h_o [(1 - \cos \alpha_n (h - h_o))] + \alpha_n h (h - h_o) \sin \alpha_n (h - h_o) \quad (4-36)$$

The pressure drop in Eq. (4-35) is a combination of pressure drop due to viscous and field-dependent yield stress as represented in Eq. (4-1). The pressure drop due to yield stress fluid is not generally affected by the fluid unsteady behaviour [29] and can be represented as:

$$\Delta P_\tau = \frac{cL\tau_y}{d} \quad (4-37)$$

The pressure drop due to the viscous contribution (ΔP_η) can be derived by making the distance from the centreline to the point that the fluid begins to yield as shown in Figure 4-3 equals to zero ($h_o = 0$). ΔP_η thus, can be represented as:

$$\Delta P_\eta = -\frac{\rho L \omega A_0}{2} [\Gamma_o(-i\omega)e^{-i\omega t} + \Gamma_o(i\omega)e^{i\omega t}] + 2\rho L A_0 \omega v^2 h \sum_{n=1}^{\infty} \frac{\alpha_n^4}{(\alpha_n^4 v^2 + \omega^2)} \frac{\cos(\alpha_n h) e^{-\alpha_n^2 v t}}{\alpha_n h^2 \sin(\alpha_n h)} \quad (4-38)$$

where

$$\Gamma_o(s) = \frac{mh \cosh(mh)}{mh \cosh(mh) - \sinh(mh)} \quad (4-39)$$

The pressure drop through the designed MR valve shown in Figure 4-1 can be obtained by superposition of the pressure drop through the annular and two radial gaps, which can thus be obtained via Eq. (4-35). The total pressure drop for the designed MR valve can be represented as:

$$\Delta P_{MRV} = 2\Delta P_{orifice} + \Delta P_{annular} + 2\Delta P_{radial} \quad (4-40)$$

where

$$\Delta P_{orifice} = \frac{8\eta L_o Q}{\pi R_i^4} \quad (4-41)$$

$$\begin{aligned} \Delta P_{annular} = & -\frac{\rho(L_a - L_c)\omega A_0}{2} [\Gamma_o(-i\omega)e^{-i\omega t} + \Gamma_o(i\omega)e^{i\omega t}] \\ & + 2\rho(L_a - L_c)A_0\omega v^2 h \sum_{n=1}^{\infty} \frac{\alpha_n^4}{(\alpha_n^4 v^2 + \omega^2)} \frac{\cos(\alpha_n h) e^{-\alpha_n^2 vt}}{\alpha_n h^2 \sin(\alpha_n h)} \\ & + \frac{c(L_a - L_c)\tau_{ya}}{d} \end{aligned} \quad (4-42)$$

$$\begin{aligned} \Delta P_{radial} = & -\frac{\rho(R_o - R_i)\omega A_0}{2} [\Gamma_o(-i\omega)e^{-i\omega t} + \Gamma_o(i\omega)e^{i\omega t}] \\ & + 2\rho(R_o - R_i)A_0\omega v^2 h \sum_{n=1}^{\infty} \frac{\alpha_n^4}{(\alpha_n^4 v^2 + \omega^2)} \frac{\cos(\alpha_n h) e^{-\alpha_n^2 vt}}{\alpha_n h^2 \sin(\alpha_n h)} \\ & + \frac{c(R_o - R_i)\tau_{yr}}{d} \end{aligned} \quad (4-43)$$

where, the field-dependent yield stress $\tau_{ya(r)}$ for the MRF-132DG in the annular and radial gaps can be estimated according to Eq. (3-23).

Thus, the dynamic damping force F_D of the designed bypass MR damper with annular-radial MR valve can be finally represented as:

$$F_D = F_{sg} + \Delta P_{MRV}(A_p - A_r) + F_f \text{sgn}(\dot{x}_p) \quad (4-44)$$

4.4.2 Modified dynamic model: considering the fluid compressibility effect

As discussed in the introduction section, MR fluid compressibility can considerably contribute to the hysteretic response of MR dampers. Therefore, in this section, the developed dynamic model in the previous section (see Eq. (4-44)) is further modified to also predict the MR fluid's compressibility effect on the hysteretic response of the designed MR damper. As the piston moves downward due to the excitation condition, the pressure inside the lower (compression) chamber increases, compressing the internal spring while increasing the air pressure inside the spring chamber. When the pressure exceeds the minimum pressure drop of the MR valve, the MR fluid moves from the lower chamber to the upper (rebound) chamber. When the piston motion is reversed, the MR fluid moves from the upper chamber to the lower chamber, releasing the spring

force and reducing the air pressure. Due to the compressibility effect, this process causes a significant non-linearity in the MRFD behaviour. For considering the compressibility effect, the volume flow rate in Eq. (4-34) should be re-evaluated through the determination of the dynamic pressure inside the upper (rebound) and lower (compression) chambers instantaneously using the continuity equation [207]. The continuity equation in the upper chamber can be represented as:

$$Q - (A_p - A_r)\dot{x}_p - \left[\frac{V_{ui} + (A_p - A_r)x_p}{B_u} \right] \frac{dP_u}{dt} = 0 \quad (4-45)$$

in which V_{ui} and B_u are the initial volume and bulk modulus of MR fluid in the upper chamber, respectively. It is noted that the last term, in Eq. (4-45) represents the compressibility effect in the upper chamber. The initial volume in the upper chamber, V_{ui} , can be evaluated as:

$$V_{ui} = (A_p - A_r)L_u \quad (4-46)$$

where L_u is the length of the upper chamber. In a similar manner, the continuity equation in the lower chamber can be described as:

$$A_p\dot{x}_p - Q - A_f\dot{x}_f - \left[\frac{V_{li} + A_p x_p + A_f x_f}{B_l} \right] \frac{dP_l}{dt} = 0 \quad (4-47)$$

in which V_{li} and B_l are the initial volume and bulk modulus of MR fluid in the lower chamber. The last term in Eq. (4-47) also represents the compressibility effect in the lower chamber. The initial volume in the lower chamber, V_{li} , can also be written as:

$$V_{li} = A_p L_l \quad (4-48)$$

in which L_l is the length of the lower chamber. The piston motion contributes to the dissolution of air bubbles in the MR fluid [208]. The variation of bulk moduli for the air-fluid mixture of the upper and lower chambers can be calculated as [190]:

$$B_u = \left(\frac{1}{B_f} + \frac{\varphi_u}{B_{air}} \right)^{-1} \quad (4-49)$$

$$B_l = \left(\frac{1}{B_f} + \frac{\varphi_l}{B_{air}} \right)^{-1} \quad (4-50)$$

B_f and B_{air} are the reference bulk moduli of the MR fluid and air, respectively. φ_u and φ_l are the air volume fractions in upper (rebound) and lower (compression) chambers, respectively. Moreover, the variation of the bulk modulus in the compression chamber is also due to the variation of the pressure inside the spring chamber. Thus, this pressure should be added to the calculated pressure inside the compression chamber. The variation of the gas pressure in the spring chamber can be obtained via assuming adiabatic process, as:

$$P_g = P_{air} \left(\frac{V_{si}}{V_{si} + A_f x_f} \right)^\gamma \quad (4-51)$$

in which γ is adiabatic gas index which is about 1.4 for the air, P_{air} is the reference atmospheric pressure, and V_{si} is the initial volume of the spring chamber which can be obtained as:

$$V_{si} = A_f L_f \quad (4-52)$$

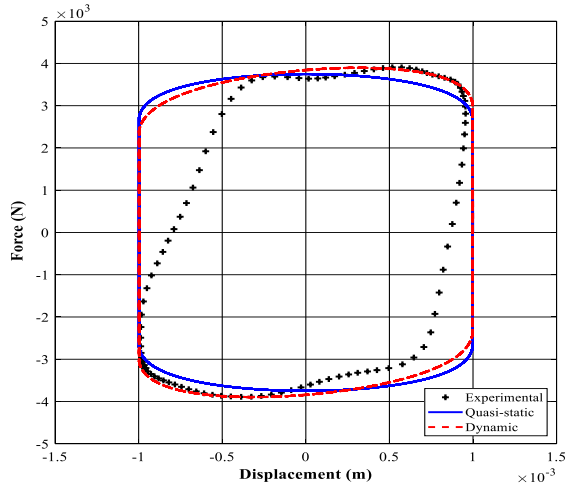
in which A_f and L_f are the cross-sectional area and length of the cylindrical spring chamber, respectively. Air content in the compression chamber is typically higher than rebound chamber air content due to the presence of air in the spring chamber. However, improper sealing caused by piston rod motion may result in aeration in the rebound chamber. It is also possible that dissolved air bubbles in the MR fluid is responsible for the air in both chambers. Thus, the bulk modulus in the rebound chamber is generally much higher than that in the compression chamber. It is assumed that the air volume fraction in rebound is 0.0001%, while the air volume fraction in the compression chamber is assumed to be 0.01%. The required data to consider the compressibility effect are listed in Table 4-2. It is noted that Eqs. (4-45) and (4-47) are solved with the volume flow rate based on the unsteady fluid behaviour described by Eq. (4-35) to determine the pressure inside each chamber. Thus, the pressure drop between the upper and lower chamber can be evaluated with considering the unsteady MR fluid behaviour and compressibility effect.

Table 4-2. Main parameters of the model.

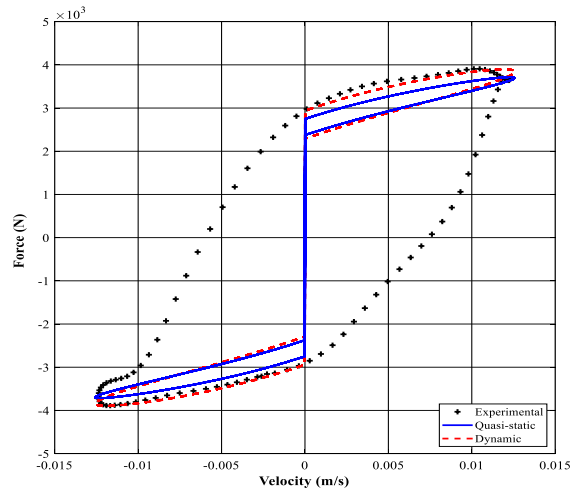
Parameter	Symbol	Value	units
Reference bulk modulus of MR fluid	B_f	1.05	Gpa
Reference bulk modulus of air	B_{air}	0.142	Gpa
Length of the upper chamber	L_u	0.02	m
Length of the lower chamber	L_l	0.16	m
Length of the air chamber	L_f	0.064	m
Atmospheric pressure	P_{air}	1.013	bar
Adiabatic coefficient of air	γ	1.4	

4.5 Validation of the Dynamic modeling

The optimally designed MRFD has been experimentally characterized under harmonic excitation to validate the proposed analytical dynamic model. The experimental test setup and procedure were explained in section 2.6.2. The results presented in Figures 3-4 to 3-6 compare the MRFD response predicted by the quasi-static and the proposed analytical dynamic model based on the unsteady fluid behaviour with those obtained experimentally. The force-displacement and force-velocity results are obtained under an excitation frequency of 2 Hz and amplitude of 1mm at applied currents of 0.5 A, 1 A and 2 A. Results reveal relatively a good agreement between the quasi-static model and dynamic model (ignoring effect of fluid compressibility) at low excitation conditions. This is partially due to the fact that at relatively lower levels of frequency and amplitude the effect of the unsteady fluid behaviour is not notable. Both static and dynamic models were able to accurately predict the peak damping force compared with experimental results. It is, however, noted that the hysteresis observed in the experimental force-velocity curve, as shown in Figures 3-4(b), 3-5(b) and 3-6(b) could not be captured by the static model and developed dynamic model in which the effect of fluid compressibility has been ignored. The force-velocity hysteresis characteristics are in part attributed to other factors, such as the viscoelastic effect and fluid compressibility effect. Also, the quasi-static and dynamic models have a dead zone or discontinuous jump in force-velocity response near zero velocity region. This jump is due to the fact that these models utilize BP behaviour which can only describe post-yield region of MRFD [165,209,210].

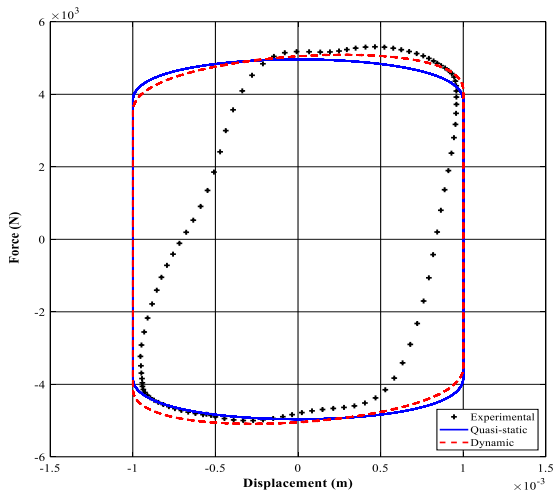


(a)

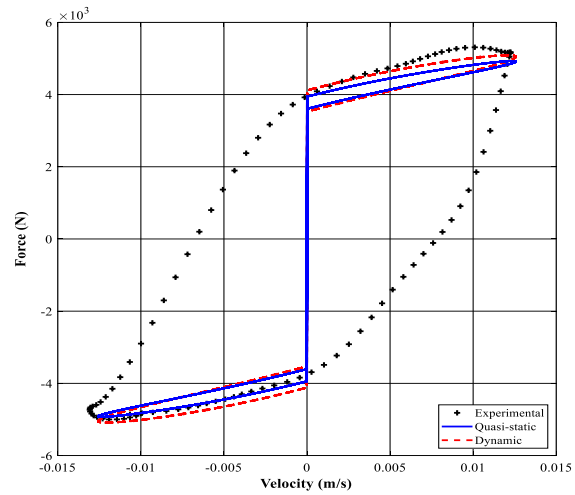


(b)

Figure 4-4. MRFD characteristics under sinusoidal excitation of frequency 2 Hz and displacement of 1 mm at applied current of 0.5 A (a) force-displacement, (b) force-velocity.



(a)



(b)

Figure 4-5. MRFD characteristics under sinusoidal excitation of frequency 2 Hz and displacement of 1 mm at applied current of 1 A (a) force-displacement, (b) force-velocity.

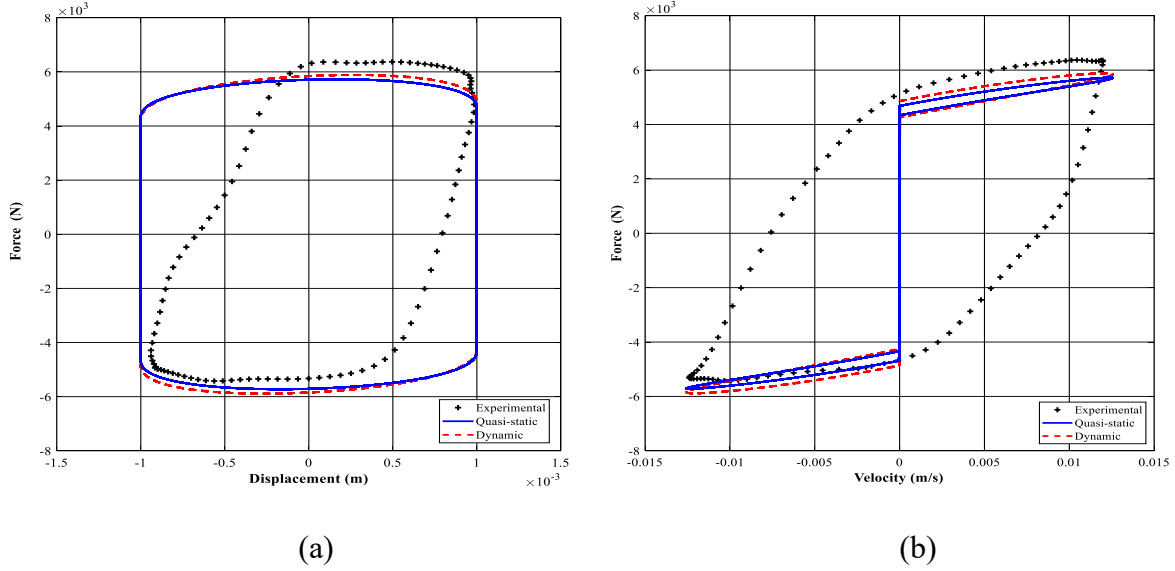


Figure 4-6. MRFD characteristics under sinusoidal excitation of frequency 2 Hz and displacement of 1 mm at applied current of 2 A (a) force-displacement, (b) force -velocity.

To highlight the influence of the unsteady fluid behaviour on the damper hysteresis behaviour, the MRFD response was simulated by the proposed static and dynamic models at a higher loading frequency and displacement. For instance, Figures 3-7 and 3-8 show the predicted force-displacement and force-velocity of the MRFD under an excitation frequency of 20 Hz and amplitudes of 10 mm and 30 mm, respectively. The simulation results are obtained at an applied current of 1 A. These figures reveal that the effect of the unsteady fluid behaviour is remarkable at higher ranges of loading conditions. By increasing the excitation amplitude from 10 mm to 30 mm, a low to a medium deviation between the quasi-static and dynamic results is observed, as shown in Figures 3-7 and 3-8. Thus, for higher amplitudes, the MRFD shows a hysteresis phenomenon due to the effect of the unsteady fluid behaviour, as shown in Figures 3-7(b) and 3-8(b). Figure 4-9 shows the force-displacement and force-velocity characteristics at an excitation displacement of 30 mm but at a higher loading frequency of 40 Hz. Results demonstrate a considerable difference between the quasi-static and the dynamic modelling by increasing frequencies due to the effect of the unsteady fluid behaviour. The hysteresis in the quasi-static modelling in the post-yield region is due to the high stiffness of the spring-based volume compensator and the friction force as presented in Eq. (4-1) and shown in Figures 3-7(b) and 3-8(b) and 3-9(b). Therefore, the quasi-static modelling is not valid at high frequencies and amplitudes conditions. As a result, the dynamic modelling based on the unsteady fluid behaviour

has to be considered in the earlier stage of the design of MRFDs operating at high frequencies and large displacements.

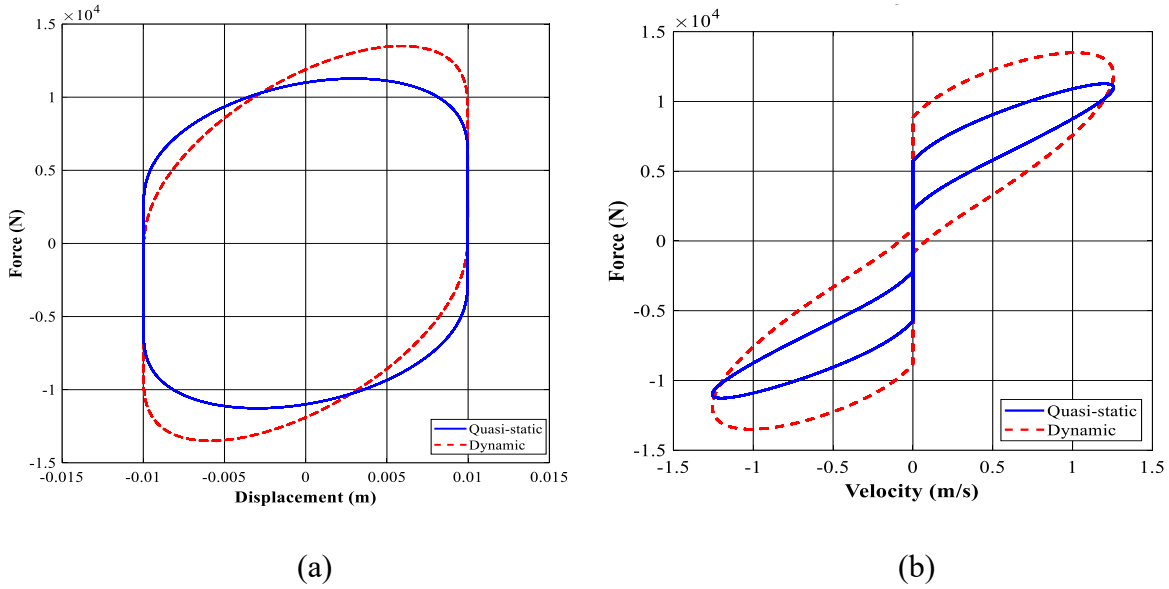


Figure 4-7. MRFD characteristics under sinusoidal excitation of frequency 20 Hz and displacement of 10 mm at applied current of 1 A (a) force-displacement, (b) force-velocity.

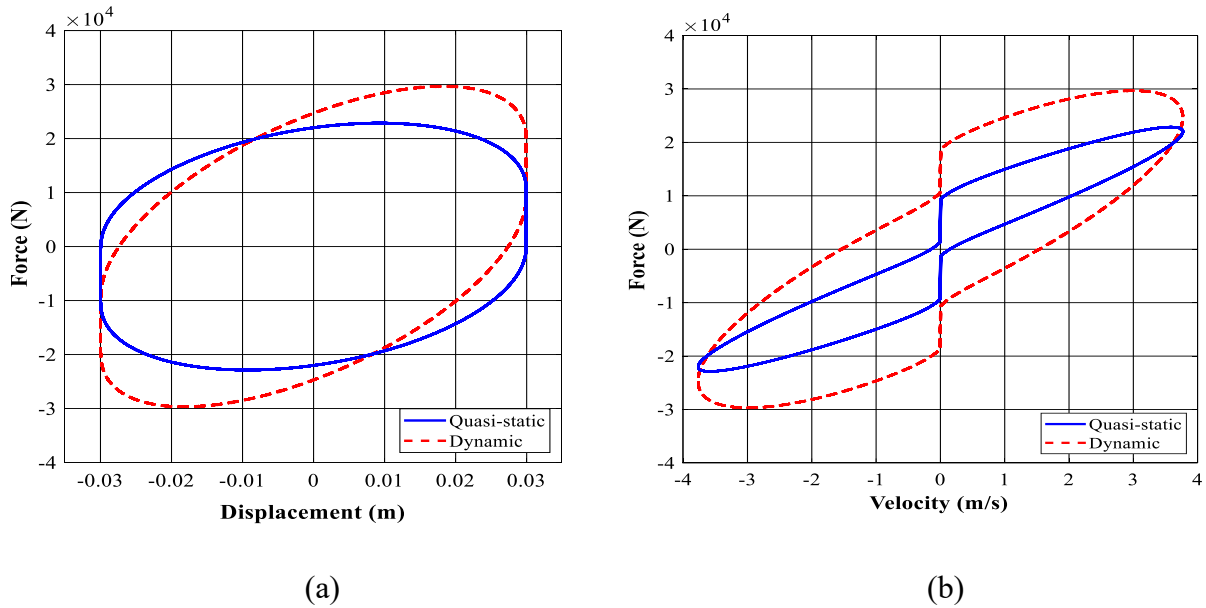


Figure 4-8. MRFD characteristics under sinusoidal excitation of frequency 20 Hz and displacement of 30 mm at applied current of 1 A (a) force-displacement, (b) force -velocity.

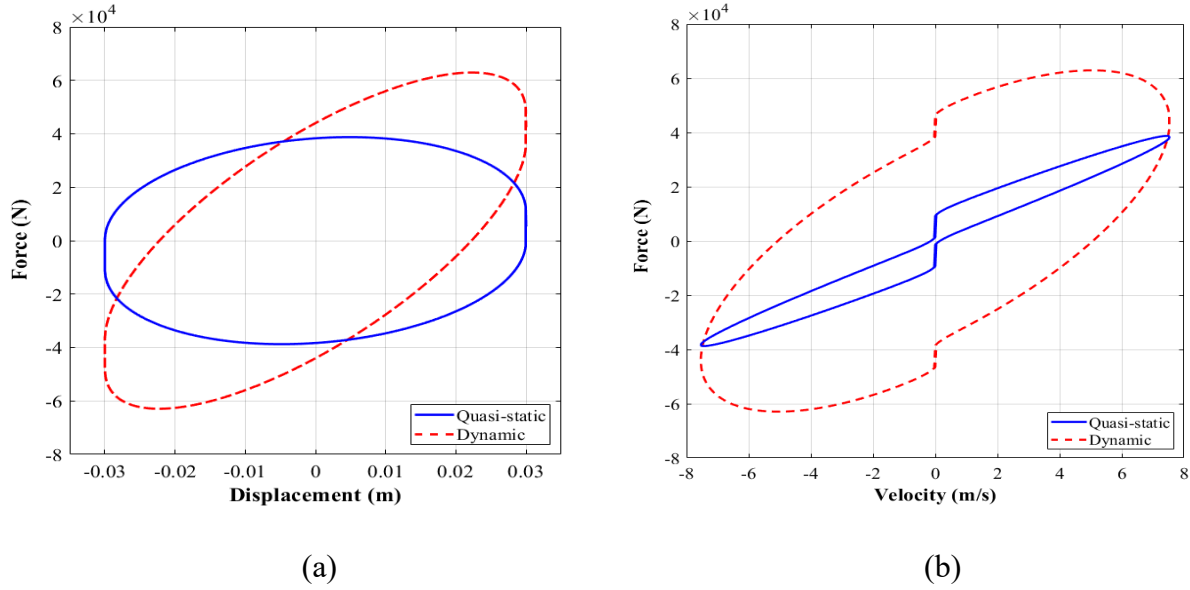
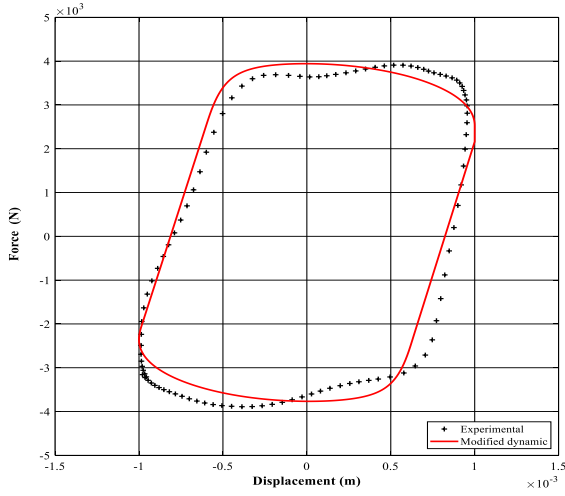
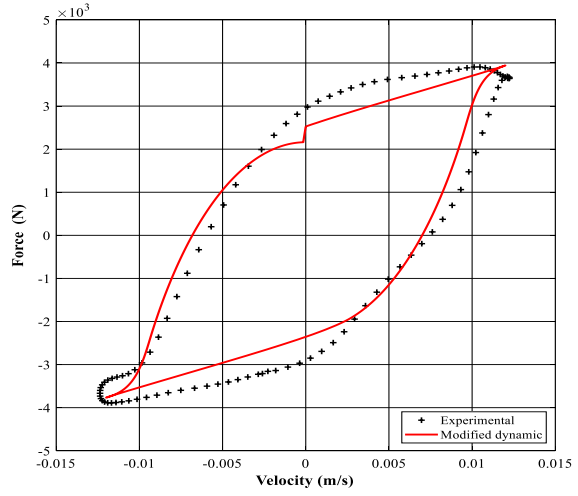


Figure 4-9. MRFD characteristics under sinusoidal excitation of frequency 40 Hz and displacement of 30 mm at applied current of 1 A (a) force-displacement, (b) force -velocity.

For improving the dynamic model in capturing the non-linear hysteresis of the proposed MRFD, the dynamic model was modified to consider the MR fluid compressibility effect as illustrated in section 4.4.2. Force-displacement and force-velocity responses of the designed MRFD tested under the same excitation frequency of 2 Hz and amplitude of 1 mm at applied currents of 0.5 A, 1 A and 2 A are shown in Figures 3-10 to 3-12. Results demonstrate a good agreement between the proposed modified dynamic model and experimental data at different applied magnetic fields. It is worth mentioning that the friction effect, spring force, unsteady fluid behaviour and compressibility effect are considered in the modified dynamic model. Comparing Figures 3-10 to 3-12 with Figures 3-4 to 3-6 reveals that the compressibility effect is the main source of hysteresis at low ranges of frequencies and amplitudes as mentioned also in [198,208]. As mentioned before, unlike the phenomenological models, the proposed physic-based modified dynamic model does not require any characteristic parameters to be identified experimentally [42,90,131,184,185]. In the recent work of Du et al. [144], for instance, the hysteresis part was obtained via a data-driven model from another study using experimental data to identify the model parameters [211].

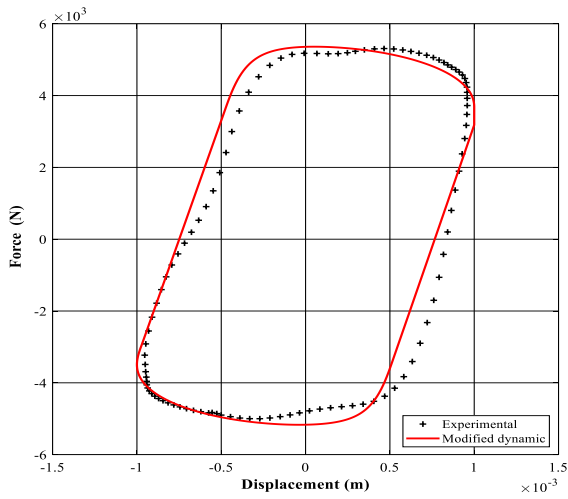


(a)

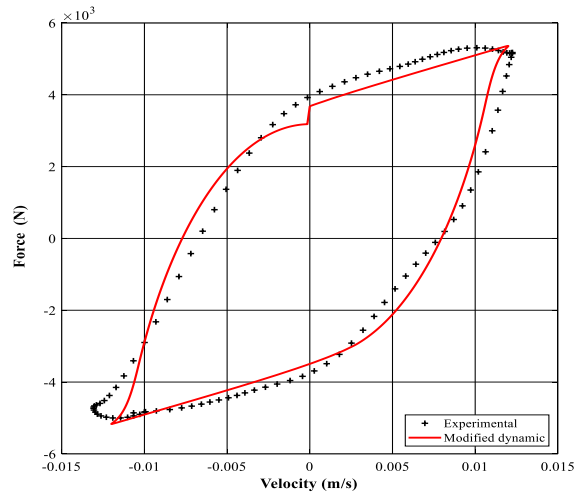


(b)

Figure 4-10. MRFD characteristics under sinusoidal excitation of frequency 2 Hz and displacement of 1 mm at applied current of 0.5 A(a) force-displacement, (b) force-velocity.



(a)



(b)

Figure 4-11. MRFD characteristics under sinusoidal excitation of frequency 2 Hz and displacement of 1 mm at applied current of 1 A(a) force-displacement, (b) force-velocity.

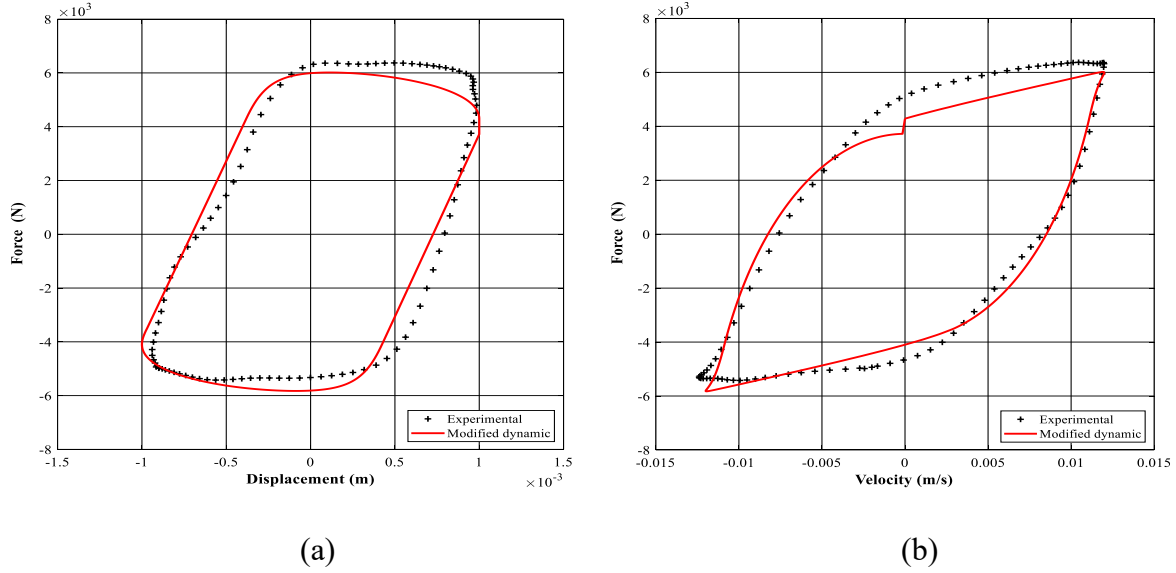


Figure 4-12. MRFD characteristics under sinusoidal excitation of frequency 2 Hz and displacement of 1 mm at applied current of 2 A (a) force-displacement, (b) force-velocity.

4.6 Summary

In this chapter, the response of a bypass MRFD with annular and radial fluid gaps was modelled under quasi-static and dynamic loading conditions based on Bingham Plastic fluid behaviour. The developed dynamic model considered the unsteady fluid behaviour. The Laplace transform technique together with the complex variable theory and Cauchy residue theorem were utilized to derive the fluid pressure drop in rectangular duct due to viscous and yield shear stress. The damping force-displacement and the damping force-velocity of the designed MRFD were subsequently estimated by the proposed models for different amplitudes and frequencies. To validate the developed models, the dynamic response of the designed MRFD was experimentally characterized under sinusoidal excitation. The results showed that the effect of the unsteady fluid behaviour at small amplitudes and low frequencies is negligible. Thus, both the developed quasi-static and dynamic models were able to predict the MRFD behaviour effectively at low frequencies and small amplitude ranges. However, the unsteady fluid effect is becoming significant at large amplitude and high frequencies, and subsequently, a considerable difference between the quasi-static and the unsteady fluid behaviour dynamic model was observed at this range of loading conditions. Also, results showed that the developed models were not able to predict the hysteresis force-velocity characteristic response of the MRFD. The dynamic model was then modified by considering the fluid compressibility, which has a substantial effect on the non-linear hysteresis behaviours of MRFDs, especially at a low range of loading conditions (low-velocity region).

Results were indicative of a good agreement between the modified dynamic model and the experimentally obtained data. The proposed physic-based modified dynamic model based on the unsteady fluid behaviour and compressibility effect can provide an accurate description of the non-linear behaviour of the MRFDs in the early stage of design without experiment identification requirement.

CHAPTER 4

COMPREHENSIVE DYNAMIC CHARACTERIZATION OF A LARGE-CAPACITY ANNULAR-RADIAL MAGNETORHEOLOGICAL DAMPER

5.1 Introduction

To develop MRFDs, many studies have reported the design, modelling and prototyping of MR valves with varied configurations [94,198,203]. The MR valves, as the main part of MRFDs, generally consist of an electromagnetic circuit together with a hydraulic channel [212]. MR valves, which can be designed to be inside or outside of a cylinder-piston system, basically resist the passage of the MR fluids within a narrow channel. The resistance can be effectively enhanced with the application of a magnetic field, thereby increasing the inlet pressure, and thus the damping force of MRFDs. Many efforts have been dedicated toward designing complicated MR valves to enhance the field-controllable dynamic force range of MRFDs while minimizing their response time, power consumption, size, and weight [114,213]. These studies are included but not limited to advancing and optimizing electromagnet units (magnetic cores and coils) [166,214,215], designing MR valves with complex fluid flow paths and geometries [216], and developing innovative arrangements of MR valves and cylinder-piston systems [217,218].

MR valves can be also categorized into annular gaps, radial gaps and multiple annular and radial gaps. Advantages of the annular gap in MR valves include but are not limited to a compact design, faster response time and high efficiency in on/off state. However, it leads to elongation of the MR valves, especially when high damping force is required [124,183,219,220]. On the other hand, radial gap MR valves have the flexibility to generate high damping force with a shorter longitudinal flow channel length. Besides, they are easier to be fabricated. However, radial gap MRFDs are hard to be designed in a compact size [101,221–223]. Multiple annular-radial MR valves have shown great potential for producing higher yield stress, but they have a complex design and manufacturing [100,224–226]. There is a trade-off between the MR valve's damping force and its flow channel capacity for MR fluid passage. Increasing the effective fluid volume channel can guarantee producing higher field-dependent damping force but at the expense of large-size MR valves, and the associated higher power consumption. Hence, the miniaturization of the MR

valve continued to be challenging, especially for applications that require high damping force. Among the above-mentioned factors, the position of MR valve units with respect to MRFDs together with a type of fluid flow channel may substantially affect the dynamic range of MRFDs [48,213]. For instance, it has been shown that the bypass MRFD can yield a superior dynamic force range (ratio of maximum forces generated by the MRFD at the maximum applied current to the one at zero current) compared to traditional cylinder-piston MRFD [227], albeit at expense of relatively lower response time [228] and bulkier configuration [75]. MR bypass dampers, which were firstly developed by Crowell [229], hold great promise for a wide scalability of damping force in different applications [108,230].

Bypass MR valves can be designed to be placed in the exterior part of the cylinder-piston system of dampers, namely the outer bypass MR valve. They generally offer a higher dynamic force range, lower sedimentation rate, easier maintenance and better heat dissipation as compared with inner bypass valves and also traditional bobbin-in-piston MRFDs [110]. Gue et al. [231] developed an MRFD equipped with an outer bypass MR valve for lateral vibration suppression of railway vehicles. The damping force increased from 1 kN to 9 kN, corresponding to a high dynamic range of nine, under a loading frequency of 1 Hz and excitation amplitude of 15 mm. However, the lower off-state dynamic force of the damper is quite high at a relatively lower frequency of 1 Hz. McLaughlin et al. [232] characterized the dynamic behaviour of an MRFD with three different bypasses MR valve configurations (spiral channel, spiral channels with beads and straight channel with beads) under a constant amplitude of 12.7 mm. Results showed that the spiral channels without beads can offer the highest controllable dynamic force range, varying from 4.6 to 3.5, when the frequency increased from 0.25 Hz to 1 Hz. Hitchcock et al. [108] also designed and tested a novel bypass MRFD under varied levels of frequency (0.0625-2 Hz), and amplitude (3.2-12.8 mm). They observed dynamic range of the damper varying from 1.4 to 4 when the loading frequency decreased from 2 Hz to a 0.0625 Hz. To obtain a higher dynamic range and larger stroke, Bai et al. [75] designed and tested a novel inner bypass damper for advancing the seat suspensions of ground vehicles. They showed that the inner bypass MRFDs possess a higher dynamic range than traditional bobbin-in-piston MRFDs in a velocity range of 0-5.2 m/s. Their results were indicative of an exceptional dynamic range of 13 under a constant amplitude of 38.1 mm and frequency of 1 Hz. However, the maximum controllable damping force was limited to only 3.6 kN.

Apart from employing bypass flow, it has been theoretically [100] and experimentally [19] shown that the dynamic range of MRFDs can be substantially enhanced when their MR valves equipped with both annular and radial flow channels. Ai et al. [100], for instance, presented a theoretical model for predicting the pressure drop of MR valves with both annular and radial flow paths. Their simulation results were indicative of the superior performance of MR valves with both radial and annular flow channels compared to MR valves with only annular or radial flow paths. Zhu et al. [20] designed and tested a novel MRFD with both annular and radial channels. Results showed a dynamic controllable range of two. However, the effect of loading displacement and displacement rate on its force-displacement characteristics were not investigated. These characteristics are of paramount importance for developing a reliable model that can predict dynamic characteristics of MRFDs over wide ranges of loading conditions. Bai et al. [225] developed a new MRFD possessing both annular and radial fluid flow resistance gaps and tested the damper under sinusoidal oscillations with a constant amplitude of 10 mm. Results revealed a dynamic range of 2.81 corresponding to a relative increment of 3 kN damping force at 3 Hz but the stroke of the designed damper was limited to about 34mm. The effect of loading frequency and displacement amplitude on both force-displacement and force-velocity characteristics of the presented MRFDs were also not investigated. The development of miniaturized MR valves has been received much more attention in the last decade. Hu et al. [162] designed and experimentally investigated a relatively compact MR valve (outer diameter of 62 mm and overall length of 80 mm) having both radial and annular fluid flow paths, which can be potentially used for the design development of MRFDs. The proposed MR valves can yield an improved pressure drop of 2.65 MPa under 1.2 A.

Recently fewer studies have improved the dynamic range and damping force of MRFDs by taking advantage of both bypass arrangements and enhanced effect of annular-radial MR valves. For instance, Wang et al. [222] proposed a novel bifold inner bypass MRFD where its design of MR valves permits field-dependent pressure drop in both annular and radial fluid flow channels. The dynamic performance of the MRFD was experimentally examined under varied sinusoidal excitations, and they observed a dynamic range of 5.1 under 2 Hz. The effect of loading frequency and displacement amplitude on hysteresis force-displacement characteristics of the damper were not assessed over the entire range of loading condition considered. Idris et al. [105] also designed and prototyped a novel MRFD with an outer concentric bypass valve, where its gaps resistance

path includes both radial and annular channels via a serpentine flux path. Despite the relatively large dynamic range of 3.8, the maximum damping force was limited to 0.75 kN which is quite low for automotive suspension applications.

Table A-1 (Appendix A) further summarizes the reported studies on design development and experimental characterization of different MRFDs under harmonic excitation. Generally, low off-state and high on-state dynamic force and dynamic range besides large stroke are desirable requirements for the development of effective on-and off-road ground vehicle suspensions. However, according to Table A-1, very few studies have considered these requirements simultaneously, unless at a relatively limited range of dynamic loading conditions. For instance, Hu et al. [233] and McLaughlin [232] have designed outer bypass MRFDs with a large dynamic force range of 8 and 8.6, respectively; however, the dynamic performances of their prototyped dampers were limited to only 1 Hz, which is not adequate for vehicle suspension applications. In addition, the developed MRFDs for automotive applications have a limited damping force and damper travel that restricted their integration in off-road vehicles. Examination of Table A-1 further reveals that employing either outer/inner bypass MR valves or hybrid annular-radial fluid flow channels can contribute to larger dynamic range, yet few studies have considered these two enhancement techniques simultaneously. Moreover, designing a bypass MRFD with annular-radial fluid flow channels has not been presented yet for high-payload applications, such as off-road vehicle suspensions. This chapter include detailed experimental investigation of the dynamic properties of the proposed optimally designed bypass MR damper featuring annular-radial gap under a relatively wide range of sinusoidal oscillations (displacement and frequency) and electrical currents. The equivalent viscous damping coefficient together with the dynamic range of the proposed MR damper were subsequently calculated from the force-displacement/velocity curves as functions of loading amplitude, frequency, and applied current. Additionally, the MR bypass valve was modified to increase the damper's dynamic range and damping force. The efficiency of the proposed MR damper was consequently confirmed by comparing its dynamic range with that of the conventional MR dampers reported in the literature.

5.2 Development of the MRFD prototype

The proposed MRFD has been initially fabricated, as shown in Figure 5-1 based on the optimally designed parameters with modifications as mentioned in Table 3-11. A low carbon steel

AISI 1006 that has high magnetic permeability was used in the design of the MR valve. The MRF-132DG purchased from Lord Corporation was used in the MR damper. This MR fluid has the specific gravity of 3, a viscosity of 0.112 Pa.s. at 40 °C. The MR valve contains a miniaturized electromagnet with 340 turns of conductor wire with American Wire Gauge of 24. The electromagnetic unit is capable of operating up to 3 A over a relatively limited working time whereas under 1 A, it can continuously operate. The MR valve is connected to the MRFD via a high-pressure rubber-based hydraulic hose, as shown in Figure 5-1.



Figure 5-1. MRFD prototyped.

5.3 Experimental characterization

An extensive experimental investigation was carried out to evaluate the dynamic hysteresis performance of the prototyped outer bypass MRFD over a relatively wide range of mechanical and magnetic loadings. The experiments are included but not limited to the identification of the force-displacement and force-velocity characteristics together with friction feature of the prototyped MRFD in both static and dynamic regimes. In the following the test-setup design and experimental measurements are discussed.

5.3.1 Test setup

Figure 5-2 shows a test rig, designed to realize the aforesaid experimental characterization of the designed MRFD. A material testing system (MTS) machine was utilized to provide a series of sinusoidal loadings. The pictorial view of the MRFD is illustrated in Figure 5-2(a) and the full test setup for implementing the dynamic analysis is presented in Figure 5-2(b). Two grippers (upper and lower) were used to connect the MRFD to the MTS machine. The rod of the MRFD was

attached to the upper gripper to a loadcell with force capacity of 9 kN (A-Tech Instrument Ltd, Canada). From the lower side, the MRFD was connected to an electrodynamic hydraulic actuator via the lower gripper. The displacement of the actuator can be controlled using a digitally supervised servo-controller (MTS Model 407 Controller) capable of providing both DC and AC transducer conditioning. The displacement was measured employing an electromechanical transducer. The recorded force and displacement were transferred to a workstation through a data acquisition board (BNC 2110, National Instruments Corp.), as shown in Figure 5-2(b). The LABVIEW software was utilized to analyze, filter, and export the force-displacement and force-velocity data. The electrical current, ranging from 0.25 A to 2 A, was provided to the MR valve' coil using a power supplier.

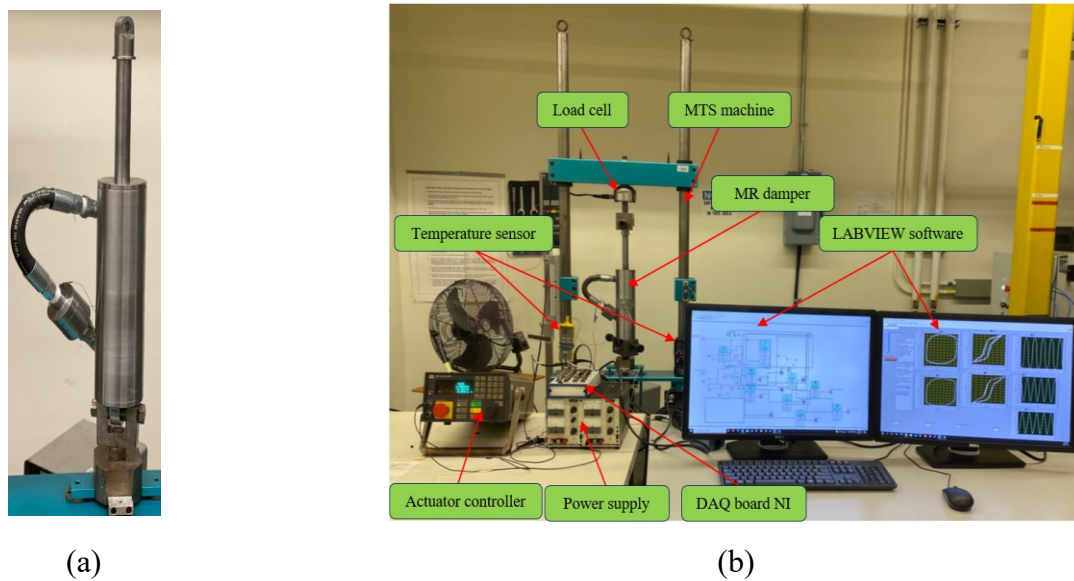


Figure 5-2. Experimental characterization test setup: (a) the prototyped MRFD filled with MR fluid, and (b) the full test rig for implementing the dynamic analysis of the MRFD.

5.3.2 Experimental measurements

The experimental measurements were performed for measuring force-time, force-displacement and force-velocity of the MRFD at different frequencies and amplitudes of the piston motion as well as different excitation currents supplied to the MR valves. The experiment involved factorial combinations of five levels of excitation frequency ($f= 0.5, 1, 2, 3, \text{ and } 4 \text{ Hz}$), five displacement amplitudes ($X= 1, 2.5, 5 \text{ and } 7 \text{ mm}$) and six levels of the applied currents ($I= 0, 0.25, 0.5, 1, 1.5 \text{ and } 2 \text{ A}$). For each testing condition mentioned above, force-time, force-displacement and force-velocity were measured for five consecutive cycles once the data become steady-state,

and subsequently, averaged for characterization of the MRFD performance. Before testing the magneto-mechanical testing of the MRFD, a series of harmonic tests were applied to identify the friction force of the MRFD with and without MR fluid.

5.3.3 Friction test

The friction force between a damper's moving contact surfaces, as shown in Figure 5-3(a) via red encircled paths, affects the damper's behaviour. The friction force become especially considerable at the start of a movement between rod and cylinder. Friction within the damper increases the damping force throughout the entire excitation spectrum, which tends to improve vibration dissipation. Generally, the friction force is measured for a fully assembled damper filling with oil at a very low velocity to remove the effect of viscous damping force from the measurement. However, this method doesn't guarantee to describe the damper friction behaviour, especially at relatively large amplitudes. It is noted that the purpose of the friction test is to characterize the friction properties by measuring the output friction force without considering the influence of the viscous damping. Thus, in this study, to evaluate the damper friction force, a series of experiments was performed by measuring force-time, force-displacement and force-velocity at different loading conditions before filling the damper with MR fluid. These experiments involve sinusoidal excitation of the damper under different frequencies and displacement amplitudes as listed in Table 5-1.

Table 5-1. The test matrix of the friction experiments.

Excitation frequency	Displacement amplitude		
1 Hz	3 mm	5 mm	10 mm
2 Hz	3 mm	5 mm	10 mm
5 Hz	3 mm	5 mm	10 mm

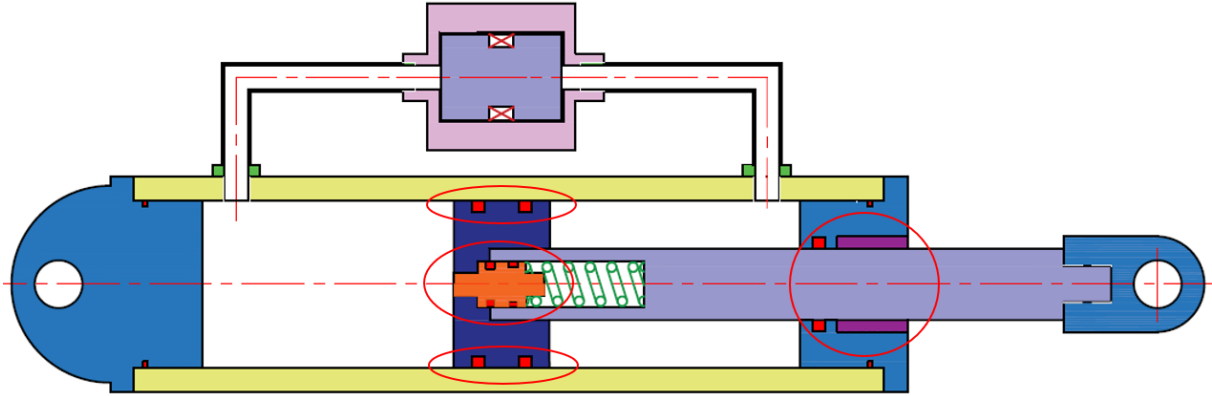
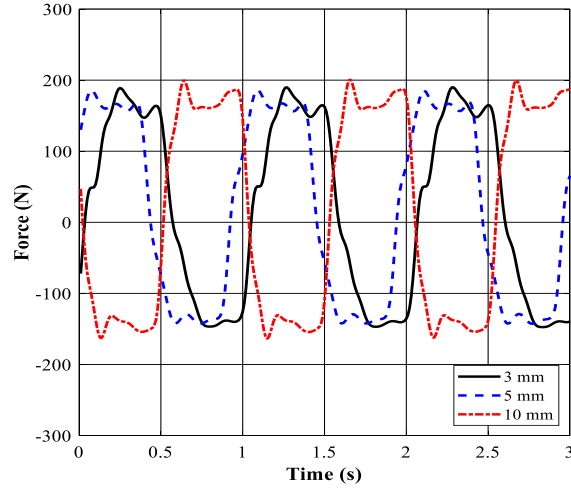


Figure 5-3. Friction surfaces in the proposed MRFD.

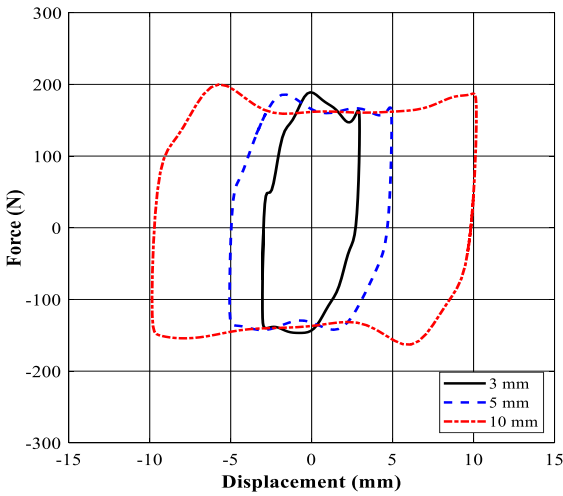
5.4 Experimental analysis

5.4.1 Friction analysis

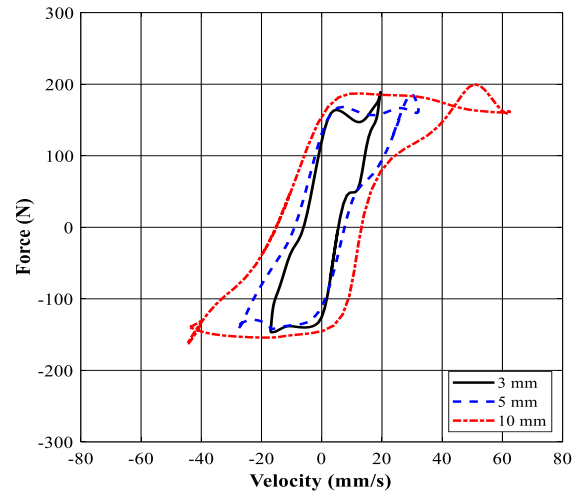
This section provides the friction characteristics of the prototyped MRFD for two cases: (a) when the damper is empty, and (b) when the damper is filled with the MR fluid. Figure 5-4, for instance, shows the measured friction force in the absence of MR fluid in the damper in terms of the force-time behaviour together with the force-displacement and the force-velocity hysteresis characteristics under sinusoidal loading frequency of 1 Hz and varied displacement amplitudes of (3, 5 and 10 mm). Figure 5-4(a) implies that the friction force of the MRFD is quite nonlinear due to the contribution of higher harmonics, showing a peak force of about 200 N. Relatively slightly higher peak force is observed at higher amplitude, as shown in Figure 5-4. Besides, higher amplitude yielded a greater enclosed area by the force-displacement, thereby suggesting more energy dissipation properties as shown in Figure 5-4(b). As expected, Figure 5-4(b) also shows nearly abrupt changes in the force at peak displacements which is indicative of the existence of Coulomb-type friction force. This behaviour was also consistently observed at other loading frequencies. The crossover regions, shown in Figure 5-4(c), are in part due to time-dependent viscoelastic properties associated with the rubber-like O-ring seal, thereby leading to the occurrence of the peak force before the velocity reaches its maximum value. The time-dependent viscoelastic behaviour of the O-ring seal, thus, yielded the friction force that lagged behind the displacement at higher velocities. This sub-hysteresis/secondary loop has also been observed in other studies focusing on the characterization of MRFDs [234,235]



(a)



(b)



(c)

Figure 5-4. The measured friction force of the MRFD under loading frequency of 1 Hz in the absence of the MR fluid: (a) force-time, (b) force-displacement and (c) force-velocity.

Figures 4-5 and 4-6 also show the measured friction force of the MRFD in terms of the force-displacement and force-velocity characteristics under two different peak-to-peak displacement amplitudes of 3 mm and 5 mm, respectively and loading frequency of 1, 2 and 5 Hz. According to Figures 4-5(a) and 4-6(a), the friction force of the MRFD is relatively frequency independent particularly at higher loading amplitude. In other words, the friction force is more dominant by displacement amplitude and show a slight frequency dependence property at lower amplitude. Figures 4-5(b) and 4-6(b) also illustrate that the crossover regions which are more dominant by the loading amplitude rather than loading frequency.

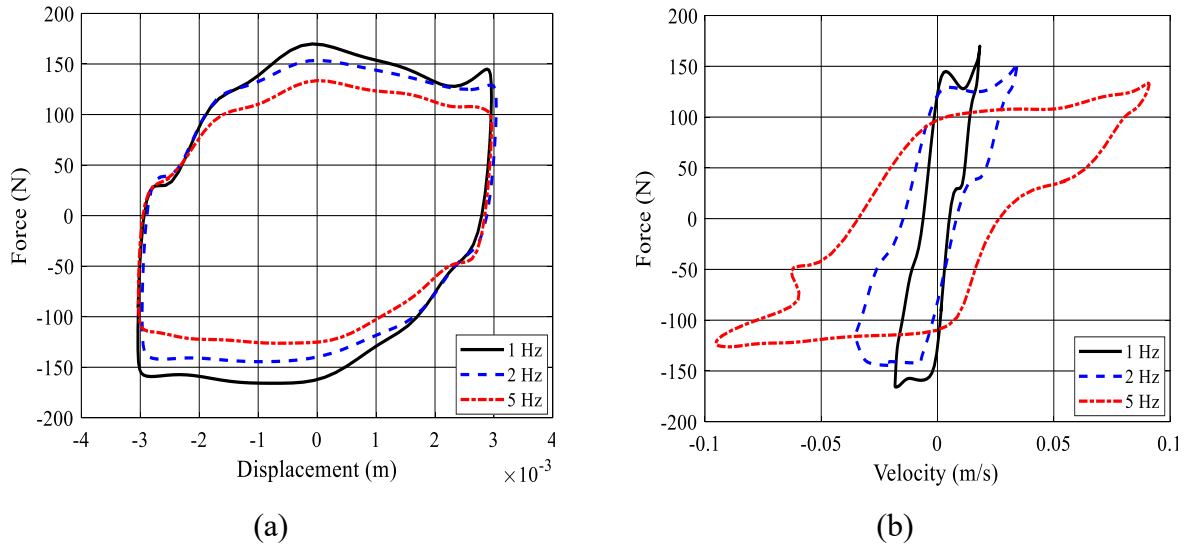


Figure 5-5. The measured friction force of the MRFD under displacement amplitude of 3 mm in the absence of the MR fluid: (a) force-displacement and (b) force-velocity.

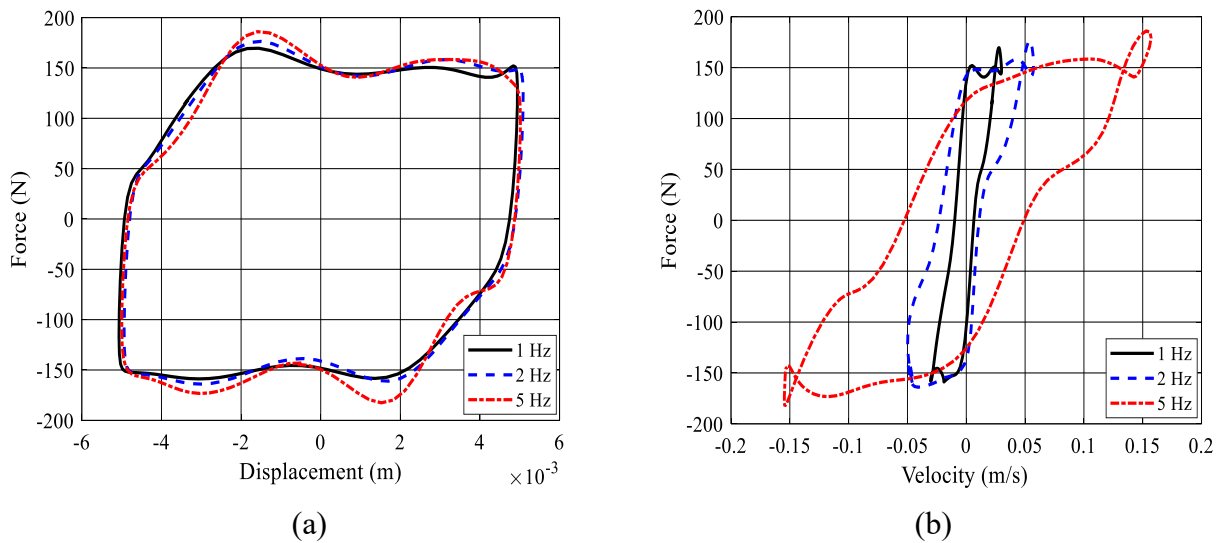


Figure 5-6. The measured friction force of the MRFD under displacement amplitude of 5 mm in the absence of the MR fluid: (a) force-displacement and (b) force-velocity.

The friction force of the MRFD filled with the MR fluid is presented in Figure 5-7. The friction force is measured at a very low loading frequency of 0.09 Hz under varied amplitude of 3, 5, and 10 mm. Again, the influence of Coulomb friction type force can be observed in sudden vertical changes in damping force at peak displacements. The substantial increase in damping force (nearly 550 N) is mainly due to existence of viscous effect of MR fluid, even at very low frequencies.

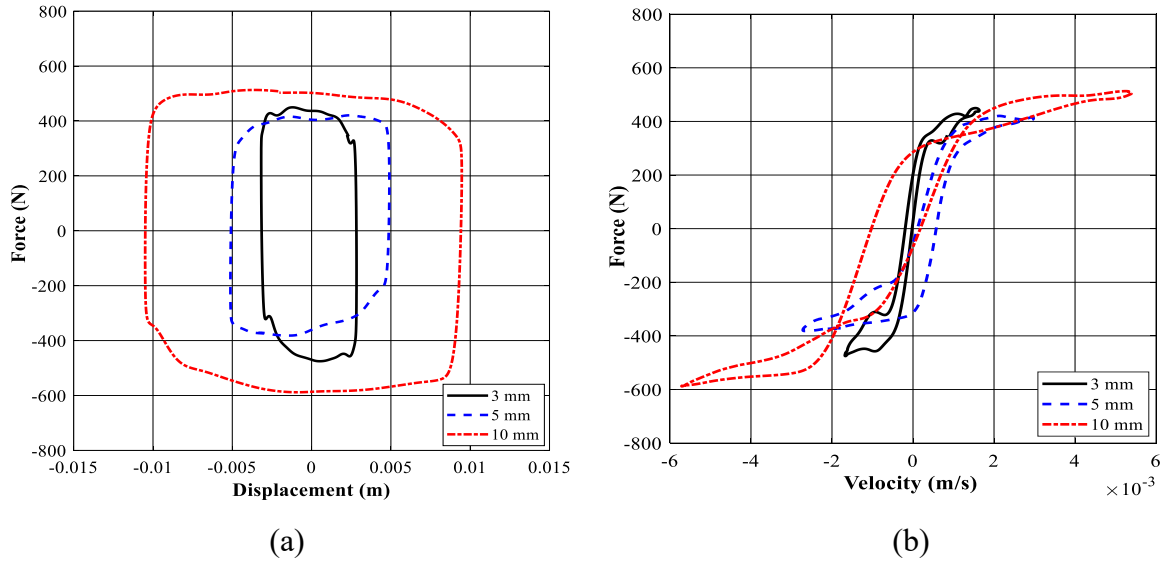
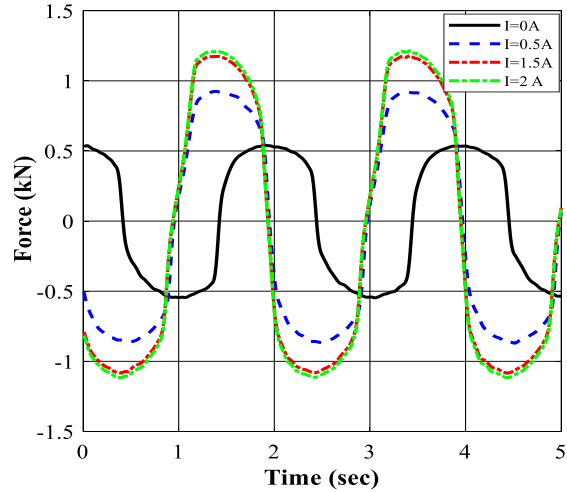


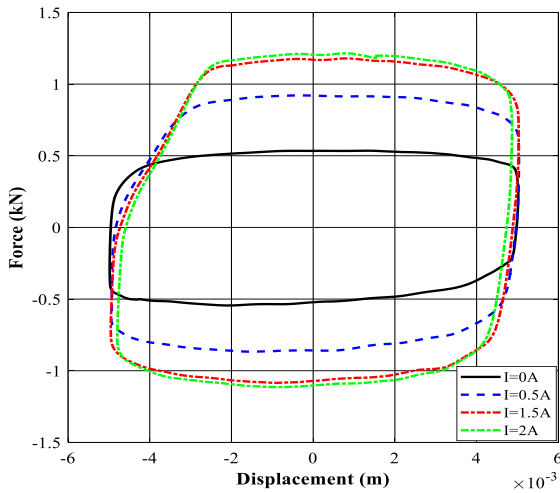
Figure 5-7. The measured friction force of the MRFD under excitation frequency of 0.09 Hz and displacement of 3, 5 and 10 mm in the presence of the MR fluid: (a) force-displacement and (b) force-velocity.

5.4.2 Nonlinear hysteresis dynamic analysis of the MRFD

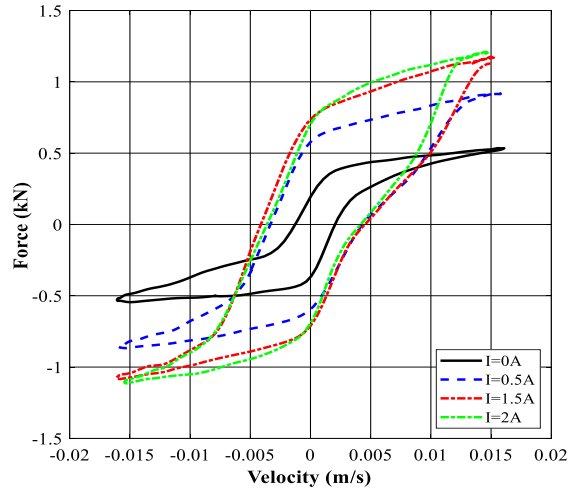
In this section, the dynamic characteristics of the prototyped MRFD under a wide range of mechanical and magnetic loadings are presented and discussed. Figure 5-8 shows the force-time response as well as the force-displacement and the force-velocity features of the MRFD at loading frequency of 0.5 Hz, displacement amplitude of 5 mm and different electrical currents of 0, 0.5, 1.5 and 2 A. Results show typical hysteresis characteristics which become more enhanced with increasing the current. Similar behaviour was also observed at other loading conditions. The area enclosed by the force-displacement loops represents the amount of energy dissipation per cyclic loading of the damper, while the slope of the main axis of the force-velocity curves represents the equivalent damping characteristic of the damper. These are important criterion for evaluating the dynamic performance of MRFDs. Results show that the peak force increased from about 510 N in the absence of the current to nearly 1173 N under current 1.5 A, showing a dynamic range of 2.3. As shown in Figures 4-8(b) and (c), the difference between peak forces decreases as the applied current increases demonstrating the magnetic saturation of the MR fluid when applied current exceeds 1.5 A.



(a)



(b)



(c)

Figure 5-8. The measured time-response (a), force-displacement (b) and force-velocity (c) characteristics of the MRFD under loading frequency of 0.5 Hz at the displacement amplitude of 5 mm.

Figure 5-9 shows the dynamic response of the MRFD at a loading frequency of 1 Hz under a displacement amplitude of 2.5 mm. The applied current was limited to 1.5 A due to the observed saturation in Figure 5-8. The MRFD shows higher peak force as the loading frequency increases. The peak force at this loading condition increases from nearly 600 N in the absence of the current to about 1320 N under an applied current of 1.5 A, indicating a dynamic range of 2.2. Figure 5-9 also reveals that the dynamic response of the fabricated MR damper has good repeatability over the five cycles. Results consistently show that the area encircled by the force–displacement curve

gradually increases with increasing the applied current. This indicates that the amount of energy dissipated by the damper becomes higher by increasing the applied currents, and the damping force of the MRFD is controllable.

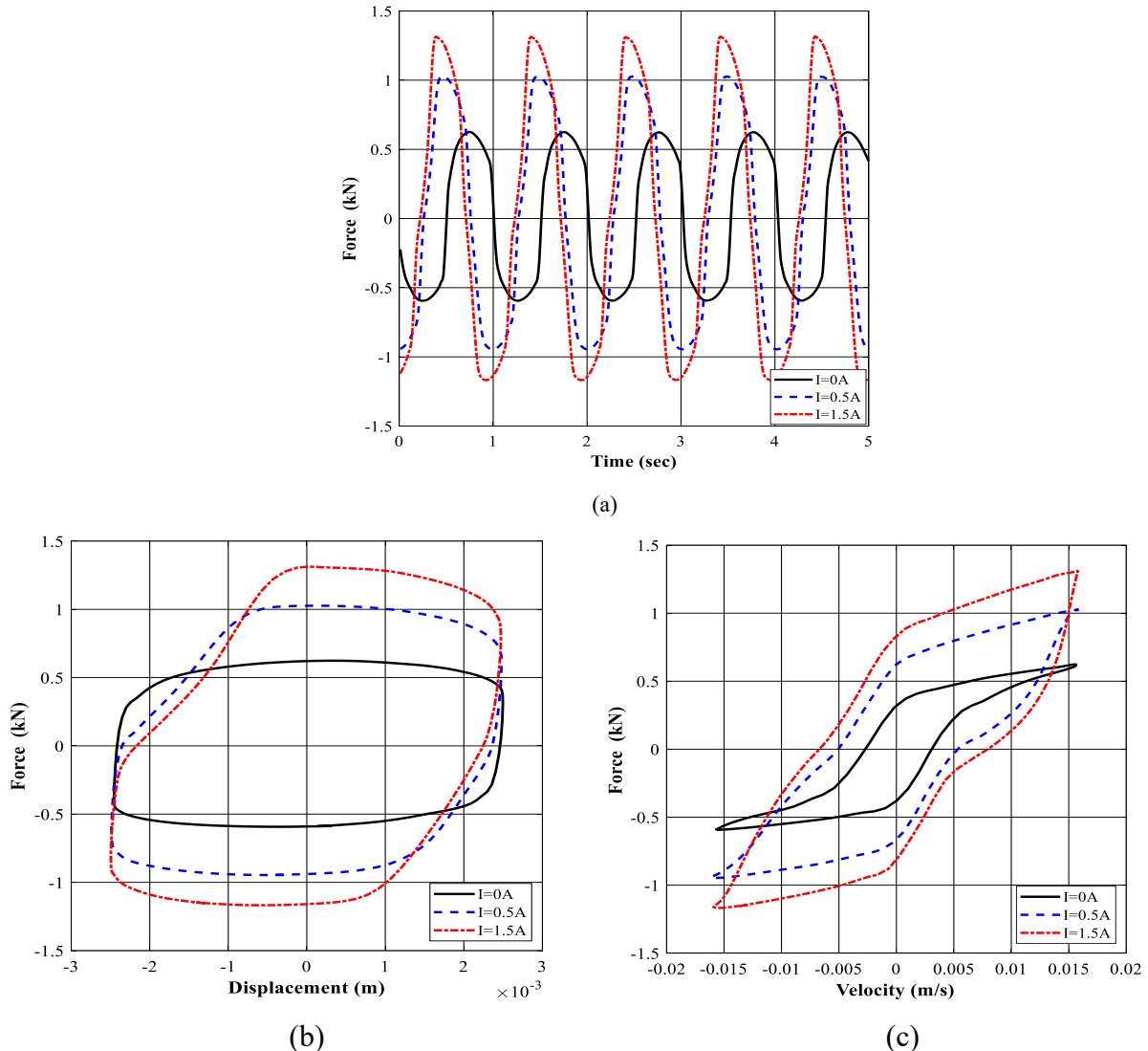


Figure 5-9. The measured time-response (a), force-displacement (b) and force-velocity (c) characteristics of the MRFD under loading frequency of 1 Hz at the displacement amplitude of 2.5 mm.

Figures 4-10 and 4-11 show the effect of loading frequency on the force-displacement and force-velocity characteristics of the MRFD under electrical current of zero and 0.5 A, respectively. The results are presented for the constant displacement amplitude of 2.5mm, as example. Results illustrated in Figure 5-10 reveal that the increasing the loading frequency from 0.5 H to 4 Hz substantially increases the energy dissipation properties together with the damping force of the

MRFD. The peak force of the MRFD also increases with loading frequency, as shown in Figure 5-10(a). Figure 5-10(b) shows that the loading curve of force-velocity curve is relatively independent of the loading frequency. At the same time, the slope of the force-velocity curves, representing the equivalent damping coefficient of the MRFD, tends to decrease with increasing the loading frequency. Moreover, Figures 4-8(b) and 4-9(b) show light variations in the slope of loading/unloading cycles in the corners of the force-displacement curves by increasing the applied currents. This may be in part due to the stiffness variability of the proposed damper. This is because of the presence of the high stiffness spring inside the damper. Rather than using an air accumulator for compensating the added volume of the rod entered into the cylinder, a hollow piston rod with an internal spring was designed to be connected to a floating piston, as shown in Figure 5-3. It should be also noted that, when applied current increases, MR fluids become solid-like materials and show field-dependent stiffness property before shear stress reaches the yield stress during displacement of the piston. This stiffness together with the stiffness of possible air trapped within MRFD may become series with the stiffness of the spring within the piston, thereby showing a field-stiffening effect. This means that when the current increases, the force-displacement characteristics of the damper show a slight stiffening effect.

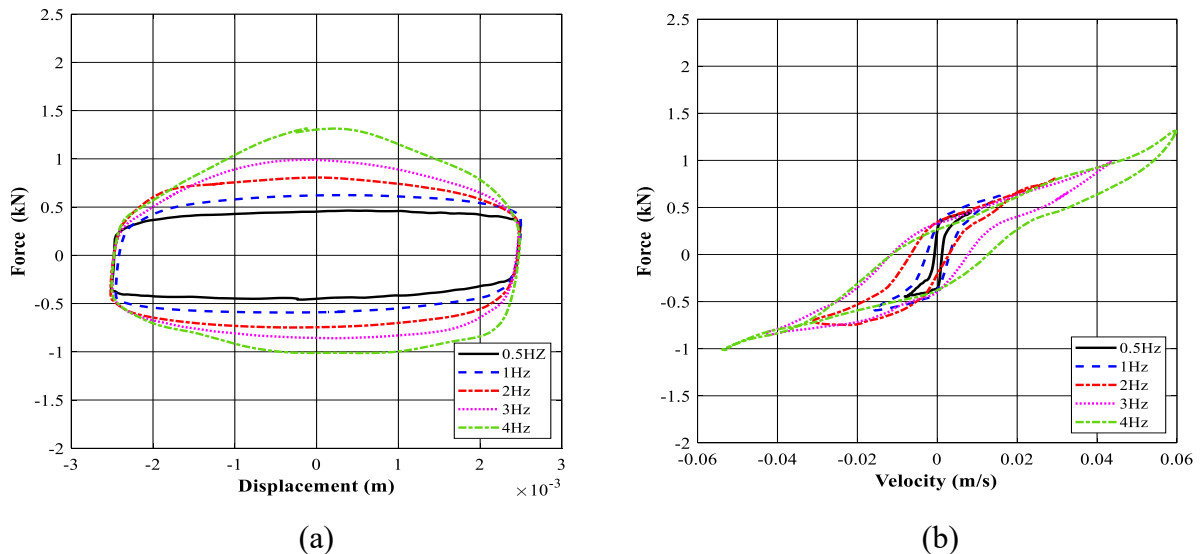


Figure 5-10. The frequency dependent characteristics of the MRFD under zero electrical current and constant displacement amplitude of 2.5 mm: (a) force-displacement and (b) force-velocity.

Figure 5-11 shows the frequency-dependent properties of the MRFD when 0.5 A is provided to the MR valve's coil. As compared with the off-state properties presented in Figure 5-10, the

increasing the loading frequency yielded more nonlinear hysteresis effect on both force-displacement and force-velocity characteristics of the MRFD. For instance, at higher frequencies such as 3 Hz, and 4 Hz, the loading paths of the corresponding hysteresis loops presented in Figure 5-11(b), tend to turn toward up, showing an enhancement in intra-cycle damping coefficient locally. Further analysis of Figures 4-10 and 4-11 also reveals that increasing the current from zero to 0.5 A dramatically enhanced the energy dissipation properties, and damping force of the MRFD. Furthermore, the force-displacement hysteresis characteristics presented in Figure 5-10(a) and Figure 5-11(a) show peaks at different locations rather than when displacement is zero. Correspondingly, the force-velocity curves presented in Figure 5-11(b), reveals secondary loop/sub-hysteresis (cross-over points) near the maximum and minimum velocities particularly at higher frequencies. In other words, the peak force location is occurred before the instance of the maximum velocity. The reasons for shifting the maximum damping force from the instance of the maximum and minimum velocities (or zero displacement) may be in part due to the friction force originating from the mechanical friction between the seals and the shaft/piston, which has also been observed in other studies [234–236]. Moreover, such behaviour may also be partially attributed to the inertia effect of the MR fluid (1000 ml of MR fluid is inside the damper) [237,238], together with possible entrapped air in the damper [239–241].

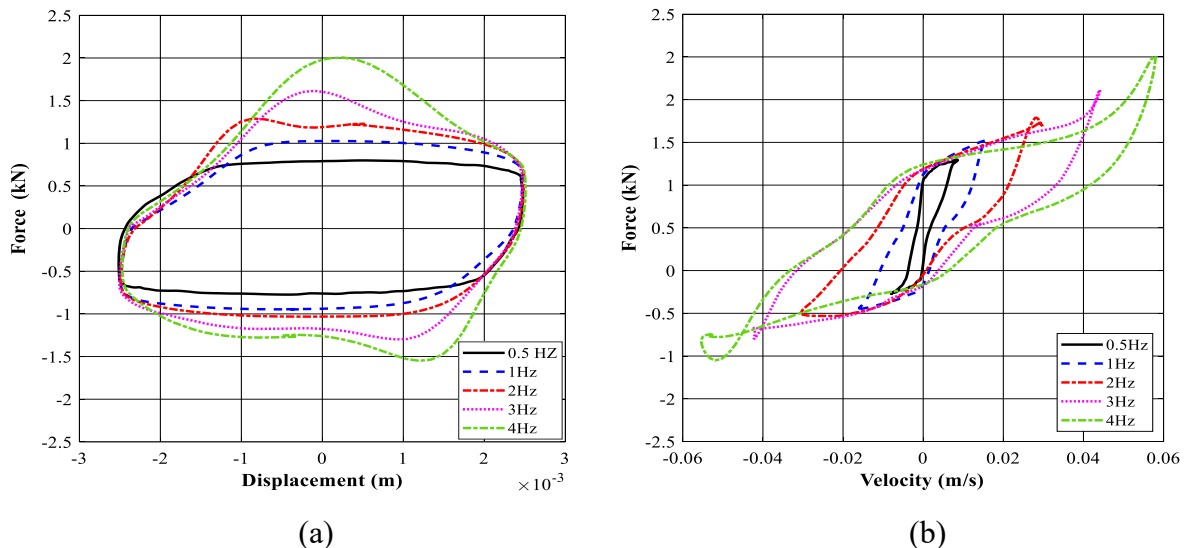


Figure 5-11. The frequency dependent characteristics of the MRFD under 0.5 A electrical current and constant displacement amplitude of 2.5 mm: (a) force-displacement and (b) force-velocity.

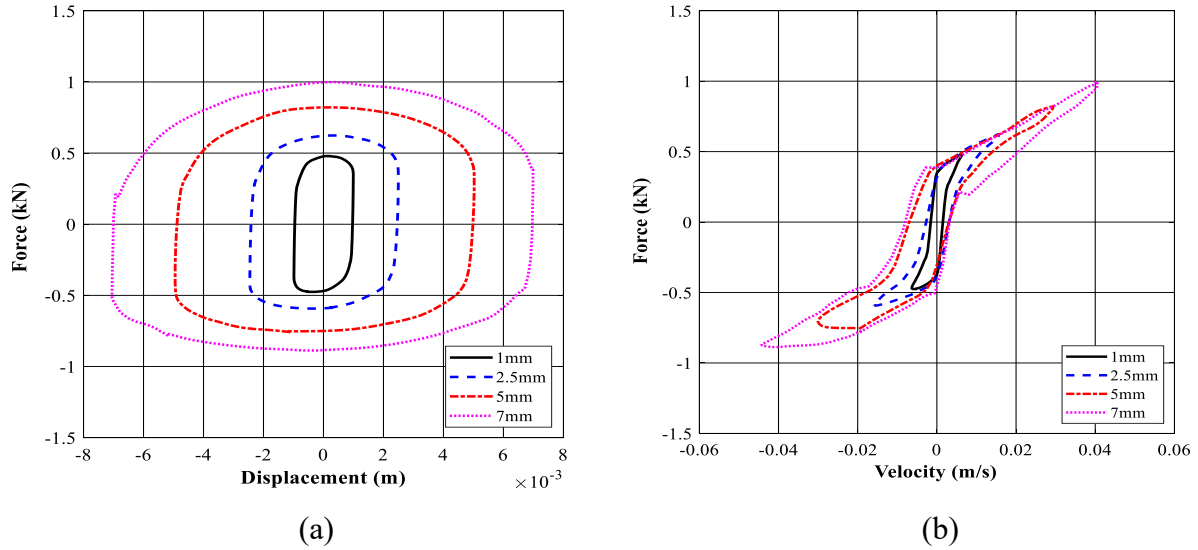


Figure 5-12. The amplitude dependent characteristics of the MRFD under zero electrical current and constant loading frequency of 1 Hz: (a) force-displacement and (b) force-velocity.

Figures 4-12 and 4-13 explain the effect of displacement amplitude on the force-displacement and force-velocity attributes of the MRFD under electrical current of zero and 1.5 A, respectively. The results are given for the constant loading frequency of 1 Hz, as an example. Results in Figure 5-12 show that the increasing the displacement amplitude, ranging from 1 mm to 7 mm, considerably increases the energy dissipation properties together with the damping force of the MRFD. The peak force of the MRFD also increases with loading amplitude, as shown in Figure 5-12(a). Figure 5-12(b) reveals that the loading path of the force-velocity curves are relatively independent of the displacement amplitude. However, the slope of the main axis of the force-velocity loops, representing the equivalent damping coefficient of the MRFD, tends to slightly decrease with increasing the displacement amplitude.

It is worth noting that similar amplitude dependencies were also observed at the same loading frequency under electrical current of 1.5 A, as shown in Figure 5-13. Results presented in Figures 4-10 to 4-13 further emphasize that even at low frequencies (0.5-2 Hz) and small amplitudes, the proposed MRFD can generate a high peak damping force, which is quite essential for applications requiring high damping force, such as high-pay load/off road ground vehicle suspension system. For instance, the damping force at a frequency of 2 Hz and displacement amplitude of 1 mm varies between 520 N to 1200 N when electrical current increased from zero to 1.5 A. Furthermore, the force-velocity curve presented in Figure 5-13(b) also shows a crossover point occurrence near the maximum velocity for higher displacement amplitude of 7 mm.

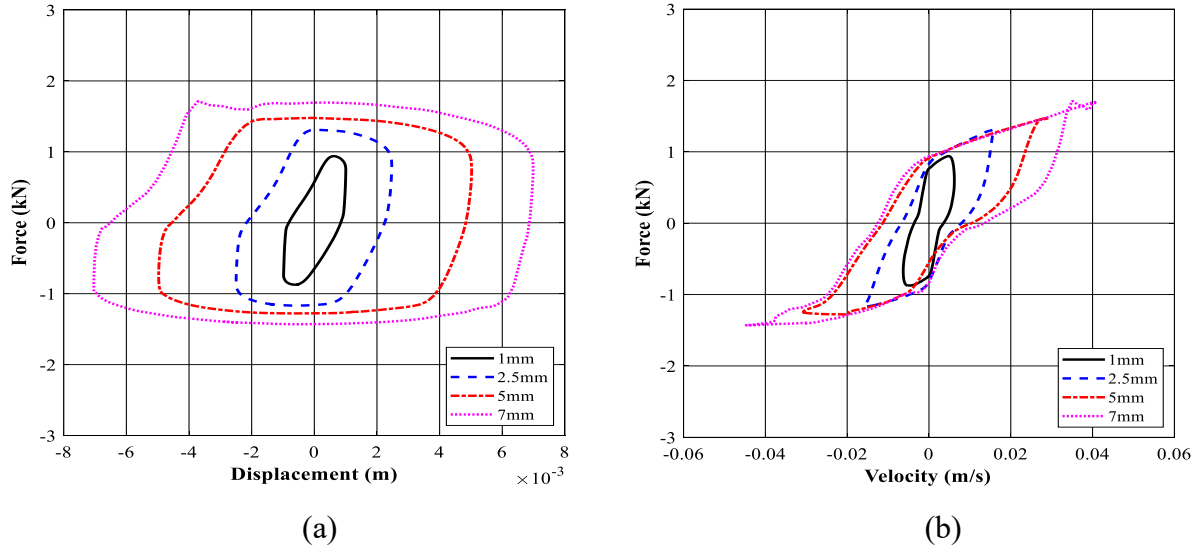


Figure 5-13. The amplitude dependent characteristics of the MRFD under 1.5 A electrical current and constant loading frequency of 1 Hz: (a) force-displacement and (b) force-velocity.

It should be noted that the maximum force generated by the proposed bypass MRFD were measured as 5.54 kN corresponding to the loading frequency and displacement amplitude of 4 Hz and 7 mm, respectively, as shown in Figure 5-14.

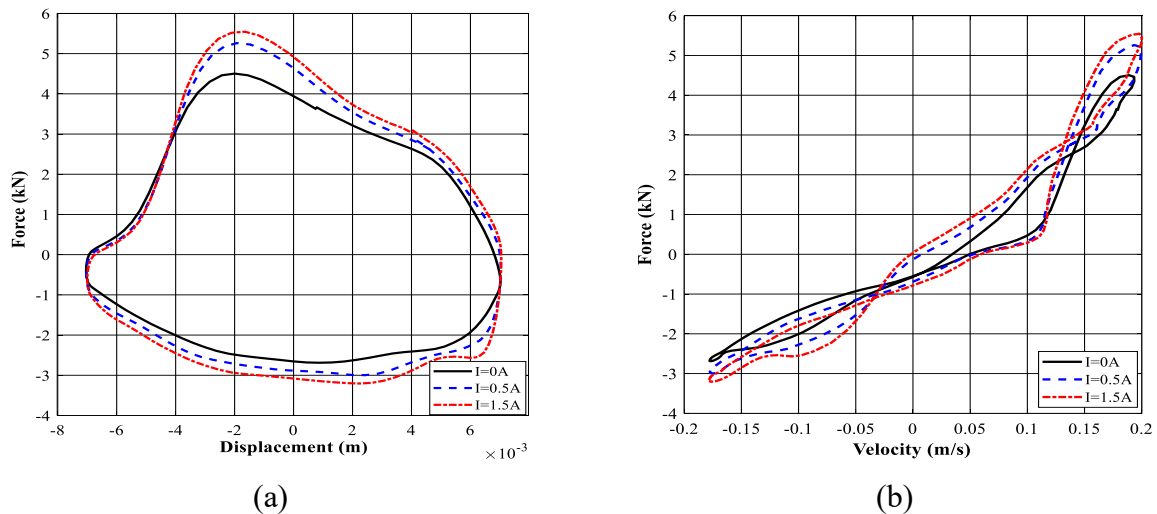


Figure 5-14. The measured data (a) force-displacement and (b) force-velocity characteristics of the MRFD under loading frequency of 4 Hz at the displacement amplitude of 7 mm.

5.4.3 Dynamic range and equivalent viscous damping

Apart from dynamic analysis of the MRFD in qualitative manner presented in the previous section, here we present a quantitative investigation of the prototyped MRFD in terms of two important figure of merits, namely, dynamic range and equivalent viscous damping coefficient. In this section, these indices have been evaluated considering wide ranges of loading conditions and

electrical current. Dynamic range plays a crucial role in evaluating the overall control performance of MRFDs. Wide bandwidth MRFDs are expected to have a wide control range with a large dynamic range. The dynamic range can thus be mathematically represented as:

$$\lambda_d = \frac{F_{I_{max}}}{F_{I_0}} \quad (5-1)$$

where F_{I_0} is the measured off-state damping force while $F_{I_{max}}$ is the measured damping force at the maximum applied current. The dynamic range was measured over the entire range of loading conditions considered. Figures 4-15(a) and (b), for instance, show the calculated dynamic range considering the effect of displacement amplitude and loading frequency, respectively, apart from the electrical current. Results clearly show that the dynamic range substantially increases as the applied current increases. The dynamic range of the MRFD slightly decreases at higher loading frequencies and amplitudes, although the effect of displacement amplitude on the dynamic range is more noticeable than that of loading frequency. This may be partly attributed to higher off-state damping forces at relatively higher loading frequencies and displacement amplitudes, thereby leading to a lower dynamic range. The maximum dynamic range of the proposed damper was calculated as 2.3 under a loading frequency of 2 Hz and displacement amplitude of 1 mm. Such a large controllable damping force of 5.54 kN together with a large dynamic range of 2.3 for a bypass MRFD with both annular-radial gap were not simultaneously presented before, as can be noted from Appendix A.

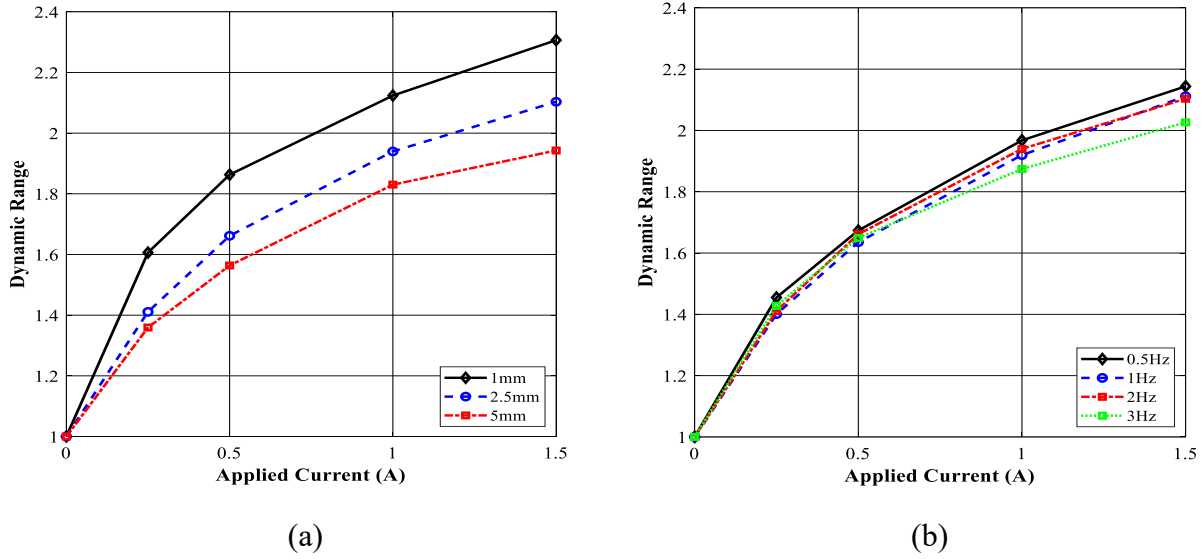


Figure 5-15. The effect of displacement amplitude and loading frequency on the dynamic range of the fabricated MRFD under: (a) loading frequency of 2 Hz and (b) displacement amplitude of 2.5 mm.

The damping characteristics of the proposed MRFD can be quantitatively evaluated from the enclosed area of the force-displacement curves together with the slope of the major axis of the force-velocity curves as discussed in previous section. The equivalent viscous damping coefficient C_{eq} has been traditionally calculated using the energy dissipation method. The energy dissipated over one cycle (U) is calculated from the enclosed area of the force-displacement curve at a certain frequency f as:

$$U = \oint_0^{2\pi/\omega} F(t) dx = \int_0^{2\pi/\omega} F(t) v(t) dt \quad (5-2)$$

The equivalent viscous damping coefficient (C_{eq}) can be, thus, calculated as [242]:

$$C_{eq} = \frac{U}{2\pi^2 f X_0^2} \quad (5-3)$$

where X_0 is the excitation amplitude of a sinusoidal oscillation. The equivalent viscous damping coefficient may also be obtained from the slope of major axis of the force-velocity curves as:

$$C_{eq} = \frac{F|_{v_{max}} - F|_{v_{min}}}{v_{max} - v_{min}} \quad (5-4)$$

$F|_{v_{max}}$ and $F|_{v_{min}}$ are the measured force of the MRFD corresponding to the maximum and minimum values of the piston velocity, namely, as v_{max} , and v_{min} , respectively. This schematically is shown in Figure 5-16.

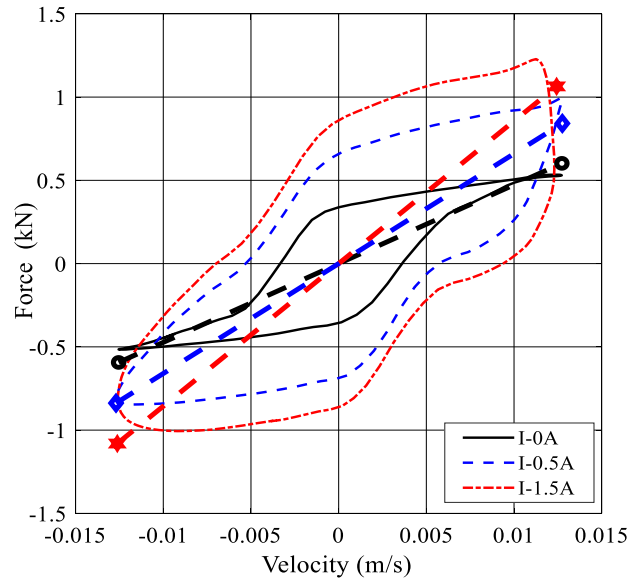


Figure 5-16. The schematical representation of the equivalent viscous damping coefficient (C_{eq}) as the slope of major axis of the measured force-velocity curves under loading frequency of 2 Hz and displacement amplitude of the 1 mm.

The C_{eq} was calculated using the above two methods and summarized in Table 5-2, as example, for the loading frequency of 1 Hz. Analysis of the Table 5-2 reveals comparable values of C_{eq} calculated via two methods. The maximum relative difference between the two approaches was found to be nearly 4.5% at the displacement amplitude of 1mm and the applied current of 0.5 A. Besides, increasing the displacement amplitude resulted in decrement in the C_{eq} , as noticed before in results presented in section 5.4.2.

Table 5-2. The calculated equivalent viscous damping coefficient (C_{eq}) of the MRFD using two methods.

Amplitude	Applied current	Energy dissipated method (kN.s/m)	Slope of force-velocity curve (kN.s/m)
1 mm	0.5 A	120.3	125.7
	1.5 A	156.3	158
2.5 mm	0.5 A	63.6	62.1
	1.5 A	75.74	78.56
5 mm	0.5 A	39.84	37.79
	1.5 A	46.24	45.55

The variation of C_{eq} with respect to loading frequency and displacement amplitude were shown in Figures 4-17 and 4-18. Figures 4-17(a) and (b) show the variations of the calculated C_{eq} , obtained by means of the two aforementioned approaches, with respect to the applied current considering varied displacement amplitude, ranging from the 1mm to 5 mm and loading frequency of 1 Hz. The C_{eq} increases with applied current from 0 to 0.5 A in a nonlinear manner, while tends to increase with current nearly linearly, when applied current increased from 0.5 A to 1.5 A. Results are also suggestive of a considerable decrement in C_{eq} with increasing displacement amplitude as predicted before.

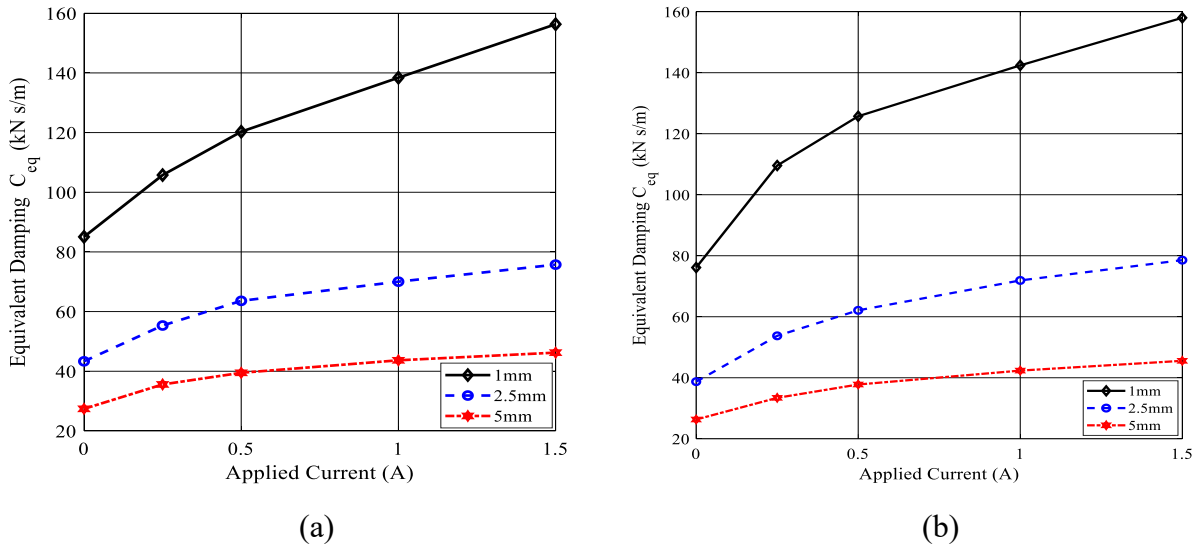


Figure 5-17. The variations of the calculated the equivalent viscous damping coefficient (C_{eq}) with respect to applied current considering different displacement amplitudes. C_{eq} calculated by the energy method (a) and the slope of major axis of the measured force-velocity curves (b) under loading frequency of 1 Hz.

Figures 4-18(a) and (b) also show the variations of the calculated C_{eq} , obtained through the two aforementioned methods, with respect to the applied current considering various loading frequency, ranging from the 0.5 Hz to 3 Hz and displacement amplitude of 2.5 mm. Results consistently show an increase in C_{eq} with increasing applied current in a nonlinear manner while diminishing with increasing loading frequency, which is consistent with previous observation in section 5.4.2. Further examination of results in Figures 4-17 and 4-18 also reveal that the C_{eq} tends to saturate at higher level of applied current.

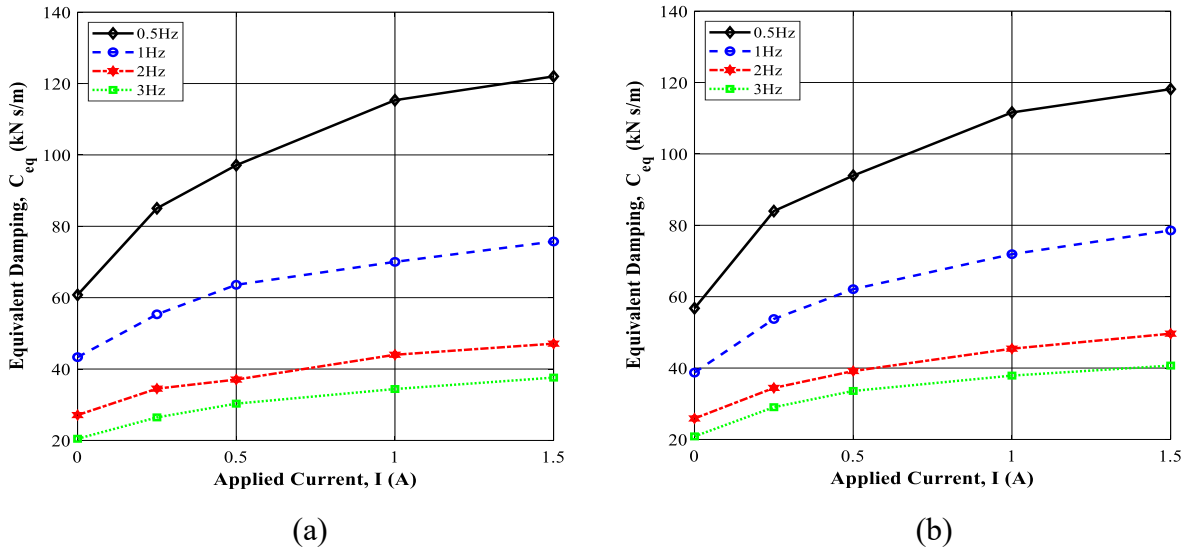


Figure 5-18. The variations of the calculated the equivalent viscous damping coefficient (C_{eq}) with respect to applied current considering varied loading frequencies. C_{eq} calculated by the energy method (a) and the slope of major axis of the measured force-velocity curves (b) under displacement amplitude of 2.5 mm.

5.5 Modification in the MR bypass valve design

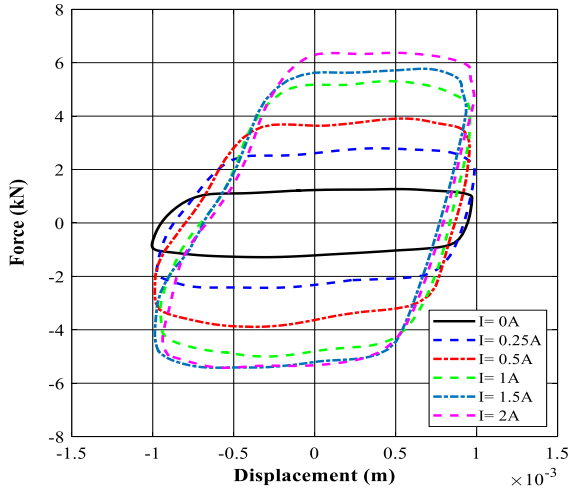
One of the main advantages of bypass MR dampers is ease of modification in the design of MR valve in order to further expand damper's dynamic range and damping force without modifying the damper design, apart from ease of maintenance, assembly, and better heat transfer of coils, as compared with those typical cylinder-piston MR dampers embedded MR valves. For instance, in this study, the magnetic materials of the MR valve bobbin in the design of MR valve is changed from low carbon steel AISI 1006 to a new magnetic core with higher magnetic permeability (AISI 1117), in addition to changing the material of the spacer between the bobbin and the outer cover from AISI 1018 to Nylon 6/6 in the annular gap and stainless-steel SS 304 in

the radial gaps. These modifications yielded a dramatic improvement in the dynamic indices of the proposed MR damper. Table 5-3 shows the comparison of the physical parameters of the coil in the initial design of MR valve and those at the modified design. A significant increase was observed via modification of the valve design. The proposed by-pass MR damper has the flexibility that modification by can be added to the initial design in order to satisfy multiple design conditions and requirements for broad range of vibration mitigation application in different off-road vehicles.

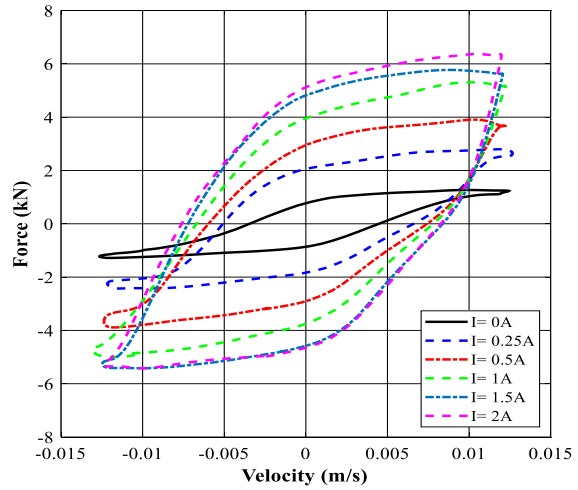
Table 5-3. Comparison of physical parameter and dynamic index of the initial MR valve with the modified design.

Parameter	Initial design	Modified design
Bobbin core material	AISI 1006	AISI 1117
spacer material in annular gap	AISI 1018	Nylon 6/6
spacer material in radial gap	AISI 1018	SS 304
Number of turns	340	215
Duct gap	1.2 mm	1.2 mm
Dynamic indices at velocity 12.5 mm/s		
Max. Dynamic range	2.3	5.06
Max. damping force	1.21 kN	6.61 kN

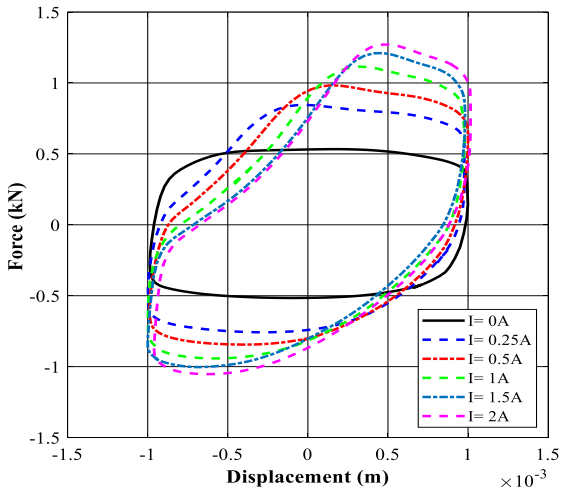
The modified MR valve was fabricated and assembled to the MR bypass damper and its dynamic performance was investigated under different dynamic loading conditions at different levels of applied currents. The results, qualitatively, presented in Figures 4-19(a) and (b) for loading frequency of 2 Hz, as example, display that the bypass MR damper with new modified MR valve has substantially higher dynamic force range as compared with initial design of MR valve's performance presented in Figures 4-19(c) and (d).



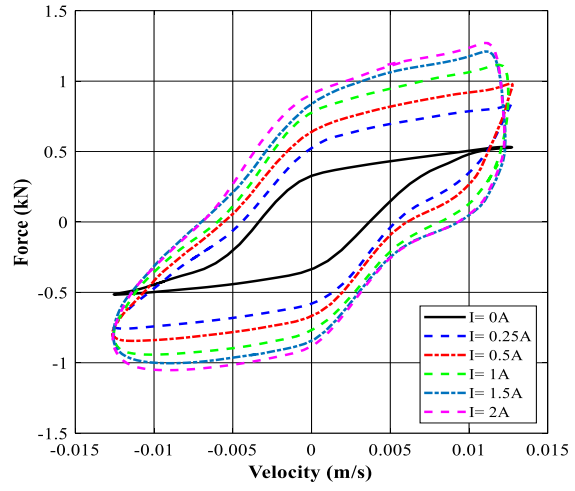
(a)



(b)



(c)



(d)

Figure 5-19. The comparison of force–displacement and force-velocity characteristics of the MR damper with modified MR valve (a), (b) with the initial design of MR valve (c), (d) under at excitation frequency of 2 Hz and displacement of 1 mm.

Figure 5-20 quantitatively compares the dynamic performance of the modified MR valves with initial design valve in terms of dynamic range as well as equivalent viscous damping coefficient under loading frequency of 2 Hz and displacement amplitude of 1 mm under varied levels of applied current. The results were indicative of a dramatic improvement in dynamic indices of the prototyped MR damper with modified MR valve over the initially design valve. For instance, the maximum dynamic range was increased from 2.3 to 5.06 via valve modification, corresponding to a relative increment of 120 %.

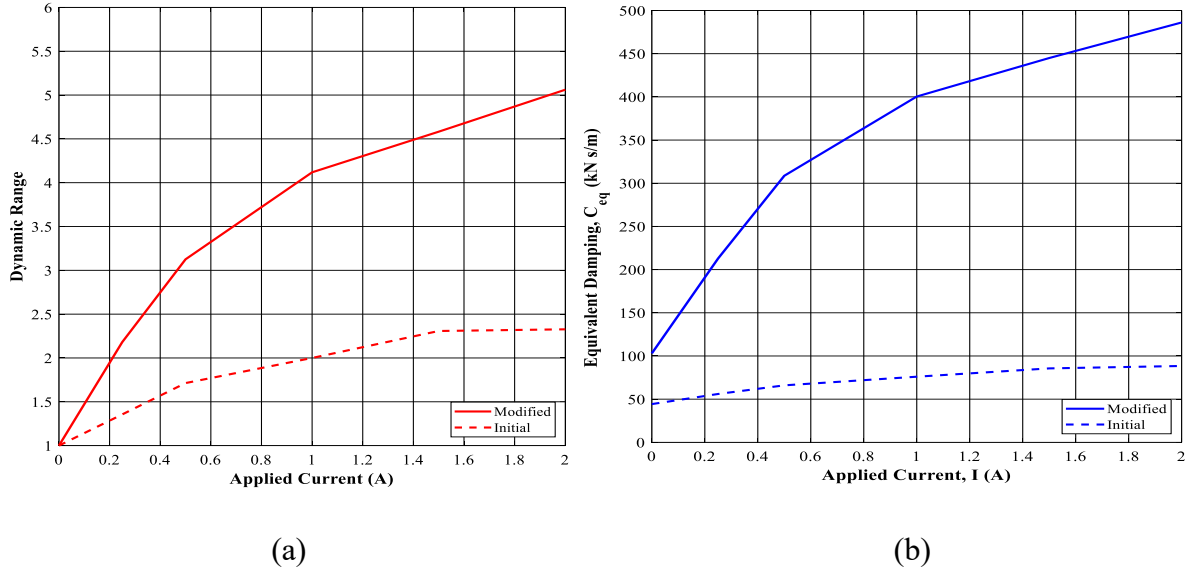


Figure 5-20. The comparison of the dynamic indices (dynamic range (a) and equivalent damping (b)) characteristics of the modified MR valve with the initial design of MR valve under at excitation frequency of 2 Hz and displacement of 1 mm.

Table 5-4 compares the dynamic performance of the prototyped MRFD with both initial and modified designs with those MR bypass dampers with annular-radial gap flow reported in the previous studies. Even though Keslo et al. [243] obtained a high dynamic range of 5.5, however, their damper's maximum force is limited to only 2.2 kN, which is far below the requirement for many off-road applications especially tracked vehicles. The proposed bypass MRFD even with the initial design of the MR valve can simultaneously reach a reasonably good dynamic range of 2.3 and also a maximum force of 5.54 kN as well as a large stroke of 180 mm, considering the fact that a lower dynamic range at high frequencies leads to reducing damping ratios that are required for good ride quality at higher speeds [244]. The prototyped MRFD in this study with the modified valve even reached to a dramatic dynamic range of 5.06 and a maximum dynamic damping force of 6.61 kN, outperforming the reported studies in terms of dynamic indices. It is also noted that the fail-safe capability of the current damper (off-state configuration) is quite more noticeable than the current state of the art, which can assure high damping force in case of malfunction in the electromagnetic circuit. The current MRFD can be easily integrated into an off-road tracked vehicle such as M113 suspension system that requires a damping force of 4.4 kN at a corresponding piston velocity of 0.2 m/s and a large stroke of 180 mm [173].

Table 5-4. Comparison of research MRFD to reported studies for off-road vehicles.

Reference	Corresponding Velocity (m/s)	Off-state damping force (kN)	Max damping force (kN)	Max dynamic range	Stroke (mm)
Keslo [243], 1998	0.13	1.1	2.2	5.5	122.6
Makowski [245], 2018	0.15	2	2.5	1.34	40
Zhang [246], 2020	0.26	1.07	3.73	4.66	100
Current study (Initial valve)	0.2	4.5	5.54	2.3	180
Current study (Modified valve)	0.0125	1.31	6.61	5.06	180

5.6 Summary

In this chapter, a novel outer bypass MRFD equipped with a miniaturized MR valve possessing an annular-radial fluid flow gap was tested over a wide range of mechanical and magnetic loadings. The friction force of the damper was initially measured with and without MR fluid in the damper under different loading conditions. The force-displacement and force-velocity characteristics of the prototyped MRFD were measured and discussed as a function of loading conditions and applied current. The equivalent viscous damping coefficient together with dynamic range were also calculated over the entire ranges of loading conditions considered. The experimental characterization was performed for the MRFD with initial and modified bypass valve. The friction force of the MR damper showed a relatively frequency-independent tendency, particularly at higher loading amplitude. Increasing displacement amplitude did not affect the peak friction force while showing an enhancement in the friction-based energy dissipation by increasing the amplitude of displacement. The peak force and area enclosed by force-displacement hysteresis loops of the MR damper increased with increasing applied current, loading frequency and displacement amplitude. Results also show that both the equivalent viscous damping, calculated via two approaches, as well as the dynamic range increased with increasing applied current while decreasing with increasing loading frequency and displacement amplitude. Results also were suggestive of a large controllable force of 5.54 kN and a good dynamic range of 2.3, simultaneously. The bypass configuration of the MR damper allowed modification of MR valve design in terms of physical parameters, which yielded dramatically higher dynamic indices, including a maximum dynamic range of 5.06 and maximum damping force of 6.61 kN.

CHAPTER 5

DYNAMIC CHARACTERIZATION OF VARIABLE STIFFNESS- VARIABLE DAMPING MAGNETORHEOLOGICAL DAMPER

6.1 Introduction

Semi-active suspension systems utilizing MRFDs are a compromise between passive and active systems. Since they have fail-safe and reliability of passive systems while maintaining the fast-response and damping force adaptability of active systems without requiring complex control systems and high power [10–12]. Therefore, semi-active systems have recently received growing interest in improving the ride comfort, handling and stability of ground vehicles [247,248].

In recent years, VSVD-MRFDs capability have received growing interest as they have shown better performance to control vibration in a broad range of frequencies compared with MRFDs with only damping variability. Damping variability is mainly effective to reduce vibration amplitude, particularly at the resonance frequency. In contrast, variation in the stiffness allows adaptively to vary the natural frequency of the system in such a way that can efficiently reduce the transmitted vibration over a broad range of frequencies [27,145]. Furthermore, variability of stiffness permits to overcome the conflict between the ride comfort and good handling stability of vehicle suspension design. Since good ride comfort requires soft stiffness while good handling and vehicle stability requires the suspension system to be stiffer [149,249]. Liu et al. [148] proposed a theoretical model and an experimental configuration to accomplish the VSVD system using two springs and two MRFDs based on the parallel connection. Results revealed superior vibration isolation performance. Sun et al. [149] experimentally stated that the sprung mass acceleration of quarter car system with the VSVD suspension is reduced significantly besides improving the ride comfort when compared with other types of suspension system. Deng et al. [150] integrated a VSVD device in an off-road military vehicle seat suspension subjected to harsh operation excitations with low frequencies and large amplitudes. The results show the importance of the VSVD in reducing the vibration amplitude at resonance and changing the natural frequency of the system, respectively.

Different configurations were proposed for realizing the VSVD System, as shown in Table B-1 in Appendix B. Sun et al. [145] proposed a mechanical system based on a series connection. The

system consists of two MRFDs that are connected in series using a spring element. The equivalent stiffness varies through the application of the current to one MRFD while applying the current to the other MRFD provides damping variability. Sun et al. [159] later enhanced their design by presenting another mechanical device based on the parallel connection assembly of two coaxial MR damping cylinders, two springs, and two connectors. The equivalent stiffness of the system was varying between two modes by adjusting the applied current to the outer damping cylinder. The stiffness and damping variability were tested experimentally. It was shown that the damping coefficients can vary from 16.24 to 29.72 kN s/m by adjusting the current of the inner damping cylinder from 0 to 2 A. The equivalent stiffness was also varied from 8.7 to 24.5 kN/m by controlling current to the outer damping cylinder from 0 to 1 A. Moreover, the results stated that the loading frequency has a negligible effect on the equivalent stiffness and damping. The maximum stroke of the proposed adaptive device was reported to be 71 mm. Zhu et al. [27] developed a compact long-stroke VSVD-MRFD of 105 mm with self-powered generation capability. The damper consists of two springs with different stiffness and a MR damping cylinder. The piston rod is connected to the generator hollow shaft through a ball screw. The equivalent stiffness can vary between three modes corresponding to the applied current. The proposed damper was tested experimentally under a harmonic motion of 0.15 Hz and 30 mm displacement. The testing results stated that the effective stiffness can increase from 17.6 to 30 N/mm as the excitation current changes from 0 to 2 A. While the equivalent damping coefficients fluctuated between 11.78 to 18.68 kN/(m/s). It is noted that the proposed VSVD-MRFD systems in previous studies generally composed of two MRFDs and two mechanical springs. One MRFD provides damping variability, while the other MRFD controls the stiffness variability. While damping and stiffness can be varied independently in these systems, they have a complex design, bulky shape, high cost and limited stroke to be implemented in a vehicles suspension system.

Petter et al. [160] proposed, analyzed and tested a simple variable VSVD system. The system consists of three fluid chambers (one input and two output chambers). The two output chambers are connected to the input chamber using two MR fluid valves that are also connected to two springs with different stiffness coefficients through two pistons. However, the system stiffness could only be varied among three discrete values, depending on the state of the two MR valves (open/close), besides it has a limited damping force and stroke.

Another configuration for achieving the concept of VSVD systems was proposed based on connecting a pneumatic spring with MRVs. Youn and Hac' [155] proposed a VSVD suspension system based on using air springs. The system stiffness varied between three definite values. Li et al. [157] achieved VSVD through controlling air spring stiffness and damping by controlling the applied current to the MRV coil. Zhang et al. [158] presented an MR fluid with a VSVD isolator. Stiffness variability was attained through using the MRV to control the MR fluid flow between two air connectors. Zhu et al. [156] proposed an MRFD with an embedded pneumatic vibration isolator in a compact structure. The stiffness is adjusted through changing the average pressures of the working gas chambers using four pneumatic high speed on-off valves. The suspension system performance was improved by MRV control of the air spring to achieve the VSVD principle also due to the nonlinearity and capability of air springs in absorbing more shocks. However, VSVD systems based on the MR air spring are bulbous, high cost and have complicity in control and design due to the coupling between the fluid dynamics and the pneumatic dynamics.

Examination of Table B-1 further reveals that the previous studies provided several conceptual designs for realizing VSVD-MRFDs. However, these VSVD-MRFDs have many drawbacks regarding complexity in design and control, besides the bulky shape, unreliability and high cost. Also, the reported VSVD-MRFDs have low damping force and low strokes and thus very limited applications. Limited research has also been conducted on design and dynamic characterization of VSVD based MRFD systems with large dynamic range in view of both stiffness and damping. This chapter thus aims to provide conceptional design and experimental dynamic characterization for a compact large-capacity VSVD-MRFD with an annular-radial bypass valve. The proposed VSVD-MRFD has been fabricated and tested under a wide range of loading conditions and applied electric currents. The dynamic properties in terms of dynamic range, equivalent damping and equivalent stiffness have been experimentally investigated. Also, the effect of loading conditions (frequencies, amplitudes, and applied currents) on the dynamic properties has been discussed.

6.2 Design and analysis of the VSVD-MRFD

6.2.1 Structure configuration of the proposed VSVD-MRFD

Figure 6-1 shows the proposed VSVD-MRFD with an annular-radial bypass valve. The VSVD-MRFD mainly composes of main piston, piston rod inside a cylindrical housing, two different stiffness springs and external bypass fluid valve. The cylindrical housing is divided by

main piston into two upper and lower chambers that are filled with the MR fluid. The housing is connected with end cap and cylinder cover at both its ends. The main piston is threaded with the piston rod and is sealed with the cylindrical housing. The piston rod is connected to external mechanical spring, end cap and attached to the cylindrical housing by a sliding guider. The piston rod has a chamber with certain dimensions which accommodates a floating piston connected to mechanical spring. This chamber with internal mechanical spring basically serves as an accumulator to compensate the change in MR fluid volume due to movement of the piston rod. Compared with conventional bulky gas accumulator (gas spring), the proposed design yielded a compact and reliable MRFD with no issues related to gas leakage and fluid-gas dynamics.

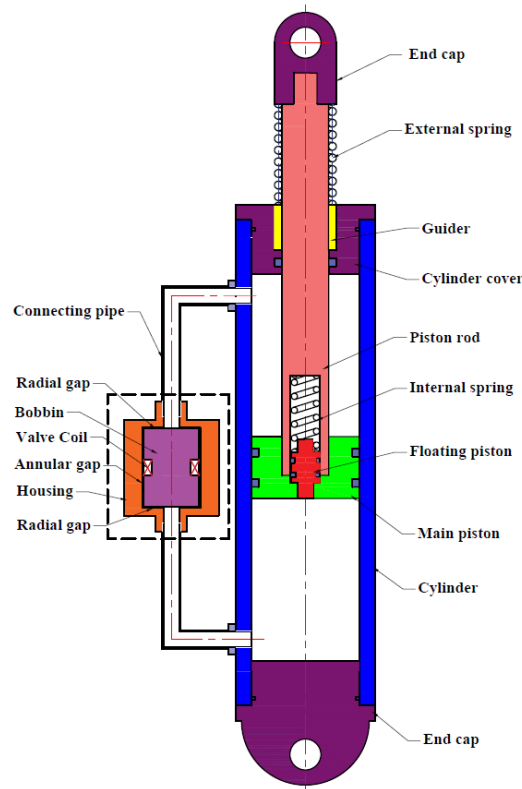


Figure 6-1. Cross-sectional view of the proposed VSVD-MRFD with annular-radial bypass valve.

The external bypass fluid valve, shown by the dashed line in Figure 6-1 consists of housing, MR valve bobbin with impeded magnetic coil and also spacer to allow annular-radial gaps. The annular-radial bypass valve provides design freedom to generate high dynamic force and dynamic range and also facilitates installation and maintenance. Moreover, the bypass MR valve provides better

heat dissipation compared with internal MR valves under high currents thus allowing the damper to operate for a longer time under harsh environmental conditions.

6.2.2 Working principle

The working principle of the proposed VSVD-MRFD is based on the series connection between the MR damping element and the spring as demonstrated in Figure 6-2. The series connection type provides easy practical implementation of the VSVD-MRFD in real world applications. The damping variability is realized by controlling the applied magnetic field to the annular-radial bypass valve. Since the damping element is in series connection with the internal spring k_1 , the equivalent damping is not depending only on the damping constant of the valve but also, it depends on the stiffness rate of the internal spring and excitation frequency as represented in Eq. (6-1). The stiffness variability of the proposed damper is achieved via a spring element k_2 in parallel with the series connection of MR damping element and internal spring. By adjusting the applied current, the force applied on the internal spring and external spring will be varied. The equivalent stiffness of the damper can be expressed as in Eq. (6-2).

$$C_{eq} = \frac{ck_1^2}{c^2\omega^2 + k_1^2} \quad (6-1)$$

$$k_{eq} = k_2 + \frac{ck_1\omega^2}{c^2\omega^2 + k_1^2} \quad (6-2)$$

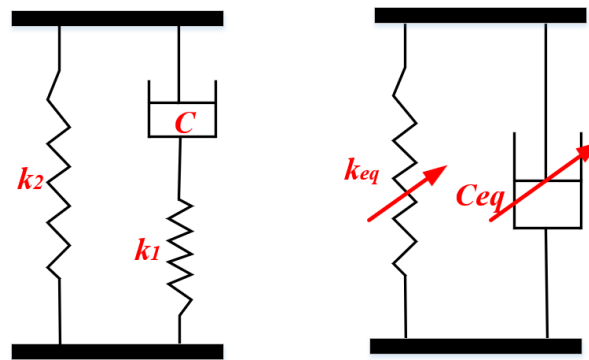


Figure 6-2. Scheme of the working principle of the VSVD-MRFD.

6.2.3 Fabrication of the proposed VSVD-MRFD

The basic geometry of the fabricated VSVD-MRFD is shown in Figure 6-3 and its main dimensions are listed in Table 6-1. Figures 5-4(a) and (b) show the prototype and components of the VSVD-MRFD. The housing cylinder of the damper is fabricated from heat-treated alloy steel 4140 that has good hardness and surface roughness to withstand the friction of the other parts. The carbon steel 1045 was used in the manufacturing of the main piston, piston rod and floating piston. A bronze guider was used to connect the piston rod with the housing cylinder and to provide sufficient lubricant for the piston rod during movement. For reducing the magnetic circuit reluctance, a low carbon steel AISI 1117 was used as the material of the bobbin and steel AISI 1006 was used for shell of the MR bypass valve. The spacer material between the bobbin is Nylon 6/6 in the annular gap and stainless-steel SS 304 in the radial gaps. Lord Corporation's MRF-132DG MR fluid was utilized to fill the MRFD. The specific gravity of this MR fluid is 3, and its viscosity is 0.112 Pa.s at 40°C. The MR valve electromagnet coil has 215 turns of the copper American Wire Gauge 24. Two heavy duty spring from Lee Company with different stiffness coefficients were utilized in to provide stiffness variability. Table 6-2 shows the details parameters of the two springs.

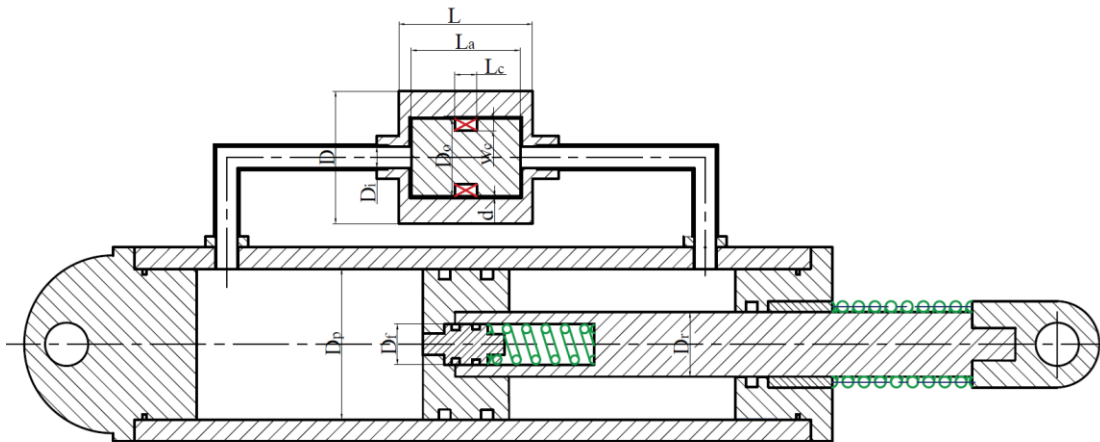
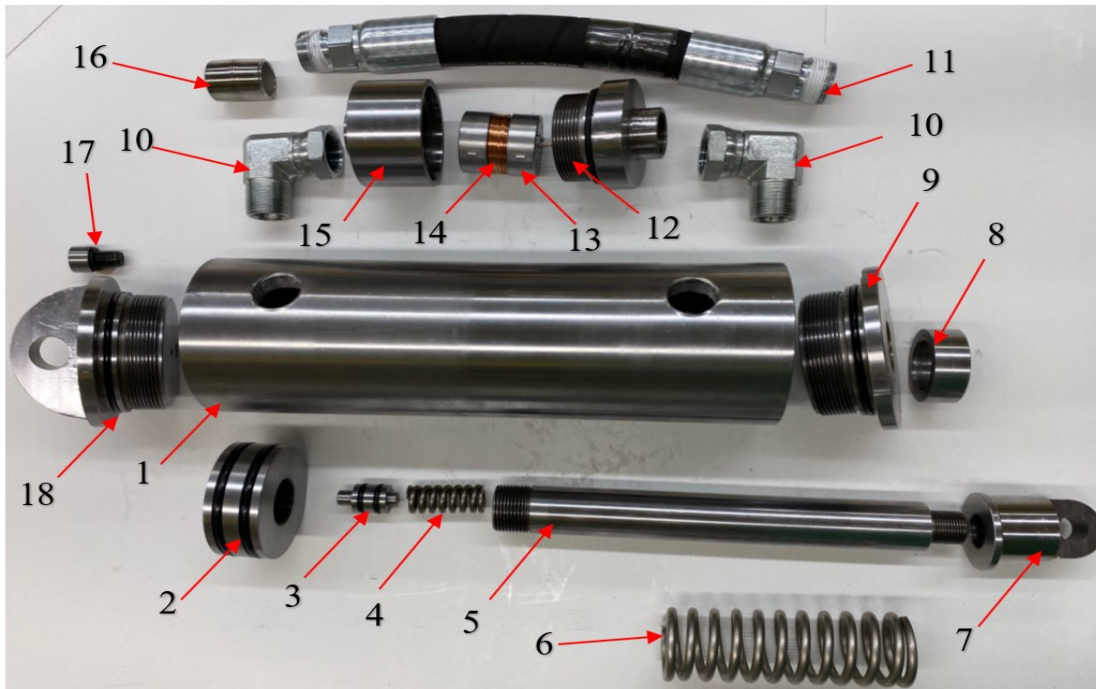
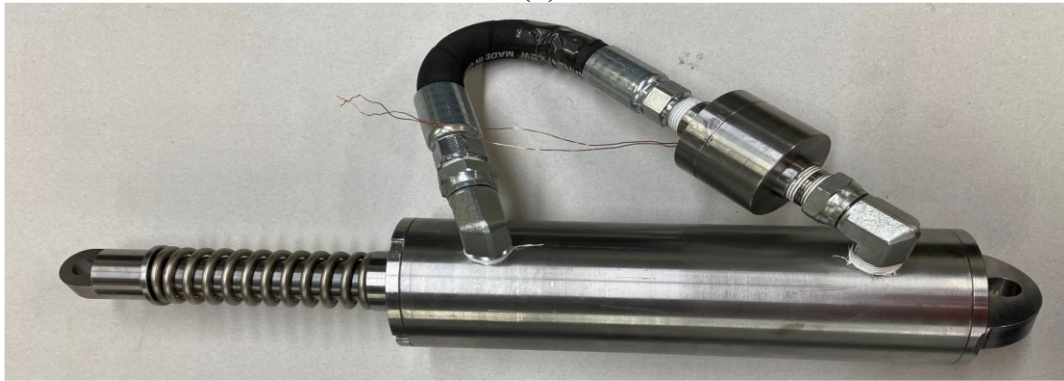


Figure 6-3. Basic dimensions of the proposed VSVD-MRFD.



- | | | | | | |
|---|-----------------|----|----------------------|----|----------------------|
| 1 | Damper cylinder | 7 | End cap | 13 | MR valve-Bobbin |
| 2 | Main piston | 8 | Guider | 14 | MR valve-Coil |
| 3 | Floating piston | 9 | Cylinder cover | 15 | MR valve-Lower shell |
| 4 | Internal spring | 10 | Hydraulic elbow | 16 | Connetor |
| 5 | Piston rod | 11 | Hydraulic hose | 17 | Filling hole bolt |
| 6 | External spring | 12 | MR valve-upper shell | 18 | Cylinder end cap |

(a)



(b)

Figure 6-4 (a). The main components of the proposed VSVD-MRFD and (b) the prototyped VSVD-MRFD.

Table 6-1. Main parameters of the proposed VSVD-MRFD.

Parameter	Symbol	Value (mm)
Duct gab	d	1.2
Coil width	w_c	7
Piston diameter	D_p	70
Piston rod diameter	D_r	30
Floating piston diameter	D_f	19.05
Radial duct outer diameter	D_o	38.1
Radial duct inner diameter	D_i	10
MR valve whole diameter	D	64.5
Annular duct length	L_a	43.9
Coil length	L_c	10.7
MR valve height	L	60

Table 6-2. Specification of the Springs.

Specification	Internal spring	External spring
Stiffness	120 N/mm	15.5 N/mm
Free Length	44.5 mm	127 mm
Outside diameter	18.29 mm	42.85 mm
Hole diameter	19.05 mm	44.45 mm
Rod diameter	9.53 mm	30.58 mm

6.3 Experimental characterization of the VSVD-MRFD

6.3.1 Test setup

A comprehensive experimental investigation was conducted to evaluate the dynamic performance of the fabricated VSVD-MRFD in terms of force-displacement and force-velocity under a variety of mechanical and magnetic loading conditions. The designed test rig and specifications utilized in measurements were discussed in section 5.3.1. A photograph of the full test setup for implementing the dynamic analysis is illustrated in Figure 6-5.

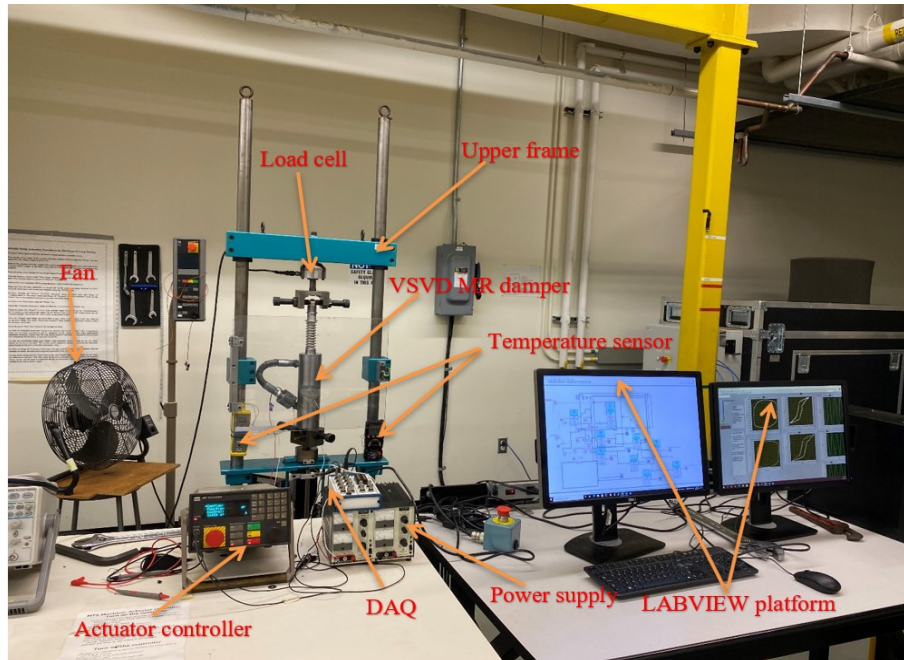


Figure 6-5. Photograph of the full test setup implemented with the fabricated VSVD-MRFD.

6.3.2 Experimental measurements

The experimental measurements were conducted to measure force-time, force-displacement, and force-velocity of the MRFD under various piston motion frequencies and excitation currents. Experiments were performed with five levels of excitation frequency ($f = 0.5, 1, 2, 3,$ and 4 Hz), two levels of displacement amplitude ($X = 1$ and 2.5 mm), and six levels of applied current ($I = 0, 0.25, 0.5, 1, 1.5$ and 2 A). For each test condition, force-displacement and force-velocity were measured in five consecutive cycles once steady-state was achieved and then averaged for characterization.

6.4 Results and discussion

6.4.1 Nonlinear hysteresis dynamic analysis of the VSVD-MRFD

The dynamic characteristics of the prototyped VSVD-MRFD under a wide range of loading conditions are stated and discussed in this section. Figure 6-6 shows the force-displacement and the force-velocity characteristics of the VSVD-MRFD at an excitation frequency of 0.5 Hz, displacement amplitude of 1 mm and applied electrical currents ranging from 0 to 2 A. Results show that hysteresis characteristics become more noticeable and enhanced with increasing the applied current. As it can be realized, the area enclosed by the force-displacement hysteresis loops (representing the amount of energy dissipation per cyclic loading) is substantially increasing with

increasing the applied current. This is also confirmed by the slope of the main axis of the force-velocity curves (representing the equivalent damping) which is increased by increasing the applied current. Similar behaviour was also observed at other loading conditions. Figure 6-6 demonstrates that under this loading condition, the peak force is increased from about 1.53 kN in the absence of the current to nearly 5.44 kN under current 2 A, thus yielding a dynamic range of 3.56. The saturation phenomenon can also be observed as the applied current above increases beyond 1.5 A.

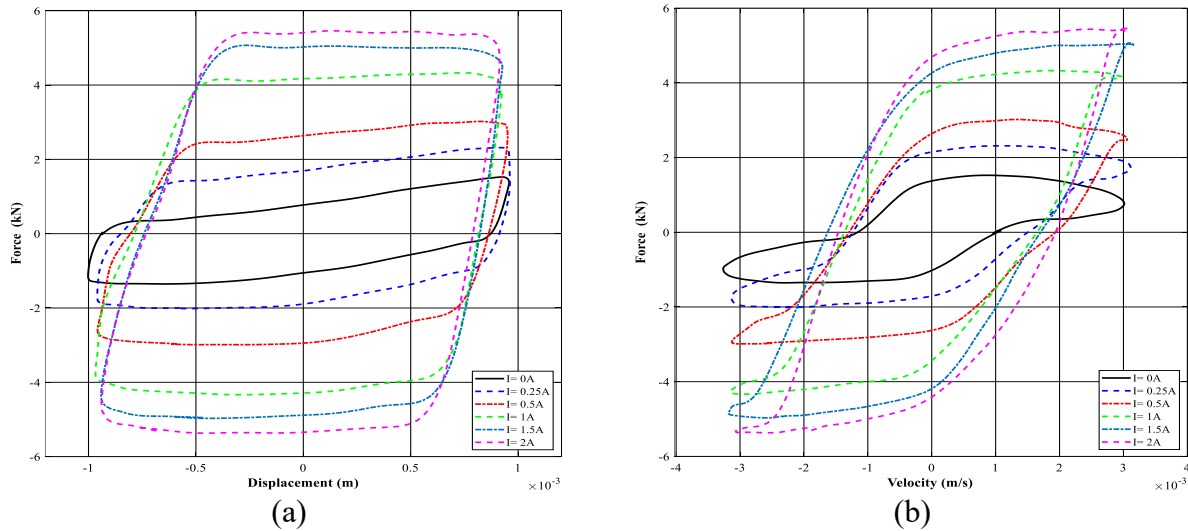


Figure 6-6. The measured dynamic characteristics of VSVD-MRFD under loading frequency of 0.5 Hz at the displacement amplitude of 1 mm (a) force-displacement and (b) force-velocity.

Figure 6-7 exhibits the dynamic characteristics of the VSVD-MRFD at an excitation frequency of 1 Hz and displacement of 2.5 mm. At this loading condition, the damper's peak force ranges between 2 kN to 7.2 kN as the applied current ranges from zero to 2 A, rendering a dynamic range of 3.6. Results consistently confirm that the encircled area by the force-displacement loops (energy dissipation) amplifies as the applied current increases. Figures 5-6(b) and 5-7(b) also demonstrate that the damping force increases with increasing velocity of the damper piston rod.

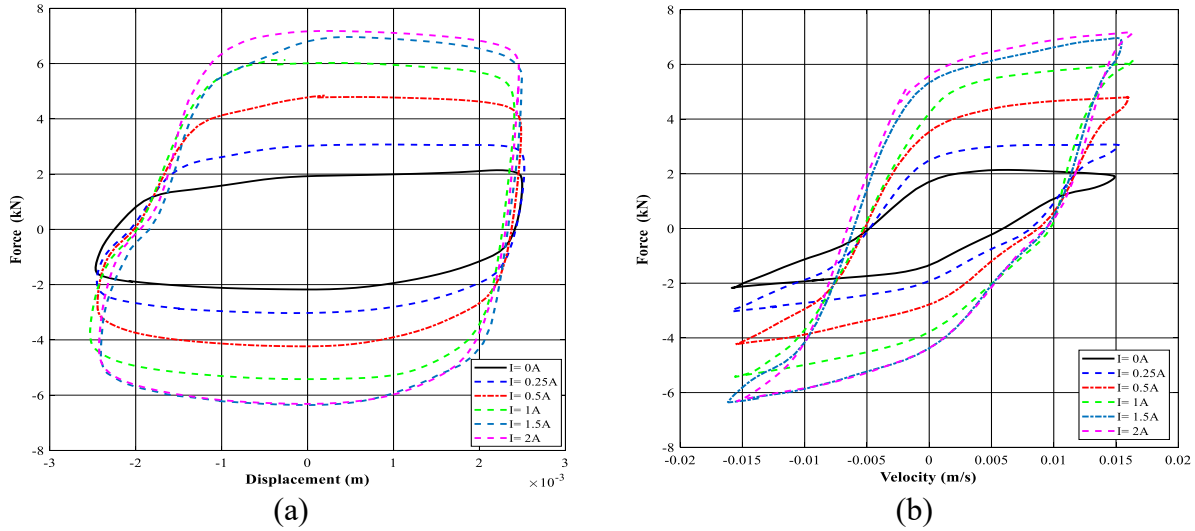


Figure 6-7. The measured dynamic characteristics of VSVD-MRFD under loading frequency of 1 Hz at the displacement amplitude of 2.5 mm (a) force-displacement and (b) force-velocity.

Figure 6-8 exhibits the dynamic characteristics of the VSVD-MRFD at an excitation frequency of 2 Hz and displacement of 1 mm. At this loading condition, the damper's peak force ranges between 1.64 kN to 6.73 kN as the applied current ranges from zero to 2 A, representing a higher dynamic range of 4.1.

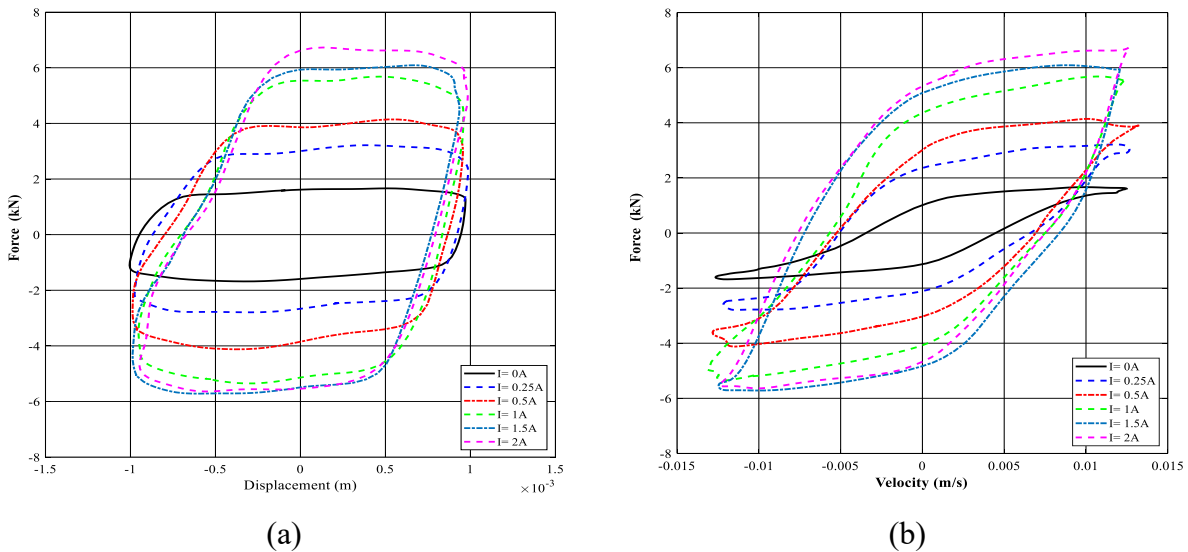


Figure 6-8. The measured dynamic characteristics of VSVD-MRFD under loading frequency of 2 Hz at the displacement amplitude of 1 mm (a) force-displacement and (b) force-velocity.

Figures 5-9 and 5-10 reveal the effect of excitation frequency on the dynamic properties of the VSVD-MRFD in terms of force-displacement and force-velocity characteristics at a constant displacement amplitude of 1 mm under applied current of 1 A and 2 A, respectively. Results show the damping force of the MRFD, are substantially enhanced when the loading frequency increases from 0.5 to 4 Hz. Moreover, as the loading frequency increases, the slope of the force-velocity curves, representing the equivalent damping coefficient of the MRFD, decreases. It should be noted that the loading passes, as observed in force-velocity hysteresis loops in Figure 6-9(b) is relatively independent of the excitation frequency.

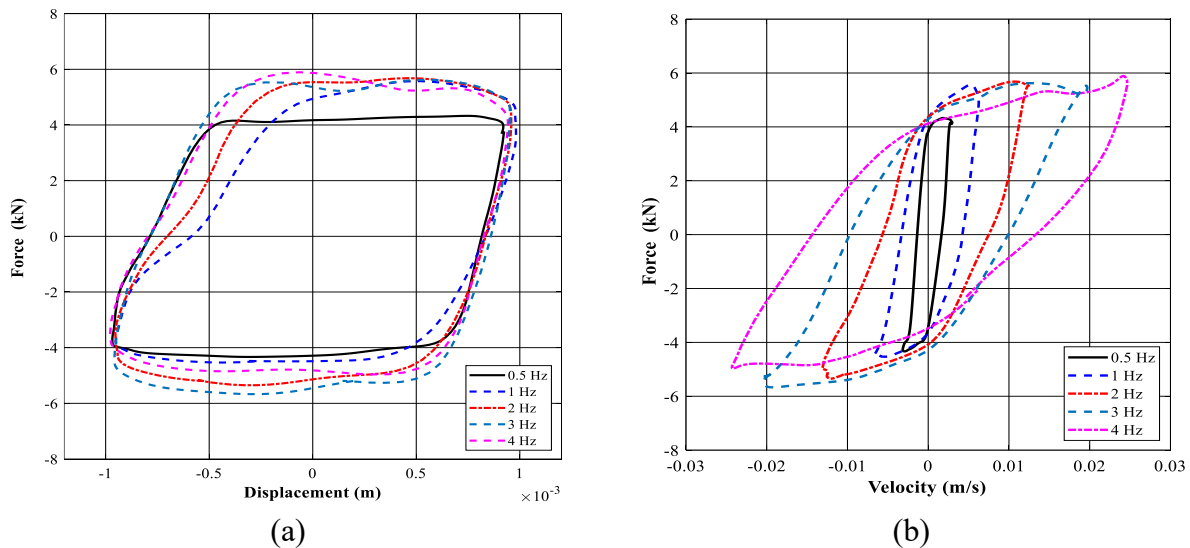


Figure 6-9. The frequency dependent characteristics of the VSVD-MRFD under 1 A electrical current and constant displacement amplitude of 1 mm: (a) force–displacement, (b) force–velocity.

Figure 6-10 presents the frequency dependent characteristics of the VSVD-MRFD when 2 A is applied to the MR valve’s coil. Results show that by increasing the current to 2 A, the excitation frequency yields more nonlinear hysteresis effect on both force-displacement and force-velocity characteristics of the VSVD-MRFD. For instance, at a higher frequency, such as 4 Hz, the loading paths of a hysteresis loop presented in Figure 6-10(b), tend to be upward, enhancing the intra-cycle damping coefficient locally. Further analysis of Figures 5-9 and 5-10 also reveals that increasing the magnetic field of the MR valve leads to a substantial increase in the energy dissipation properties, and damping force of the VSVD-MRFD, as also confirmed by results presented in Figures 5-6 to 5-8.

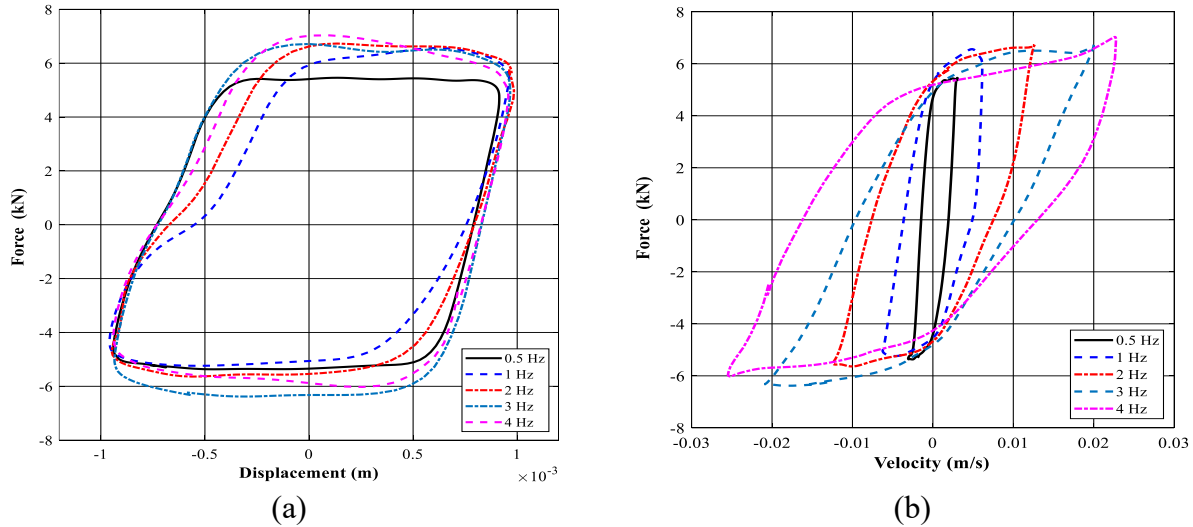
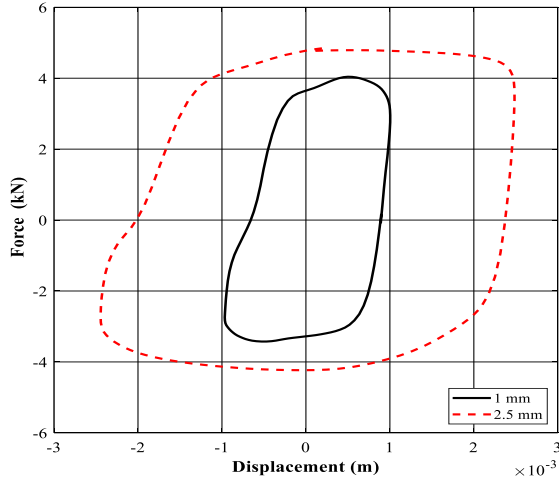
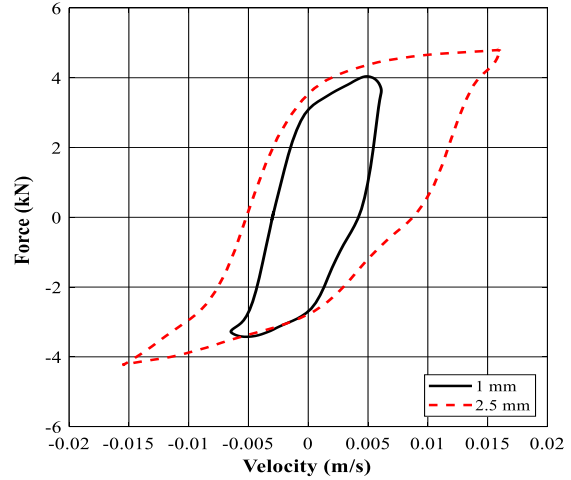


Figure 6-10. The frequency dependent characteristics of the VSVD-MRFD under 2 A electrical current and constant displacement amplitude of 1 mm: (a) force–displacement, (b) force–velocity.

Figures 5-11 and 5-12 explain the displacement dependent properties of the fabricated VSVD-MRFD in terms of force-displacement and force-velocity under excitation currents of 0.5 A and 1.5 A, respectively. Here, these characteristics were studied at a constant excitation frequency of 1 Hz as an example. Results show that the energy dissipation properties and damping force of the VSVD-MRFD is considerably increased by increasing the displacement amplitude from 1 mm to 2.5 mm. Figures 5-11(a) and 5-12(a) clearly show the increase in the peak force as the loading displacement increases from 1 mm to 2.5 mm. Figures 5-11(b) and 5-12(b) also manifest that the loading paths of the force-velocity curves are relatively independent of the excitation displacement. Similar to Figures 5-9 and 5-10, the slope of the main axis of the force-velocity loops, which represents the equivalent damping coefficient of the MRFD, tends to decrease with increasing the displacement amplitude.

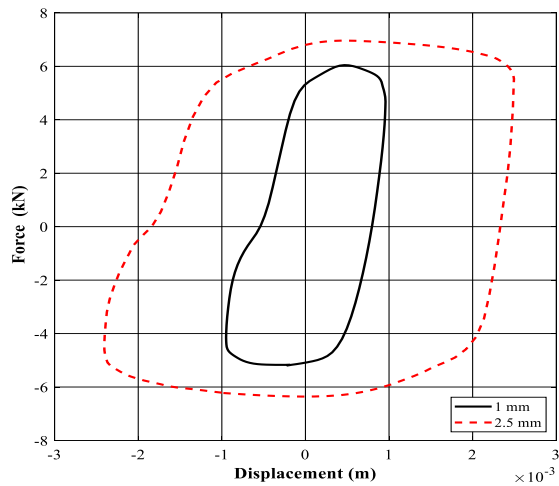


(a)

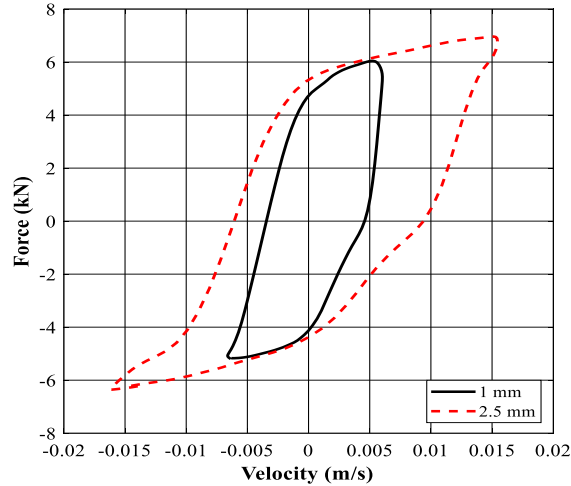


(b)

Figure 6-11. The amplitude dependent characteristics of the VSVD-MRFD under 0.5 A electrical current and constant loading frequency of 1 Hz: (a) force-displacement, (b) force-velocity.



(a)



(b)

Figure 6-12. The amplitude dependent characteristics of the VSVD-MRFD under 1.5 A electrical current and constant loading frequency of 1 Hz: (a) force-displacement, (b) force-velocity.

It should be noted that the maximum force generated by the modified bypass MRFD was measured as 7.82 kN corresponding to the loading frequency and displacement amplitude of 4 Hz and 2.5 mm, respectively as shown in Figure 6-12. The damper could not be tested at higher frequencies and amplitudes due to the limitation of the MTS system and load cell capacity.

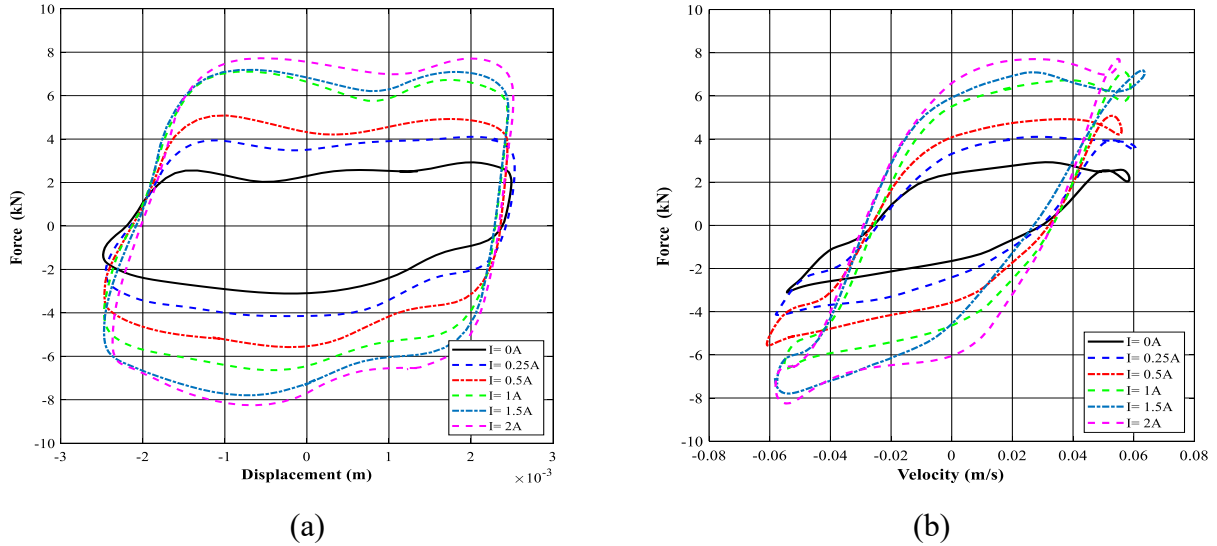


Figure 6-13. The measured data (a) force-displacement and (b) force-velocity characteristics of the VSVD-MRFD under loading frequency of 4 Hz at the displacement amplitude of 2.5 mm.

Results shown provide a qualitative analysis of the prototyped VSVD-MRFD. The following subsections will present quantitative assessments of the fabricated VSVD-MRFD in terms of dynamic range, equivalent viscous damping coefficient, and equivalent stiffness coefficient. An investigation of these indices under various loading conditions and magnetic fields is discussed.

6.4.2 Dynamic range analysis

The dynamic range is an important figure of merit which is indicative of bandwidth and control performance of VSVD-MRFDs to mitigate vibrations under different environmental conditions. The dynamic range (λ_d) can be calculated as in Eq.(5-1). The dynamic range was evaluated under the entire range of mechanical and magnetic loading conditions considered. Figures 5-14(a) and (b) illustrate the influence of the excitation displacement and loading frequency on the evaluated dynamic range under different applied currents, respectively. Results clearly reveal that for the given loading condition, the dynamic range substantially increases as the magnetic field increases. Further examination of results shows that the dynamic range decreases at higher displacement and loading frequency, while the influence of displacement is more obvious than that of loading frequency. This is in part due to the greater off-state damping forces at higher loading frequencies and displacement amplitudes, which decreases the dynamic range. Results show that the damper can reach a maximum dynamic range of 4.5 at the loading frequency of 1 Hz and a displacement amplitude of 1 mm.

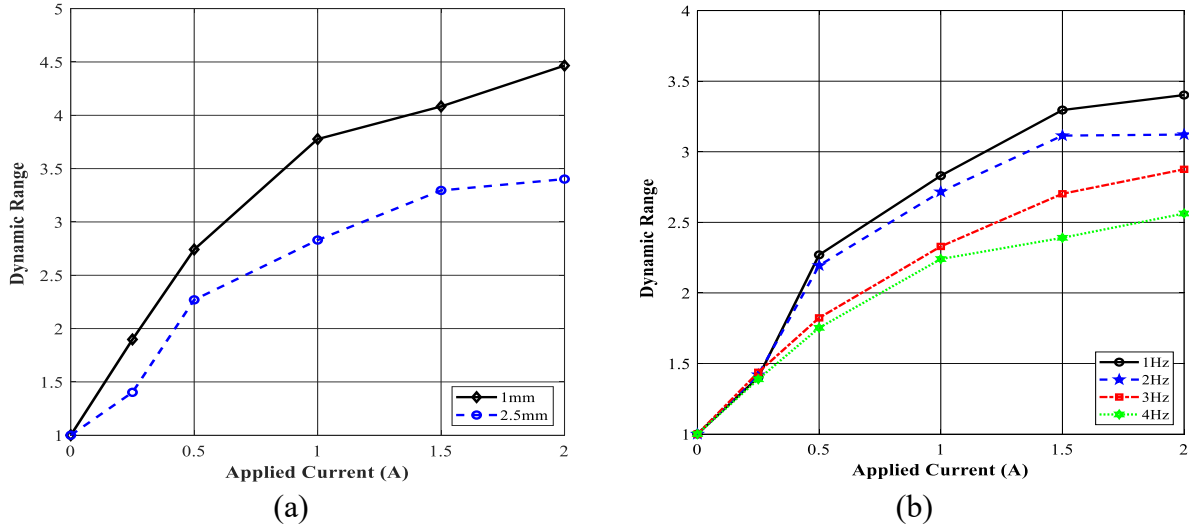


Figure 6-14. The effect of displacement amplitude and loading frequency on the dynamic range of the VSVD-MRFD under: (a) loading frequency of 1 Hz, (b) displacement amplitude of 2.5 mm.

6.4.3 Damping variability

Similar to MRFD characteristics discussed in section 6.4.1, VSVD-MRFD characteristics can be quantified either using the enclosed area of the force-displacement curves (the equivalent viscous damping coefficient (C_{eq})) using the energy dissipation method or the slope of major axis of the force-velocity. These methods are represented in Eqs. (5-2) to (5-4). The equivalent viscous damping was evaluated using the above two approaches for loading frequency of 2 Hz and was summarized in Table 6-3 as an example. Results show that the equivalent viscous damping evaluated using both approaches are nearly comparable. It was found that the maximum relative difference between the two approaches was almost 2.1%. Furthermore, increasing the excitation displacement leads to a decline in the equivalent viscous damping confirming the observation in Figures 5-11 and 5-12.

Table 6-3. The calculated equivalent viscous damping coefficient (C_{eq}) of the MR damper using two approaches.

Amplitude	Applied current	Energy dissipated method (kN s/m)	The slope of idealized force-velocity (kN s/m)
1 mm	0.0 A	143.5	135.19
	0.5 A	318.09	320.66
	1.0 A	397.75	405.38
	2.0 A	485.58	505.61
2.5 mm	0.0 A	74.99	78.22
	0.5 A	158.56	165.84
	1.0 A	203.04	208.4
	2.0 A	221.54	224.6

The influence of loading displacement and frequency on the variation of the equivalent viscous damping versus applied current is also shown in Figures 5-15 and 5-16. Figures 5-15(a) and (b) show the variation of the calculated equivalent viscous damping based on the two approaches, considering different displacement amplitudes of 1mm and 2.5 mm, as a function of applied current. Results indicate a significant decrease in the equivalent viscous damping as displacement amplitude increases.

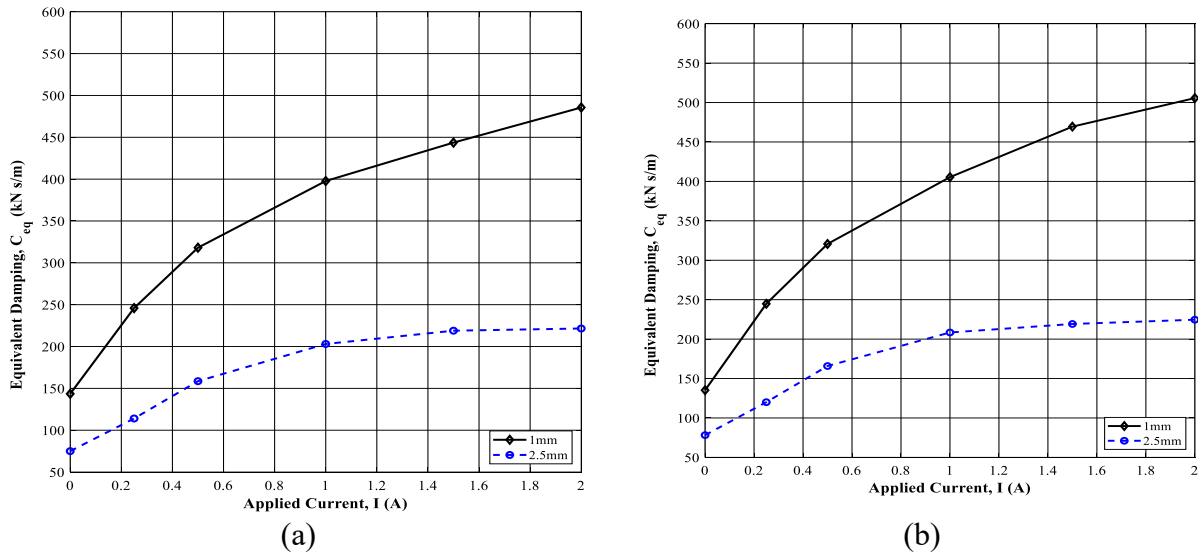


Figure 6-15. The variations of the calculated the equivalent viscous damping coefficient (C_{eq}) with respect to applied current considering different displacement amplitudes. C_{eq} calculated by the energy method (a) and the slope of major axis of the measured force-velocity curves (b) under loading frequency of 2 Hz.

Furthermore, Figures 5-16(a) and (b) show the variations of calculated equivalent viscous damping versus applied current for various loading frequencies, ranging from 0.5 Hz to 3 Hz, calculated by two aforementioned methods. Results reveal a nonlinear increment in equivalent viscous damping with increasing applied current while it diminishes for higher loading frequency, which confirms the observation in section 6.4.1. A closer examination of Figures 5-15 and 5-16 also reveal that the equivalent viscous damping is prone to saturation at higher levels of the applied current.

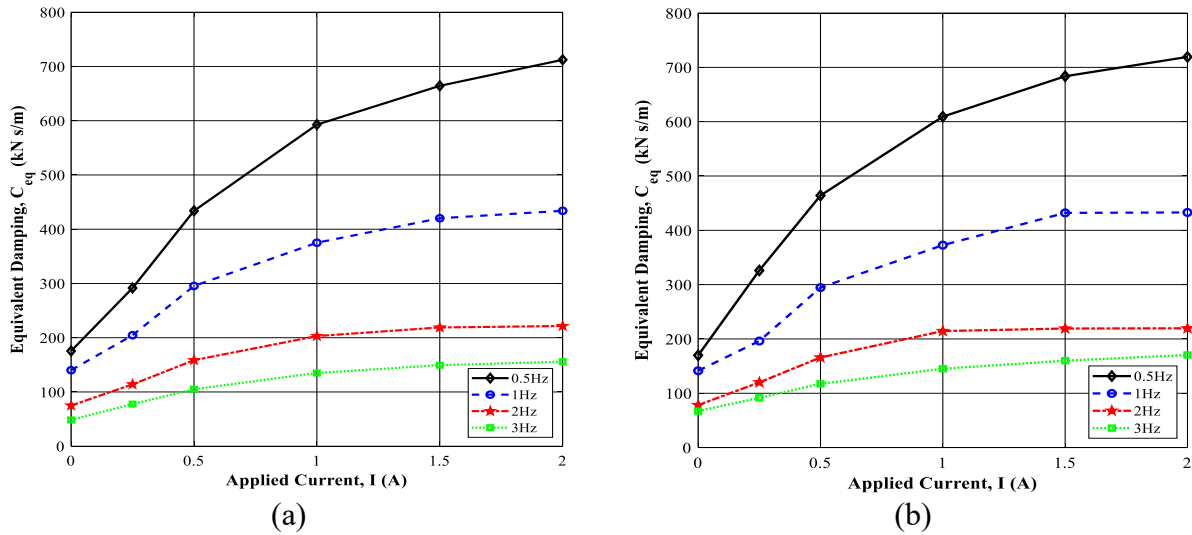


Figure 6-16. The variations of the calculated the equivalent viscous damping coefficient (C_{eq}) with respect to applied current considering varied loading frequencies. C_{eq} calculated by the energy method (a) and the slope of major axis of the measured force-velocity curves (b) under displacement amplitude of 2.5 mm.

6.4.4 Stiffness variability

The proposed VSVD-MRFD is also characterized to examine its stiffness variability by evaluating the equivalent stiffness of the system. MRFD featuring stiffness variability can be effectively utilized to significantly reduce the transmitted vibration by varying the natural frequency of the system to avoid resonance occurrence. Moreover, it can also overcome the conflict between good handling and ride comfort for off/on-road vehicles. The equivalent stiffness (K_{eq}) of the fabricated VSVD-MRFD can be evaluated from the slope of the axis line intersecting the point at maximum and minimum force-displacement hysteresis cycle. This slope is varied according to the applied current and can be estimated from the following equation as [145]:

$$K_{eq} = \frac{[F_d]_{D_{max}} - [F_d]_{D_{min}}}{D_{max} - D_{min}} \quad (6-3)$$

where $[F_d]_{D_{max}}$ and $[F_d]_{D_{min}}$ are the maximum and minimum forces generated by the damper at the maximum and minimum value of the stroke, respectively; D_{max} and D_{min} are the maximum and minimum value of the stroke, respectively.

Figures 5-17 and 5-18 exhibit the effect of the loading displacement and frequency on the variation of the equivalent stiffness of the proposed VSVD-MRFD with respect to the applied current. Figures 5-17 (a) and (b) reveal the influence of the excitation displacements of 1 mm and 2.5 mm on the evaluated equivalent stiffness at loading frequencies of 1 Hz and 2 Hz, respectively as a function of the applied current. The results indicate that the K_{eq} significantly increases as the magnetic field increases. However, similar to the equivalent viscous damping, the rate of increasing is reduced as the applied electric current increases from 1 A to 2 A indicating the saturation. Moreover, results reveal a remarkable reduction in the K_{eq} as the excitation displacement increases.

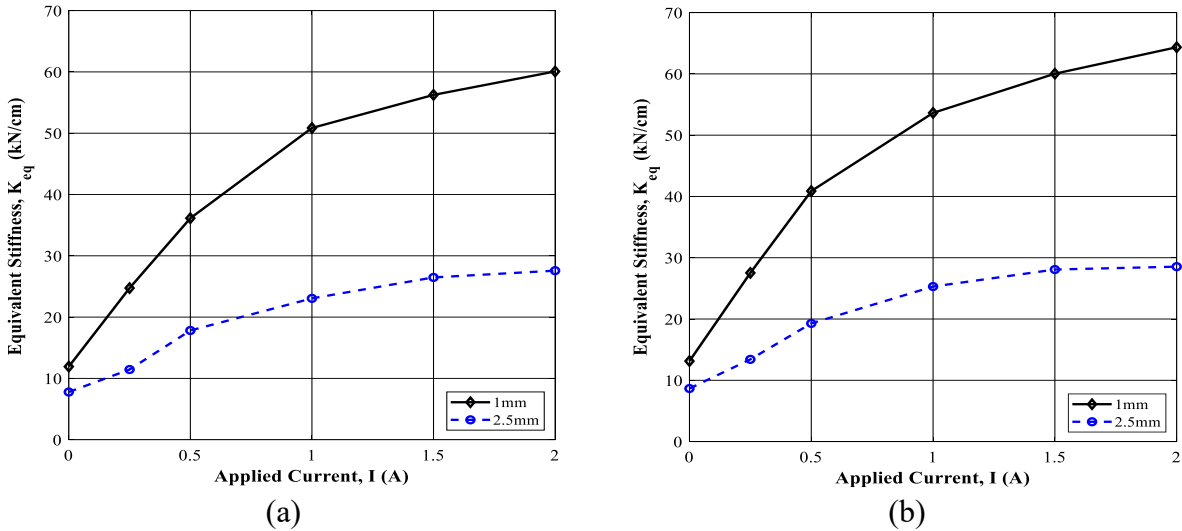


Figure 6-17. The variations of the calculated equivalent stiffness coefficient (K_{eq}) with respect to applied current considering different displacement amplitudes (a) under loading frequency of 1 Hz and (b) under loading frequency of 2 Hz.

Additionally, Figures 5-18(a) and (b) show the variation of the evaluated K_{eq} under various loading frequencies, ranging from 0.5 Hz to 3 Hz, as a function of the applied current, calculated for excitation displacements of 1 mm and 2.5 mm, respectively. Results also reveal a nonlinear

increasing in K_{eq} with increasing applied current while it has a slightly increasing tendency for higher loading frequency. Further observation of Figures 5-17 and 5-18 reveal the saturation of the K_{eq} at higher levels of applied current.

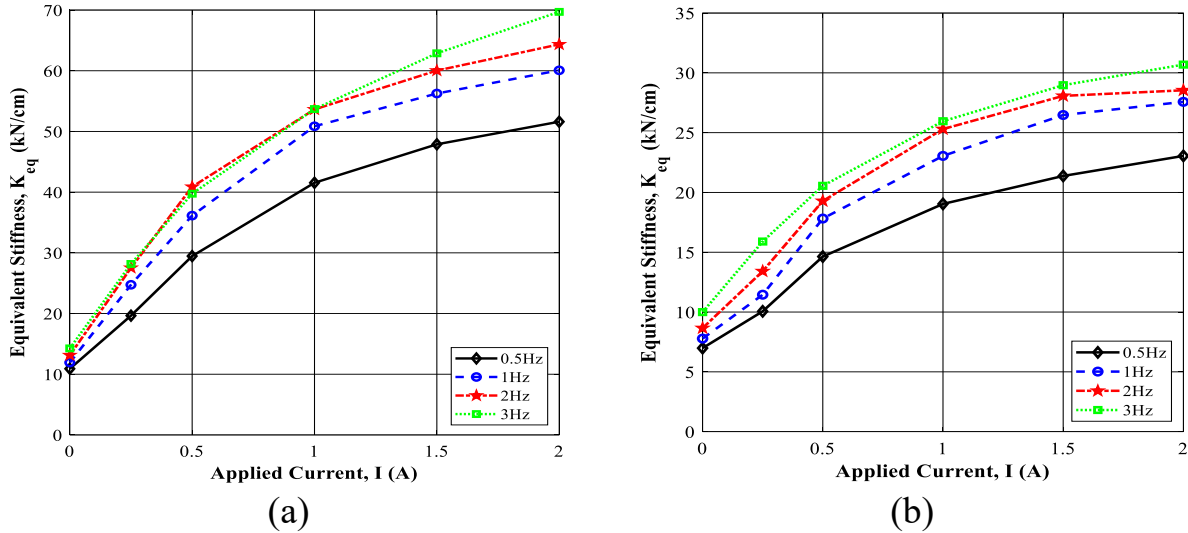


Figure 6-18. The variations of the calculated equivalent stiffness coefficient (K_{eq}) with respect to applied current considering varied loading frequencies. (a) under displacement amplitude of 1 mm and (b) under displacement amplitude of 2.5 mm.

The equivalent stiffness coefficient was quantitatively evaluated for loading frequency of 1 Hz and displacement of 2.5 mm under various applied currents and was summarized in Table 6-4 as an example. Results show that wide range variability of the K_{eq} with the applied current. The equivalent stiffness increases from 7.78 kN/cm at zero current to almost 27.57 kN/cm at the applied current of 2 A, rendering a dynamic range of almost 3.5 in view of stiffness.

Table 6-4. The calculated equivalent stiffness coefficient (K_{eq}) of the VSVD-MRFD under different applied currents.

Applied current	Equivalent Stiffness, K_{eq} (kN/cm)
0	7.78
0.25	11.44
0.5	17.81
1	23.05
1.5	26.47
2	27.57

6.5 Summary

In this chapter, a novel VSVD-MRFD featuring annular-radial bypass fluid valve was experimentally characterized over a wide range of loading conditions and the applied magnetic field. The fabricated VSVD-MRFD was tested and characterized with regard to their force-displacement and force-velocity response behaviour for varied loading conditions and the applied current. Figure of merits, including equivalent viscous damping coefficient, dynamic range, and equivalent stiffness coefficient were quantitatively evaluated over the entire range of loading conditions. The proposed VSVD-MRFD exhibits increasing peak forces and areas enclosed by force-displacement hysteresis loops as loading frequency, displacement amplitude, and current increase. Additionally, results reveal that both the equivalent viscous damping and dynamic range increase as the applied current increase, whereas they decrease with increasing loading frequency and displacement amplitude. The observed decrement was more noticeable with increasing the displacement amplitude. Further results demonstrate that the proposed VSVD-MRFD has a high uniformity and repeatability performance and it has wide stiffness variability according to the loading and magnetic conditions. The equivalent stiffness significantly increases as the magnetic field increases and slightly increases with loading frequency while it has a remarkable reduction as the excitation displacement increases. Based on the presented results, the concept of large-capacity VSVD-MRFD has been accomplished in a compact design. Results also suggest that the proposed VSVD-MRFD can be effectively utilized in off-road vehicle suspension systems for avoiding the harmful vibration under different environmental conditions.

CHAPTER 6

CONTRIBUTIONS, CONCLUSIONS AND RECOMMENDATIONS

7.1 Major contributions

This dissertation presents a development, optimal design, modelling, fabrication and dynamic characterization of a large-capacity VSVD-MRFD with an annular-radial bypass valve for off-road and high payloads applications. The mathematical modeling based on the quasi-static modelling based using Bingham plastic MR fluids behaviour has been first formulated. The MR valve magnetic circuit has been solved analytically and numerically. Subsequently, a formal design optimization problem was formulated to maximize the MRFD's dynamic range. The optimally designed MRFD was finally fabricated considering the design requirements. Moreover, a novel physic-dynamic model has been developed for capturing the hysteresis phenomenon observed in MRFD. The fabricated MRFD featuring VSVD has been comprehensively characterized to evaluate its dynamic performance in view of damping and stiffness variability. The major contributions of this PhD dissertation research are summarized below:

- I. Using the Bingham plastic model, a quasi-static model for a large-capacity annular-radial MRFD and large stroke was formulated for determining the total damping force as a function of the MR valves' geometrical and magnetic parameters, piston velocity and MR fluid property.
- II. The magnetic circuit of the MR valve has been analytically solved to evaluate the magnetic flux density in the MR fluid within active regions of the MR valve for different coil currents. A Finite element simulation using FEMM software was also performed to further realize the distribution of magnetic flux density within the gaps using geometrical and material specifications corresponding to the designed MR fluid bypass valve.
- III. Development of a formal multidisciplinary design optimization strategy using magnetic circuit analysis and geometrical and magnetic parameters of the MRFD in order to maximize the MRFD's dynamic range and improve its dynamic performance. Genetic Algorithm (GA) combined with Sequential Quadratic Programming (SQP) has been effectively used for capturing the global optimal geometric and magnetic circuit parameters of the proposed MRFD.

- IV. Design and fabrication of large-capacity MRFD with an annular-radial bypass valve with the optimal dimensions and the proper tolerances and surface roughness. A mechanical spring accommodated into the piston rod was used as the accumulator to provide the compact design.
- V. Developing a novel physic-based dynamic model based on MR fluid Bingham plastic behaviour to predict the non-linear hysteresis behaviour of MRFDs with an annular-radial bypass valve without experimental identification parameters. The proposed model considers the unsteady behaviour of the MR fluid, compressibility effect, and friction effect. The effectiveness of the proposed model has been demonstrated by comparing the model-predicted responses with the experimental data.
- VI. A comprehensive dynamic characterization of the fabricated MRFD has been performed under a board range of loading conditions and applied currents. The friction force of the damper was measured with and without MR fluid in the damper under different loading conditions. The dynamic properties in terms of the equivalent viscous damping coefficient and dynamic range have also been investigated over the entire ranges of loading conditions considered.
- VII. Developing and experimental characterization of VSVD-MRFD with an annular-radial bypass valve under a wide range of excitation frequencies, displacement and electrical current. The dynamic properties in terms of equivalent damping, equivalent stiffness dynamic range, and their dependency on the loading conditions were thoroughly investigated.

7.2 Major Conclusions

In light of the results presented in the dissertation, the major conclusions drawn from the study are summarized below:

- A relatively well agreement between the analytical and numerical solution of the magnetic circuit of the MR valve was observed. These solutions have been validated experimentally by measuring the average steady-state magnetic flux density along the annular gaps without MR fluid.

- The proposed optimally designed MRFD has a considerable enhancement in the dampers' performance (large damping force and dynamic range) compared with the initial design. Also, utilizing the GA combined with SQP can accurately capture the global optimum solution.
- Comparing the quasi-static modelling with experimental results reveals a very good agreement between simulation and experimental results for damper performance (dynamic range and damping force). Under applied current of 2 A, the simulation and experimental results revealed a large damping force of 6.61 kN and 7.41 kN, respectively, as well as a high dynamic range of 5.06, and 6.7, correspondingly, under piston velocity of 12.5 mm/s. The proposed MRFD has a large stroke of 180 mm compared with the previously developed MRFDs. With these specifications, the prototyped MRFD can be effectively employed for vibration control applications, particularly in off-road tracked vehicles and high payload applications.
- The response of the bypass MRFD with annular and radial fluid gaps has been modelled using the quasi-static model and the physic-dynamic model based on Bingham fluid behaviour. The mathematical formulation of the dynamic model has been derived for considering the unsteady fluid behaviour, friction effect and compressibility effect. The Laplace transform technique, the complex variable theory, the Cauchy residue theorem and the continuity equation have been utilized in the dynamic model.
- Both the quasi-static and dynamic models have been validated with measured data. Results revealed that the effect of unsteady fluid behaviour at small amplitudes and low frequencies is negligible. However, the unsteady fluid effect is becoming significant at large amplitudes and high frequencies. Subsequently, a considerable difference between the quasi-static and the unsteady fluid behaviour dynamic model was observed in this range of loading conditions.
- Results also showed that the quasi-static model and the dynamic model considering the fluid inertia and friction effect can effectively capture the damping force. However, these developed models were not able to predict the hysteresis force-velocity characteristic response of the MRFD.
- The proposed physic-based modified dynamic model based on the unsteady fluid behaviour, friction effect and compressibility effect can provide an accurate description of the non-linear hysteresis behaviour of the MRFDs in the early stage of design without experiment identification requirement.

- Results revealed that the fluid compressibility effect is the main source of the non-linear hysteresis behaviour of MRFDs, especially at a low range of loading conditions.
- Utilization of a bypass MR valve gains the advantages of ease of maintenance and modification in the design for further expanding the damper's performance without modifying the damper design. Thus, a comprehensive characterization of the MRFD with two MR bypass valves (initial and modified) has been carried out under a wide range of loading conditions and applied currents.
- Results showed that the friction force of the MRFD offered a relatively frequency-independent tendency, particularly at higher loading amplitude. Increasing displacement amplitude did not affect the peak friction force while showing an enhancement in the friction-based energy dissipation by increasing the amplitude of displacement.
- The peak force and area enclosed by force-displacement hysteresis loops of the MRFD increased with increasing applied current, loading frequency and displacement amplitude. Results also show that both the equivalent viscous damping, calculated via two approaches, as well as the dynamic range increased with increasing applied current while decreasing with increasing loading frequency and displacement amplitude.
- Results also were suggestive of a large controllable force of 5.54 kN and a good dynamic range of 2.3, simultaneously with the initial bypass MR valve. The bypass configuration of the MRFD allowed modification of the MR valve design in terms of physical parameters, which yielded dramatically higher dynamic indices, including a maximum dynamic range of 5.06 and a maximum damping force of 6.61 kN.
- The proposed VSVD-MRFD exhibits increasing peak forces and areas enclosed by force-displacement hysteresis loops as loading frequency, displacement amplitude, and applied current become higher. Additionally, results reveal that both the equivalent viscous damping and dynamic range increased as the applied current increased, whereas they decreased with increasing loading frequency and displacement amplitude.
- The observed decrement was more noticeable with increasing displacement amplitude. Further results demonstrate that the novel VSVD-MRFD has a high uniformity and repeatability performance and it has stiffness variability according to the loading and magnetic conditions.

- The equivalent stiffness significantly increases as the magnetic field increases and slightly increases with loading frequency while it has a remarkable reduction as the excitation displacement increases.
- High dynamic range and damping force have been obtained using the VSVD-MRFD. For instance, the damping force and the dynamic range at an excitation frequency of 1 Hz and displacement of 1 mm are equal to 7.2 kN and 4.5, respectively.

7.3 Publications

1. Abdalaziz M, Sedaghati R and Vatandoost H, (2022), Design Optimization and Experimental Evaluation of a Large Capacity Magnetorheological Damper with Annular and Radial Fluid Gaps, *Journal of Intelligent Material Systems and Structures* (Under review).
2. Abdalaziz M, Sedaghati R and Vatandoost H, (2022), Development of a New Dynamic Hysteresis Model for Annular-Radial Magnetorheological Dampers considering Fluid Inertia and Compressibility, *Journal of Sound and Vibration* (Under review).
3. Abdalaziz M, Vatandoost H, Sedaghati R and Rakheja S, (2022), Development and Experimental Characterization of a Large-Capacity Magnetorheological Damper with Annular-Radial Gaps, *Smart Mater. Struct.* 31 (11): 115021 (Published).
4. Abdalaziz M, Sedaghati R, Vatandoost H and Rakheja S, (2022), Design and Experimental Characterization of a Bypass Magnetorheological Damper Featuring Variable Damping and Stiffness, *Journal of Smart Materials and Structures* (Under review).

7.4 Recommendations for future works

The presented dissertation established a comprehensive framework for the development, design optimization, modelling and characterization of a VSVD-MRFD with an annular-radial bypass valve. The proposed damper has a large capacity of damping force, high dynamic range and large stroke to be able to attenuate vibration in heavy-duty automotive and high payload applications. Furthermore, the developed physic-dynamic models may serve as a significant design tool for designing and predicting the non-linear hysteresis behaviour of MRFDs in the early stages of design. More efforts, however, are desirable for the implementation of VSVD MRFD within the vehicle suspension system. Some of the desirable further studies are listed below:

- The effect of the Reynolds number on the performance of developed MRFD is a significant factor to be investigated.
- Developing a phenomenological model capable of predicting the performance and capturing the non-linear hysteresis of VSVD-MRFD over a wide range of loading conditions and applied magnetic field.
- Development of suitable control strategies to provide effective VSVD under unpredicted environmental conditions.
- There are many design factors, which have a significant influence on the VSVD design, such as the shapes of the MR valve, the types of the valve orifice (annular, radial, or combined), and the number of valve coils. Thus, it is of paramount importance to systematically investigate the effect of different geometrical and material design factors on the VSVD capability of the adaptive devices.
- Further efforts in integrating the VSVD-MRFD in tracked vehicles' suspension system model and evaluating its dynamic performance are required.
- The influence of the VSVD-MRFD designs on the whole-body vibration and reducing the transmitted vibration at low and high frequencies are also important issues that required to be explored.

REFERENCES

- [1] Griffin M J 1990 *Handbook of Human Vibration* (London: Academic Press)
- [2] Hulshof C and Veldhuijzen van Zanten B 1987 Whole-body vibration and low-back pain - A review of epidemiologic studies *Int. Arch. Occup. Environ. Health* **59** 205–20
- [3] Seidel H and Heide R 1986 Long-term effects of whole-body vibration: a critical survey of the literature *Int. Arch. Occup. Environ. Health* **58** 1–26
- [4] Burdorff A and Swuste P 1993 The effect of seat suspension on exposure to whole-body vibration of professional drivers *Ann. Occup. Hyg.* **37** 45–55
- [5] Cole D J 2001 Fundamental Issues in Suspension Design for Heavy Road Vehicles *Veh. Syst. Dyn.* **35** 319–60
- [6] Cebon D 1989 Vehicle-Generated Road Damage: A Review *Veh. Syst. Dyn.* **18** 107–50
- [7] Kirstein J C 2005 *Suspension system optimisation to reduce whole body vibration exposure on an articulated dump truck* (Matieland, South Africa: Stellenbosch : University of Stellenbosch)
- [8] Dindarloo S 2016 *Dynamic impact of ageing dump truck suspension systems on whole-body vibrations in high-impact shovel loading operations* (Rolla: Missouri University of Science and Technology)
- [9] Zhang M and Yong Z 2008 Fuzzy Control of Semi-Active Suspension Based on 7-DOF Tracked Vehicle *J. Beijing Inst. Technol.* **17** 5–9
- [10] Goncalves F D 2001 *Dynamic analysis of semi-active control techniques for vehicle applications* (Master's Thesis, Virginia Polytechnic Institute and State University, Blacksburg)
- [11] Faris W F, BenLahcene Z and Ihsan S I 2010 Assessment of different semi-active control strategies on the performance of off-road vehicle suspension systems *Int. J. Veh. Syst. Model. Test.* **5** 254–71
- [12] Lam A H-F and Liao W-H 2003 Semi-active control of automotive suspension systems with magneto-rheological dampers *Int. J. Veh. Des.* **33** 50–75

- [13] Butz T and Von Stryk O 2002 Modelling and simulation of electro- and magnetorheological fluid dampers *ZAMM Zeitschrift fur Angew. Math. und Mech.* **82** 3–20
- [14] Sun Q, Zhang L, Zhou J and Shi Q 2003 Experimental study of the semi-active control of building structures using the shaking table *Earthq. Eng. Struct. Dyn.* **32** 2353–76
- [15] Bai X-X, Wereley N M and Hu W 2015 Maximizing semi-active vibration isolation utilizing a magnetorheological damper with an inner bypass configuration *J. Appl. Phys.* **117** 17C711
- [16] Rashid M M, Aziz M A and Khan M R 2017 An experimental design of bypass magnetorheological (MR) damper *IOP Conference Series: Materials Science and Engineering* vol 260 (IOP Publishing) p 12021
- [17] Ferdek U and Łuczko J 2018 Nonlinear modeling and analysis of a shock absorber with a bypass *J. Theor. Appl. Mech.* **56**
- [18] Liu Y, Matsuhisa H, Utsuno H and Park J 2006 Vibration control by a variable damping and stiffness system with magnetorheological dampers *JSME Int. J.* **49**
- [19] Wang D H, Ai H X and Liao W H 2009 A magnetorheological valve with both annular and radial fluid flow resistance gaps *Smart Mater. Struct.* **18** 16
- [20] Zhu S, Tang L, Liu J, Tang X and Liu X 2016 A novel design of magnetorheological damper with annular radial channel *Shock Vib.* **2016**
- [21] Munyaneza O, Turabimana P, Oh J S, Choi S B and Sohn J W 2022 Design and Analysis of a Hybrid Annular Radial Magnetorheological Damper for Semi-Active In-Wheel Motor Suspension *Sensors* **22**
- [22] Dutta S and Choi S-B 2016 A nonlinear kinematic and dynamic modeling of Macpherson suspension systems with a magneto-rheological damper *Smart Mater. Struct.* **25** 035003
- [23] Choi S-B and Han. Y 2003 MR seat suspension for vibration control of a commercial vehicle *Int. J. Veh. Des.* **31** 202–15
- [24] Weber F and Distl H 2015 Amplitude and frequency independent cable damping of Sutong Bridge and Russky Bridge by magnetorheological dampers *Struct. Control Heal. Monit.* **22**

- [25] Hahm D, Ok S Y, Park W, Koh H M and Park K S 2013 Cost-effectiveness evaluation of an MR damper system based on a life-cycle cost concept *KSCE J. Civ. Eng.* **17** 145–54
- [26] Kamel A 2008 *theory of suspension sytem* (Cairo, Egypt: MTC)
- [27] Zhu X, Deng L, Sun S, Yan T, Yu J, Ma Z and Li W 2020 Development of a variable stiffness magnetorheological damper with self-powered generation capability *J. Intell. Mater. Syst. Struct.* **31** 209–19
- [28] Yu J, Dong X, Su X and Qi S 2022 Development and characterization of a novel rotary magnetorheological fluid damper with variable damping and stiffness *Mech. Syst. Signal Process.* **165**
- [29] Nguyen Q H and Choi S B 2009 Dynamic modeling of an electrorheological damper considering the unsteady behavior of electrorheological fluid flow *Smart Mater. Struct.* **18**
- [30] Yu M, Wang S, Fu J and Peng Y 2013 Unsteady analysis for oscillatory flow of magnetorheological fluid dampers based on Bingham plastic and Herschel-Bulkley models *J. Intell. Mater. Syst. Struct.* **24** 1067–78
- [31] Rabinow J 1948 The magnetic fluid clutch *Electr. Eng. -AIEE Trans.* **67** 1167–1167
- [32] Jacob R 1951 Magnetic fluid torque and force transmitting device *U.S. Pat. No. 2575360*
- [33] Corp L Industrial Suspension Systems <https://www.lord.com/products-and-solutions/active-vibration-control/industrial-suspension-systems>
- [34] Chooi W 2005 *Experimental characterisation of the properties of magnetorheological (MR) fluids and MR damper* (PhD dissertation, The University of Manchester)
- [35] Park J H and Park O O 2001 Electrorheology and magnetorheology *Korea-Australia Rheol. J.* **13** 13–7
- [36] Fang C, Yuan Z Bin, Chen L S, Qing W, Nan L and Hu K A 2005 The effect of the green additive guar gum on the properties of magnetorheological fluid *Smart Mater. Struct.* **14**
- [37] Truong D and Ahn. K 2012 MR Fluid Damper and Its Application to Force Sensorless

- [38] Ahamed R, Choi S B and Ferdaus M M 2018 A state of art on magneto-rheological materials and their potential applications *J. Intell. Mater. Syst. Struct.* **29** 2051–95
- [39] Yao G Z, Yap F F, Chen G, Li W H and Yeo S H 2002 MR damper and its application for semi-active control of vehicle suspension system *Mechatronics* **12** 963–73
- [40] Choi S-B, And N and Lee B-K 2001 Vibration Control of a MR Seat Damper for Commercial Vehicles
- [41] McManus S J, St. Clair K A, Boileau P É, Boutin J and Rakheja S 2002 Evaluation of vibration and shock attenuation performance of a suspension seat with a semi-active magnetorheological fluid damper *J. Sound Vib.* **253** 313–27
- [42] Spencer B F, Dyke S J, Sain M K and Carlson J D 1997 Phenomenological Model for Magnetorheological Dampers *J. Eng. Mech.* **123** 230–8
- [43] Yang G 2002 *Large-scale magnetorheological fluid damper for vibration mitigation: modeling, testing and control* (University of Notre Dame)
- [44] Liu Y, Gordaninejad F, Evrensel C, Wang X and Hitchcock G 2005 Comparative Study on Vibration Control of a Scaled Bridge Using Fail-Safe Magneto-Rheological Fluid Dampers *J. Struct. Eng.* **13** 743–51
- [45] Ahmadian M and Poynor J C 2001 An evaluation of magneto rheological dampers for controlling gun recoil dynamics *Shock Vib.* **8** 147–55
- [46] Batterbee D C, Sims N D, Stanway R and Wolejsza Z 2007 Magnetorheological landing gear: 1. A design methodology *Smart Mater. Struct.* **16** 2429
- [47] Choi Y-T, Wereley N M and Jeon Y-S 2005 Semi-Active Vibration Isolation Using Magnetorheological Isolators *J. Aircr.* **42** 1244–51
- [48] Gołdasz J and Sapiński B 2015 Insight into Magnetorheological Shock Absorbers *Switz. Springer Int. Publ.* 1–224
- [49] Hong S-R and Choi S-B 2005 Vibration Control of a Structural System Using Magneto-Rheological Fluid Mount *J. Intell. Mater. Syst. Struct.* **16** 931–6

- [50] Ahn Y K, Ahmadian M, Morishita S and Kong Ahn Y 1999 On the Design and Development of a Magneto-Rheological Mount *Veh. Syst. Dyn.* **32** 199–216
- [51] Choi S and Han Y M 2012 *Magnetorheological fluid technology: applications in vehicle systems* (London, Newyork: Taylor & Francis Group, CRC press)
- [52] Li W H and Du H 2003 Design and Experimental Evaluation of a Magnetorheological Brake *Int J Adv Manuf Technol* **21** 508–15
- [53] Karakoc K, Park E J and Suleman A 2008 Design considerations for an automotive magnetorheological brake *Mechatronics* **18** 434–47
- [54] Neelakantan V A and Washington G N 2005 Modeling and Reduction of Centrifuging in Magnetorheological (MR) Transmission Clutches for Automotive Applications *J. Intell. Mater. Syst. Struct.* **9** 703–11
- [55] Choi S B, Song H J, Lee H H, Lim S C, Kim J H and Choi H J 2003 Vibration control of a passénger vehicle featuring magnetorheological engine mounts *Int. J. Veh. Des.* **33** 2–16
- [56] Bossis G, Lacis S, Meunier A and Volkova O 2002 Magnetorheological fluids *J. Magn. Magn. Mater.* **252** 224–8
- [57] Goncalves F and Carlson J 2009 An alternate operation mode for MR fluids—magnetic gradient pinch *J. Phys. Conf. Ser.* **149** 012050
- [58] Gołdasz J and Sapiński B 2017 Magnetostatic analysis of a pinch mode magnetorheological valve *acta Mech. Autom.* **11**
- [59] Tao and Rongjia 2019 Reducing Blood Viscosity and Suppressing Turbulence with Magnetic Field to Prevent Heart Attack and Stroke *APS* **2019** F29.012
- [60] Meyers M A and Chawla K K 2008 *Mechanical behavior of materials* (New York: Cambridge University Press)
- [61] Gurubasavaraju T M, Kumar H and Mahalingam A 2018 An approach for characterizing twin-tube shear-mode magnetorheological damper through coupled FE and CFD analysis *J. Brazilian Soc. Mech. Sci. Eng.* **40**
- [62] Syrakos A, Dimakopoulos Y and Tsamopoulos J 2018 Theoretical study of the flow in a

- fluid damper containing high viscosity silicone oil: Effects of shear-thinning and viscoelasticity *Phys. Fluids* **30**
- [63] Syrakos A, Dimakopoulos Y, Georgiou G C and Tsamopoulos J 2016 Viscoplastic flow in an extrusion damper *J. Nonnewton. Fluid Mech.* **232** 102–24
- [64] Bingham E 1922 *Fluidity and plasticity* (New York: McGraw-Hill Book Company, Inc)
- [65] Herschel V 1926 Consistency of measurements rubber-benzene solutions *Kolloid-Zeit* **39** 291–300
- [66] Carlson J D and Jolly M R 2000 MR fluid, foam and elastomer devices *Mechatronics* **10** 555–69
- [67] Phillips R 1969 *Engineering applications of fluids with a variable yield stress* (Berkeley: University of California)
- [68] Ashour O, Rogers C A and Kordonsky W 1996 Magnetorheological fluids: Materials, characterization, and devices *J. Intell. Mater. Syst. Struct.* **7** 123–30
- [69] Fujitani H, Sodeyama H, Hata K, Komatsu Y, Iwata N, Sunakoda K and Soda S 2002 Dynamic performance evaluation of 200kN magnetorheological damper *Tech. Note Natl. Inst. L. Infrastruct. Manag.* **41** 349–56
- [70] Automotive Suspension Systems | LORD Corp <https://www.lord.com/products-and-solutions/active-vibration-control/automotive-suspension-systems>
- [71] Smart Structures and Systems Laboratory http://www.ssslab.com/ehtml/3_2.php?ckattempt=3
- [72] Li W H, Du H and Guo N Q 2003 Design and testing of an MR steering damper for motorcycles *Int. J. Adv. Manuf. Technol.* **22** 288–94
- [73] Ha S H, Seong M S and Choi S B 2013 Design and vibration control of military vehicle suspension system using magnetorheological damper and disc spring *Smart Mater. Struct.* **22** 065006
- [74] Simon D and Ahmadian M 2001 Vehicle evaluation of the performance of magneto rheological dampers for heavy truck suspensions *J. Vib. Acoust. Trans. ASME* **123** 365–75

- [75] Bai X X, Hu W and Wereley N M 2013 Magnetorheological damper utilizing an inner bypass for ground vehicle suspensions *IEEE Trans. Magn.* **49** 3422–5
- [76] Shutto S and Toscano J 2005 Magnetorheological (Mr) Fluid and Its Applications *Proc. JFPS Int. Symp. Fluid Power* **2005** 590–4
- [77] Chae H D and Choi S B 2015 A new vibration isolation bed stage with magnetorheological dampers for ambulance vehicles *Smart Mater. Struct.* **24** 017001
- [78] Kim H C, Shin Y J, You W, Jung K C, Oh J S and Choi S B 2017 A ride quality evaluation of a semi-active railway vehicle suspension system with MR damper: Railway field tests *Proc. Inst. Mech. Eng. Part F J. Rail Rapid Transit* **231** 306–16
- [79] Sun S S, Ning D H, Yang J, Du H, Zhang S W and Li W H 2016 A seat suspension with a rotary magnetorheological damper for heavy duty vehicles *Smart Mater. Struct.* **25** 105032
- [80] Hiemenz G J, Hu W and Wereley N M 2008 Semi-active magnetorheological helicopter crew seat suspension for vibration isolation *J. Aircr.* **45** 945–53
- [81] Liu S C, Tomizuka M and Ulsoy G 2006 Strategic issues in sensors and smart structures *Struct. Control Heal. Monit.* **13** 946–57
- [82] Park J, Yoon G H, Kang J W and Choi S B 2016 Design and control of a prosthetic leg for above-knee amputees operated in semi-active and active modes *Smart Mater. Struct.* **25** 085009
- [83] Carlson. J and Sproston J 2000 Controllable fluids in 2000-status of ER and MR fluid technology *Proc. 7th Int. Conf. New Actuators* pp 126–30
- [84] Spelta C, Previdi F, Savaresi S M, Fraternali G and Gaudio N 2009 Control of magnetorheological dampers for vibration reduction in a washing machine *Mechatronics* **19** 410–21
- [85] Singh H J, Hu W, Wereley N M and Glass W 2014 Experimental validation of a magnetorheological energy absorber design optimized for shock and impact loads *Smart Mater. Struct.* **23**
- [86] Han C, Kang B H, Choi S B, Tak J M and Hwang J H 2019 Control of landing efficiency

- of an aircraft landing gear system with magnetorheological dampers *J. Aircr.* **56** 1980–6
- [87] Hu H, Jiang X, Wang J and Li Y 2012 Design, modeling, and controlling of a large-scale magnetorheological shock absorber under high impact load *J. Intell. Mater. Syst. Struct.* **23** 635–45
- [88] Li Z C and Wang J 2012 A gun recoil system employing a magnetorheological fluid damper *Smart Mater. Struct.* **21** 105003–13
- [89] Hitchcock G H, Wang X and Gordaninejad F 2007 A New Bypass Magnetorheological Fluid Damper *J. Vib. Acoust. Trans. ASME* **129**
- [90] Stanway R, Sproston J L and Stevens N G 1987 Non-linear modelling of an electro-rheological vibration damper *J. Electrostat.* **20** 167–84
- [91] Parlak Z, Engin T and Şahin I 2013 Optimal magnetorheological damper configuration using the taguchi experimental design method *J. Mech. Des. Trans. ASME* **135** 1–9
- [92] Avinash B, Sundar S S and Gangadharan K V 2014 Experimental Study of Damping Characteristics of Air, Silicon Oil, Magneto Rheological Fluid on Twin Tube Damper *Procedia Mater. Sci.* **5** 2258–62
- [93] Wang Q, Ahmadian M and Chen Z 2014 A novel double-piston magnetorheological damper for space truss structures vibration suppression *Shock Vib.* **2014**
- [94] Fatah A Y A, Mazlan S A, Koga T, Zamzuri H, Zeinali M and Imaduddin F 2015 A review of design and modeling of magnetorheological valve *Int. J. Mod. Phys. B* **29**
- [95] Gordaninejad F and Kelso S 2001 Fail-safe magneto-rheological fluid dampers for off-highway, high-payload vehicles *J. Intell. Mater.* **11** 395–406
- [96] Boese H and Ehrlich J 2010 Performance of magnetorheological fluids in a novel damper with excellent fail-safe behavior *J. Intell. Mater. Syst.* **21** 1537–42
- [97] Nguyen Q H, Han Y M, Choi S B and Wereley N M 2007 Geometry optimization of MR valves constrained in a specific volume using the finite element method *Smart Mater. Struct.* **16** 2242–52
- [98] Sahin H, Gordaninejad F, Wang X and Liu Y 2012 Response time of magnetorheological

- fluids and magnetorheological valves under various flow conditions *J. Intell. Mater. Syst. Struct.* **23** 949–57
- [99] Gordaninejad F, Wang X, Ruan S, Gordaninejad F, Wang ; X, Hitchcock ; G, Bangrakulur ; K, Ruan ; S and Siino M 2010 Modular high-force seismic magneto-rheological fluid damper *J. Struct. Eng.*
- [100] Ai H X, Wang D H and Liao W H 2016 Design and Modeling of a Magnetorheological Valve with Both Annular and Radial Flow Paths *J. Intell. Mater. Syst. Struct.* **17** 327–34
- [101] Imaduddin F, Mazlan S A and Zamzuri H 2013 A design and modelling review of rotary magnetorheological damper *Mater. Des.* **51** 575–91
- [102] Wang D H and Liao W H 2009 Semi-active suspension systems for railway vehicles using magnetorheological dampers. Part I: system integration and modelling *Veh. Syst. Dyn.* **47** 1305–25
- [103] Yoon D-S, Kim G-W and Choi S-B 2021 Response time of magnetorheological dampers to current inputs in a semi-active suspension system: Modeling, control and sensitivity analysis *Mech. Syst. Signal Process.* **146** 106999
- [104] Zhang H H, Liao C R, Yu M and Huang S L 2007 A study of an inner bypass magneto-rheological damper with magnetic bias *Smart Mater. Struct.* **16** N40
- [105] Idris M H, Imaduddin F, Ubaidillah, Mazlan S A and Choi S B 2020 A concentric design of a bypass magnetorheological fluid damper with a serpentine flux valve *Actuators* **9**
- [106] Unsal M 2006 *Semi-active vibration control of a parallel platform mechanism using magnetorheological damping* (University of Florida)
- [107] Dogruoz M B, Wang E L, Gordaninejad F and Stipanovic A J 2003 Augmenting heat transfer from fail-safe magneto-rheological fluid dampers using fins *J. Intell. Mater. Syst. Struct.* **14** 79–86
- [108] Hitchcock G H, Wang X and Gordaninejad F 2007 A new bypass magnetorheological fluid damper *J. Vib. Acoust. Trans. ASME* **129** 641–7
- [109] Imaduddin F, Mazlan S A, Zamzuri H and Abdul Rahman M A 2014 Bypass rotary

- magnetorheological damper for automotive applications *Applied Mechanics and Materials* vol 663 (Trans Tech Publ) pp 685–9
- [110] Aziz M A and Aminossadati S M 2021 State-of-the-art developments of bypass Magnetorheological (MR) dampers: A review *Korea-Australia Rheol. J.* **33** 225–49
- [111] Nam Y-J and Park M-K 2007 Performance evaluation of two different bypass-type MR shock dampers *J. Intell. Mater. Syst. Struct.* **18** 707–17
- [112] Kim B-G, Yoon D-S, Kim G-W, Choi S-B, Tan A S and Sattel T 2020 Design of a novel magnetorheological damper adaptable to low and high stroke velocity of vehicle suspension system *Appl. Sci.* **10** 5586
- [113] Li G and Yang Z-B 2020 Modelling and analysis of a magnetorheological damper with nonmagnetized passages in piston and minor losses *Shock Vib.* **2020**
- [114] Zhu X, Jing X and Cheng L 2012 Magnetorheological fluid dampers: a review on structure design and analysis *J. Intell. Mater. Syst. Struct.* **23** 839–73
- [115] Ruan X, Xuan S, Zhao J, Bian H and Gong X 2020 Mechanical performance of a novel magnetorheological fluid damper based on squeeze-valve bi-mode of MRF *Smart Mater. Struct.* **29** 55018
- [116] Nguyen Q H and Choi S B 2009 Optimal design of a vehicle magnetorheological damper considering the damping force and dynamic range *Smart Mater. Struct.* **18** 015013
- [117] Nguyen Q H and Choi S B 2009 Optimal design of MR shock absorber and application to vehicle suspension *Smart Mater. Struct.* **18** 035012
- [118] Nguyen Q H, Choi S B, Lee Y S and Han M S 2009 An analytical method for optimal design of MR valve structures *Smart Mater. Struct.* **18** 095032
- [119] Yang L, Duan F and Eriksson A 2008 Analysis of the optimal design strategy of a magnetorheological smart structure *Smart Mater. Struct.* **17** 015047
- [120] Rosenfeld N C and Wereley N M 2004 Volume-constrained optimization of magnetorheological and electrorheological valves and dampers *Smart Mater. Struct.* **13** 1303–13

- [121] Gavin H, Hoagg J and Dobossy M 2001 Optimal design of MR dampers *Proc. U.S.-Japan Work. Smart Struct. Improv. Seism. Perform. Urban Reg.* 225–36
- [122] Nguyen Q-H and Choi S-B 2009 A new approach for dynamic modeling of an electrorheological damper using a lumped parameter method *Smart Mater. Struct.* **18** 11
- [123] Hong S R, John S, Wereley N M, Choi Y T and Choi S B 2008 A unifying perspective on the quasi-steady analysis of magnetorheological dampers *J. Intell. Mater. Syst. Struct.* **19** 959–76
- [124] Chooi W and Olutunde O 2009 Mathematical modeling, analysis, and design of magnetorheological (MR) dampers *J. Vib. Acoust. Trans. ASME* **131** 0610021–06100210
- [125] Wang X and Gordaninejad F 2000 Study of field-controllable, electro- and magnetorheological fluid dampers in flow mode using Herschel-Bulkley theory Xiaojie *Smart Struct. Mater. 2000 Damping Isol.* **3989** 232–43
- [126] Gavin H P, Hanson R D and Filisko F E 1996 Electrorheological dampers, part II: testing and modeling *Trans. ASME* **63**
- [127] Kamath G and Wereley N 1997 A nonlinear viscoelastic-plastic model for electrorheological fluids *Smart Mater. Struct.* **6** 351–9
- [128] Lee D and Wereley N 2000 Analysis of electro-and magneto-rheological flow mode dampers using Herschel-Bulkley model *Smart Struct. Mater. Beach, CA, United States*
- [129] Ahmadian M, Norris J A and Ahmadian M 2008 Experimental analysis of magnetorheological dampers when subjected to impact and shock loading *Commun. Nonlinear Sci. Numer. Simul.* **13** 1978–85
- [130] Wang D H and Liao W H 2011 Magnetorheological fluid dampers: a review of parametric modelling *Smart Mater. Struct.* **20** 23001
- [131] Choi S B, Lee S K and Park Y P 2001 A hysteresis model for the field-dependent damping force of a magnetorheological damper *J. Sound Vib.* **245** 375–83
- [132] Stanway R, Sproston J L and Stevens N G 1985 Non-Linear Identification of an Electro-Rheological Vibration Damper *IFAC Proc. Vol.* **18** 195–200

- [133] Gamota D and Filisko F 1991 Dynamic mechanical studies of electrorheological materials: moderate frequencies *J. Rheol. (N. Y. N. Y.)*. **35** 399
- [134] Bouc R 1971 Modèle mathématique d'hystérésis *Acta Acust. united with Acust.* **24** 16–25
- [135] Wen Y K 1976 Method for random vibration of hysteretic systems *J. Eng. Mech. Div.* **102** 249–63
- [136] Dominguez A, Sedaghati R and Stiharu I 2006 A new dynamic hysteresis model for magnetorheological dampers *Smart Mater. Struct.* **15** 1179
- [137] Kim K J, Lee C W and Koo J H 2008 Design and modeling of semi-active squeeze film dampers using magneto-rheological fluids *Smart Mater. Struct.* **17**
- [138] Jin G, Sain M K, Pham K D, Spencer J and Ramallo J C 2001 Modeling MR-dampers: a nonlinear blackbox approach *Proc. Am. Control Conf.* **1** 429–34
- [139] Yijian H, Xiaomei L and Bingsan C 2006 Autoregressive trispectral characteristics of magnetorheological damping device *IEEE Int. Conf. Intell. Robot. Syst.* 5878–82
- [140] Koga K and Sano A 2006 Query-based approach to prediction of MR damper force with application to vibration control *Proc. Am. Control Conf.* **2006** 3259–65
- [141] Cao M, Wang K W and Lee K Y 2008 Scalable and invertible PMNN model for MagnetoRheological fluid dampers *JVC/Journal Vib. Control* **14** 731–51
- [142] Jin G, Sain M K and Spencer B F 2005 Nonlinear blackbox modeling of MR-dampers for civil structural control *IEEE Trans. Control Syst. Technol.* **13** 345–55
- [143] Kim H S and Roschke P N 2006 Fuzzy control of base-isolation system using multi-objective genetic algorithm *Comput. Civ. Infrastruct. Eng.* **21** 436–49
- [144] Du X, Zhang Y, Li J, Liao C, Zhang H, Xie L, Gan B and Lu J 2022 Unsteady and hysteretic behavior of a magnetorheological fluid damper: Modeling, modification, and experimental verification *J. Intell. Mater. Syst. Struct.* 1045389X221111555
- [145] Sun S, Yang J, Li W, Deng H, Du H and Alici G 2015 Development of a novel variable stiffness and damping magnetorheological fluid damper *Smart Mater. Struct.* **24** 085021

- [146] Liu Y, Matsuhisa H, Utsuno H and Park J G 2005 Vibration isolation by a variable stiffness and damping system *JSME Int. J. Ser. C Mech. Syst. Mach. Elem. Manuf.* **49** 305–10
- [147] Liu Y, Matsuhisa H, Utsuno H and Park J G 2006 Vibration control by a variable damping and stiffness system with magnetorheological dampers *JSME Int. Journal, Ser. C Mech. Syst. Mach. Elem. Manuf.* **49** 411–7
- [148] Liu Y, Matsuhisa H and Utsuno H 2008 Semi-active vibration isolation system with variable stiffness and damping control *J. Sound Vib.* **313** 16–28
- [149] Sun S, Tang X, Yang J, Ning D, Du H, Zhang S and Li W 2019 A New Generation of Magnetorheological Vehicle Suspension System With Tunable Stiffness and Damping Characteristics *IEEE Trans. Ind. Informatics* **15** 4696–708
- [150] Deng H, Deng J, Yue R, Han G, Zhang J, Ma M and Zhong X 2019 Design and verification of a seat suspension with variable stiffness and damping *Smart Mater. Struct.* **28** 065015
- [151] Ning D, Du H, Sun S, Zheng M, Li W, Zhang N and Jia Z 2020 An Electromagnetic Variable Stiffness Device for Semiactive Seat Suspension Vibration Control *IEEE Trans. Ind. Electron.* **67** 6773–84
- [152] Yang J, Du H, Li W, Li Y, Li J, Sun S and Deng H 2013 Experimental study and modeling of a novel magnetorheological elastomer isolator *Smart Mater. Struct.* **22** 117001
- [153] Li J F and Gong X L 2008 Dynamic damping property of magnetorheological elastomer *J. Cent. South Univ. Technol. (English Ed.)* **15** 261–5
- [154] Chen L, Gong X and Li W 2008 Damping of magnetorheological elastomers *Chinese J. Chem. Phys.* **21**
- [155] Youn I and Hać A 1995 Semi-active suspensions with adaptive capability *J. Sound Vib.* **180** 475–92
- [156] Zhu X, Jing X and Cheng L 2011 A magnetorheological fluid embedded pneumatic vibration isolator allowing independently adjustable stiffness and damping *Smart Mater. Struct.* **20** 085025
- [157] Li W H, Wang X Y, Zhang X Z and Zhou Y 2009 Development and analysis of a variable

- stiffness damper using an MR bladder *Smart Mater. Struct.* **18** 074007
- [158] Zhang X, Wang X and Li W 2009 Variable stiffness and damping MR isolator *J. Phys. Conf. Ser. 11th Conf. Electrorheological Fluids Magnetorheol. Suspens.* **149** 012088
- [159] Sun S, Deng H, Du H, Li W, Yang J, Liu G, Alici G and Yan T 2015 A Compact Variable Stiffness and Damping Shock Absorber for Vehicle Suspension *IEEE/ASME Trans. Mechatronics* **20** 2621–9
- [160] Greiner-Petter C, Tan A S and Sattel T 2014 A semi-active magnetorheological fluid mechanism with variable stiffness and damping *Smart Mater. Struct.* **23** 115008
- [161] Manjeet K and Sujatha C 2019 Magnetorheological valves based on Herschel–Bulkley fluid model: modelling, magnetostatic analysis and geometric optimization *Smart Mater. Struct.* **28** 115008
- [162] Hu G, Liao M and Li W 2017 Analysis of a compact annular-radial-orifice flow magnetorheological valve and evaluation of its performance *J. Intell. Mater. Syst. Struct.* **28** 1322–33
- [163] Hu G, Zhang J, Liao M and Ding R 2018 Effect of radial resistance gap on the pressure drop of a compact annular-radial-orifice flow magnetorheological valve *J. Beijing Inst. Technol.* **27** 535–546
- [164] Ai H X, Wang D H and Liao W H 2006 Design and modeling of a magnetorheological valve with both annular and radial flow paths *J. Intell. Mater. Syst. Struct.* **17** 327–34
- [165] Parlak Z and Engin T 2012 Time-dependent CFD and quasi-static analysis of magnetorheological fluid dampers with experimental validation *Int. J. Mech. Sci.* **64** 22–31
- [166] Nguyen Q H, Choi S B and Wereley N M 2008 Optimal design of magnetorheological valves via a finite element method considering control energy and a time constant *Smart Mater. Struct.* **17** 025024
- [167] Abouobaia E, Sedaghati R and Bhat R 2020 Design optimization and experimental characterization of a rotary magneto-rheological fluid damper to control torsional vibration *Smart Mater. Struct.* **29** 045010

- [168] Hadadian A, Sedaghati R and Esmailzadeh E 2014 Design optimization of magnetorheological fluid valves using response surface method *J. Intell. Mater. Syst. Struct.* **25** 1352–71
- [169] Bai X-X, Wang D-H and Fu H 2013 Principle, modeling, and testing of an annular-radial-duct magnetorheological damper *Sensors Actuators A Phys.* **201** 302–9
- [170] Ichwan B, Mazlan S A, Imaduddin F, Ubaidillah, Koga T and Idris M H 2016 Development of a modular MR valve using meandering flow path structure *Smart Mater. Struct.* **25**
- [171] Hu G, Long M, Yu L and Li W 2014 Design and performance evaluation of a novel magnetorheological valve with a tunable resistance gap *Smart Mater. Struct.* **23** 127001
- [172] Imaduddin F, Mazlan S A, Zamzuri H and Yazid I I M 2015 Design and performance analysis of a compact magnetorheological valve with multiple annular and radial gaps *J. Intell. Mater. Syst. Struct.* **26** 1038–49
- [173] Dhir A 1993 *Ride dynamics of high mobility wheeled/tracked off-road vehicles : computer simulation with field validation* (PhD thesis, Concordia university (Canada))
- [174] Sutey M W K 1992 *Light Infantry, Augmentation, and the M113A3 Armored Personnel Carrier A Step in the Direction of Versatility* vol 26
- [175] Lord C 2011 MRF-132DG Magneto-Rheological Fluid *Lord Prod. Sel. Guid. lord Magnetorheol. fluids* **54** 11
- [176] Hemmatian M, Sedaghati R and Rakheja S 2020 Temperature dependency of magnetorheological fluids' properties under varying strain amplitude and rate *J. Magn. Mater.* **498** 166109
- [177] Shamieh H and Sedaghati R 2017 Multi-objective design optimization and control of magnetorheological fluid brakes for automotive applications *Smart Mater. Struct.* **26** 125012
- [178] Baltzis K B 2010 The finite element method magnetics (FEMM) freeware package: May it serve as an educational tool in teaching electromagnetics? *Educ. Inf. Technol.* **15** 19–36
- [179] Salloom M Y and Samad Z 2011 Finite element modeling and simulation of proposed

- design magneto-rheological valve *Int. J. Adv. Manuf. Technol.* **54** 421–9
- [180] Saleh M, Sedaghati R and Bhat R 2019 Design optimization of a bi-fold MR energy absorber subjected to impact loading for skid landing gear applications *Smart Mater. Struct.* **28** 035031
- [181] Phillips R W 1969 *Engineering applications of fluids with a variable yield stress* (Berkeley: University of California)
- [182] Gavin H P, Hanson R D and Filisko F E 1996 Electrorheological dampers, part i: Analysis and design *J. Appl. Mech. Trans. ASME* **63** 669–75
- [183] Wereley N M and Pang L 1998 Nondimensional analysis of semi-active electrorheological and magnetorheological dampers using approximate parallel plate models *Smart Mater. Struct.* **7** 732–43
- [184] Bouc R 1971 Mathematical Models for Hysteresis Author (s): Jack W . Macki , Paolo Nistri , Pietro Zecca Published by : Society for Industrial and Applied Mathematics Stable URL : <http://www.jstor.org/stable/2132527> *Acta Acust. united with Acust.* **24** 16-25(10)
- [185] Kwok N M, Ha Q P, Nguyen M T, Li J and Samali B 2007 Bouc-Wen model parameter identification for a MR fluid damper using computationally efficient GA *ISA Trans.* **46** 167–79
- [186] Dominguez A, Sedaghati R and Stiharu I 2004 Modelling the hysteresis phenomenon of magnetorheological dampers *Smart Mater. Struct.* **13** 1351–61
- [187] Ahmadian M and Norris J A 2008 Experimental analysis of magnetorheological dampers when subjected to impact and shock loading *Commun. Nonlinear Sci. Numer. Simul.* **13** 1978–85
- [188] Kim H-C, Oh J-S and Choi S-B 2014 The field-dependent shock profiles of a magnetorheological damper due to high impact: an experimental investigation *Smart Mater. Struct.* **24** 25008
- [189] Elsaady W, Oyadiji S O and Nasser A 2020 A one-way coupled numerical magnetic field and CFD simulation of viscoplastic compressible fluids in MR dampers *Int. J. Mech. Sci.*

- [190] Guo P, Guan X and Ou J 2014 Physical modeling and design method of the hysteretic behavior of magnetorheological dampers *J. Intell. Mater. Syst. Struct.* **25** 680–96
- [191] Guo P, Xie J, Dong X and Huang Y 2019 A two-dimensional axisymmetric finite element analysis of coupled inertial-viscous-frictional-elastic transients in magnetorheological dampers using the compressible Herschel-Bulkley fluid model *Front. Mater.* **6** 293
- [192] Xu Z-D, Jia D-H and Zhang X-C 2012 Performance tests and mathematical model considering magnetic saturation for magnetorheological damper *J. Intell. Mater. Syst. Struct.* **23** 1331–49
- [193] Bhatnagar R M 2013 Transient effect modelling of magnetorheological fluid-based damper at low speed and its comparison with the existing magnetorheological damper models *J. Intell. Mater. Syst. Struct.* **24** 1506–23
- [194] Li W H, Yao G Z, Chen G, Yeo S H and Yap F F 2000 Testing and steady state modeling of a linear MR damper under sinusoidal loading *Smart Mater. Struct.* **9** 95–102
- [195] Zheng P, Hou B and Zou M 2022 Magnetorheological Fluid of High-Speed Unsteady Flow in a Narrow-Long Gap: An Unsteady Numerical Model and Analysis *Mathematics* **10** 2493
- [196] Chen C I, Chen C K and Yang Y T 2004 Unsteady unidirectional flow of Bingham fluid between parallel plates with different given volume flow rate conditions *Appl. Math. Model.* **28** 697–709
- [197] Mao M, Hu W, Choi Y-T, Wereley N M, Browne A L, Ulicny J and Johnson N 2013 Nonlinear modeling of magnetorheological energy absorbers under impact conditions *Smart Mater. Struct.* **22** 115015
- [198] Çeşmeci Ş and Engin T 2010 Modeling and testing of a field-controllable magnetorheological fluid damper *Int. J. Mech. Sci.* **52** 1036–46
- [199] Chooi W W and Oyadiji S O 2008 Design, modelling and testing of magnetorheological (MR) dampers using analytical flow solutions *Comput. Struct.* **86** 473–82
- [200] Hong S R, Choi S B, Choi Y T and Wereley N M 2005 Non-dimensional analysis and

- design of a magnetorheological damper *J. Sound Vib.* **288** 847–63
- [201] Khan M, Suresh A and Ramaiah N 2012 Investigation on the performance of MR damper with various piston configurations *Int. J. Sci. Res. Publ.* **2** 28–34
- [202] Fathima S, Muthalif A G A and Raisuddin Khan M 2014 Investigation of annular gap size for optimizing the dynamic range of MR damper using comsol multiphysics software *Appl. Mech. Mater.* **606** 187–92
- [203] Hu G, Yi F, Tong W and Yu L 2020 Development and Evaluation of a MR Damper with Enhanced Effective Gap Lengths *IEEE Access* **8** 156347–61
- [204] Berasategui J, Elejabarrieta M J and Bou-Ali M M 2014 Characterization analysis of a MR damper *Smart Mater. Struct.* **23**
- [205] Costa E and Branco P J C 2009 Continuum electromechanics of a magnetorheological damper including the friction force effects between the MR fluid and device walls: analytical modelling and experimental validation *Sensors Actuators A Phys.* **155** 82–8
- [206] Arpaci V 1966 Conduction Heat Transfer *Reading, MA, Univ. Michigan, Addison-Wesley, USA* **237**
- [207] Kundu P K, Cohen I M and Dowling D R 2015 *Fluid mechanics* (Academic press)
- [208] Elsaady W M A A 2020 Time-Dependent Computational Fluid Dynamics and Quasi-static Analysis of Smart Dampers
- [209] Pang L, Kamath G M and Wereley N M 1998 Analysis and testing of a linear stroke magnetorheological damper *Collect. Tech. Pap. - AIAA/ASME/ASCE/AHS/ASC Struct. Struct. Dyn. Mater. Conf.* **4** 2841–56
- [210] Dimock G A, Yoo J H and Wereley N M 2002 Quasi-steady Bingham biplastic analysis of electrorheological and magnetorheological dampers *J. Intell. Mater. Syst. Struct.* **13** 549–59
- [211] Zhang Z and Peng Y 2020 Dynamic Physical Model for MR Damper Considering Chain Deflection in Preyield Stage *J. Eng. Mech.* **146** 4020122
- [212] Nordin N H D, Muthalif A G A, Razali M K M, Ali A and Salem A M 2022 Development

- and implementation of energy-efficient Magnetorheological Fluid bypass damper for prosthetics limbs using a fuzzy-logic controller *IEEE Access* **10** 18978–87
- [213] Yuan X, Tian T, Ling H, Qiu T and He H 2019 A review on structural development of magnetorheological fluid damper *Shock Vib.* **2019**
- [214] Zheng J, Li Z, Koo J and Wang J 2014 Magnetic circuit design and multiphysics analysis of a novel MR damper for applications under high velocity *Adv. Mech. Eng.* **6** 402501
- [215] Elsaady W, Oyadiji S O and Nasser A 2020 Magnetic circuit analysis and fluid flow modeling of an MR damper with enhanced magnetic characteristics *IEEE Trans. Magn.* **56** 1–20
- [216] Nguyen Q H, Han Y M, Choi S B and Wereley N M 2007 Geometry optimization of MR valves constrained in a specific volume using the finiteelement method *Smart Mater. Struct.* **16** 2242
- [217] Sassi S, Cherif K, Mezghani L, Thomas M and Kotrane A 2005 An innovative magnetorheological damper for automotive suspension: from design to experimental characterization *Smart Mater. Struct.* **14** 811
- [218] Jiang R, Rui X, Zhu W, Yang F, Zhang Y and Gu J 2022 Design of multi-channel bypass magnetorheological damper with three working modes *Int. J. Mech. Mater. Des.* **18** 155–67
- [219] Kordonsky W 1993 Elements and Devices Based on Magnetorheological Effect *J. Intell. Mater. Syst. Struct.* **4** 65–9
- [220] Daniel Cruze, Gladston H, Loganathan S, Dharmaraj T and Solomon S M 2021 Study on Magnatec oil-based MR fluid and its damping efficiency using MR damper with various annular gap configurations *Energy, Ecol. Environ.* **6** 44–54
- [221] Wang X and Gordaninejad F 1999 Flow analysis of field-controllable, electro- and magneto-rheological fluids using Herschel-Bulkley model *J. Intell. Mater. Syst. Struct.* **10** 601–8
- [222] Wang M, Chen Z and Wereley N M 2019 Magnetorheological damper design to improve

- vibration mitigation under a volume constraint *Smart Mater. Struct.* **28**
- [223] Liao C R, Zhao D X, Xie L and Liu Q 2012 A design methodology for a magnetorheological fluid damper based on a multi-stage radial flow mode *Smart Mater. Struct.* **21**
- [224] Maharani E T, Ubaidillah U, Imaduddin F, Wibowo W, Utami D and Mazlan S A 2021 A mathematical modelling and experimental study of annular-radial type magnetorheological damper *Int. J. Appl. Electromagn. Mech.* **66** 543–60
- [225] Bai X X, Wang D H and Fu H 2013 Principle, modeling, and testing of an annular-radial-duct magnetorheological damper *Sensors Actuators, A Phys.* **201** 302–9
- [226] Munyaneza O, Turabimana P, Oh J and Choi S 2022 Design and Analysis of a Hybrid Annular Radial Magnetorheological Damper for Semi-Active In-Wheel Motor Suspension *Sensors*
- [227] Hu W, Cook E and Wereley N 2007 Energy absorber using a magnetorheological bypass valve filled with ferromagnetic beads *IEEE Trans. Magn.* **43** 2695
- [228] Lee T-H and Choi S-B 2018 On the response time of a new permanent magnet based magnetorheological damper: experimental investigation *Smart Mater. Struct.* **28** 14001
- [229] Crowell S L and Garden C city 1958 Valve mechanisms for magnetic fluid conduits and devices employing the same *United States Pat. Off.* **2,820,471**
- [230] Fujitani H, Sodeyama H, Tomura T, Hiwatashi T, Shiozaki Y, Hata K, Sunakoda K, Morishita S and Soda S 2003 Development of 400kN magnetorheological damper for a real base-isolated building *Smart Struct. Mater. 2003 Damping Isol.* **5052** 265–76
- [231] Guo C, Gong X, Zong L, Peng C and Xuan S 2015 Twin-tube-and bypass-containing magneto-rheological damper for use in railway vehicles *Proc. Inst. Mech. Eng. Part F J. Rail Rapid Transit* **229** 48–57
- [232] McLaughlin G, Hu W and Wereley N M 2014 Advanced magnetorheological damper with a spiral channel bypass valve *J. Appl. Phys.* **115** 17B532
- [233] Hu G, Zhang J, Zhong F and Yu L 2019 Performance evaluation of an improved radial

- magnetorheological valve and its application in the valve controlled cylinder system *Smart Mater. Struct.* **28**
- [234] Huang L, Li J and Zhu W 2017 Mathematical model of a novel small magnetorheological damper by using outer magnetic field *AIP Adv.* **7** 35114
- [235] Tu J, Li Z, Zhang J, Gao K, Liao J and Gao J 2019 Development, test, and mechanical model of the leak-proof magnetorheological damper *Front. Mater.* **6** 118
- [236] Hong S R, Wereley N M, Choi Y T and Choi S B 2008 Analytical and experimental validation of a nondimensional Bingham model for mixed-mode magnetorheological dampers *J. Sound Vib.* **312** 399–417
- [237] Elsaady W, Oyadiji S O and Nasser A 2020 Evaluation of nonlinear dynamic phenomena in the hysteretic behaviour of magnetorheological dampers *Appl. Eng. Sci.* **3** 100019
- [238] Case D, Taheri B and Richer E 2013 Multiphysics modeling of magnetorheological dampers *Int. J. Multiphys.* **7** 61–76
- [239] Cesmeci S 2017 *A fail-safe, bi-linear liquid spring, controllable magnetorheological fluid damper for a three-dimensional earthquake isolation system* (PhD dissertation, University of Nevada, Reno)
- [240] Bharathi Priya C and Gopalakrishnan N 2019 *Experimental investigations of the effect of temperature on the characteristics of MR damper* vol 12 (Springer Singapore)
- [241] Cruze D, Gladston H, Farsangi E N, Banerjee A, Loganathan S and Solomon S M 2021 Seismic Performance Evaluation of a Recently Developed Magnetorheological Damper: Experimental Investigation *Pract. Period. Struct. Des. Constr.* **26** 1–14
- [242] Pang L, Kamath G M and Wereley N M 1998 Dynamic characterization and analysis of magnetorheological damper behavior *Smart Struct. Mater. 1998 Passiv. Damping Isol.* **3327** 284–302
- [243] Kelso S P 1998 *Development and investigation of magneto-rheological fluid (MRF) dampers for off-highway, high-payload vehicles* (University of Nevada, Reno)
- [244] Yang L, Chen S Z, Zhang B and Feng Z Z 2011 A rotary magnetorheological damper for

- a tracked vehicle *Adv. Mater. Res.* **328–330** 1135–8
- [245] Makowski M and Knap L 2018 Investigation of an off-road vehicle equipped with magnetorheological dampers *Adv. Mech. Eng.* **10** 1687814018778222
- [246] Zhang X, Yang Y, Guo K, Sun S, He G and Li Z 2020 Methodology on a novel magnetorheological valve controlled damper synthesis design *Smart Mater. Struct.* **29**
- [247] Karnopp D, Crosby M J and Harwood R A 1973 Vibration Control Using Semi-Active Force Generators. *ASME Pap* 619–26
- [248] Rakheja S and Sankar S 1985 Vibration and shock isolation performance of a semi-active “on-off” damper *J. Vib. Acoust. Stress. Reliab. Des.* **107** 398–403
- [249] Sun S, Yang J, Wang P, Nakano M, Shen L, Zhang S and Li W 2021 Experimental study of a variable stiffness seat suspension installed with a compact rotary MR damper *Front. Mater.* **8** 594843
- [250] Sapiński B 2011 Experimental study of a self-powered and sensing MR-damper-based vibration control system *Smart Mater. Struct.* **20**
- [251] Boada M J L, Calvo J A, Boada B L and Díaz V 2011 Modeling of a magnetorheological damper by recursive lazy learning *Int. J. Non. Linear. Mech.* **46** 479–85
- [252] Kasprzyk J, Wyrwał J and Krauze P 2014 Automotive MR damper modeling for semi-active vibration control *IEEE/ASME International Conference on Advanced Intelligent Mechatronics (AIM)* (Besançon, France)
- [253] Sohn J W, Oh J S and Choi S B 2015 Design and novel type of a magnetorheological damper featuring piston bypass hole *Smart Mater. Struct.* **24**
- [254] Kim K, Chen Z, Yu D and Rim C 2016 Design and experiments of a novel magnetorheological damper featuring bifold flow mode *Smart Mater. Struct.* **25**
- [255] Kubík M, Macháček O, Strecker Z, Roupec J and Mazůrek I 2017 Design and testing of magnetorheological valve with fast force response time and great dynamic force range *Smart Mater. Struct.* **26**
- [256] Gurubasavaraju T M, Kumar H and Mahalingam A 2018 An approach for characterizing

- twin-tube shear-mode magnetorheological damper through coupled FE and CFD analysis *J. Brazilian Soc. Mech. Sci. Eng.* **40** 1–14
- [257] Cheng M, Chen Z B and Xing J W 2018 Design, Analysis, and Experimental Evaluation of a Magnetorheological Damper with Meandering Magnetic Circuit *IEEE Trans. Magn.* **54**
- [258] Huang H, Sun S, Chen S and Li W 2019 Numerical and experimental studies on a new variable stiffness and damping magnetorheological fluid damper *J. Intell. Mater. Syst. Struct.* **30** 1639–52
- [259] Yoon D, Park Y and Choi S 2019 An eddy current effect on the response time of a magnetorheological damper: Analysis and experimental validation *Mech. Syst. Signal Process.* **127** 136–58
- [260] Meng F and Zhou J 2019 Modeling and Control of a Shear-Valve Mode MR Damper for Semiactive Vehicle Suspension *Math. Probl. Eng.* **2019**
- [261] Liu X, Wang N, Wang K, Chen S, Sun S, Li Z and Li W 2020 A new AI-surrogate model for dynamics analysis of a magnetorheological damper in the semi-active seat suspension *Smart Mater. Struct.* **29**
- [262] Devikiran P, Puneet N P, Hegale A and Kumar H 2022 Design and development of MR damper for two wheeler application and Kwok model parameters tuning for designed damper *Proc. Inst. Mech. Eng. Part D J. Automob. Eng.* **236** 1595–606
- [263] Devikiran P, Shravya P, Puneet N P and Kumar H 2022 Design, characterization and control of MR damper for two-wheeler applications *Mater. Today Proc.* **62** 2056–2063
- [264] Marathe A P, Khot S M and Nagler J 2022 Development of Low-Cost Optimal Magnetorheological Damper for Automotive Application *J. Vib. Eng. Technol.* 1–20
- [265] Raja P, Wang X and Gordaninejad F 2014 A high-force controllable MR fluid damper–liquid spring suspension system *Smart Mater. Struct.* **23** 10
- [266] Deng L, Sun S, Jin S, Li Z, Du H, Zhang S and Li W 2022 Development of a new magnetorheological impact damper with low velocity sensitivity *Smart Mater. Struct.* **31**

- [267] Sun Q, Zang L, Zhou J and Shi Q 2003 Experimental study of the semi-active control of building structures using the shaking table *Earthq. Eng. Struct. Dyn.* **32** 2353–76
- [268] Caterino N, Spizzuoco M and Occhiuzzi A 2011 Understanding and modelling the physical behaviour of magnetorheological dampers for seismic structural control *Smart Mater. Struct.* **20**
- [269] Ding Y, Zhang L, Zhu H-T and ZX L 2013 A new magnetorheological damper for seismic control *Smart Mater. Struct.* **22** 115003–15
- [270] Ulasyar A and Lazoglu I 2018 Design and analysis of a new magneto rheological damper for washing machine *J. Mech. Sci. Technol.* **32** 1549–61
- [271] Case D, Taheri B and Richer E 2014 Dynamical modeling and experimental study of a small-scale magnetorheological damper *IEEE/ASME Trans. Mechatronics* **19** 1015–24
- [272] Liu G, Gao F and Liao W H 2021 Magnetorheological damper with multi-grooves on piston for damping force enhancement *Smart Mater. Struct.* **30**
- [273] Lee T H, Kang B H, Kim G W and Choi S B 2021 A new design of magnetic circuits in magnetorheological dampers for simple structure subjected to small stroke and low damping force *Smart Mater. Struct.* **30**
- [274] Deng H, Wang M, Han G, Zhang J, Ma M, Zhong X and Yu L 2017 Variable stiffness mechanisms of dual parameters changing magnetorheological fluid devices *Smart Mater. Struct.* **26** 125014
- [275] Zidan A 1995 *undercarriage of tracked vehicles* (Cairo, Egypt)
- [276] Kasim S Y 1991 *Ride Analysis For Suspension System of Off-Road Tracked Vehicles*
- [277] United States 1984 *Operator's manual : carrier, personnel, full tracked, armored M113A2 2350-01-068-4077 carrier, command post, light, tracked M577A2 2350-01-068-4089 carrier, mortar, 107-MM, self-propelled M106A2 2350-01-069-6931 carrier, mortar, 81-MM, self-propelled M125* (Washington, DC: Headquarters, Dept. of the Army)
- [278] Long B and Comito A 1979 *Development of Armored Personnel Carrier M113A1E1* *SAE*

Tech. Pap. **790414**, 12

- [279] Siorek R 1973 Experimental Investigation of Effect of Wheel Travel on Tracked Vehicle Mobility *SAE Tech. Pap.*
- [280] Ata W, Dynamics A S-V S and 2017 undefined 2017 Semi-active control of tracked vehicle suspension incorporating magnetorheological dampers *Taylor Fr.* **55** 626–47
- [281] Dhir A and Sankar S 1995 Assessment of tracked vehicle suspension system using a validated computer simulation model *J. Terramechanics* **32** 127–49
- [282] Dhir A, Student G, Sankar & S, Dhir' A and Sankar~ S 1994 Ride Dynamics of High-Speed Tracked Vehicles: Simulation with Field Validation *Veh. Syst. Dyn.* **23** 379–409
- [283] Harris F E 2014 *Mathematics for physical science and engineering: symbolic computing applications in Maple and Mathematica* (Academic Press)

Appendix A

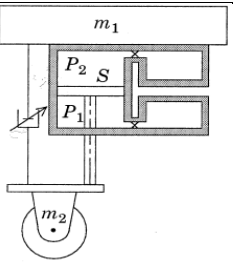
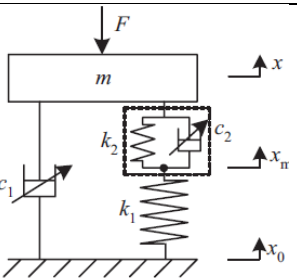
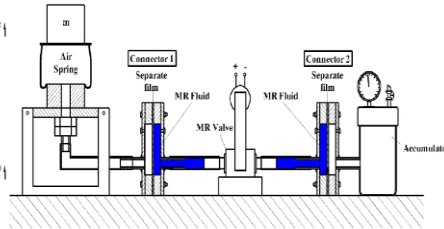
Table A-1. Summary of studies reporting experimental characterization of MRFDs.

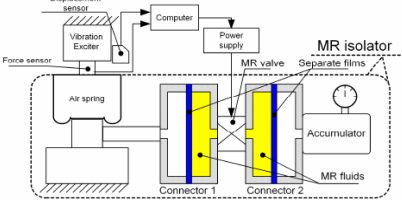
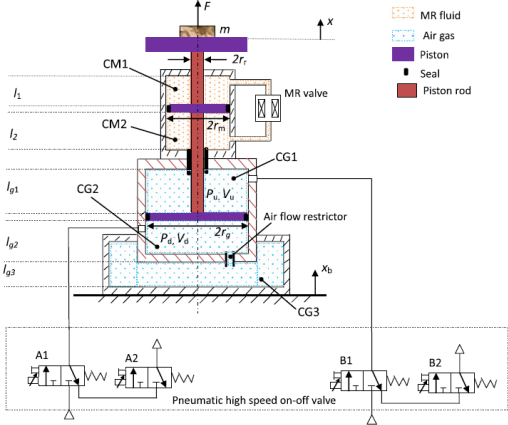
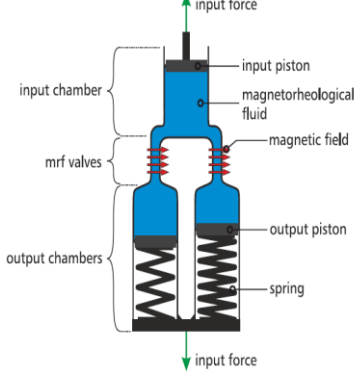
Reference	Application	Off-state force (kN)	Max force (kN)	Dynamic range	Fluid path type	frequency (Hz)	Max displacement (mm)	Stroke (mm)
Hu [227], 2007	Automotive Applications	1.23	8	6.5	Tortuous Channel	0.1-1	12.7-25.4	152.4
Çeşmeci et al [198], 2010		0.75	2	2.67	Annular	2.45	12.5	55
Sapiński [250], 2011		-	0.6	-	Annular	4.5	6	-
Boada et al. [251], 2011		0.65	2.4	3.7	Annular	2	16	-
Bai [75], 2013		0.2	2.4	12	Annular	1	38.1	-
Bai [169], 2013		0.14	3.15	2.81 at 3 Hz	Annular-radial	1-3	10	~34
Kasprzyk [252], 2014		0.15	1.8	12	Annular	0.5-6	5-25	74
Sohn [253], 2015		0.1	4.65	10	Annular	0.1-12	20	-
Kim [254], 2016		0.24	3.15	13.5	Bifold annular	1-3	10-20	31
Zhu [20], 2016		2	4	2	Annular-radial	0.16-6	50	150
Kubík [255], 2017		0.225	2	8	Annular	0.1-8	5	-
Gurubasavaraju et al. [256], 2018		0.06	0.117	1.95	Annular	2	0.005	10
Cheng [257], 2018		0.1	3.4	34	Annular	1-2	4-12	~57
Huang et al. [258], 2019		0.075	0.17	2.26	Annular	2	0.01	-
Yoon [259], 2019		0.34	1.34	3.9	Annular	5	10	-
Meng [260], 2019		0.2	1.4	7	Shear-valve mode	2	4	-
Wang [222], 2019		0.7	3.6	5.1 at 2 Hz	Annular-radial	2	10-15	32
Hu [233], 2019		1	4	4	Annular-radial	0.25-1	5-10	-
Liu et al. [261], 2020		0.442	2.53	5.7	Annular	3.32	25	-
Idris [105], 2020		0.5	0.75	3.8	Annular-radial	0.016-0.1	10	100
Devikiran et al. [262], 2021		0.17	0.2	1.17	Annular	1	16	-
Devikiran et al. [263], 2022		0.71	0.9	1.2 at 3 Hz	Radial	2.5-3	5-10	-
Marathe and Nagler [264], 2022		0.17	0.26	1.5	Annular	1-10	-	-
Keslo [243], 1998			0.4	2.2	5.5	Rectangular	2-4	2.5-10

Yang [244], 2011	High payload vehicle and railway vehicle	0.5	3.5	7	Annular	0.5-4	30-150	-
Raja [265], 2014		2.5	4.8	1.92	Annular	0.1-1	2.54-12.7	80
Zhang [246], 2020		0.8-1.23	3.95	4.86	Radial	0.16-1.66	50	100
Kim et al. [78], 2017		5.52	15.36	2.78	Annular	3.2	15	150
Ahmadian et al [129], 2007		25.8	27.6	1.07	Annular	-	-	104.14
Hu et al. [87], 2012	Guns	1.4	2.3	1.64	Annular	-	0.6	350
Deng et al.[266] ,2022		1.05	1.31	1.24	Annular	-	10	-
Sun [267], 2003	Civil Engineering Applications	2.3	8	3.8	Annular	0.5-2	10	-
Fujitani [230], 2003		3	300	3	Annular	0.01-3	10-250	950
Hitchcock [108], 2007		0.5	4	8	Annular	0.0625-2	3.2-8	50.8
Caterino et al. [268], 2011		2	27	13.5	annular	1.5	20	50
Ding et al. [269], 2013		3.89	20.3	17.3		1	0.01	-
Chae and Choi [77], 2014	Ambulance bed	0.07	0.294	4.2	annular	2.4	0.013	-
Ulasyar et al [270], 2018	Washing machine	0.01076	0.19	17.65	Annular	3	0.006	30
Case et al. [271], 2014	Prosthesis and medical devices	0.0061	0.0095	1.56	Annular	10	25	60
Liu [272], 2021,		0.179	1.24	6.88	Annular	1	10	54
Lee [273], 2021		0.02	0.26	281	Annular	0.17	25-35	70

Appendix B

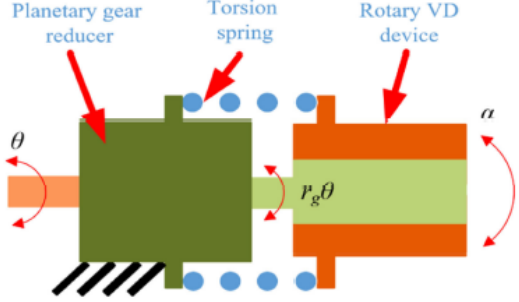
Table B-1. Developed VSVD-MRFDs.

Reference	Schematic of VSVD system	Objective and method of analysis	Stiffness element type	Major findings	Force range (N)	Stiffness range (kN/m)	Stroke (mm)	Protentional applications
Youn and Hac' [155], 1995		Proposed synthesis of control for a variable stiffness and damping suspension system	Air spring	<ul style="list-style-type: none"> Improve ride comfort The stiffness was varied between three definite levels 	-	Between 3 discrete levels	-	Automotive suspension
Liu et al [148], 2008		Proposed configuration and control for VSVD system using two MRFD and two constant springs	Mechanical spring	<ul style="list-style-type: none"> Superior vibration isolation performance. Stiffness variation is affected by spring ratio. the system on-off control exhibited perfect vibration isolation performance. 	-	1.64-4.67	-	Automotive Application
Li et al [157], 2009		Development of MRFD based variable stiffness using MR valve and bladders	Air spring	Continuous variable stiffness and damping	2.82-12.37	5-29	-	Earthquake applications

<p>Zhang et al [158],2009</p>		<p>Presented MR variable stiffness and damping isolator using MR fluid valve and two connectors</p>	<p>Air spring</p>	<ul style="list-style-type: none"> • Simple, cheaper, and easy maintenance • bulky, costly and complex 	<p>2.5-113.1</p>	<p>5.5-25</p>	<p>-</p>	<p>Civil engineering</p>
<p>Zhu et al [156], 2011</p>		<p>Proposed an MRFD with an embedded pneumatic vibration isolator for adjusting stiffness and damping of the system</p>	<p>Air spring</p>	<ul style="list-style-type: none"> • Changing the gas pressure leads to a variation in the system stiffness. • Pneumatic isolators can provide high payload, reliable and inexpensive maintenance for low natural frequency applications 	<p>-</p>	<p>-</p>	<p>-</p>	<p>Civil engineering</p>
<p>Petter et al [160], 2014</p>		<p>Proposed a compact VSVD MR based device using two MR valves and two different stiffness springs.</p>	<p>Mechanical spring</p>	<ul style="list-style-type: none"> • The system stiffness could be varied among three discrete values; depending on the state of the two MR valves (open/close). • Stiffness and damping vary independently. 	<p>2-19</p>	<p>1.67-14.433</p>	<p>-</p>	<p>-</p>
				<ul style="list-style-type: none"> • 				

<p>Sun et al, [145] 2015</p>		<p>Proposed variable damping and stiffness damper using two MRF damping units and a spring</p>	<p>Mechanical spring</p>	<ul style="list-style-type: none"> Stiffness and damping can be controlled dependently. VSVD-MRFD is feasible 	<p>120-300</p>	<p>11.3-30.5</p>	<p>-</p>	<p>Automotive Application</p>
<p>Sun et al [159], 2015</p>		<p>Designed variable damping and stiffness shock absorber using two coaxial damping cylinders, two springs</p>	<p>Mechanical spring</p>	<ul style="list-style-type: none"> Stiffness varies between two modes Stiffness and damping are in depending on frequency. 	<p>300-600</p>	<p>8.7-24.5</p>	<p>71</p>	<p>Automotive Application</p>
<p>Deng et al [274], 2017</p>		<ul style="list-style-type: none"> Provided a theoretical investigation for the force transmissions between the elements of the VSVD system of Sun et al. [108P]. Obtaining The relationships between the equivalent stiffness and the geometrical parameters 	<p>Mechanical spring</p>	<ul style="list-style-type: none"> The stiffness variability is influenced by the structural parameters such as the effective length, cross-sectional area and gap of the piston. The stiffness and damping variability are affected by stiffness ratio and current, also. 	<p>140-200</p>	<p>11.9-20</p>	<p>71</p>	<p>Automotive Application</p>
<p>Sun et al [149], 2019</p>		<ul style="list-style-type: none"> Designed variable damping and stiffness shock absorber using two coaxial damping 	<p>Mechanical spring</p>	<ul style="list-style-type: none"> Significantly reducing in sprung mass acceleration. Improving the ride comfort when comparing with other 	<p>500-900</p>	<p>25.4-45.2</p>	<p>71</p>	<p>Automotive Application</p>

		<p>cylinders, two springs for Improving the previous design [108P]</p> <ul style="list-style-type: none"> • study of the effect of variable stiffness and damping suspension on a quarter car system 		types of the suspension system				
Deng et al. [150],2019		<p>Implemented a VSVD-MRFD in an off-road military vehicle seat suspension to enhance ride comfort.</p>	Mechanical spring	<ul style="list-style-type: none"> • In comparison to passive and VD controls, the seat suspension with VSVD control has the lowest seat acceleration and most effective vibration attenuation. • VSVD system reduces seat acceleration by 22.1% compared to the excitation one. 	100-250	5.06-10.4	-	Seat suspension
Zhu et al. [27], 2019		<p>Developed a long-stroke VSVD-MRFD with self-powered generation capability</p>	Mechanical spring	<ul style="list-style-type: none"> • The stiffness can be varied up to 70.4% with variation of the applied current from 0 to 2 A. • An effective power output of 2.595 W is possible from the damper. 	1600-2000	17.6-25.93	105	Automotive Application

<p>Ning et al. [151], 2020</p>	 <p>Planetary gear reducer</p> <p>Torsion spring</p> <p>Rotary VD device</p> <p>θ</p> <p>$r_g \theta$</p> <p>α</p>	<p>proposed a rotary semi-active variable stiffness and damping device for seat suspension based on series. Connection using electromagnetic MR device</p>	<p>Mechanical spring</p>	<ul style="list-style-type: none"> • The mechanical spring methods with is suitable for a large stiffness variation range application • The acceleration of seat suspension with VSVD device reduced by 19.0% compared passive seat suspension. 	<p>(170-480) Nm</p>	<p>0.084-13.259</p>		<p>Seat suspension</p>
--------------------------------	--	--	--------------------------	---	---------------------	---------------------	--	------------------------

Appendix C

Suspension systems utilize in off road tracked vehicles.

Tracked vehicles undercarriage has the most arduous operating conditions. Undercarriages of various tracked vehicles have widely different configurations in terms of arrangement and construction of individual components. The undercarriage of tracked vehicles consists of two main systems: track drive system and suspension system [275]. The track drive system provides the vehicle motion by converting the drive sprocket rotary movement into vehicle translational movement. Vehicle suspension systems comprise all linked elements between the road wheel. They have to mitigate vibration that the vehicle body experience from the road irregularities generated during its cross-country drive. Moreover, high vehicle maneuverability and maintaining combat activities have to be achieved. Further, vehicle mobility performance is limited by the operator's endurance to withstand the transmitted shocks and impacts and his ability to conserve control. Thus, suspension systems permit a sufficient level of comfort for the vehicle crew to enhance their field operation effectively [276].

Tracked vehicle suspension systems are categorized, according to the wheel-hull connection to block suspension and individual suspension. In block suspension, two or more road wheels join together in a group to connect a vehicle hull. While the individual suspension is the most utilized suspension system in a tracked vehicle where each road wheel is linked to the vehicle hull independently. The Armored Personnel Carrier (APC) M113 undercarriage is a clear example of a tracked vehicle suspension system. M113 undercarriage, as shown in Figure C-1 composed of a track drive system and suspension system. The former system includes two driving sprockets, two idler wheels and a track. The subsequent system consists of five road wheels with five road wheel arms on each side connecting the vehicle hull to the track. Each road wheel arm is anchored to the vehicle hull using a torsion bar (elastic element). Also, there are three shock absorbers (damping element) attached to the first, second and last road wheel station on each side. The torsion bar softens the generated shocks form uneven terrain to minimize vehicle hull vibration while, the hydraulic shock absorber damps the transmitted vibration to the hull.

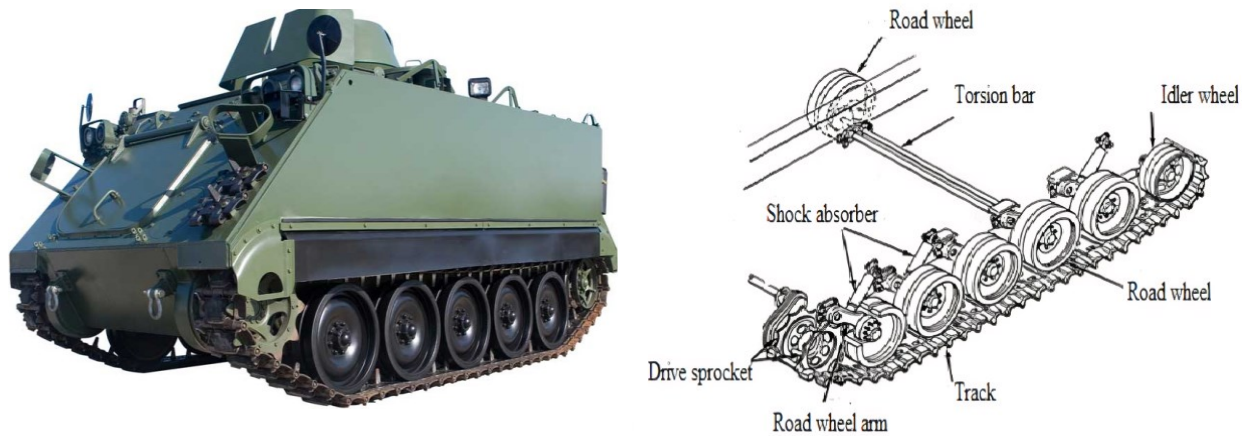


Figure C-1 APC M113 undercarriage b- M113 half mathematical model [277].

In 1960, the Armour personal carrier M113 was produced to replace the M59 vehicle in the US army. The tracked vehicle M113 and its family have to improve continuously to increase compact activity and weights. Thus, the vehicle’s suspension system should be improved. Some studies have been done for the vehicle suspension dynamics, as summarized in Table C-1.

Table C-1. Summarized studies for improving M113 suspension dynamics

Reference	Objective and method of analysis	Major Conclusion
Long and Comito [278]	<ul style="list-style-type: none"> Improved M113 suspension system through. changing the torsion bar with a high-strength steel. Removing support arm bump stops Increasing the number of the shock absorber to be 3 instead of 2 in each side. 	<ul style="list-style-type: none"> Increasing the vehicle ground clearance decreasing its spring rate by 17% for more ride comfort. lengthening wheel travel increasing the damping ability for absorbing more shocks.
Siorek [279]	<ul style="list-style-type: none"> Investigated the effect of increasing the M113 wheel travel on the vehicle mobility capabilities to cross the countered obstacles 	<ul style="list-style-type: none"> the vehicle's capability to overcome the barrier will increase with These capabilities will be enhanced to be 25%, 55 %, 65% and 75 % if the wheel travel becomes 6-814, 17, and 30-35 inches respectively.
Ata and Salem [280]	<ul style="list-style-type: none"> Developed 7 DOF suspension systems fitted with commercial MRFDs to theoretically investigate the proper control algorithm among skyhook, hybrid and fuzzy-hybrid controllers 	<ul style="list-style-type: none"> the performance of the vehicle suspension system has been improved with using MRFDs. Fuzzy-hybrid controller manifests considerable improvement in reducing the vehicle hull accelerations.
Anil and Sankar [281]	<ul style="list-style-type: none"> Evaluated the ride comfort for M113 through developing a time-domain computer simulation The effect of the conventional suspension system and hydro-gas suspension system on ride performance has been investigated. 	<ul style="list-style-type: none"> The ride comfort is considerably enhanced by increasing the number of shock absorbers. replacing the conventional suspension with hydro-gas suspension at all

		roadwheels will improve the ride acceleration response
Anil and Sankar [282]	Developed a computer simulation to study the ride dynamic behaviour for M113 under different road configurations and speeds. validated the simulation result by field testing	a good agreement between the field results and simulation can be a tool in evaluating the ride performance for tracked vehicles.

The existing M113 tracked vehicle conventional suspension system prevents its high mobility, speed and maneuverability, apart from its inadaptability to various operating conditions and excitation [9]. Further enhancing the vehicle's cross-country ability is required to enlarge the vehicle's wheel travel. However, enlarging the vehicle wheel travel requires considerable improvements in the torsion bar spring rate, the shock absorber damping rate and the wheelbase, all of that is limited by the existing torsion bar. Moreover, the crossed-vehicle torsion bar has many drawbacks, such as increasing the vehicle height, easy vehicle observation, increasing the possibility of the vehicle's crew being shot, and decreasing ground clearance.

Appendix D

Detail drawings of the proposed MRFD

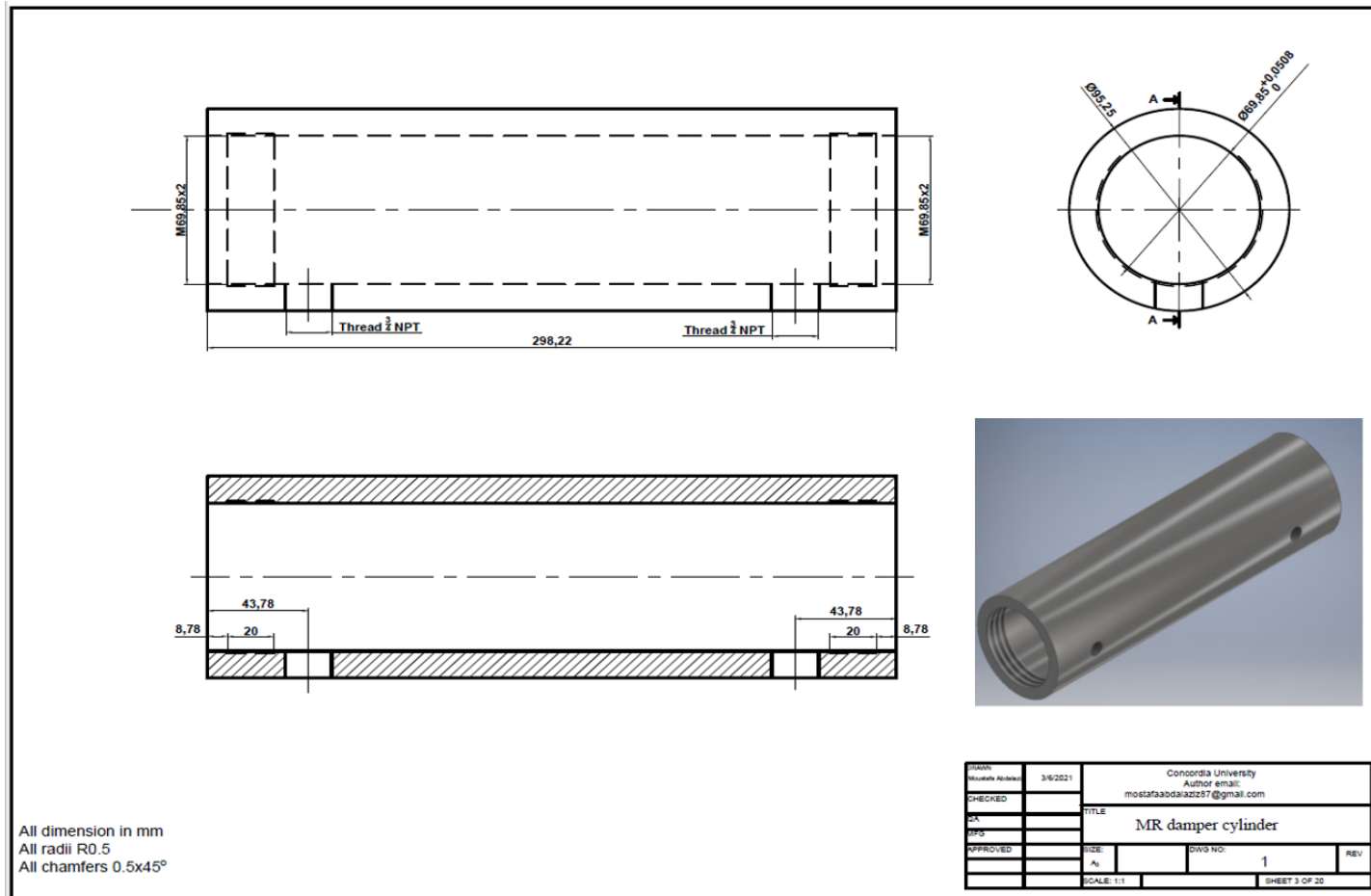


Figure D-1. MRFD cylinder.

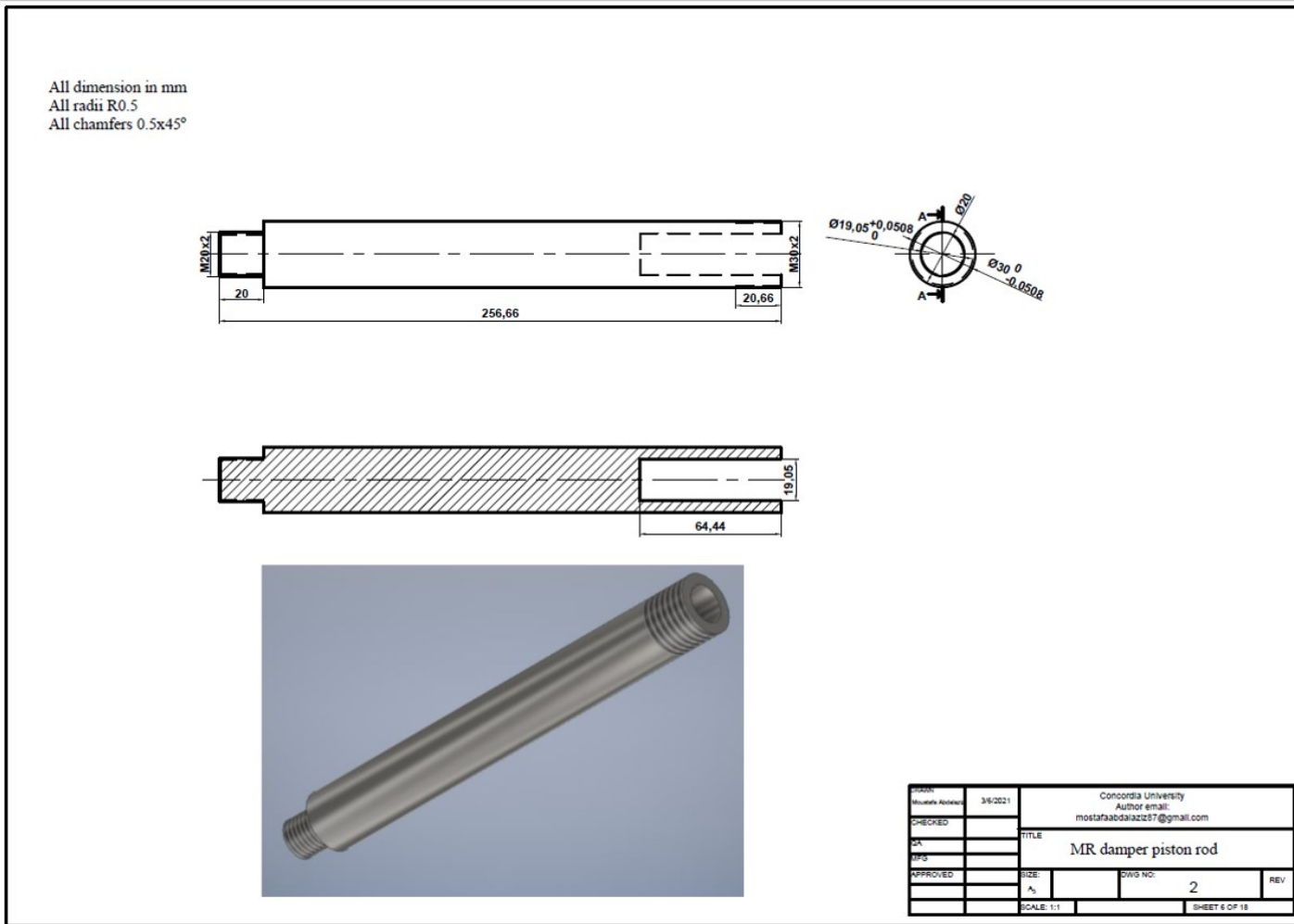
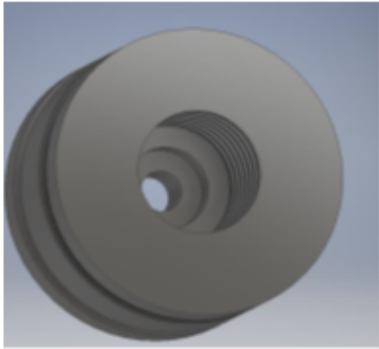
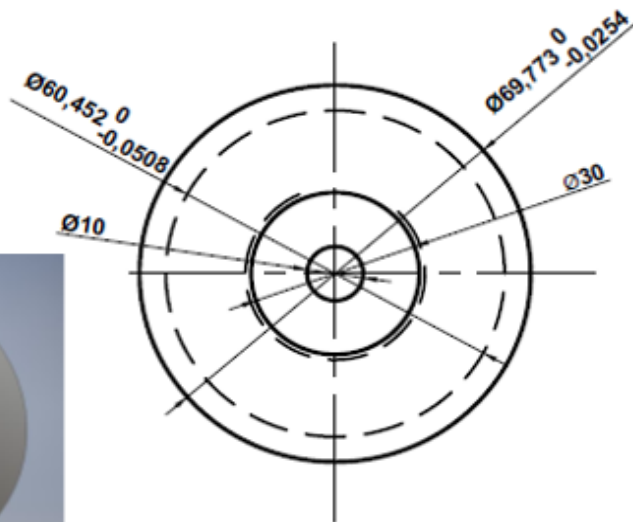
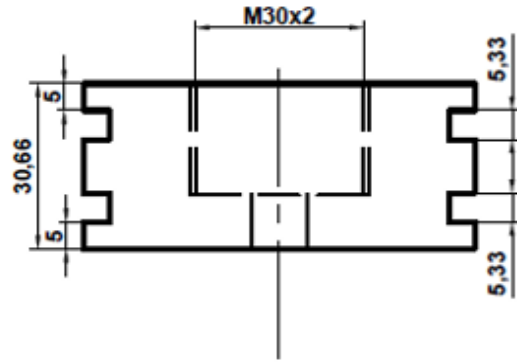


Figure D-2. MRFD piston rod.

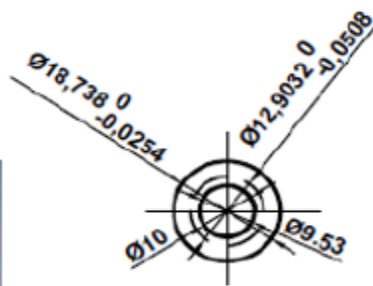
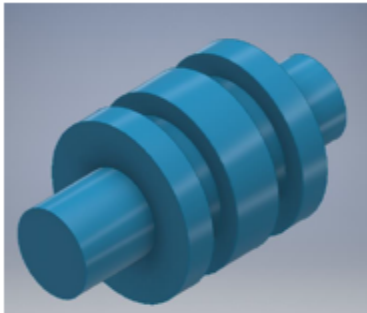
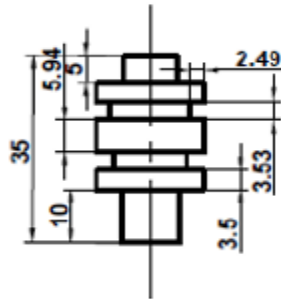
All dimension in mm
 All radii R0.5
 All chamfers 0.5x45°



DRAWN	Moustafa Abdalaziz	3/6/2021	Concordia University Author email: mostafaabdalaziz87@gmail.com			
CHECKED			TITLE			
QA			MR-damper Main piston			
MFG			SIZE:		DWG NO:	3
APPROVED			A ₄			REV
			SCALE: 1:1			SHEET 4 OF 20

Figure D-3. MRFD main piston.

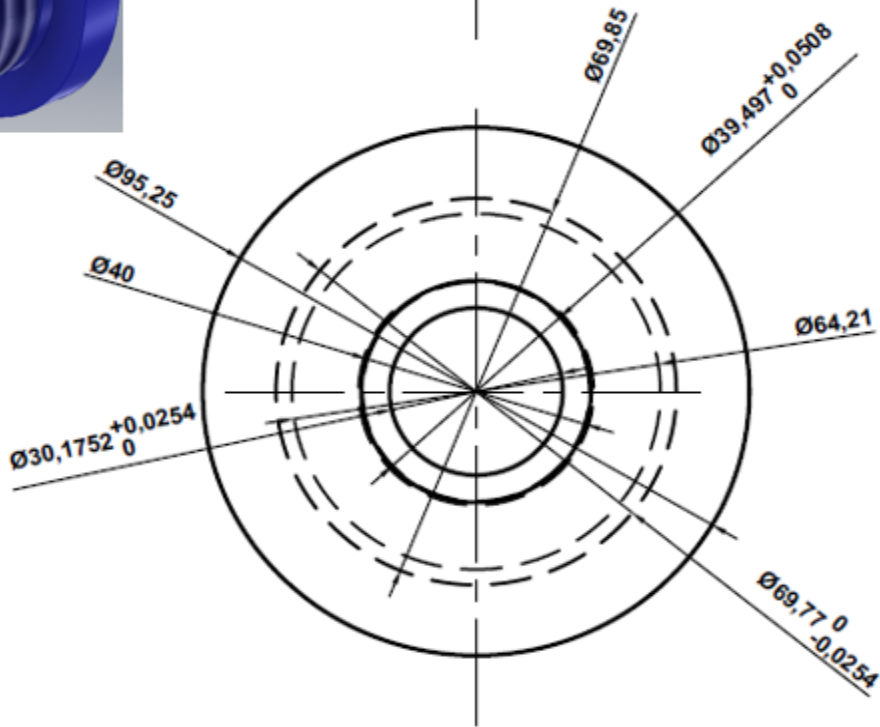
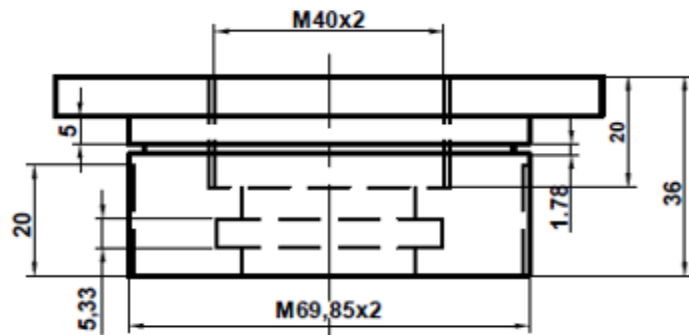
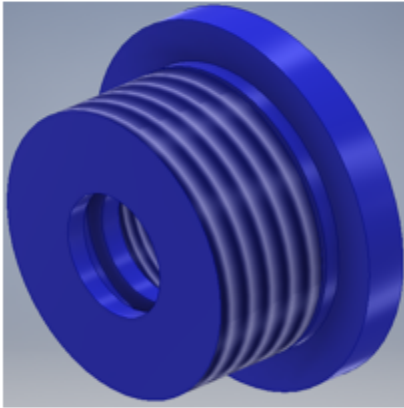
All dimension in mm
 All radii R0.5
 All chamfers 0.5x45°



DRAWN	Moustafa Abdalaziz	3/6/2021	Concordia University Author email: mostafaabdalaziz87@gmail.com		
CHECKED			TITLE		
QA			MR-damper Floating piston		
MFG			SIZE:	DWG NO:	REV
APPROVED			A ₄	4	
			SCALE: 1:1		SHEET 8 OF 20

Figure D-4. Floating piston.

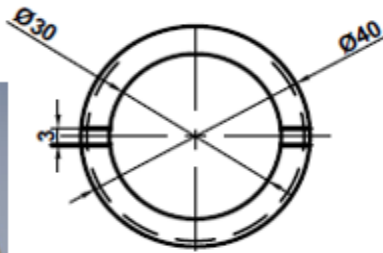
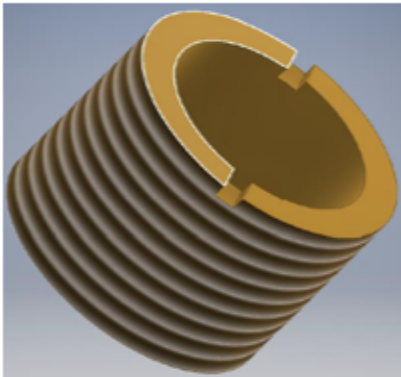
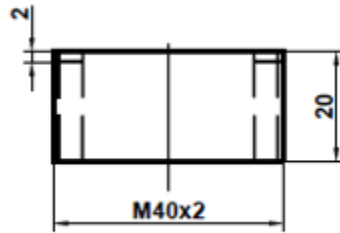
All dimension in mm
 All radii R0.5
 All chamfers 0.5x45°



DRAWN	Moustafa Abdalaziz	3/6/2021	Concordia University Author email: mostafaabdalaziz87@gmail.com			
CHECKED			TITLE Cylinder cover			
QA						
MFG						
APPROVED			SIZE: A ₄	DWG NO: 5	REV	
			SCALE: 1:1		SHEET 7 OF 18	

Figure D-5. Upper cylinder cover.

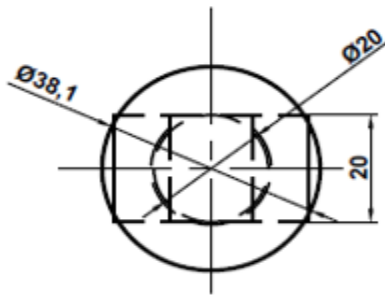
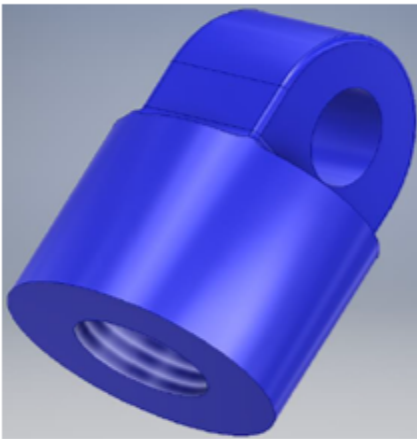
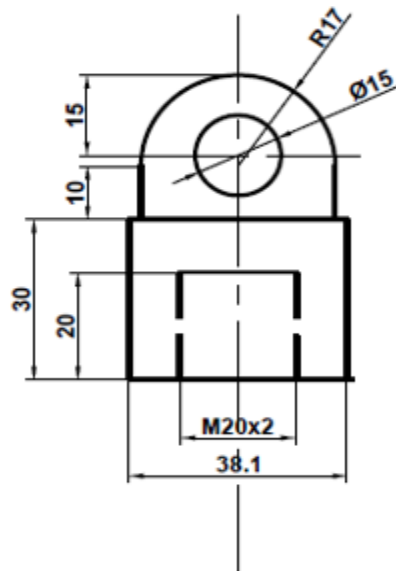
All dimension in mm
 All radii R0.5
 All chamfers 0.5x45°



DRAWN	Moustafa Abdalaziz	3/6/2021	Concordia University Author email: mostafaabdalaziz87@gmail.com			
CHECKED			TITLE Piston rod guider			
QA			SIZE:		DWG NO:	6
MFG			A ₄			REV
APPROVED			SCALE: 1:1			SHEET 11 OF 17

Figure D-6. Piston rod guider.

All dimension in mm
 All radii R0.5
 All chamfers 0.5x45°



DRAWN	Moustafa Abdalaziz	3/6/2021	Concordia University Author email: mostafaabdalaziz87@gmail.com			
CHECKED			TITLE			
QA			Piston rod end cap			
MFG			SIZE:		DWG NO:	7
APPROVED			A ₃			REV
			SCALE: 1:1			SHEET 12 OF 18

Figure D-7. Piston rod end cap.

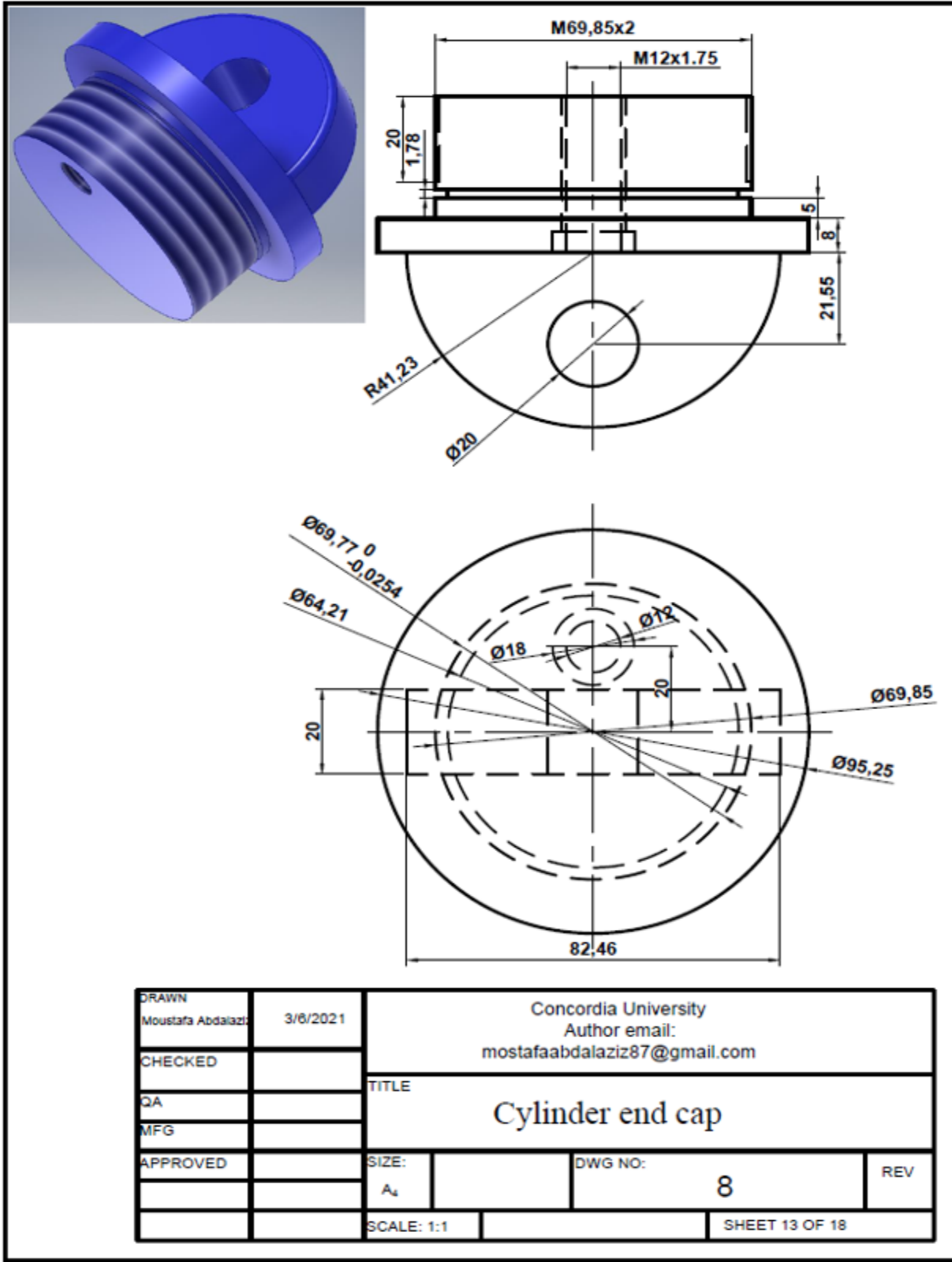
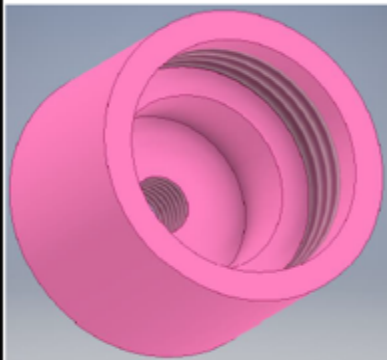
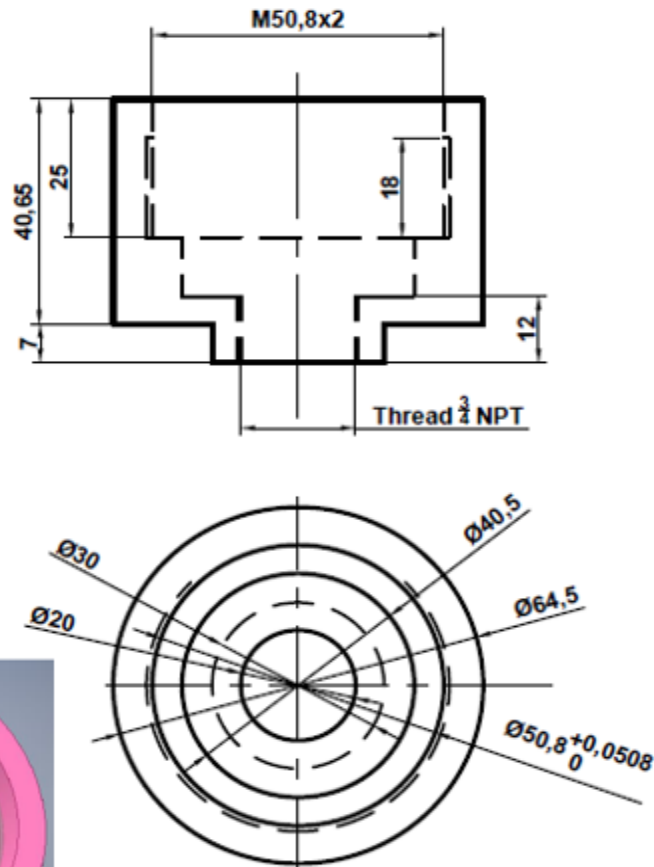


Figure D-8. Cylinder end cap.

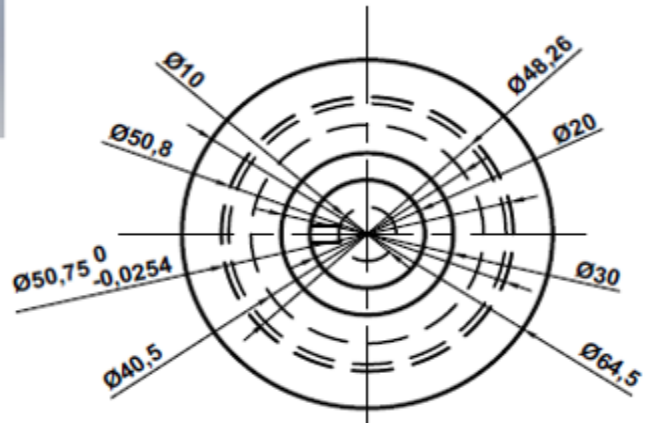
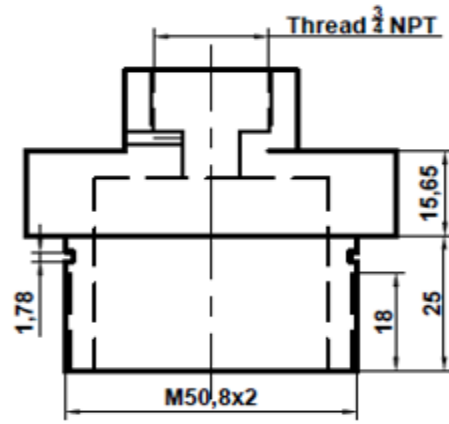
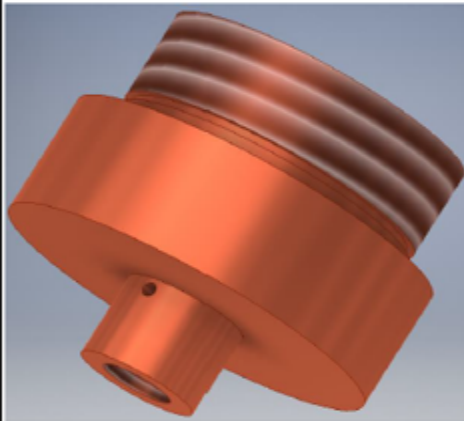
All dimension in mm
 All radii R0.5
 All chamfers 0.5x45°



DRAWN	Moustafa Abdalaziz	3/6/2021	Concordia University Author email: mostafaabdalaziz87@gmail.com			
CHECKED			TITLE			
QA			MR valve- Lower shell			
MFG			SIZE:		DWG NO:	9
APPROVED			A ₄			REV
			SCALE: 1:1			SHEET 14 OF 18

Figure D-9. MRV- Lower shell.

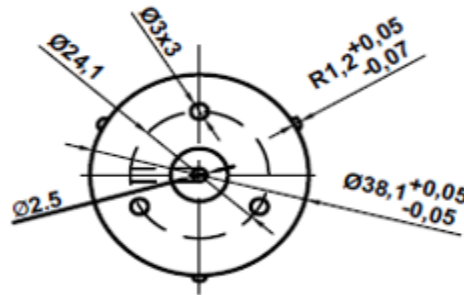
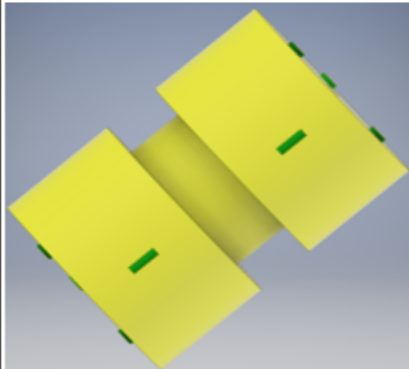
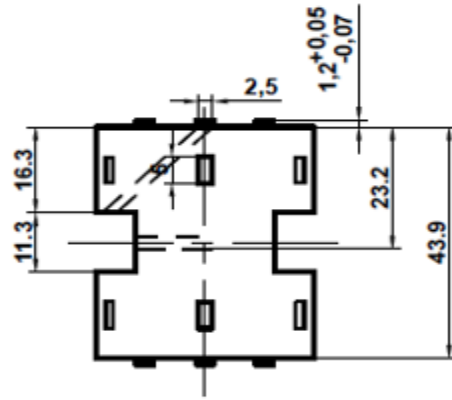
All dimension in mm
 All radii R0.5
 All chamfers 0.5x45°



DRAWN	Moustafa Abdalaziz	3/6/2021	Concordia University Author email: mostafaabdalaziz87@gmail.com			
CHECKED			TITLE			
QA			MR valve- Upper shell			
MFG						
APPROVED			SIZE:	DWG NO:	REV	
			A ₄	10		
			SCALE: 1:1		SHEET 15 OF 18	

Figure D-10. MRV- Upper shell.

All dimension in mm
 All radii R0.5
 All chamfers 0.5x45°



DRAWN Moustafa Abdalaziz	3/6/2021	Concordia University Author email: mostafaabdalaziz87@gmail.com		
CHECKED		TITLE MR valve- Bobbin		
QA		SIZE: A ₄	DWG NO: 11	REV
MFG		SCALE: 1:1		
APPROVED		SHEET 16 OF 18		

Figure D-11. MRV-Bobbin with spacers.

Appendix E

(a) Solving the differential Eq. (4-17) using variable separation method and obtaining the constants in Eq. (4-22)

Let

$$m = \sqrt{\frac{s}{v}}, C_1 = \frac{A+B}{2}, C_2 = \frac{A-B}{2} \quad (13-1)$$

Using trigonometry relations, the homogenous solution

$$u_H(y, s) = \left(\frac{A+B}{2}\right)e^{my} + \left(\frac{A-B}{2}\right)e^{-my} \quad (13-2)$$

$$u_H(y, s) = \frac{A}{2}[e^{my} - e^{-my}] + \frac{B}{2}[e^{my} + e^{-my}] \quad (13-3)$$

$$u_H(y, s) = C_1 \sinh(my) + C_2 \cosh(my) \quad (13-4)$$

The general solution can be written as

$$u(y, s) = C_1 \sinh(my) + C_2 \cosh(my) + \psi_p \quad (13-5)$$

Using separation of variable method and applying the boundary conditions in Eqs. (4-18) and (4-19) into the general solution in Eq. (4-22), the constants can be calculated as

$$C_1 = \frac{-\psi_p \sinh(mh_o)}{\sinh(mh) \sinh(mh_o) - \cosh(mh) \cosh(mh_o)} \quad (13-6)$$

$$C_2 = \frac{\psi_p \cosh(mh_o)}{\sinh(mh) \sinh(mh_o) - \cosh(mh) \cosh(mh_o)} \quad (13-7)$$

Substituting of Eqs. (13-6) and (13-7) into Eq. (13-5), the general solution can be calculated as

$$\begin{aligned}
u(y, s) &= \psi_p \left[1 + \frac{\cosh(mh_o) \cosh(my) - \sinh(mh_o) \sinh(my)}{\sinh(mh) \sinh(mh_o) - \cosh(mh) \cosh(mh_o)} \right] \\
&= \psi_p \left[1 - \frac{\cosh m(h_o - y)}{\cosh m(h - h_o)} \right]
\end{aligned} \tag{13-8}$$

Let

$$\begin{aligned}
\Delta &= \sinh(mh) \sinh(mh_o) - \cosh(mh) \cosh(mh_o) \\
&= -\cosh m(h - h_o)
\end{aligned} \tag{13-9}$$

The particular solution can be evaluated by Substituting in additional condition

$$\begin{aligned}
&\psi_p \left\{ h_o \left[1 + \frac{(\cosh mh_o)^2 - (\sinh mh_o)^2}{\Delta} \right] \right. \\
&\quad \left. + \int_{h_o}^h \left[1 + \frac{\cosh mh_o \cosh my - \sinh mh_o \sinh my}{\Delta} \right] dy \right\} \\
&= u_p(s)h
\end{aligned} \tag{13-10}$$

then

$$\psi_p = \frac{u_p(s)mh\Delta}{mh\Delta + mh_o\epsilon} \tag{13-11}$$

where

$$\begin{aligned}
\epsilon &= \cosh mh_o (\sinh mh - \sinh mh_o) \\
&\quad - \sinh mh_o (\cosh mh - \cosh mh_o) \\
&= -\sinh m(h_o - h)
\end{aligned} \tag{13-12}$$

Substituting from Eq. (13-11) into Eq. (13-8), the flow velocity can be evaluated as:

$$u(y, s) = \frac{u_p(s)mh(\Delta + \cosh mh_o \cosh my - \sinh mh_o \sinh my)}{mh\Delta + mh_o + \epsilon} \quad (13-13)$$

then

$$u(y, s) = \frac{u_p(s)mh[\cosh m(h_o - y) - \cosh m(h - h_o)]}{mh\Delta + mh_o + \epsilon} \quad (13-14)$$

Let

$$\Omega(y, s) = \frac{mh[\cosh m(h_o - y) - \cosh m(h - h_o)]}{mh\Delta + mh_o + \epsilon} \quad (13-15)$$

(b) Obtaining the flow velocity profile in Eq. (4-29) using Laplace inverse techniques (Cauchy Residue theory and complex variable theory) [283].

$$f(y, t) = \frac{1}{2\pi i} \int_{\gamma-i\infty}^{\gamma+i\infty} f(y, s) e^{st} ds = \sum_0^{\infty} Res(f(s), z_j) \quad (13-16)$$

Since

$$Res(f(s), z_j) = \frac{1}{(N-1)!} \lim_{s \rightarrow z_j} \frac{d^{N-1}}{ds^{N-1}} [(s - z_j)f(s)] \quad (13-17)$$

Substituting of Eqs. (4-23), (4-28) into Eq. (13-16).

$$\begin{aligned} & u(y, t) \\ = & \frac{1}{2\pi i} \int_{\gamma-i\infty}^{\gamma+i\infty} \frac{A_0 \omega}{s^2 + \omega^2} \frac{mh(\Delta + \cosh mh_o \cosh my - \sinh mh_o \sinh my)}{mh\Delta + mh_o + \epsilon} e^{st} ds \\ = & \sum_0^{\infty} Res(f(s), z_j) \end{aligned} \quad (13-18)$$

Where

$$\begin{aligned} & f(s) \\ = & \frac{A_0 \omega}{s^2 + \omega^2} \frac{mh(\Delta + \cosh mh_o \cosh my - \sinh mh_o \sinh my)}{mh\Delta + mh_o + \epsilon} e^{st} \end{aligned} \quad (13-19)$$

The poles (z_j) of the Eq. (13-18) that is equal to the two simple poles of the piston velocity motion and the roots of Eq. (13-21)

$$z_{1,2} = \pm i\omega \quad (13-20)$$

$$\begin{aligned} z_n &= mh\Delta + mh_o + \epsilon \\ &= mh_o - \cosh m(h - h_o) - \sinh m(h_o - h) = 0 \end{aligned} \quad (13-21)$$

The solution of the flow velocity profile in Eq. (13-18) can be evaluated as:

$$u(y, t) = \text{Res}(f(s), -i\omega) + \text{Res}(f(s), i\omega) + \text{Res}(f(s), z_n) \quad (13-22)$$

Where

$$\text{Res}(f(s), -i\omega) = [(s + i\omega)f(-i\omega)] = \frac{A_0 i}{2} \Omega(y, -i\omega) e^{-i\omega t} \quad (13-23)$$

$$\text{Res}(f(s), i\omega) = [(s - i\omega)f(i\omega)] = -\frac{A_0 i}{2} \Omega(y, i\omega) e^{i\omega t} \quad (13-24)$$

For calculation of the residue function of the poles (z_n)

Let

$$m = i\alpha \Rightarrow s_n = -\alpha_n^2 v \quad , n = 1, 2, 3, \dots \dots \dots \infty \quad (13-25)$$

Since all (α_n) are symmetrically placed about zero on the real axis and all the poles (z_n) lie on the negative real axis. Then the residues of the other poles can be obtained as in [196].

$$\begin{aligned} &\text{Res}(f(s), z_n) \\ &= \sum_{n=1}^{\infty} \frac{2A_0 \omega \alpha_n^2 v h}{(\alpha_n^4 v^2 + \omega^2)} \frac{[\cos \alpha_n(h - h_o) - \cos \alpha_n(y - h_o)]}{\xi} e^{-\alpha_n^2 v t} \end{aligned} \quad (13-26)$$

Since (α_n) has the values that makes Eq. (50) equals to zero

$$\alpha_n h_o + \alpha_n h \cos \alpha_n(h - h_o) - \sin \alpha_n(h_o - h) = 0 \quad (13-27)$$

Now, from Eqs. (13-23)-(13-26), the flow velocity profile can be expressed as:

$$\begin{aligned}
u(y, t) &= \frac{A_0 i}{2} [\Omega(y, -i\omega)e^{-i\omega t} - \Omega(y, i\omega)e^{i\omega t}] \\
&+ \sum_{n=1}^{\infty} \frac{2A_0 \omega \alpha_n^2 v h}{(\alpha_n^4 v^2 + \omega^2)} \frac{[\cos \alpha_n (h - h_0) - \cos \alpha_n (y - h_0)]}{\xi} e^{-\alpha_n^2 v t}
\end{aligned} \tag{13-28}$$

Similarly, the pressure gradient of Eq. (4-32) can be obtained by taking the same Laplace inverse techniques

$$\begin{aligned}
\frac{dP(x, t)}{dx} &= \frac{1}{2\pi i} \int_{\gamma-i\infty}^{\gamma+i\infty} -\rho s \frac{u_p(s) m h \Delta}{m h \Delta + m h_0 + \epsilon} e^{st} ds \\
&= \sum_0^{\infty} Res(g(s), z_j)
\end{aligned} \tag{13-29}$$

$$g(s) = -\rho s \frac{u_p(s) m h \Delta}{m h \Delta + m h_0 + \epsilon} e^{st} \tag{13-30}$$

Let

$$\Gamma(s) = \frac{m h \Delta}{m h \Delta + m h_0 + \epsilon} \tag{13-31}$$

The poles of the Eq. (13-29) are the same poles of the flow velocity profile in Eqs. (13-20) and (13-21) therefore the pressure gradient can be described as:

$$\frac{dP(x, t)}{dx} = Res(g(s), -i\omega) + Res(g(s), i\omega) + Res(g(s), z_n) \tag{13-32}$$

Where

$$Res(g(s), -i\omega) = [(s + i\omega)g(-i\omega)] = -\frac{\rho \omega A_0}{2} \Gamma(-i\omega) e^{-i\omega t} \tag{13-33}$$

$$Res(g(s), i\omega) = [(s - i\omega)g(i\omega)] = -\frac{\rho \omega A_0}{2} \Gamma(i\omega) e^{i\omega t} \tag{13-34}$$

For calculation of the residue function of the poles (z_n)

$$Res(g(s), z_n) = \sum_{n=1}^{\infty} \frac{2\rho A_0 \omega \alpha_n^4 v^2 h [\cos \alpha_n (h - h_o)]}{(\alpha_n^4 v^2 + \omega^2) \xi} e^{-\alpha_n^2 vt} \quad (13-35)$$

Using Eqs. (13-33)- (13-35), the pressure gradient can be expressed as:

$$\begin{aligned} & \frac{dP(x, t)}{dx} \\ &= -\frac{\rho \omega A_0}{2} [\Gamma(-i\omega) e^{-i\omega t} + \Gamma(i\omega) e^{i\omega t}] \\ &+ 2\rho A_0 \omega v^2 h \sum_{n=1}^{\infty} \frac{\alpha_n^4}{(\alpha_n^4 v^2 + \omega^2)} \frac{[\cos \alpha_n (h - h_o)]}{\xi} e^{-\alpha_n^2 vt} \end{aligned} \quad (13-36)$$

For duct with length $x \rightarrow L$, the pressure drop can be calculated as the following:

$$\begin{aligned} & \Delta P(t) \\ &= -\frac{\rho L \omega A_0}{2} [\Gamma(-i\omega) e^{-i\omega t} + \Gamma(i\omega) e^{i\omega t}] \\ &+ 2\rho L A_0 \omega v^2 h \sum_{n=1}^{\infty} \frac{\alpha_n^4}{(\alpha_n^4 v^2 + \omega^2)} \frac{[\cos \alpha_n (h - h_o)]}{\xi} e^{-\alpha_n^2 vt} \end{aligned} \quad (13-37)$$